

CHAPTER 1.0

INTRODUCTION

1.1 Introduction to a Special Phase of Matter - Liquid Crystal

One of the first things we learned in school science lessons was that there are three states of matter - solid, liquid and gas. Some substances, however, exhibit intermediate state lacking some of the order found in crystalline solids, but possessing more order than found in liquids. These ordered fluids are called liquid crystals.

Crystalline solids, particles are orderly stacked in a lattice which is symmetric under discrete set of translation and rotations. Therefore, the molecules are positioned in fixed orientations with no translational freedom. Conventional liquid have neither positional nor orientational order, the molecules are mobile and have no orientations with any translational freedom. Liquid crystals, on the other hand, might have no positional order, but maintain some orientational order. The molecules in all liquid crystal phases, one molecular axis tends to point along a preferred direction as the molecules undergo diffusion. This preferred direction is called the director and is denoted by the unit vector n (Collings and Hird, 1997a). Figure 1.1 shows the comparison of orientational and positional order among crystalline solid, liquid crystal and isotropic liquid. A fully ordered crystalline solid is heated, the thermal motions of the molecules within the lattice increase and

eventually the vibrations become so intense that the regular arrangement of molecules is broken down with the loss of long-range orientational and positional order to give the disorganized isotropic liquid. When this process occurs by way of one or more intermediate phases as the temperature increased, these phases are called as mesophases and some of these mesophases are liquid crystalline (Collings and Hird, 1997a).

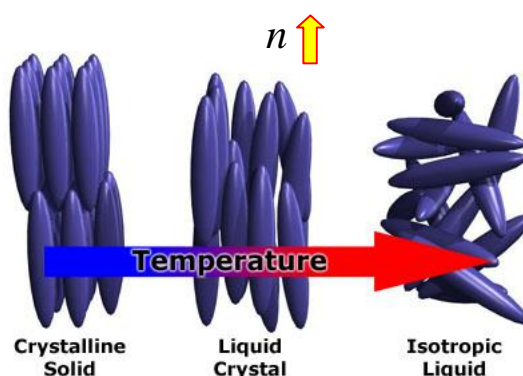


Figure 1.1: Orientational and positional orders in the crystalline solid, liquid crystal and isotropic liquid states.

1.2 Historical Perspective

Liquid crystals are recognized as a stable phase for many compounds, thus putting them on equal footing to the solid, liquid and gas phases. This situation is quite a recent development, existing for about the last 40 years.

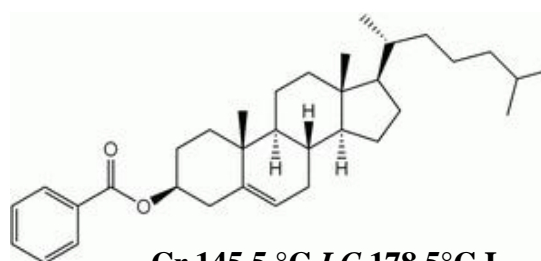
The discovery of liquid crystals was attributed to an Austrian botanist, Friedrich Reinitzer. In year 1888, he experimented with a substance related to

cholesterol and noted that it had two different melting points. He found that the substance started to melt at 145.5 °C from a solid to a cloudy liquid. At 178.5 °C, the cloudiness suddenly disappeared, giving way to a clear transparent liquid. This strange phenomenon was further investigated by Otto Lehmann, a professor of natural philosophy (physics) in Germany (Singh, 2002). After investigation, he became more convinced that the opaque phase was a uniform phase of matter sharing properties of both liquids and solids and began to name this mesomorphic state as "Flüssige Kristalle" (Liquid Crystals).



(a)

(b)



(c)

Figure: 1.2: (a) Friedrich Reinitzer and (b) Otto Lehmann. (c) Molecular structure of cholesteryl benzoate and its transition temperature (Singh, 2002).

In year 1969, Hans Kelker succeeded in synthesizing a substance

that exhibited a nematic phase at room temperature, *N*-4-methoxybenzylidene-4-butylaniline, MBBA, which is one of the most popular subjects of liquid crystal research (Kelker and Hatz, 1980).

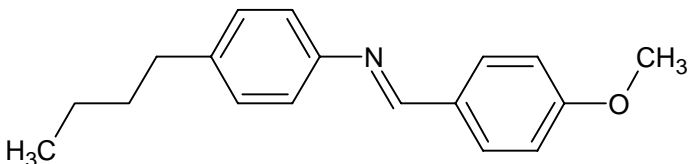


Figure: 1.3: Molecular structure of MBBA.

In order to establish a relationship between molecular structure and liquid crystalline properties, systematic modifications of the modified structure of mesogens were undertaken, leading to the discovery of the most technologically advance and commercially important class of mesogens: 4-phenyl-4'-cyanobiphenyls (CB) with low melting temperatures by George Gray (Gray *et al.*, 1973).

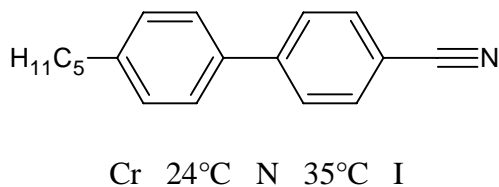


Figure: 1.4: Molecular structure and phase transition of 4-phenyl-4'-cyanobiphenyl (5CB) (Gray *et al.*, 1973).

1.3 Types of Liquid Crystals

Transitions to the mesophases may be brought about in two different ways,

one by purely thermal processes and the other by the influence of solvents. The liquid crystals obtained by the first method are called “thermotropics” whereas those obtained by the second one are “lyotropics”. This research work focused on thermotropic liquid crystals; however, a brief explanation of lyotropic liquid crystals is also given in the following section.

1.3.1 Lyotropic Liquid Crystals

Lyotropic liquid crystals are formed on the dissolution of most surfactants in a solvent (usually water). Surfactants are amphiphilic materials where constituent molecules are formed from a polar head group and a non-polar chain (often hydrocarbon). There exist several different types of lyotropic liquid crystal phase structures; each of these phases has a different arrangement of molecules within the solvent matrix (Figure 1.5). The concentration of the solute material in the solvent determines the kinds of lyotropic liquid crystal phase that is exhibited (Singh, 2002).

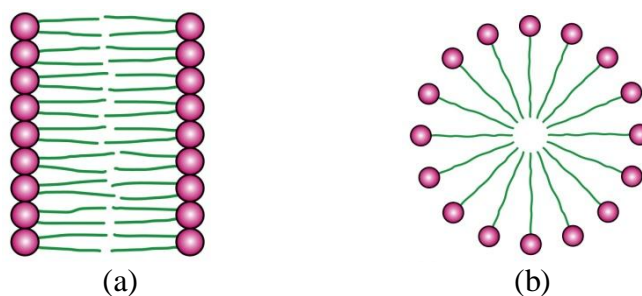


Figure 1.5: Structures formed by amphiphilic molecules in a polar solvent: (a) bilayer and (b) micelles (Singh, 2002).

1.3.2 Thermotropic liquid crystal

Considering the geometrical structure of the mesogenic molecules, the thermotropic liquid crystals can be grouped into two types. The liquid crystals derived from the rod shaped molecules are called “calamitics”. The mesophases formed from disc-like molecules are referred to as “discotics” (Figure 1.6).

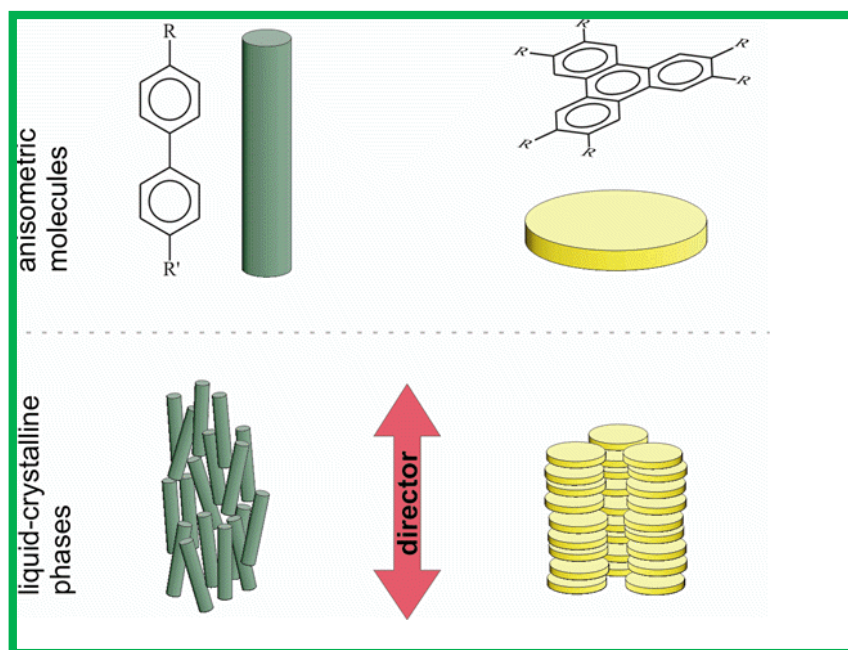


Figure 1.6: Example of the self-organization of anisometric molecules in liquid-crystalline phases.

1.3.2.1 Calamitic Liquid Crystals

Calamitic or rod-shaped liquid crystals are liquid crystal compounds that having an elongated shape as depicted in Figure 1.7, where the molecular length (L) is distinctly greater than the molecular breadth (B). It is important that the

molecule be fairly rigid for a least some portion of its length, since it must maintain an elongated shape in order to produce interactions that favour alignment (Collings and Hird, 1997b).

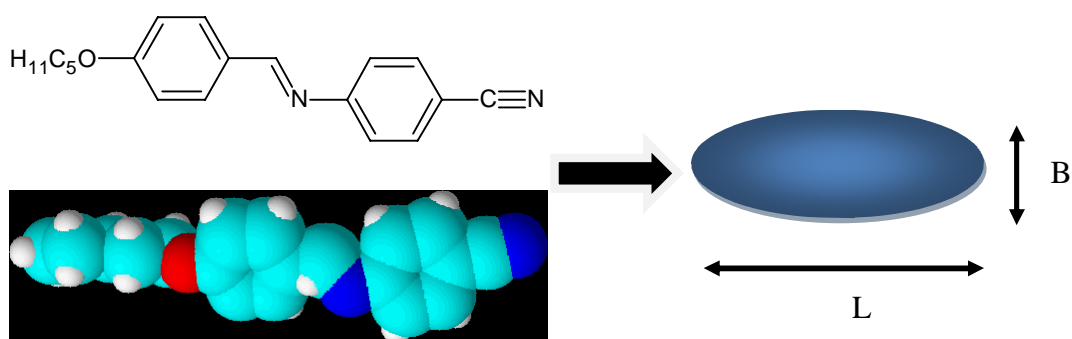


Figure 1.7: Typical calamitic liquid crystal molecule, where $L > B$.

1.3.2.2 Discotic Liquid Crystals

Discotic liquid crystals or disc shaped mesogen can orientated themselves in a layer-like fashion. Discotic molecules also show a great difference between lengths (height of the disc, L) and breadth (diameter, B). They usually consist of a rigid, flat core unit and flexible side chains, which surround the core. To ensure the disc-shaped geometry of the molecule, the core is often symmetric and an appropriate number of side chains are used. Similarly to the calamitic mesogen, the physical properties can be influenced over a wide range by variation of the core and/ or the side chains (Singh, 2002).

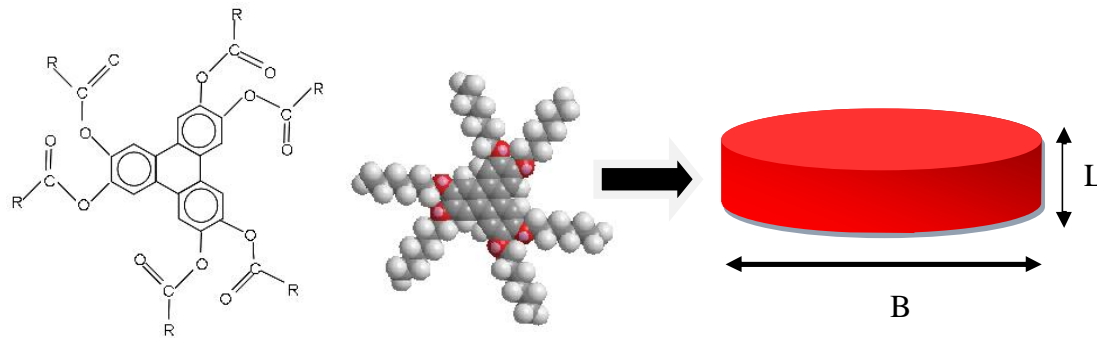


Figure 1.8: Typical discotic liquid crystal molecule, where $B > L$.

Columnar liquid crystals are different where they are shaped like discs instead of long rods. This mesophase is characterized by stacked columns of molecules. The columns are packed together to form a two-dimensional crystalline array. The arrangement of the molecules within the columns and the arrangement of the columns themselves lead to new mesophases.

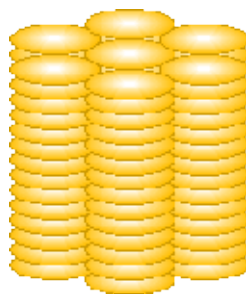


Figure 1.9: Typical columnar liquid crystals molecule.

1.4 Calamitic Liquid Crystal Phases and Textures

A typical calamitic mesogen consists of a rigid core unit, ensuring the anisotropic character, together with flexible side chains, which provide stabilizing effects within the liquid crystals phases. Certain structural features are often found

in molecules forming liquid crystal phases, and they may be summarized as follows:

1. The molecules have anisotropic shape. Liquid crystallinity is more likely to occur if the molecules have flat segments.
2. A fairly good rigid backbone containing double bonds defines the long axis of the molecule.
3. The existence of the strong dipoles and easily polarizable groups in the molecule seems important.
4. The groups attached to the extremities of the molecules are generally of lesser importance.

1.4.1 Nematic Phase

The least ordered mesophase is the nematic (n) phase. Nematic phase is the simplest liquid crystal phase. The nematic phase is the one-dimensional order elastic fluid. The molecules only have maintained a preferred orientational order and no long range positional order. In the calamitic nematic phase tend to diffuse throughout the sample where their long axes pointing in the same direction. The direction is called the director and usually denoted as n (Figure 1.10).

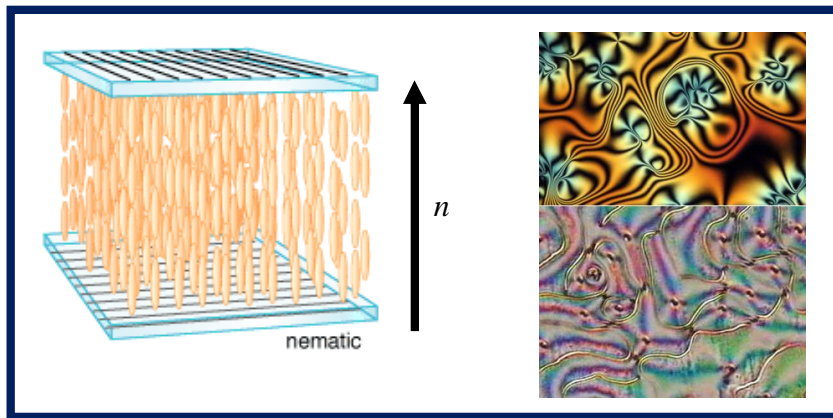


Figure 1.10: Molecular structure arrangement and liquid crystal texture (Schlieren or Tread-like) of Nematic phase (Demus and Richter, 1987 and Dierking, 2003).

1.4.2 Smectic Phase

The smectic phases are another significant mesophase of mesogenic substances. The word “smectic” is derived from the Greek word for soap. Molecules in this mesophase show a degree of translational order not present in the nematic. In smectic, the molecules maintain the general orientational order, but also tend to align themselves in layers or planes. Motion is restricted within these planes, and separate planes are observed to flow past each other. The increased order means that the smectic phase is more “solid-like” than the nematic. Smectic phases can generally divide into two kinds, smectic A and smectic C.

1.4.2.1 Smectic A phase

Generally, the molecules in smectic A phase are arranged in diffuse layers. The direction of the long axes of the molecules is perpendicular to the layer planes which the molecule are more likely to be (Figure 1.11).

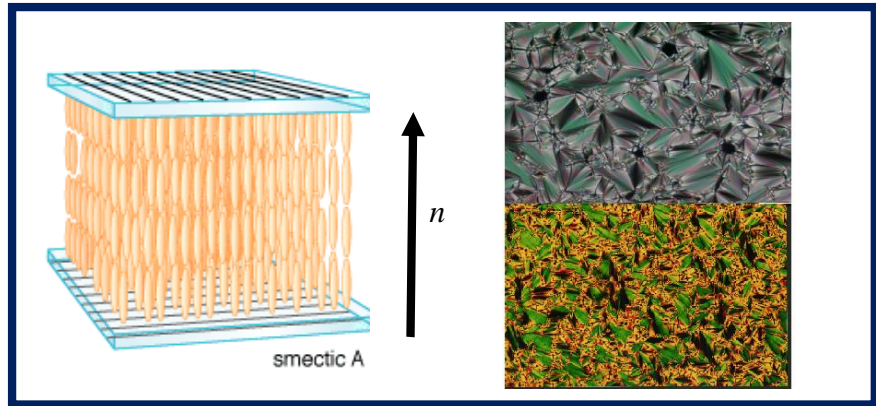


Figure 1.11: Molecular structure arrangement and liquid crystal texture (Fan-shaped or Focal-conic) of Smectic A phase (Demus and Richter, 1987 and Dierking, 2003).

1.4.2.2 Smectic C phase

For smectic C phase, the molecules are arranged in diffuse layers where the molecules are tilted at a dependent angle, q . The angle made between the layer normal and the director is called the tilt angle and generally increases with decreasing temperature (Figure 1.12). Smectic C (or simply, C) is the most important phase with regard to polar order in LCs.

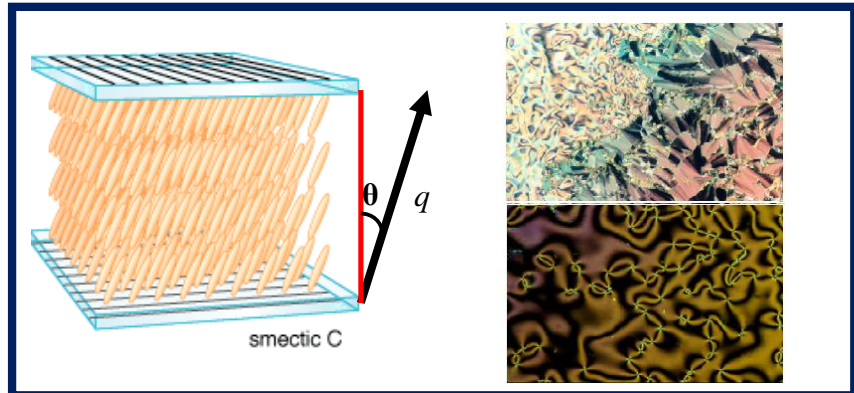


Figure 1.12: Molecular structure arrangement and liquid crystal texture (Focal-conic or Schlieren) of Smectic C phase (Demus and Richter, 1987 and Dierking, 2003).

1.4.3 Cholesteric phase

In the cholesteric phase, also known as *chiral nematic phase*, N^* , it exhibits chirality. Normally, only chiral molecules exhibit cholesteric phases; however, reduced space symmetry can also give rise to such phase. This phase exhibits a twisting of the molecules which form a helical shape and perpendicular to the director (Figure 1.13).

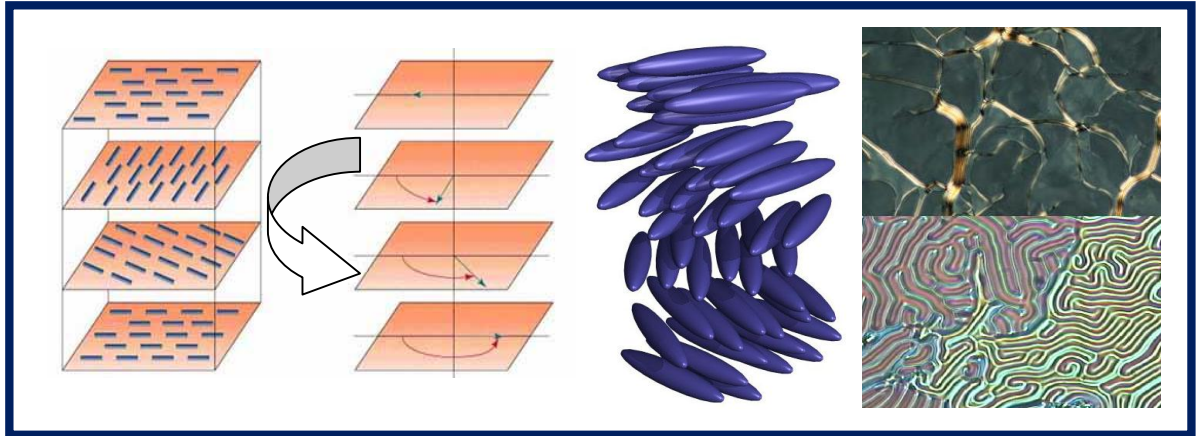


Figure 1.13: Molecular structure arrangement and liquid crystal texture (Cholesteric or Oily-streak defects) of Cholesteric phase (Demus and Richter, 1987 and Dierking, 2003).

1.5 Calamitic Liquid Crystals

Calamitic liquid crystals occur in rod-like molecules, which may consider, as the classical liquid crystals. The molecules show a large difference in length and breadth, thus delivering the required anisotropy. This class of mesogen was the first one to be detected, and the greatest part of research has also been dealing with these mesogens. A typical type calamitic mesogen consists of a rigid core unit, flexible side chains, allowing design molecules for a specific purpose. There are different possibilities for liquid crystal phases built by calamitic mesogens. A general structural model for calamitic LCs is illustrated in Figure 1.14.

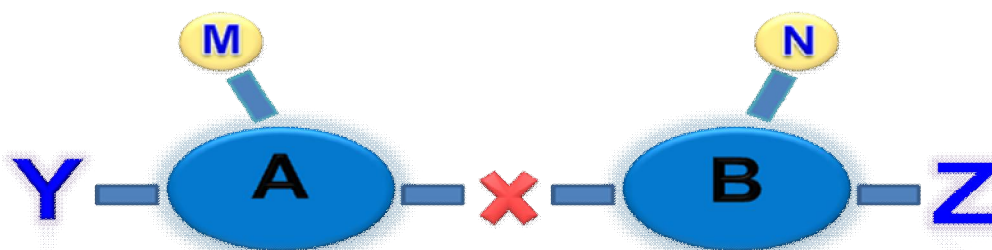


Figure 1.14: General structural template for calamitic liquid crystals (Collings and Hird, 1997b).

Rod-like molecules formed by two rings systems, A and B are the core units which are sometimes linked by a linking group (x) but more often a direct link is used. Similarly, the terminal chains (Y and Z) can be linked to the core. Lateral substituents (M and N) are often used to amend the physical properties and the mesophase morphology of liquid crystals to enhanced properties for application.

1.5.1 Core Structures

Core is usually defined as the rigid unit which is constructed from the linearly linked ring units; it also includes any linking groups and any lateral substituents connected to the rings. These range all the way from the early aromatic single benzene rings to alicyclic, heterocyclic and a wide variety of combination. Some of the common mesogenic cores are shown in Figure 1.15.

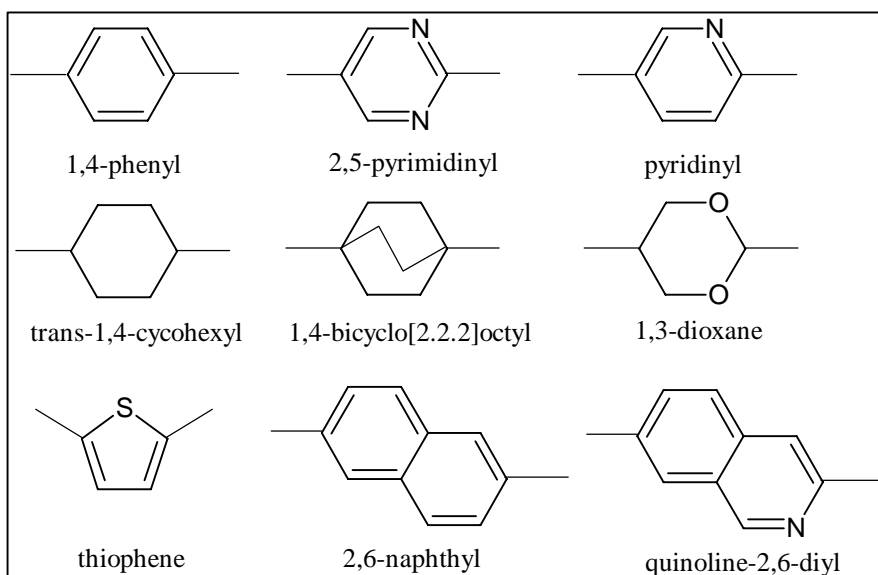
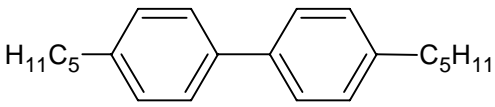
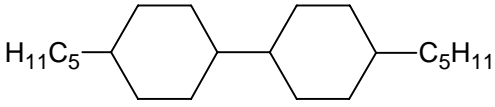


Figure 1.15: Common mesogenic core in calamitic mesogens.

The rigid core alone is not usually sufficient to generate liquid crystal phases. At least two rigid cores are needed to give a calamitic shaped molecule. For example, a biphenyl structure is a good liquid crystal with strong smectic phase stability. From Table 1.1, the core unit of compound A is wholly aromatic and this allows for good lateral attractions which are necessary for the formation of the smectic phase. Similarly, the analogous material with a wholly alicyclic core (compound B) is strongly smectic. In fact, compound B has significantly higher smectic phase stability than the aromatic material. The exceptionally high transition temperature of compound B reflects the strong ability of cyclohexane rings to pack together in a lamellar arrangement (Collings and Hird, 1997b).

Table 1.1: Transition temperature of 4,4'-dipentylbiphenyl and 4,4'-dipentyl-bicyclohexane (Collings and Hird, 1997)

	Compound	Transition temperature (°C)
A		Cr 26.0 SmX 47.6 SmY 52.2 I
B		Cr 40.0 SmB 110.4 I

1.5.2 Linking Group

Linking groups are normally those structural units, other than a direct bond, that connect one part of a core to another (Figure 1.16).

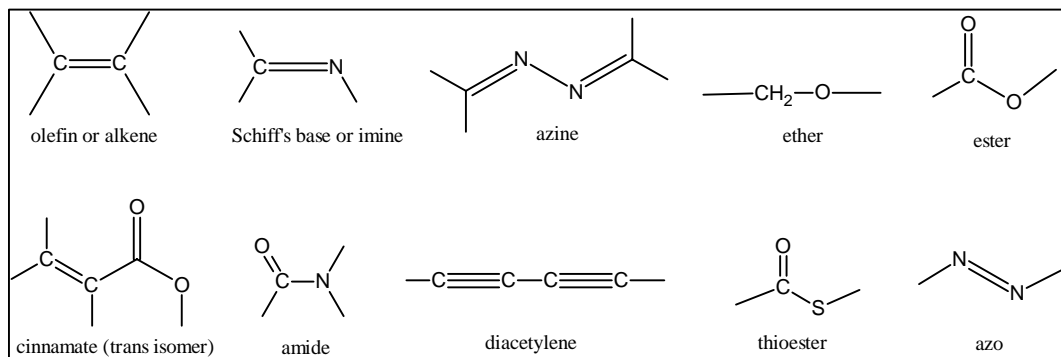
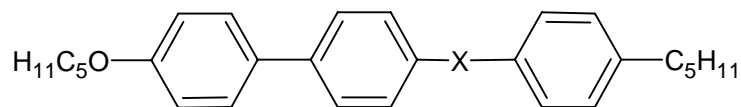


Figure 1.16: Connecting groups and their common names.

The introduction of a linking group into a mesogen increases the overall molecular length and enhances the polarizability anisotropy, hence improves the stability and range of mesogen. The effectiveness of seven different types of linking groups in the mesophase stabilization deduced from the three-ring derivatives of biphenyl is reported by Nagamine *et al.* (2008). The mesophase stabilization (clearing temperature) of the compound was strongly depending on

the linking groups (Table 1.2). In the series, the order of the effectiveness (-CH=CH- > -CONH- > -CH=N- ~ -CH=CHCOO- > -COO- > -CH₂CH₂- > -CH₂CH₂OCO-) is in general agreement with results for simple two-ring benzene derivatives. This reflects the importance of rigidity and the electronic interactions of the linking group with aromatic rings. The highest T_c (267 °C) is observed for -CH=CH- derivative (compound **5**) while the lowest T_c (111 °C) among the series is observed for -CH₂CH₂OOC- derivative (compound **7**). For -CH=CHCOO- derivative (compound **3**), it possessed higher T_c than azomethine derivative (compound **4**). This can be ascribed to the relatively large contribution of the acrylate group to the molecular anisometry in the two-ring compounds. Besides that, the comparison of the two linking groups (-CH=CHCOO- derivative and -CH₂CH₂OOC- derivative), the reduction of the double bond increases the molecular flexibility, which in turn results in the depression of the clearing temperature. The amido (-CONH-) derivative exhibited second highest T_c (260 °C). Its geometry is similar to that of ester group, but unlike the amido group is H-bond donor and capable of forming strong hydrogen bonds. The amido group increases both the melting and clearing points and preferentially stabilizes the mesophase.

Table 1.2: Transition temperature of three-ring derivatives of biphenyl (Nagamine *et al.*, 2008)



Compound	X	Clearing Temperature, T _c (°C)
1	CH ₂ CH ₂	158
2	COO	203
3	CH=CHCOO	245
4	CH=N	236
5	CH=CH	267
6	CONH	260
7	CH ₂ CH ₂ OOC	111

1.5.3 Terminal moieties

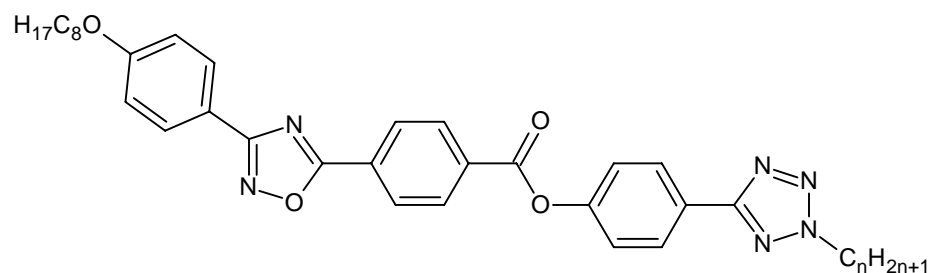
Terminal moieties are usually moderately long linear hydrocarbon alkyl chains, branched chains, or small polar substituents on the chains sometimes employed, particularly where a chiral centre is required (Hird, 2007). The choice of terminal moieties is crucial in the generation of a specific type of liquid crystal phase. Physical properties are also strongly dependent upon the choice of terminal units.

1.5.3.1 Straight Chains

Long alkyl/alkoxy chains add flexibility to the rigid core structure that tends to reduce melting points and allow liquid crystal phases to be exhibited.

Additionally, the alkyl/alkoxy chains are believed to be responsible in stabilizing the molecular orientations necessary for liquid crystal phase generation. The influence of the terminal alkyl chain on mesogenic properties was reported by Luciano *et al.* (2008). From the study, it showed that the increase of the carbon atom in the alkyl chain causes an increase in the existence range of the SmC mesophase, to the detriment of the SmA and nematic mesophases. This is due to the long aliphatic chains favour the smectic phase formation. From Table 1.3, the homolog with $n = 6$, the mesophase stability range was 104.8 °C, decreasing to 93.8 °C for the homolog with $n = 8$, and then increasing to the homolog with $n = 10$ to 102.5 °C.

Table 1.3: Transition temperatures of tetrazole and 1,2,4-oxadiazole mesogens with different carbon chain (Luciano *et al.*, 2008)

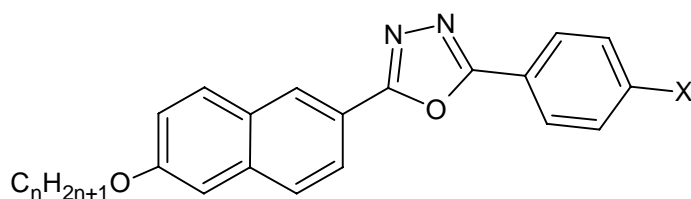


Compound	Carbon Number, n	Transition Temperature, Tc (°C)
A	6	Cr 106.3 SmC 135.0 SmA 158.2 N 211.1 I
B	8	Cr 107.7 SmC 163.7 SmA 193.8 N 201.5 I
C	10	Cr 108.1 SmC 163.4 SmA 176.2 N 210.6 I
D	12	Cr 101.7 SmC 159.5 SmA 179.0 N 194.4 I

1.5.3.2 Polar Groups

Polar groups, while not necessary reducing melting points, enable considerable and significant intermolecular forces of attraction which serve to stabilize molecular orientation. Sung and Lin (2004) had reported the influence of different polar substituents (Me, OMe, Cl, F, CN and NO₂) on a series of 1,3,4-oxadiazoles-based liquid crystals. The chloro-substituted derivatives generate a larger dipole than the fluoro-substituted derivatives because of the longer bond distance from chlorine to carbon. Both melting and liquid crystallization temperatures (on cooling) increase with the increasing terminal dipole. Besides that, the mesogenic phase range also increase with increasing terminal dipoles during heating, OMe < F < Cl < CN < NO₂. Thus, the mesogenic phase range of the oxadiazole-based structures can be enlarged by increasing the terminal dipoles, and that both melting and clearing temperatures can also be raised (Table 1.4).

Table 1.4: Transition temperature of 1,3,4-oxadiazoles-based mesogens with different terminal substituents (Sung and Lin, 2004)

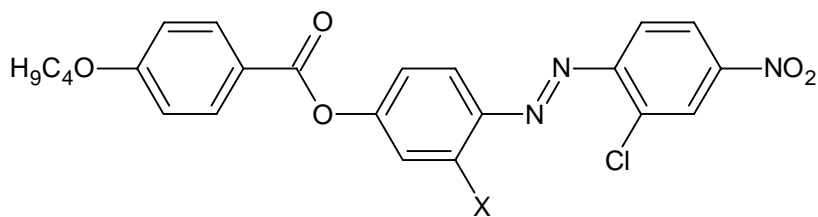


Compound	X	Transition Temperature, T _c (°C)
1	Me	Cr 121.0 I
2	OMe	Cr 109.4 N 114.6 I
3	F	Cr 100.0 SmE 127.0 SmA 134.9 I
4	Cl	Cr 105.1 Cr ₁ 143.1 SmA 159.9 I
5	CN	Cr 65.5 Cr ₁ 143.3 SmA 167.1 I
6	NO ₂	Cr 91.9 SmX 141.5 SmA 202.6 I

1.5.4 Lateral Substituents

Lateral substituent is the one that attached off the linear axis of the molecule, usually on the side of an aromatic core. Table 1.5 summarises the transition temperature and molecular structure of butyloxy derivative of compounds **A** and **B** reported by Prajapati and Varia (2008). The mesophase range of compound **A** is higher by 125.0 °C and 59.5 °C, respectively, than those of compound **B**. Molecules of compound **A** and **B** differ only in the lateral substituent at the central benzene ring. Compound **A** has a lateral phenolic –OH group, whereas compound **B** has a lateral methyl group at that position. The latter increases the breadth of the molecules leading to a decrease in mesophase thermal stabilities. The phenolic –OH group is bonded to the ortho position of azo central linkage, leading to intramolecular hydrogen bonding and higher nematic mesophase length as well as thermal stabilities.

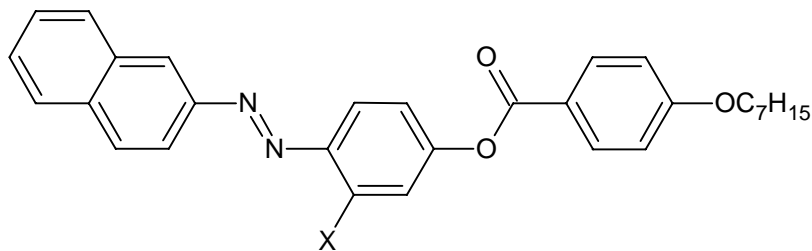
Table 1.5: Transition temperature of azo mesogens with polar chloro, nitro and phenolic –OH substituents (Prajapati and Varia, 2008)



Compound	X	Transition Temperature, T _c (°C)
A	OH	Cr 133 N 258 I
B	CH ₃	Cr 116 N 175.5 I

Table 1.6 shows the comparison of N-I transition temperature and molecular structure of compound **1**, **2** and **3**. The molecular structure of compound **1** differs from compound **2** only at the central aromatic core; compound **1** has lateral chloro group at the central benzene nucleus, whereas compound **2** has no lateral substituent at the same position. The molecule of compound **1** has increased breadth due to the lateral chloro group on central benzene ring. However, the lateral chloro group not only increases the breadth of the molecule of compound **1** but also increases the acoplanarity in the system due to steric interaction. Both these factors would eliminate the smectogenic tendencies as well as decrease the nematic mesophase range and the clearing temperature for compound **1**. The molecular structure difference between compound **1** and **3** lies only at the central aromatic core: compound **3** has a lateral methyl group. The increase in the polarizability of the compound **1** due to the polar chloro group slightly overcomes the increased molecular separation caused by the lateral substituent. Therefore, the width of the nematic mesophase as well as N-I transition temperature of compound **1** becoming a little higher than that of compound **3** (Prajapati *et al.*, 2004).

Table 1.6: Transition temperature and molecular structure of compound 1, 2 and 3 (Prajapati *et al.*, 2004)



Compound	X	Transition Temperature, T _c (°C)
1	Cl	Cr 92.0 N 171.0 I
2	H	Cr 135.0 N 218.0 I
3	CH ₃	Cr 86.0 N 147.0 I

1.6 Objectives of the Project

The objectives of the project are listed below:

- (a) To synthesize novel heterocyclic liquid crystals consisting of two to three core units (series 1, 2, 3, 5, and 6) and dimeric compounds (series 4). The compounds synthesized were as follows:

Series 1: 6-Methyl-2-(4-alkoxybenzylidenamino)benzothiazoles (**nMeBTH**), 6-methoxy-2-(4-alkoxybenzylidenamino)benzothiazoles (**nOMeBTH**), 6-ethoxy-2-(4-alkoxybenzylidenamino)benzothiazoles (**nOEtBTH**) and 2-(4-alkoxybenzylidenamino) benzothiazoles (**nHBZT**).

- Series 2: 6-Methyl-2-[4-(4-alkoxybenzoyloxy)benzyliden-amino]benzothiazoles (**nMe3R**), 6-methoxy-2-[4-(4-alkoxybenzoyloxy)benzylidenamino]benzothiazoles (**nOMe3R**) and 2-[4-(4-alkoxybenzoyloxy)benzyliden-amino]benzothiazoles (**nHB3R**).
- Series 3: 2-[3-Methoxy-(4-alkoxybenzoyloxy)phenyl]-benzothiazoles (**nMOBZT**) and 2-[3-ethoxy-(4-alkoxybenzoyloxy)phenyl]benzothiazoles (**nEOBZT**)
- Series 4: α,ω -bis[6-Methoxy-2-(4-alkoxybenzylidenamino)]-benzothiazoles (**nOMeD**) and α,ω -bis[6-ethoxy-2-(4-alkoxybenzylidenamino)]benzothiazoles (**nOEtD**)
- Series 5: 5-Methyl-2-[4-(4-alkoxybenzoyloxy)benzylidenamino]-pyridines (**nPM5B**)
- Series 6: 2-[4-(4-Alkoxybenzoyloxy)benzylidenanilines]thiophenes (**nTAP**)

(b) To elucidate the structures of the synthesized compounds via FT-IR, ^1H & ^{13}C NMR and EI-MS.

(c) To study the liquid crystalline properties of the synthesized compounds by using DSC, POM and XRD analysis.

(d) To study the influences of the structural modification on liquid crystalline properties of the synthesized compounds.

CHAPTER 2.0

LITERATURE REVIEW

2.1 Heterocyclic Core

Heterocycles are of great importance as core units in thermotropic liquid crystals due to their ability to impart lateral and/ or longitudinal dipoles combined with changes in the molecular shape (Seed, 2007).

Over many years, a larger number of liquid crystalline compounds containing heterocyclic units have been synthesized. Modern synthesis techniques allow researchers to access tailor-made materials with predictable properties, particularly in the field of liquid crystalline materials. The incorporation of heterocyclic moieties as core units in thermotropic liquid crystals can result in large changes in their mesophase and physical properties, because they possess more polarizable heteroatoms, such as nitrogen, oxygen and sulfur atoms (Lai *et al.*, 2005).

The heterocyclic compounds have lower symmetry and distinct polarizability than the corresponding phenyl analogues. The heterocyclic compounds also possess an extra permanent dipole moment that influences the dimension and direction of the total molecular dipole moment without raising the molecular breadth (Kardas *et al.*, 2001).

2.1.1 Mesomorphic Properties of Benzothiazole-based Liquid Crystals

The introduction of benzothiazole fused-ring system within the central core of a classical calamitic molecule has been found to be an interesting strategy to follow for the design of new liquid crystalline materials because of great possibilities in the variation of direction and magnitude of their permanent dipole moments and in consequence, variations of their mesomorphism and potential electro-optical properties (Belmar *et al.*, 1999). These types of heterocycles involved are usually five- or six-membered and they form part of the central core in typical rod-shape molecules. The non-linear 2,5-disubstituted benzothiazole unit (Figure 2.1a) is particular unfavorable for mesophase formation (exhibits a monotropic mesophase below 0 °C). However, the 2,6-disubstituted benzothiazole (Figure 2.1b) has a more linear molecular structure compare to that of the analogous 2,5-disubstituted and exhibit much higher clearing temperature (Aldred *et al.*, 2005a).

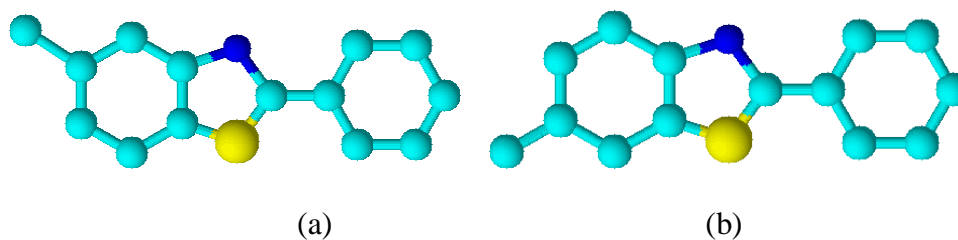
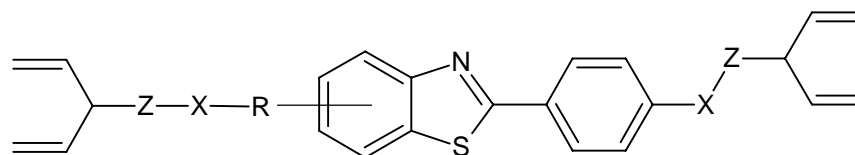


Figure 2.1: Molecular models of (a) 2,5-disubstituted benzothiazole (b) 2,6-disubstituted benzothiazole (Aldred *et al.*, 2005a).

Some liquid crystalline materials incorporating a benzothiazole-fused ring structure in the molecular core exhibit good hole-transporting properties with a low ionization potential, which make them of potential interest as hole-transporting material in Organic light-emitting devices (**OLEDs**). A series of benzothiazole liquid crystal having non-conjugated diene end groups were showed in Table 2.1.

The presence of the branching methyl group in compound **5** in the spacer led to a lower melting point as compared to compound **2** having the same spacer length owing to the steric effects related to the bulky methyl group. As expected, an additional phenyl ring in compounds **6** to **10** caused the higher melting and clearing temperatures due to the larger length-to-breadth ratio. Interestingly, the ester homologous (compounds **6** and **7**) exhibited nematic phase while ether homologous (compounds **8** to **10**) showed SmC phase (Aldred *et al.*, 2005a).

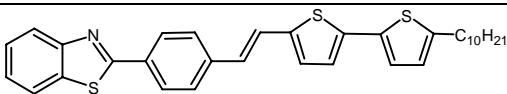
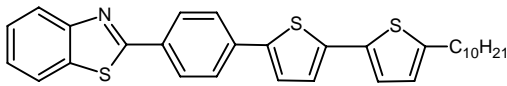
Table 2.1: Molecular structures and transition temperatures of benzothiazole liquid crystals having diene end groups (Aldred *et al.*, 2005a).



Compound	Position	R	X	Z	Transition temperature / °C () indicates monotropic
1	2,5	-	-OC ₅ H ₁₀	COO	Cr 40 (SmC-23) I
2	2,6	-	-OC ₅ H ₁₀	COO	Cr 63 (SmC 39) I
3	2,6	-	-OC ₇ H ₁₄	COO	Cr 55 SmC 64 I
4	2,6	-	-OC ₁₀ H ₂₀	COO	Cr 49 SmC 71 I
5	2,6	-	-OC ₁₀ H ₂₁	COO	Cr 53 SmC* 62 I
6	2,6	Ar	-OC ₅ H ₁₀	COO	Cr 82 N 147 I
7	2,6	Ar	-O(CH ₂) ₂ CHCH ₃ (CH ₂) ₂	COO	Cr 68 N 187 I
8	2,6	Ar	-OC ₅ H ₁₀	O	Cr 104 SmC 171 I
9	2,6	Ar	-OC ₆ H ₁₂	O	Cr 95 SmC 165 I
10	2,6	Ar	-OC ₈ H ₁₆	O	Cr 89 SmC 150 I

Two new donor-acceptor type liquid crystalline semiconductors based on benzothiazole have been studied by Dutta *et al.* (2010). The DSC and thermogravimetric analyse (TGA) show that these materials given excellent thermal stability and have decomposition temperatures in excess of 300 °C. Beyond 160 °C, both molecules show a smectic A liquid crystalline phase that exists till about 240 °C. The core benzothiazole ring acts as an electron acceptor unit because of the presence of sulfur and nitrogen atoms and alkyl substituted thiophene ring as a donor because of its high electron donating ability and charge carrier mobilities. These molecules show a smectic A liquid crystalline phase above the melting temperature, which results in a good alignment and packing of the molecule in the solid state. Other than that, the field-effect transistor performance of benzothiazole compound A shows that these materials have a great potential for future application in organic devices. The phase transition temperatures of both compounds are given in Table 2.2.

Table 2.2: Phase transition temperature of compounds A and B (Dutta *et al.*, 2010)

	Compound	Transition temperature (°C)
A		Cr 158 SmA 239 N 250 I
B		Cr 177 SmA 234 I

The carrier transport properties of liquid crystal compound, 2-(4'-heptyloxyphenyl)-6-dodecythiobenzothiazole (Figure 2.2) was studied by

Tokunaga *et al.* (2007). Liquid crystalline compounds incorporating a benzothiazole ring exhibited good hole-transporting properties with a low ionization potential. However, the compound has a relatively high melting temperature and SmA phase exhibited in a narrow range of temperature (90-100 °C). To serve as a liquid crystalline compound that can be used in the LCD devices, it has to contain at least a room or low temperature and high charge carrier mobility (Iino and Hanna, 2005).

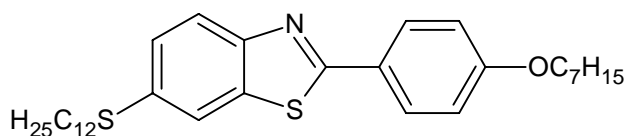
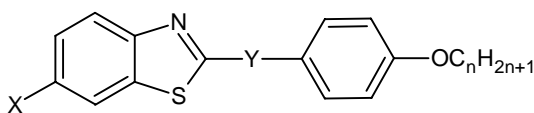


Figure 2.2: Structure of 2-(4'heptyloxyphenyl)-6-dodecythiobenzothizole (Tokunaga *et al.*, 2007).

Belmar *et al.* (1998) reported three different series of calamitic liquid crystals containing benzothiazole ring within the central core and different linking groups. From the study, the influence of the linkage group within the central core has been proven to determine the variety of mesomorphism displayed by the compounds. The compounds with imine and azo linkage behave in a similar way and exhibit typical nematic and smectic C mesophases. Compounds incorporating an amide linkage show poorer mesomorphism and mainly present a smectic C mesophase. Table 2.3 shows the molecular structures and mesomorphic properties of some benzothiazole liquid crystals comprising different linking and terminal groups. Compared among series I, II and III, series II which comprised amide

linkage possessed the highest average thermal stability of smectic and nematic phase. It was believed that the intermolecular hydrogen bonding promoted a higher thermal stability of mesophases.

Table 2.3: Molecular structures and mesomorphism properties of benzothiazole mesogens having different linking group and terminal group (Belmar *et al.*, 1998)



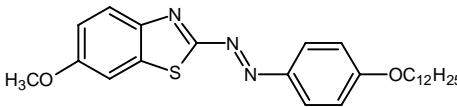
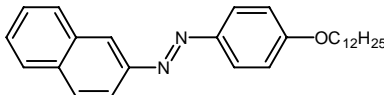
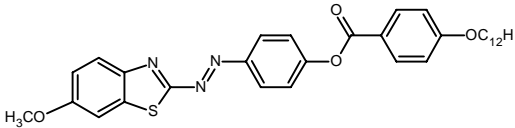
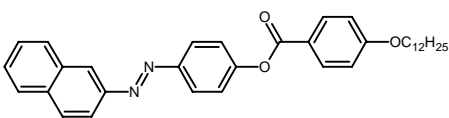
Series	n	Y	X	Average thermal stability (°C)	
				SmC	N
I	3 to 10	-N=CH-	-OC ₁₀ H ₂₁	108	118
II	3 to 10	-NHCO-	-OC ₁₀ H ₂₁	132	124
III	3 to 10	-N=N-	-OC ₁₀ H ₂₁	96	120

Prajapati and Bonde (2006b) reported two series of benzothiazole mesogens with methoxy substituents. Table 2.4 shows the comparison of transition temperatures, range (width) of mesophase phase and thermal stabilities and molecular structures of representative compounds **1** ($n = 12$) and **2** ($n = 12$) of the present series I and II with other structurally related compounds **A** and **B** reported in the literature. Both compounds **1** and **2** exhibited enantiotropic nematic mesophases. Mesophase length and nematic thermal stability of compound **2** are higher by 101 °C and 119 °C, respectively than that of compound **1**. This is due to the greater length of compound **2** provided by the additional aromatic ring and

ester linkage. This is also revealed in the comparison in between compound **A** and **B**.

Table 2.4 shows that compound **A** is non-mesogen, whereas compound **1** is mesogenic. Compound **A** differs only at one terminus where that compound **1** has a 6-methoxy benzothiazole ring at the terminus instead of naphthalene ring of compound **A**. The terminal benzothiazole ring enriches the overall polarizability of the molecule while reducing the symmetry of the molecule when compared to phenyl/ naphthyl derivatives and provides higher transition temperature.

Table 2.4: The transition temperature (°C), mesophase range and molecular structure of compounds 1, 2, A and B (Prajapati and Bonde, 2006b)

Compound	Transition temperature (°C)
1 	Cr 113 Sm (108)* N 135 I
A 	Cr 94 I
2 	Cr 131 N 254 I
B 	Cr (112) Sm 133 N 201 I

(*) Monotropic value

2.1.2 Mesomorphic Properties of Thiophene-based Liquid Crystals

Thiophene in particular has emerged as a core unit that is receiving increasing attention. Material containing thiophene core unit has significantly lateral dipole moments that help to contribute to physical parameters such as increased dielectric anisotropy and dielectric biaxiality. Five membered heterocycles have potential promise for flexoelectric application such as found in bistable nematic displays (Seed, 2007). Thiophene, and in particular oligothiophene-based materials, has merged as excellent semiconductors that show mobilities up to $1 \text{ cm}^2\text{V}^{-1}\text{s}^{-1}$. Addition of alkyl chains often leads to increased solubility that can aid in solution-based processing such as spin coating. Figure 2.3 shows the bond angles and dipole moments of thiophene ring.

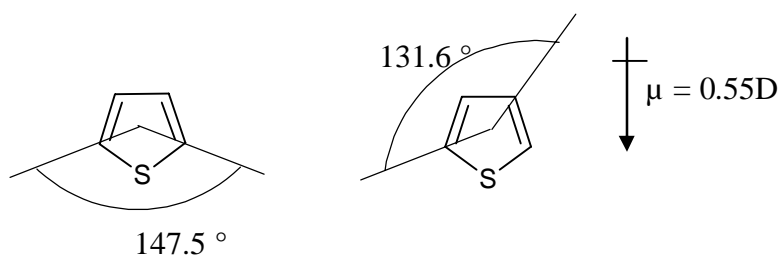
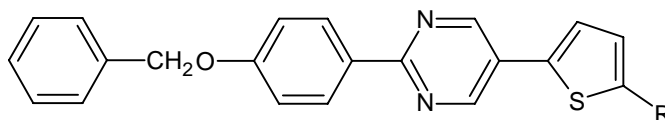


Figure 2.3: Bond angles and dipole moments of thiophene (Seed *et al.*, 2003).

Seed *et al.* (2003) reported that the incorporation of thiophene into molecular core can substantially increase the optical anisotropy and still provided molecules with relatively low melting points. The replacement of a phenyl ring with a 2,5-disubstituted thiophene leads to a reduction in the melting point.

A homologous series of thiophene-based liquid crystal compounds, 2-(4-benzyloxyphenyl)-5-(5-alkylthiophen-2-yl)pyrimidine was studied by Sharma *et al.* (2003a). From Table 2.5, compound **a** does not exhibit any mesophases. Compound **b** exhibited nematic and smectic C phase, whereas compound **c**, the nematic phase are lost and the compound exhibited smectic C, smectic X and alternating smectic C phases. By grow in number of the alkyl chain length is conducive to the formation of smectic phases. This is not surprising since the incorporation of the 2,5-disubstituted thiophene ring will give rise C-S-C angle at 148° in thiophene ring and this, coupled to fact that the thiophene ring is in a lateral position within the structure of the compounds, will give the molecule a hockey-stick-like structure. The incorporation of the alkyl group exaggerated the ‘bent’ nature of the ring. This dramatically decreased the melting point of the compounds, as well as reduced the tendency of the compounds to form the nematic phase but enhanced their ability to form smectic phases.

Table 2.5: Structure and transition temperature (°C) for the 2-(4-benzyloxyphenyl)-5-(5-alkylthiophen-2-yl)pyrimidines (Sharma *et al.*, 2003a)



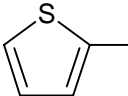
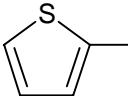
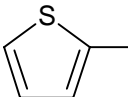
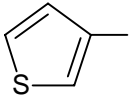
Compound	R	Transition Temperature (°C)
a	H	Cr 185.6 I
b	C ₅ H ₁₁	Cr 133.5 SmC 154.7 N 169.6 I
c	C ₁₀ H ₂₁	Cr 118.2 SmC* 121.3 SmX 133.2 SmC 166.4 I

Four homologous series of three-ring esters involving a five-membered heterocyclic ring have been synthesized in order to establish how a change in the position of the heterocyclic ring influences the liquid crystal behaviour. Table 2.6 summarizes the molecular structures and mesophases of thiophene liquid crystals having ester function. None of the compounds in series **A** give rise to liquid crystal phases. In these compounds, the heterocyclic ring occupies a central position. Conjugation is possible between the heteroatom of the rigid and both adjacent substituents, the ester function and the benzene ring. For series **B**, with the heterocyclic ring located in a terminal position, the presence of the phenyl ring restores linearity to the molecule and leads to reduce conjugation between the heteroatom and ester function. These compounds give rise to nematic phase.

In series **C**, thiophene ring maintain in the terminal position and the lone pair of the heteroatom may conjugate directly with the ester function setting up a permanent dipole, a substantial component of which is laterally disposed and hence likely to increase the lateral intermolecular cohesive forces and the tendency to form smectic mesophase. For series **D**, the 3-carboxylates are significantly more smectogenic than the 2-carboxylates. This may be due to a more substantial increase in the lateral dipolar interaction resulting from conjugation between the heteroatom of the heterocyclic ring and the ester function of the 3-carboxylates (Brown *et al.*, 1989).

Table 2.6: Molecular structures and mesophases of thiophene liquid crystals having ester function (Brown *et al.*, 1989)

$$R-X-Z-\text{C}_6\text{H}_4-\text{OC}_n\text{H}_{2n+1}$$

Series	R	X	Z	Mesophase
A	Ar		-COO-	Non-mesogen
B		Ar	-COO-	Nematic phase
C		-COO-	Ar	Nematic and Smectic phases
D		-COO-	Ar	Nematic and Smectic phases

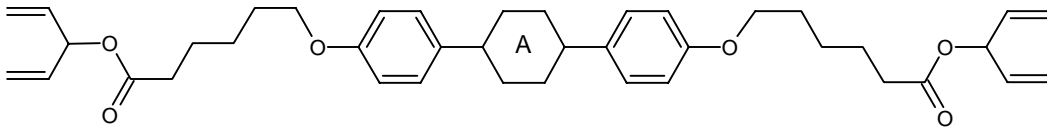
2.1.3 Mesomorphic Properties of Pyridine-based Liquid Crystals

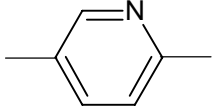
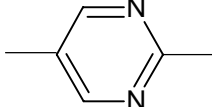
The heteroatom in a pyridine or related system is known to behave similarly in many respects to an aromatic nitro-group. The heteroatom has a high electronegativity and will therefore withdraw electrons from the other atoms of the ring system, making the ring deactivated relative to benzene. Pyridine derivatives are chosen as the rigid part of the target liquid crystalline molecules, because the lone pair electrons of the nitrogen atom in the core of the molecule generate a significant dipole moment to introduce attractive forces and thus to aid the formation of smectic phases. The lone pair electrons that introduce a dipole

moment in the molecules may also possess a high negative dielectric anisotropy. Thus, enhancing the electron affinity of a molecule can be achieved by synthesizing materials that include heterocyclic aromatic rings such as pyridine (Lai *et al.*, 1996).

The molecular structures shown in Table 2.7 differ by the number of nitrogen atoms present in the central aromatic ring. The pyridine **PYR-1** with one nitrogen atom in the central ring possesses a similar clearing point to that of the corresponding pyrimidine **PYM-1** with an otherwise identical structure apart from the replacement of another C-H unit by a nitrogen atom. However, the melting point is much higher, which leads to a narrower mesophase temperature range for the pyridine. The low melting temperature of **PYM-1** allows device fabrication to be carried out at room temperature when **PYM-1** is used as a charge-transporting layer (Aldred *et al.*, 2005b).

Table 2.7: Transition temperature (°C) of compounds PYR-1 and PYM-1 (Aldred *et al.*, 2005b)



Compound	A	Cr	SmC	I
PYR-1		● 87	● 126	
PYM-1		● 25	● 124	

A homologous series of 3-N-(4'-alkoxybenzylideneamino)-6-*n*-alkylpyridines has been synthesized by Rudolph A. Champa (1973) and compared to the carbocyclic analogs. The heterocyclic compounds exhibited lower melting point than the corresponding analogs and the results also show consistently lower clearing point for all comparable cases (Figure 2.4). The thermal nematic stabilities are lowered an average of about 40 °C for the pyridine anils. The differences in transition temperatures between the benzene and pyridine anils are dependent upon at least two factors. One is the presence of an additional permanent dipole in the pyridine anils. The second factor is the difference in symmetry. The additional permanent dipole in the pyridine anils, without an attendant increase in molecular breadth, might also be expected to increase the lateral to terminal attractive force ratio to the exclusion of a nematic phase. The reduced symmetry of the heterocyclic anils could be a factor in lowering the thermal nematic stability (Champa, 1973).

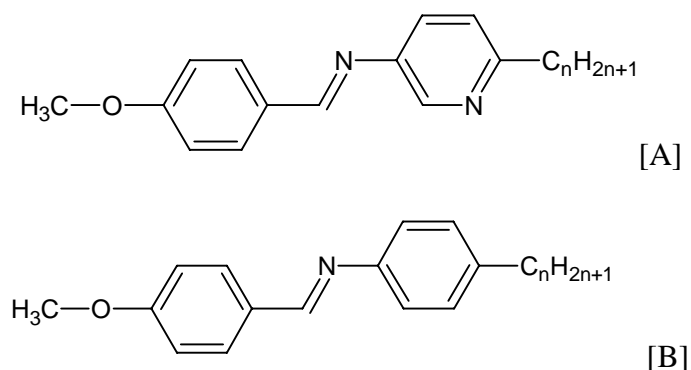
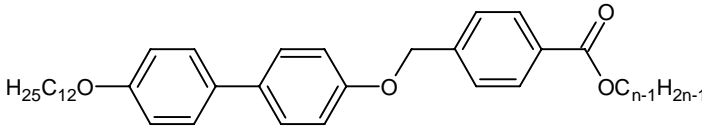
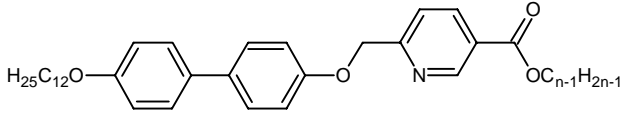


Figure 2.4: Heterocyclic pyridine anils [A] compared to carbocyclic analogs [B].

Kardas *et al.* (2001) reported two homologous new compounds forming both antiferroelectric and ferroelectric phases obtained from pyridyl and phenyl derivatives. Compounds of series **2** with the pyridine moiety substituted at the 3rd position by an n-alkyl ester group exhibit typical mesophase polymorphism. For the shortest homologues, the orthogonal SmA phase is observed whereas extension of the alkyl chain results in a sequence of tilted smectic phases. For the analogous phenyl derivatives, soft crystalline phases (CrB, CrE) appear and exist in the broad temperature range. The clearing temperatures for compounds of series **1** are about 10K higher and melting temperatures about 20K lower than for compounds of series **2** with the same molecular length. Moreover, the difference in the layer spacing in the tilted phases was observed between relevant homologues of series **2** and **1**, and higher tilt angles for pyridine compounds were observed.

Table 2.8: Phase transition temperatures (°C) for the compounds of series 1 and 2 (Kardas *et al.*, 2001)

		Series 1
		Series 2
Series	<i>n</i>	Phase Transition Temperature (°C)
1	1	Cr 136.3 CrE 172.9 CrB 198.6 SmA 204.4 I
	4	Cr 89.0 CrX 123.7 CrJ 124.6 SmI 152.8 SmC 166.6 169.9 I
	8	Cr 94.3 CrX 117.2 CrJ 120.7 SmI 142.1 SmC 158.4 I
2	1	Cr 175.2 SmA 187.3 I
	4	Cr 109.8 CrX 110.8 CrJ 113.4 SmI 125.1 SmC 153.8 I
	8	Cr 107.2 CrX 113.4 SmI 119.4 SmC 150.2 I

2.1.4 Mesomorphic Properties of Symmetrical Dimeric Liquid Crystals

Liquid crystal dimers consist of molecules involving two mesogenic units separately by a flexible spacer (even/ odd) (Figure 2.5). Dimers containing uniform mesogenic unit are referred to as symmetric dimers while non-symmetric dimers consists of two differing mesogenic groups. Four different series of dimer mesogens having ether-linked or methylene-linked spacers (Table 2.9) was studied by Henderson *et al.* (2005).

Ether- and methylene-linked dimers arise from differences in molecular geometry especially from the bond angle between the *para* axis of the mesogen and the first bond in the spacer. For the methylene-linked dimers this bond angle is 113.5° while for ether-linked dimers is 126.4° . This diversity makes the all-*trans* conformation of an ether-linked dimer more linear than that of the corresponding methylene-linked dimer. Hence, the greater shape anisotropy of the ether-linked dimers would be expected to give rise to higher mesophase transition temperatures.

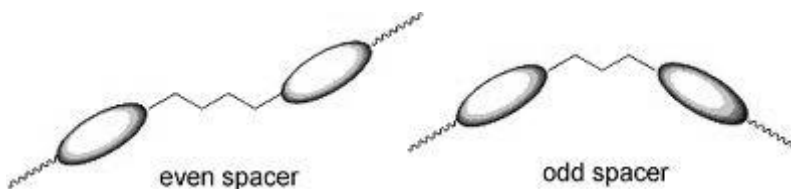
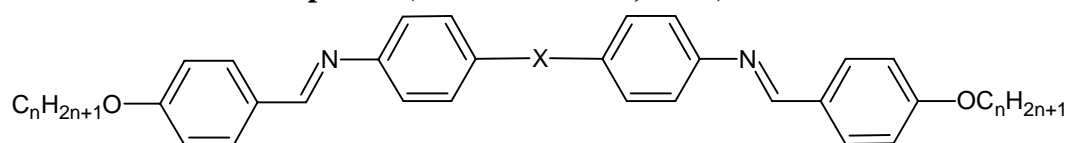


Figure 2.5: General molecular structure of dimer with even or odd spacer.

The melting temperatures of ether series were higher than the methylene dimers and the decreased in melting temperature is greatest for the even-number dimers. These rise from a subtle interplay of the effects of changing the molecular shape and the molecular interactions on switching from ether to methylene links. However, for the clearing temperatures, even-membered dimers all were exhibit higher than those of the corresponding methylene-linked dimers. Changing from an even-membered to an odd-membered spacers causing a greater reduction

Table 2.9: Molecular structures and mesomorphsim properties of liquid crystal dimers containing ether-linked or methylene-linked spacers (Henderson *et al.*, 2005)



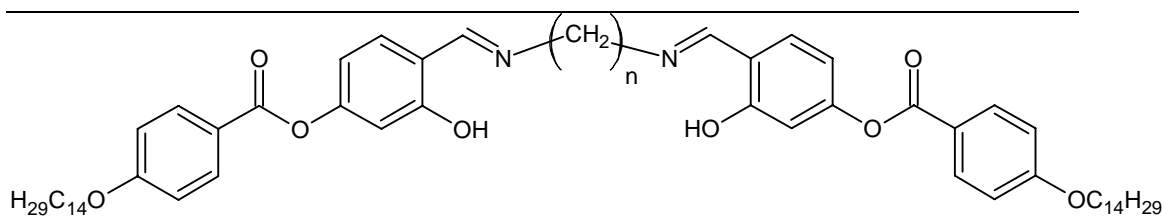
Series	n	X	Average thermal stability (°C)	
			Melting Temperature	Clearing Temperature
A	1 to 10	-(CH ₂) ₅ -	116.2	108.4
B	1 to 10	-(CH ₂) ₆ -	104	193.4
C	1 to 10	-O(CH ₂) ₃ O-	167.7	159.4
D	1 to 10	-O(CH ₂) ₄ O-	201.8	217.6

in the clearing temperature than does substituting an ether link with a methylene link. This may suggest that molecular shape plays a more important role in determining clearing temperatures than it does in determining the melting temperatures (Henderson *et al.*, 2005).

A homologous series of compounds derived from salicylaldehyde were reported by Hsieh *et al.* (2006). From Table 2.10, the results indicated that all compounds with an even-carbon spacer ($m = 2, 4, 6, 8$) exhibited SmC phase; however, all other compounds with an odd-carbon spacer ($m = 3, 5, 7$) formed banana phases. The different in phase behaviour was attributed to the dependence of the molecule shape and/or geometry on the parity of the central spacer when considered in the all-*trans*-conformation. The structural conformation and mesomorphic properties observed by this type of LC dimer are quite different from conventional molecular mesogens and are also significantly influenced by the structure and the spacer length and the linking group as well. A common spacer such as alkylene ($-\text{CH}_2-$), dioxyalkylene spacer $[-(\text{OCH}_2)_n\text{O}-]$ or ester $[-\text{COO}(\text{CH}_2)_n\text{OOC}-]$, has been widely applied to generate such twins.

In the bent-core molecules, the bent central unit, the rod-like wings and the linking (or spacer) group constitute the overall bent core. The bending angle is best estimated as $105-120^\circ$. In addition, adjacent linking groups connecting the central bent unit with the two rod-like wings are incorporated to adjust their flexibility or the bending angles. The molecule with a bridging odd number ($n = 3, 5, 7$) is shown in a more bent conformation, whereas the molecule with a bridging even number ($n = 2, 4, 6, 8$) is displayed in a more rod or linear conformation (Hsieh *et al.*, 2006).

Table 2.10: Molecular structures and mesomorphism properties of salicylaldehyde dimer mesogens having different central spacer carbon (Hsieh *et al.*, 2006)



Carbon Number (n)	Phase Transition Temperatures, °C (enthalpies, J/g)				Heating
2	Cr	125.6 (43.8)	SmC	220.0 (17.4)	I
3	Cr	102.0 (51.9)	B1	119.4 (18.1)	I
4	Cr	137.3 (53.2)	SmC	204.4 (18.6)	I
5	Cr	106.8 (45.2)	B1	119.6 (14.4)	I
6	Cr	136.4 (43.6)	SmC	178.3 (22.8)	I
7	Cr	100.5 (17.5)	B1	116.3 (17.5)	I
8	Cr	107.6 (44.8)	SmC	154.9 (23.3)	I

n represents the number of carbons in the bridging spacer. Cr = Crystal phase; SmC= smectic C phase, B1 = banana phase; I = isotropic phase.

Chapter 3.0

MATERIALS AND METHODS

3.1 Chemicals

The chemicals that were used throughout the study are listed as follows. All solvents and reagents were purchased commercially and used without any further purification.

Company	Chemicals
Chemicals obtained from Merck, Germany	Acetic acid 2-Aminothiophenol 1-Bromoethane 1-Bromopropane 1-Bromobutane 1-Bromopentane 1-Bromohexane 1-Bromoheptane 1-Bromooctane 1-Bromononane 1-Bromodecane 1-Bromododecane 1-Bromotetradecane 1-Bromohexadecane 1-Bromooctadecane 1,4-Dibromobutane 1,6-Dibromohexane 1,12-Dibromododecane 4-Dimethylaminopyridine Butyric acid Hexanoic acid Heptanoic acid Hydrochloric acid Dodecanoic acid Tetradecanoic acid Hexadecanoic acid Potassium carbonate Octadecanoic acid <i>N,N'</i> -Dicyclohexylcarbodiimine

	4-Hydroxybenzaldehyde
	4-Aminophenol
	Acetonitrile (HPLC grade)
	Methanol (HPLC grade)
	Ethyl acetate (HPLC grade)
Chemicals obtained from Acros Organics, USA	2-Amino-6-ethoxybenzothiazole
	2-Amino-6-methoxybenzothiazole
	2-Amino-6-methylbenzothiazole
	Decanoic acid
	Dimethylformamide
	Ethyl-4-hydroxybenzoate
	Octanoic acid
	Propanoic acid
	Valeric acid
	1,8-Dibromooctane
	1,10-Dibromodecane
	2-Amino-5-picoline
	2-Thiophenecarboxaldehyde
Chemicals obtained from R&M chemicals, UK	Acetone
	Dichloromethane
	Ethanol
	Methanol
	Potassium hydroxide
Chemicals obtained from Fisher Chemicals, UK	2-Aminobenzothiazole

3.2 Synthesis

3.2.1 Synthesis and Characterization of 6-Methyl-2-(4-alkoxybenzylidenamino)benzothiazoles, 6-methoxy-2-(4-alkoxybenzylidenamino)benzothiazoles, 6-ethoxy-2-(4-alkoxybenzylidenamino)benzothiazoles and 2-(4-alkoxybenzylidenamino)benzothiazoles

The synthetic way for the intermediates and final compounds are illustrated in Figure 3.1 and their synthetic methods are stated as follow.

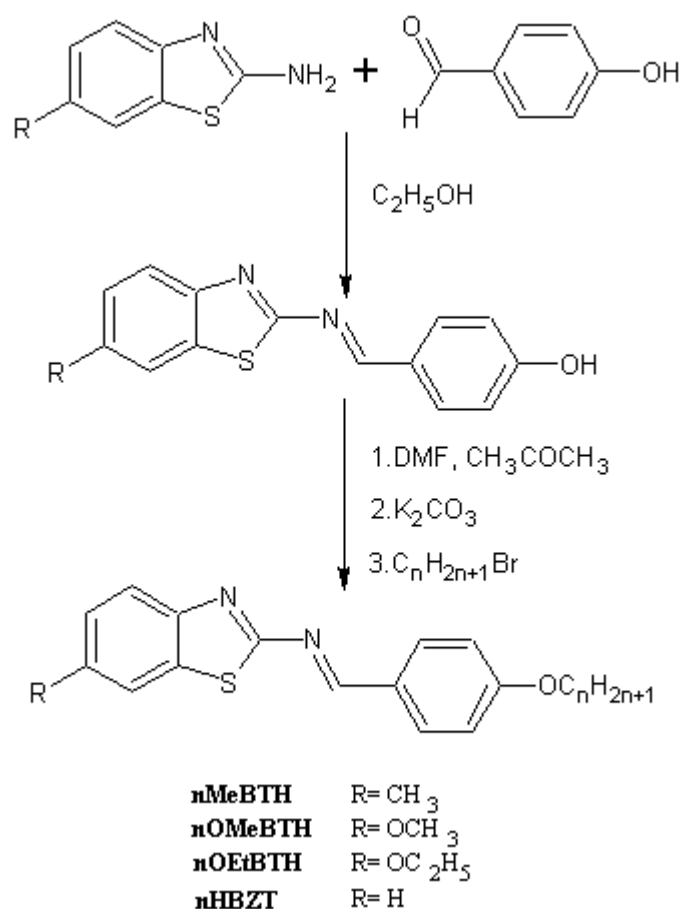
3.2.1.1 Synthesis of 6-Methyl-2-(4-hydroxybenzylidenamino)benzothiazole, 6-methoxy-2-(4-hydroxybenzylidenamino)benzothiazole, 6-ethoxy-2-(4-hydroxybenzylidenamino)benzothiazole and 2-(4-hydroxybenzylidenamino)benzothiazole

A mixture of 2-aminobenzothiazole derivatives (40 mmol) and 4-hydroxybenzaldehyde (40 mmol) in 50 mL of ethyl alcohol, with three drops of acetic acid as catalyst was added, the mixture allowed to stir and heated under refluxed for three hours. The reaction mixture was filtered and the ethanol was removed from the filtrate by evaporation. The dry yellowish solid thus obtained was recrystallized several times with ethanol.

3.2.1.2 Synthesis of 6-Methyl-2-(4-alkoxybenzylidenamino)benzothiazoles (nMeBTH), 6-methoxy-2-(4-alkoxybenzylidenamino)benzothiazoles (nOMeBTH), 6-ethoxy-2-(4-alkoxybenzylidenamino)benzothiazoles (nOEtBTH) and 2-(4-alkoxybenzylidenamino)benzothiazoles (nHBZT)

The target compounds were synthesized using a modified methodology

described by Yeap *et al.* (2009). A mixture of Schiff base intermediate (5 mmol) dissolved in minimum amount of dimethylformamide (DMF), then 40 mL of acetone was added with 5 mmol of potassium carbonate and 6 mmol of appropriate 1-bromoalkane ($n = 2$ to 10, 12, 14, 16, 18). The resulted mixture was refluxed for five hours. Then the mixture was filtered and cooled to room temperature. The yellow precipitate formed was isolated by filtration. The solid thus obtained was recrystallized three times with ethanol to obtain the pure product.



where $n = \text{C}2\text{-C}10, \text{C}12, \text{C}14, \text{C}16, \text{C}18$

Figure 3.1: Synthetic route towards the formation of the intermediate and title compounds, nMeBTH, OMeBTH, nOEtBTH and nHBZT.

3.2.2 Synthesis and Characterization of 6-Methyl-2-[4-(4-alkoxybenzoyloxy)benzylidenamino]benzothiazoles, 6-methoxy-2-[4-(4-alkoxybenzoyloxy)benzylidenamino]benzothiazoles and 2-[4-(4-alkoxybenzoyloxy)benzylidenamino]benzothiazoles

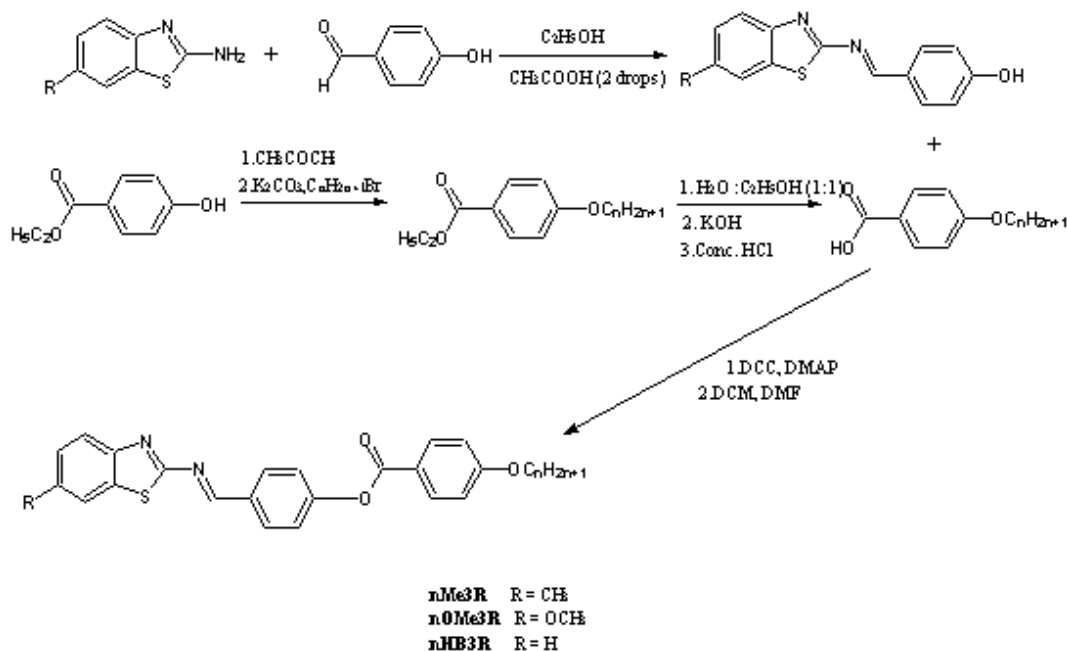
The synthetic way for the intermediates and final compounds are illustrated in Figure 3.2 and their synthetic methods are stated as follow.

3.2.2.1 Synthesis of 4-Alkoxybenzoic Acids

4-Alkoxybenzoic acid was prepared according to a method described by Kadkin *et al.* (2007). A mixture of ethyl-4-hydroxybenzoate (3.33 g, 20 mmol) and appropriate 1-bromoalkane (20 mmol, $C_nH_{2n+1}Br$ where $n = 2$ to 10, 12, 14, 16, 18) was refluxed for six hours with the presence of potassium carbonate (2.76 g, 20 mmol) in 40 mL of acetone. Inorganic salts formed were filtered off and the filtrate was evaporated to dryness to obtain crude ethyl-4-alkoxybenzoate. Then, a solution of potassium hydroxide (1.13 g, 20 mmol) in a mixture of water: ethanol (30 mL: 30 mL) was added to the residue ethyl-4-alkoxybenzoate, and the mixture was refluxed for five hours. Then, concentrated HCl (4 mL) was added to the mixture and continued to reflux for another one hour. The white precipitate was filtered off and washed several times with distilled water. The crude intermediate was then recrystallized with methanol and kept for next reaction.

3.2.2.2 Synthesis of 6-Methyl-2-[4-(4-alkoxybenzoyloxy)benzylidenamino]benzothiazoles (nMe3R), 6-methoxy-2-[4-(4-alkoxybenzoyloxy)benzylidenamino]benzothiazoles (nOMe3R) and 2-[4-(4-alkoxybenzoyloxy)benzylidenamino]benzothiazoles (nHB3R)

2-(4-Hydroxybenzylidenamino)benzothiazole derivatives (5 mmol, refer section 3.2.1.1), appropriate 5 mmol of 4-alkoxybenzoic acid and 4-dimethylaminopyridine, DMAP (1 mmol, 0.12 g) were dissolved in 40 mL mixture of DCM and DMF. 5 mmol of DCC (0.13 g) dissolved in DCM (10 mL) was added dropwise while stirring at 0 °C (one hour) and then stirred at room temperature for five hours. Lastly, the mixture was filtered evaporated to dryness. The obtained white solid was recrystallized with hexane and ethanol to obtain the pure product.



where n= C2-C10, C12, C14, C16, C18

Figure 3.2: Synthetic route towards the formation of the intermediates and title compounds, nMe3R, nOMe3R and nHB3R.

3.2.3 Synthesis and characterization of 2-[3-Methoxy-(4-alkoxybenzoyloxy)phenyl]benzothiazoles and 2-[3-ethoxy-(4-alkoxybenzoyloxy)phenyl]benzothiazoles

The synthetic route of the intermediates and final compounds are depicted in Figure 3.3 and the synthetic methods are stated as follow.

3.2.3.1 Synthesis of 2-[3-Methoxy-(4-hydroxyphenyl)]benzothiazole and 2-[3-ethoxy-(4-hydroxyphenyl)]benzothiazole

The intermediates were synthesized according to a modified method described by Toba *et al.* (2005) and Ha *et al.* (2009a). 2-Aminothiophenol (5.00 g, 40 mmol) and 3-methoxy-4-hydroxybenzaldehyde (or 3-ethoxy-4-hydroxybenzaldehyde, 40 mmol) were dissolved in 60 mL of ethanol and was refluxed with stirring for six hours at 76-78 °C. A small amount of water was added slowly to the reaction mixture until the mixture turned cloudy. The cloudy solution was left overnight in the fridge at about 2 °C. Next, the precipitate formed was collected and washed with cold ethanol-water (1:1.5) mixture followed by dichloromethane on Buchner funnel. The dried product was collected after oven drying at 50 °C. Then, the crude product was recrystallized with absolute ethanol to give the pure compound for further reaction.

3.2.3.2 Synthesis of 2-[3-Methoxy-(4-alkoxybenzoyloxy)phenyl]benzothiazoles (nMOBZT) and 2-[3-Ethoxy-(4-alkoxybenzoyloxy)phenyl]benzothiazoles (nEOBZT)

2-(4-Hydroxyphenyl)benzothiazole derivatives (5 mmol), appropriate 4-alkoxybenzoic acid (5 mmol, refer section 3.2.2.1) and DMAP (1 mmol, 0.12 g) were dissolved in 40 mL mixture of dichloromethane and dimethylformamide. The mixture was then stirred at 0 °C. DCC (5 mmol, 1.00 g) dissolved in 10 mL of DCM was added dropwise while stirring at 0 °C for an hour and then stirred at room temperature for another five hours. Lastly, the mixture was filtered and the excess solvent was removed by evaporation. The obtained white solid was recrystallized several times using mixture of hexane and ethanol to obtain the pure product.

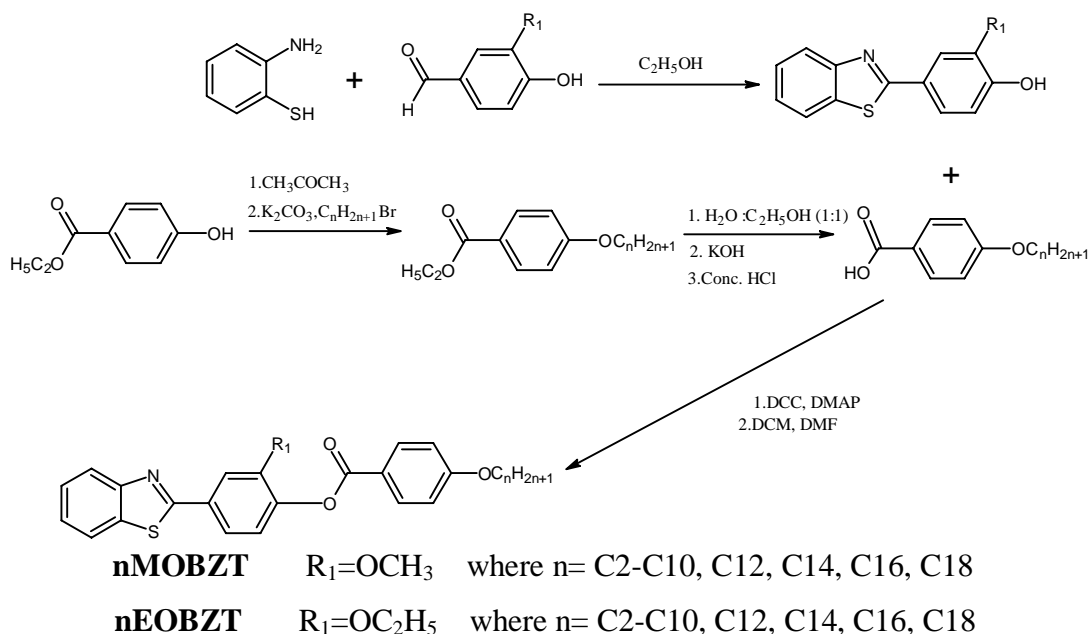


Figure 3.3: Synthetic route towards the formation of the intermediates and title compounds, nMOBZT and nEOBZT.

3.2.4 Synthesis and Characterization of α,ω -bis [6-Methoxy-2-(4-alkoxybenzylidenamino)]benzothiazoles and α,ω -bis [6-ethoxy-2-(4-alkoxybenzylidenamino)]benzothiazoles

The synthetic route of the intermediates and final compounds are illustrated in Figure 3.4 and their synthetic methods are stated as follow.

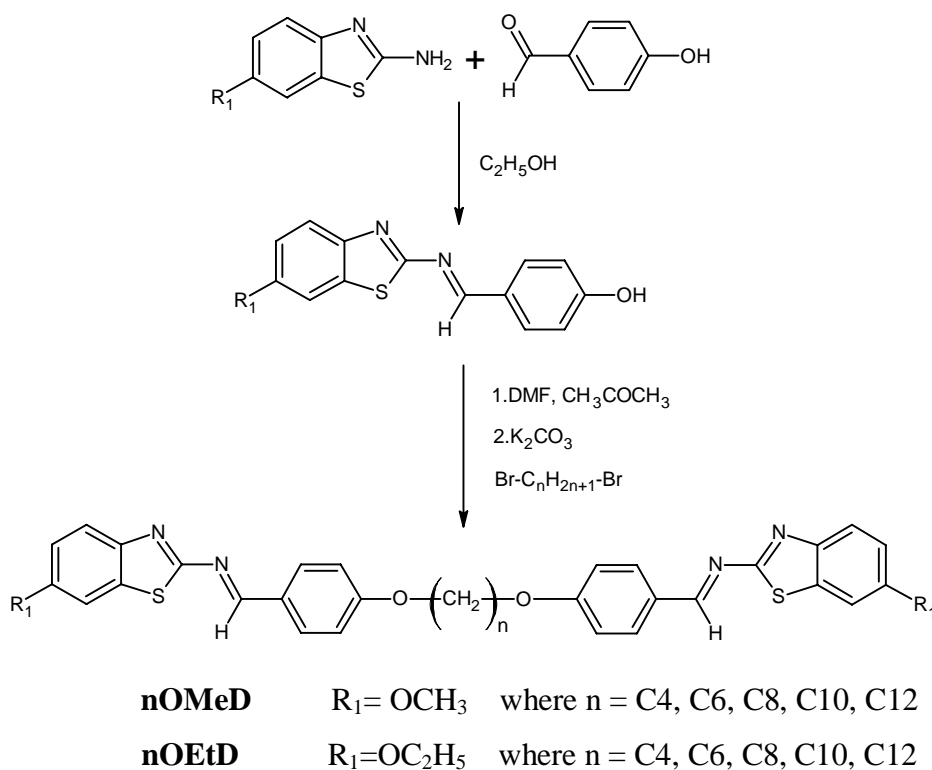


Figure 3.4: Synthetic route towards the formation of the intermediates and title compounds, nOMeD and nOEtD.

3.2.4.1 Synthesis of α,ω -bis[6-Methoxy-2-(4-alkoxybenzylidenamino)]-benzothiazoles and α,ω -bis[6-ethoxy-2-(4-alkoxybenzylidenamino)]-benzothiazoles

2-(4-Hydroxybenzylidenamino)benzothiazole derivatives (5 mmol, refer

section 3.2.1.1), was dissolved in minimum amount of DMF, then 40 ml of acetone was added with potassium carbonate (5 mmol) and 6 mmol of appropriate 1,*n*-dibromoalkane (*n* = 4, 6, 8, 10, 12) were refluxed for 19 hours. Then the reaction mixture was filtered directly and cooled to room temperature. The yellow precipitate formed was isolated by filtration. The solid thus obtained was recrystallized three times with ethanol to obtain the pure products.

3.2.5 Synthesis and Characterization of 5-Methyl-2-[4-(4-alkoxybenzoyloxy)benzylidenamino]pyridines

The synthetic scheme of the intermediates and final compounds were illustrated in Figure 3.5 and their synthetic methods are stated as follow.

3.2.5.1 Synthesis of 5-Methyl-2-(4-hydroxybenzylidenamino)pyridine

The Schiff base intermediate was prepared according to the method described by Yeap *et al.* (2002). 2-Amino-5-picoline and 4-hydroxybenzaldehyde (4.88 g, 40 mmol) in 70 mL of ethanol, with three drops of acetic acid as catalyst, was refluxed for three hours with stirring. Then, the mixture was filtered and the excess solvent was removed from the filtrate by evaporation. The yellowish solid formed was recrystallized twice with ethanol.

3.2.5.2 Synthesis of 5-Methyl-2-[4-(4-alkoxybenzoyloxy)benzylideneamino]pyridines (nPM5B)

5-Methyl-2-(4-hydroxybenzylideneamino)pyridine, appropriate 4-alkoxybenzoic acid (5 mmol, refer section 3.2.2.1) and 4-dimethylaminopyridine (1 mmol, 0.12 g) were soluble in 40 mL mixture of dichloromethane (DCM) and dimethylformamide (DMF). DCC (5 mmol, 0.13g) dissolved in 10 mL of DCM was added and stirred for an hour at 0 °C and then continuously stirred at room temperature for four hours. Lastly, the mixture was filtered and the solvent was removed by evaporation. The obtained white solid was recrystallized with mixture of hexane and ethanol to obtain the pure product.

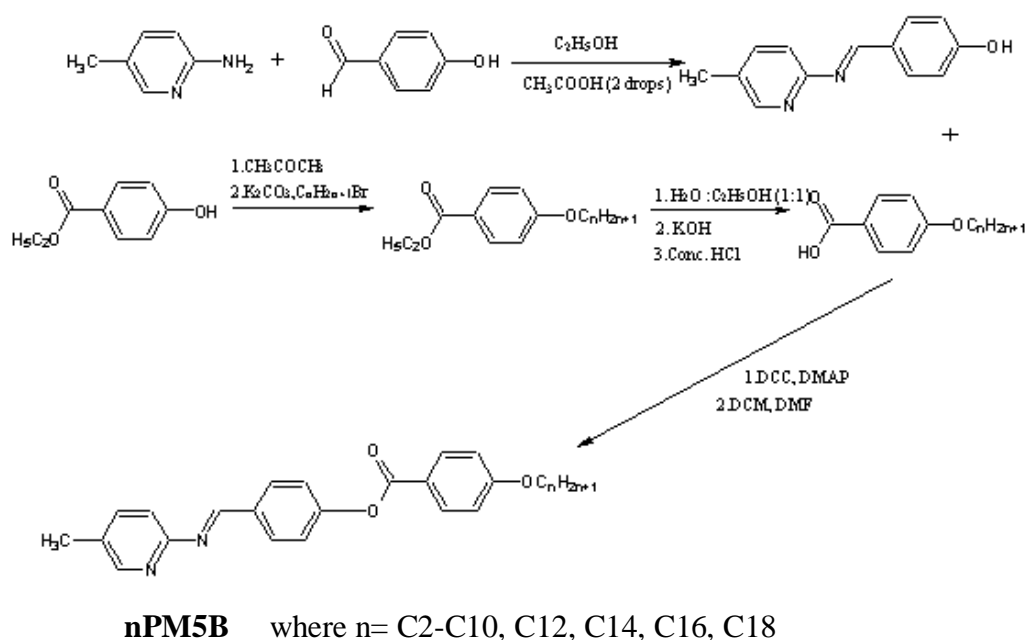


Figure 3.5: Synthetic route towards the formation of the intermediates and title compounds, nPM5B.

3.2.6 Synthesis and Characterization of 2-[4-(4-Alkoxybenzoyloxy)-benzylidenaniline]thiophenes

The synthetic scheme of the intermediates and final compounds were illustrated in Figure 3.6 and their synthetic methods are stated as follow.

3.2.6.1 Synthesis of 2-(4-Hydroxybenzylidenaniline)thiophene

The intermediate was prepared according to the method described by Yeap *et al.* (2002). 2-Thiophenecarboxaldehyde (40 mmol) and 4-aminophenol (4.88 g, 40 mmol) in 70 mL of ethanol, with three drops of acetic acid as catalyst, was refluxed for three hours with stirring. Then, the mixture was filtered and the solvent was removed by evaporation. The yellowish solid formed was recrystallized from ethanol until the transition temperatures remain constant.

3.2.6.2 Synthesis of 2-[4-(4-Alkoxybenzoyloxy)benzylidenaniline]-thiophenes (nTAP)

2-(4-Hydroxybenzylidenaniline)thiophene, appropriate 4-Alkoxybenzoic acid (5 mmol) and DMAP (1 mmol, 0.12g) were dissolved in 40 mL mixture of dichloromethane (DCM) and dimethylformamide (DMF). The mixture was then stirred at 0 °C. DCC (5 mmol, 0.13g) dissolved in 10 mL of DCM was added and stirred for an hour at 0 °C and then continuously stirred at room temperature for four hours. Lastly, the mixture was filtered and the solvent was removed by

evaporation. The obtained white solid was recrystallized with mixture of hexane and ethanol to obtain the pure product.

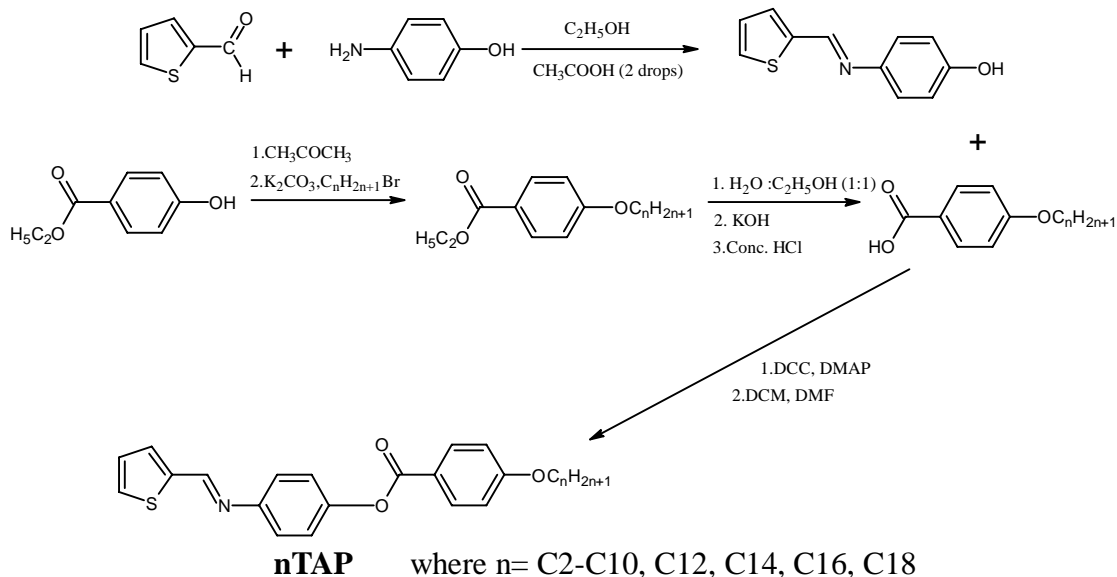


Figure 3.6: Synthetic route towards the formation of the intermediates and title compounds, nTAP.

3.3 Instruments and Characterization

The molecular structure for all the synthesized compounds were characterized by standard spectroscopic methods. The mesomorphic behaviour of the compounds was investigated by DSC, POM and XRD.

1. Electron Ionization mass spectra were obtained by Mass Spectrometer Finnigan MAT95XL-T.

2. Fourier Transform Infrared spectra were recorded by using Perkin-Elmer System 2000 FT-IR Spectrometer.
3. NMR spectra were recorded using Bruker Avance-400 MHz or JEOL LA-400 MHz NMR spectrometer.
4. Phase transition temperatures and associated enthalpy changes were measured using Differential Scanning Calorimeter Mettler Toledo DSC823^o or SII (SII Nanotechnologies Co.) DSC6100 (Japan).
5. Microscopy studies were carried using polarizing optical microscope (Carl Zeiss) equipped with a Linkam heating stage and a video camera (Video Master coomo20P) coupled to a video capture card (Video Master coomo600) for real-time video capture and image saving.
6. Synchrotron powder X-ray diffraction (XRD) measurements were carry out at beamline BL17A for compounds **16MeBTH**, **18OMeBTH**, **14OEtBTH**, **18HBZT**, **16Me3R**, **14OMe3R**, **8HB3R** and **12PM5B**.
7. Thermogravimetric analysis (TGA) was performed using Thermal Gravimetric Analyser Mettler Toledo TGA/SDTA851^o. Thermal stability of **14Me3R** and **10OMe3R** were further determined by thermogravimetric

analysis (TGA). The samples were analyzed with heating rate of 20 °C/min.

8. High Performance Liquid Chromatography system consist Diode Array Detector or variable wavelength (G1314A VWD, Agilent 1100 series), Quaternary Pump (G1311A, Agilent 1100 series), low pressure gradient unit (model and brand) and Vacuum Degasser (G1379A, Agilent 1100 series).
9. Thin layer Chromatography (TLC) was carried out on aluminium sheets coated in Merck Kieselgel silica gel 60 F254, eluting with chloroform or mixture of chloroform and ethyl acetate with ratio 1:1 for all compounds in the series.

CHAPTER 4.0

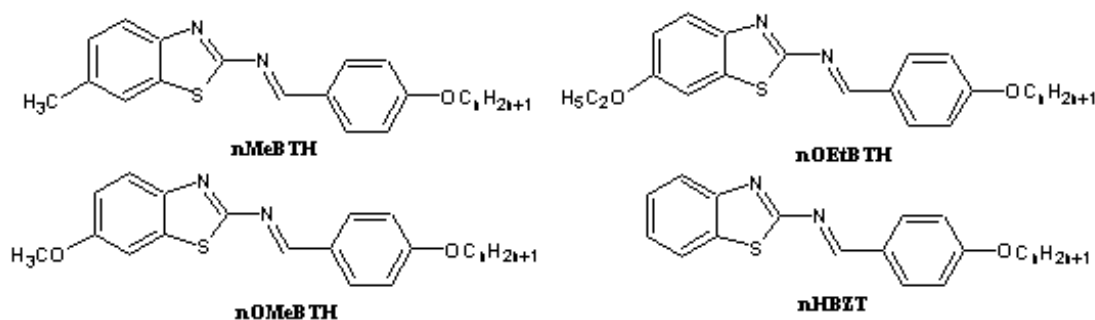
RESULTS AND DISCUSSION:

STRUCTURAL ELUCIDATION

4.1 Series 1: Structural Elucidation of 6-Methyl-2-(4-alkoxybenzylidenamino)benzothiazoles (nMeBTH), 6-methoxy-2-(4-alkoxybenzylidenamino)benzothiazoles (nOMeBTH), 6-ethoxy-2-(4-alkoxybenzylidenamino)benzothiazoles (nOEtBTH) and 2-(4-alkoxybenzylidenamino)benzothiazoles (nHBZT)

The chemical structures of the title compounds are shown at Figure 4.1.

The percentage of yields are tabulated in Table 4.1(i).



where n= C2-C10, C12, C14, C16, C18

Figure 4.1: Chemical structures of nMeBTH, nOMeBTH, nOEtBTH and nHBZT.

The HPLC analyses were performed by using Agilent with UV detector set at 286 nm and a HypersilC18 column at room temperature. The mobile phase was acetonitrile-methanol (95:5, vol/vol) and flow rate was 1 ml/min. The highest

Table 4.1(i): Percentage of yield of compounds nMeBTH, nOMeBTH, nOEtBTH and nHBZT

<u>nMeBTH</u>		<u>nOMeBTH</u>	
Compound	Percentage of yield (%)	Compound	Percentage of yield (%)
2MeBTH	32	2OMeBTH	31
3MeBTH	29	3OMeBTH	30
4MeBTH	36	4OMeBTH	35
5MeBTH	34	5OMeBTH	38
6MeBTH	45	6OMeBTH	46
7MeBTH	55	7OMeBTH	54
8MeBTH	58	8OMeBTH	59
9MeBTH	54	9OMeBTH	53
10MeBTH	66	10OMeBTH	68
12MeBTH	67	12OMeBTH	69
14MeBTH	68	14OMeBTH	70
16MeBTH	70	16OMeBTH	71
18MeBTH	72	18OMeBTH	75

<u>nHBZT</u>		<u>nOEtBTH</u>	
Compound	Percentage of yield (%)	Compound	Percentage of yield (%)
2HBZT	27	2OEtBTH	32
3HBZT	31	3OEtBTH	31
4HBZT	35	4OEtBTH	36
5HBZT	37	5OEtBTH	38
6HBZT	48	6OEtBTH	44
7HBZT	53	7OEtBTH	53
8HBZT	56	8OEtBTH	58
9HBZT	59	9OEtBTH	57
10HBZT	64	10OEtBTH	63
12HBZT	69	12OEtBTH	67
14HBZT	66	14OEtBTH	69
16HBZT	75	16OEtBTH	73
18HBZT	78	18OEtBTH	76

purity of the compound migrated as a single peak on HPLC. Representative chromatograms of the compounds **16MeBTH**, **16OMeBTH**, **8OEtBTH** and **8HBZT** migrated as a single peak (Appendices 1A, 1B). The TLC R_f data associated with compounds **nMeBTH**, **nOMeBTH**, **nOEtBTH** and **nHBZT** are listed in Appendix 1C and 1D, respectively. All the compounds gave a single spot on the TLC plate (Sharma *et al.*, 2003b).

Mass spectrometry was used to study **16MeBTH**, **14OMeBTH**, **14OEtBTH** and **16HBZT** as representative compounds for each series. Electron Ionization (EI) mass spectrum of **16MeBTH**, **14OMeBTH**, **14OEtBTH** and **16HBZT** are shown in Figures 4.2- 4.5, respectively. Recognition of the molecular ion peak was based on the molecular mass of compounds **16MeBTH**, **14OMeBTH**, **14OEtBTH** and **16HBZT** found at 492.4, 480.4, 494.4 and 478.4 m/z with relative abundance of 91.57, 100.00, 100.00 and 4.09, respectively.

In addition, **16MeBTH** may contains the less abundant isotopes, such as ^{13}C , ^2H , ^{15}N and ^{17}O and these will give rise to the “isotopes peaks” at $M+1$ (Pavia, 2001). For example, isotopes peaks ($M+1$) due to less abundant isotopes can be found at 493.4 m/z with relative abundance of 31.31. The intensity of the molecular ion peak depends on the stability of the molecular ion where the most stable molecular ions are those of purely aromatic system. Since the molecular ion peak was not the base peak (most intense peak), hence, some fragmentation maybe occurred. As aromatic ether, the molecular ion peak of aromatic ether is prominent. When the number of carbon of aromatic alkyl ether is C_2 or larger, β -cleavage to

the ring is accompanied by hydrogen migration (Silverstein and Webster, 1997). This gives rise to the most intense peak at 267.0 m/z . Similar mass spectruetry fragmentation pattern were also observed for the remaining compounds in series **14OMeBTH**, **14OEtBTH** and **16HBZT**, respectively. The detailed fragmentation is depicted in Appendixes 1E and 1H, respectively.

Selected FT-IR data associated with compounds **nMeBTH** are listed in Table 4.2 while the FT-IR spectrum of the representative compound **16MeBTH** is shown in Figure 4.6. Whilst selected FT-IR data associated with compounds **nOMeBTH**, **nOEtBTH** and **nHBZT** are summarized in Tables 4.3, 4.4 and 4.5 while the FT-IR spectrum of the representative compounds **16OMeBTH**, **16OEtBTH** and **16HBZT** are shown in Figures 4.7, 4.8 and 4.9, respectively.

By referring to the FT-IR spectrum of representative compound **16MeBTH**, it suggested that the title compounds have been successfully synthesized via (i) condensation of 2-amino-6-methylbenzothiazole with 4-hydroxybenzaldehyde and (ii) Williamson's etherification between intermediate and 1-bromohexadecane for **16MeBTH**. The Schiff base C=N linkage gave a diagnostic IR band at 1600 cm^{-1} . Another absorption band appeared at 1261 cm^{-1} was indicative of the C-O stretching of the aromatic ether (Ar-O-R) resulting from the successfully Willamson etherification. The diagnostic absorption bands at 2849 and 2955 cm^{-1} in the spectrum of **16MeBTH** provide the evidence for the existence of alkoxy chain which results from the etherification.

Similar FT-IR characteristics were also observed for the remaining compounds in series **nMeBTH**, **nOMeBTH**, **nOEtBTH** and **nHBZT**, respectively.

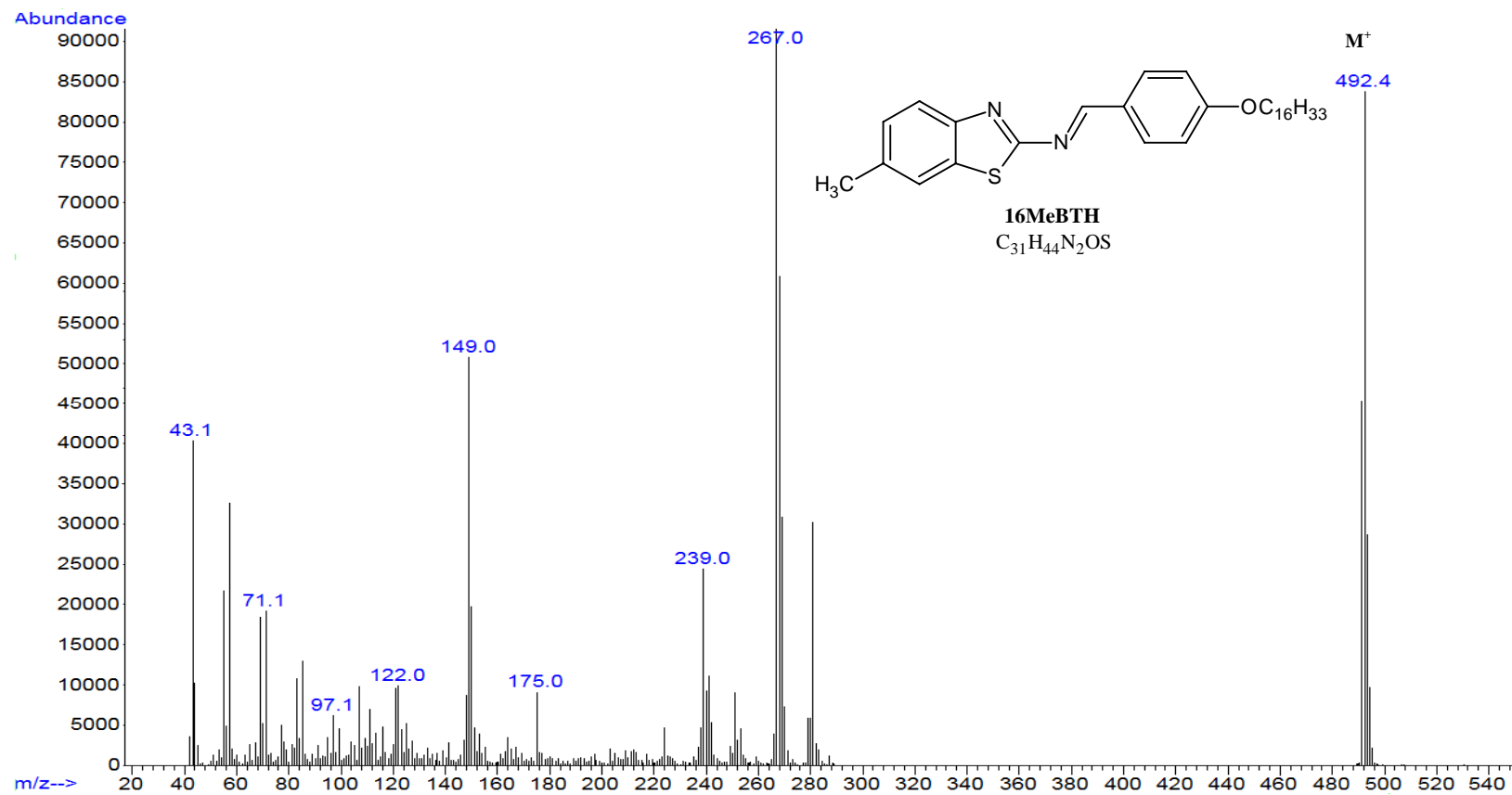


Figure 4.2: Mass spectrum of compound 16MeBTH.

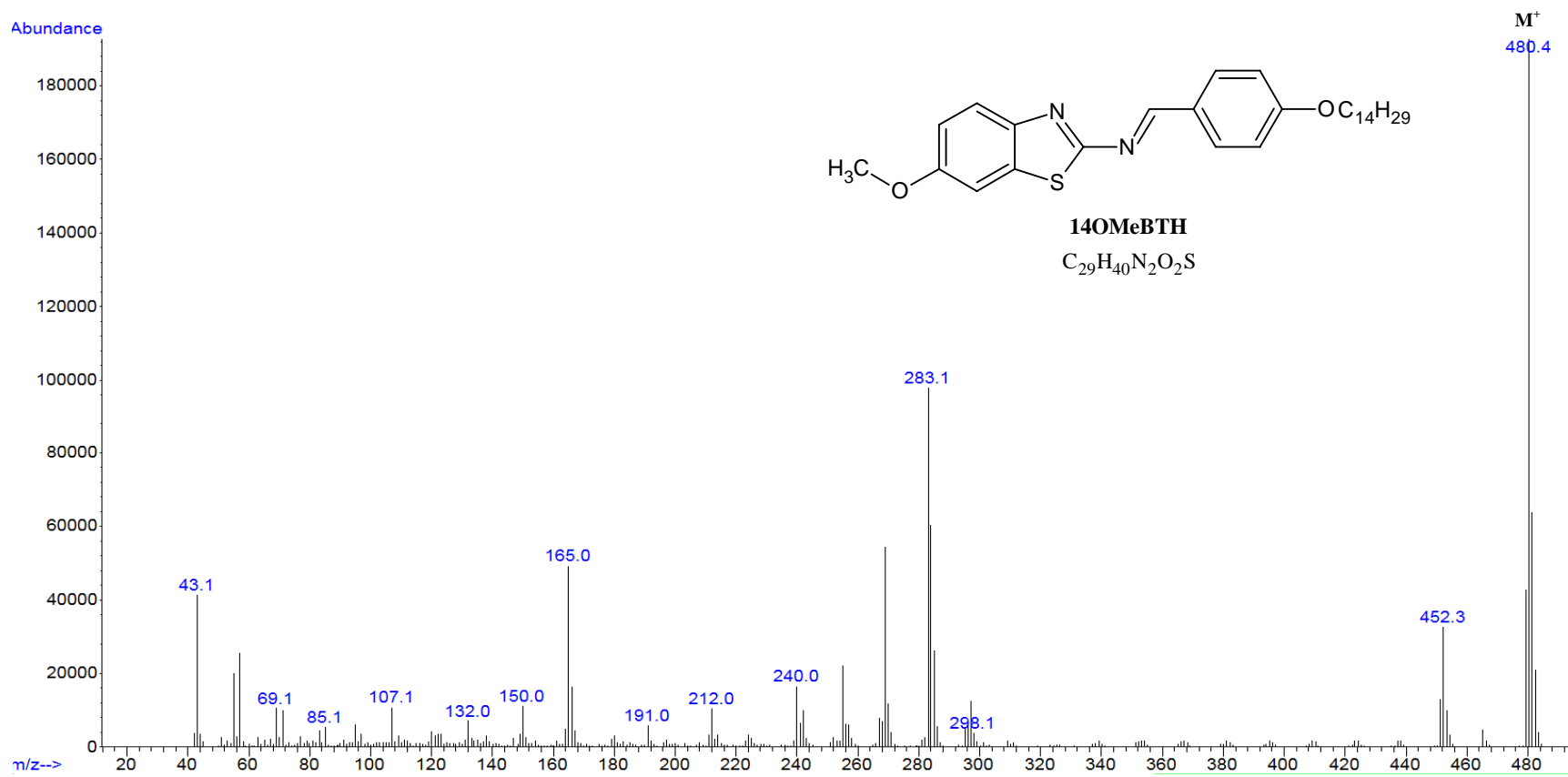


Figure 4.3: Mass spectrum of compound 14OMeBTH.

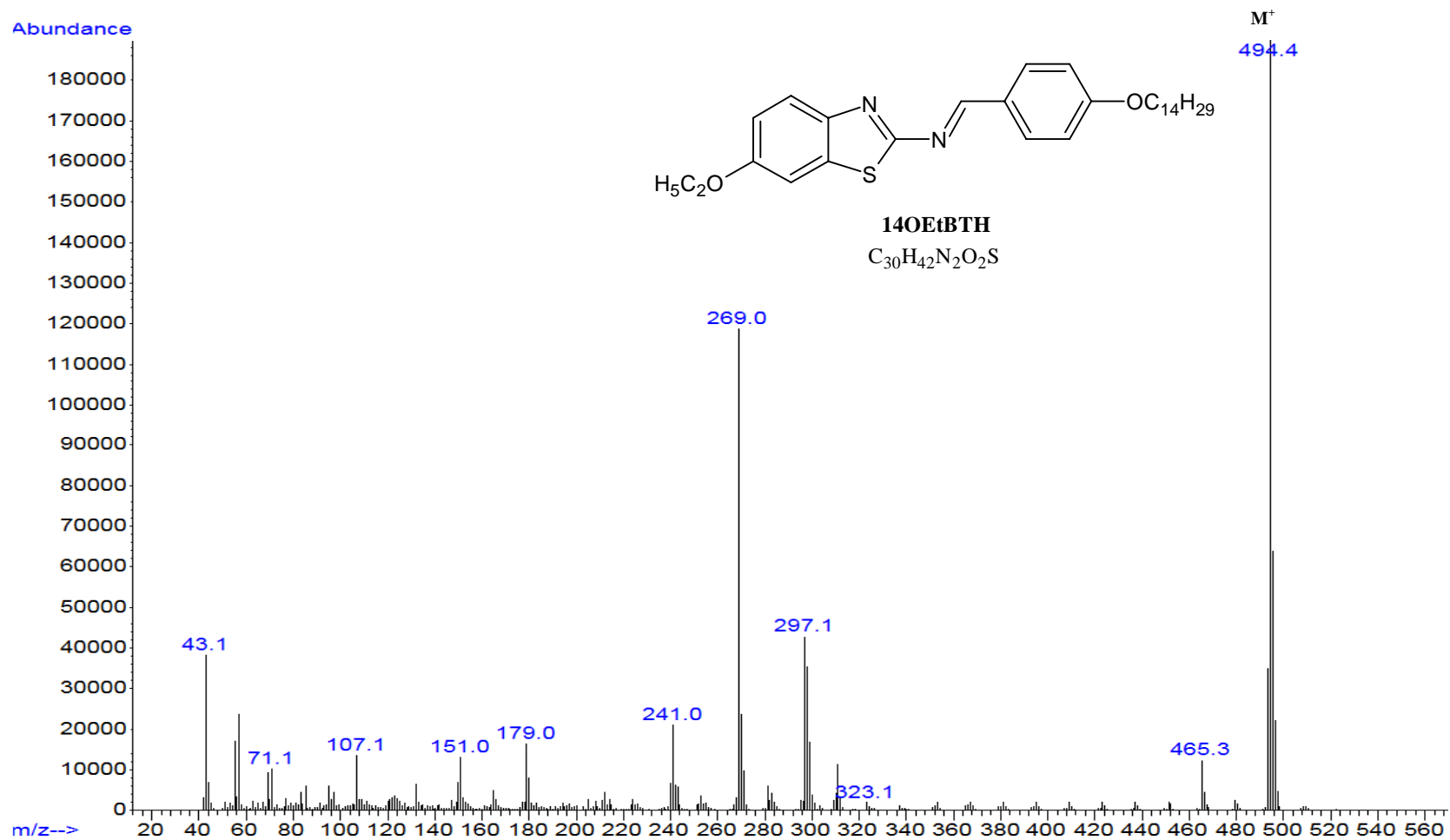


Figure 4.4: Mass spectrum of compound 14OEtBTH.

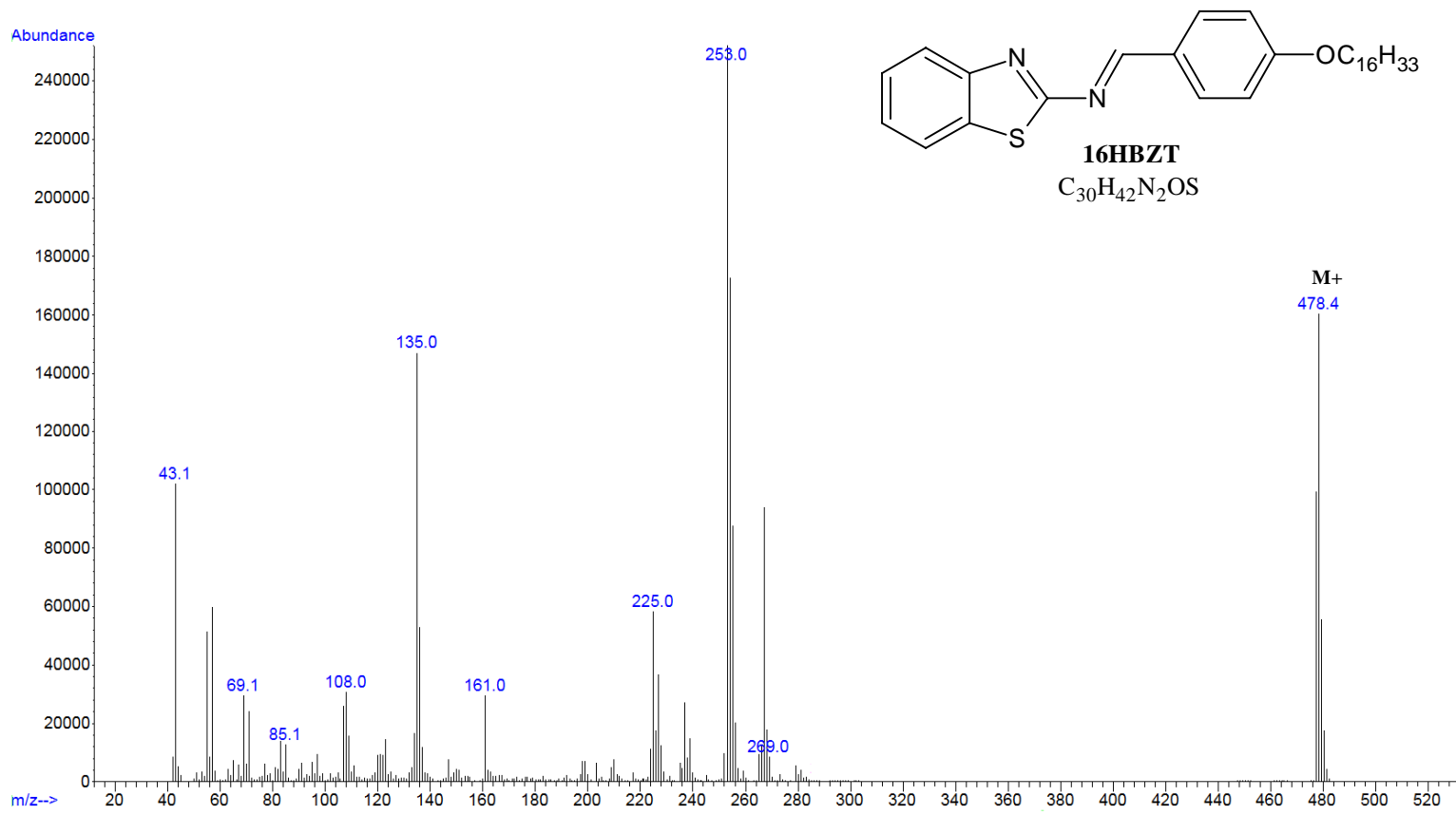


Figure 4.5: Mass Spectrum of compound 16HBZT.

Table 4.2: FT-IR spectral data of compounds nMeBTH

Compound	IR ν (cm ⁻¹)				
	sp ² C-H Stretch (aromatic)	sp ³ C-H Stretch (aliphatic)	C=N (Schiff base)	C=N (benzothiazole)	Ar-O-R (ether)
2MeBTH	3050	2986,2860	1594	1567	1265
3MeBTH	3054	2970,2865	1601	1567	1274
4MeBTH	3054	2955,2869	1594	1567	1264
5MeBTH	3053	2943,2867	1595	1564	1260
6MeBTH	3051	2943,2866	1594	1566	1259
7MeBTH	3054	2919,2856	1595	1565	1261
8MeBTH	3051	2919,2852	1595	1565	1265
9MeBTH	3054	2919,2852	1598	1567	1257
10MeBTH	3054	2919,2851	1597	1567	1257
12MeBTH	3053	2919,2849	1597	1567	1251
14MeBTH	3054	2919,2850	1600	1570	1252
16MeBTH	3052	2919,2850	1600	1570	1251
18MeBTH	3050	2919,2850	1600	1570	1253

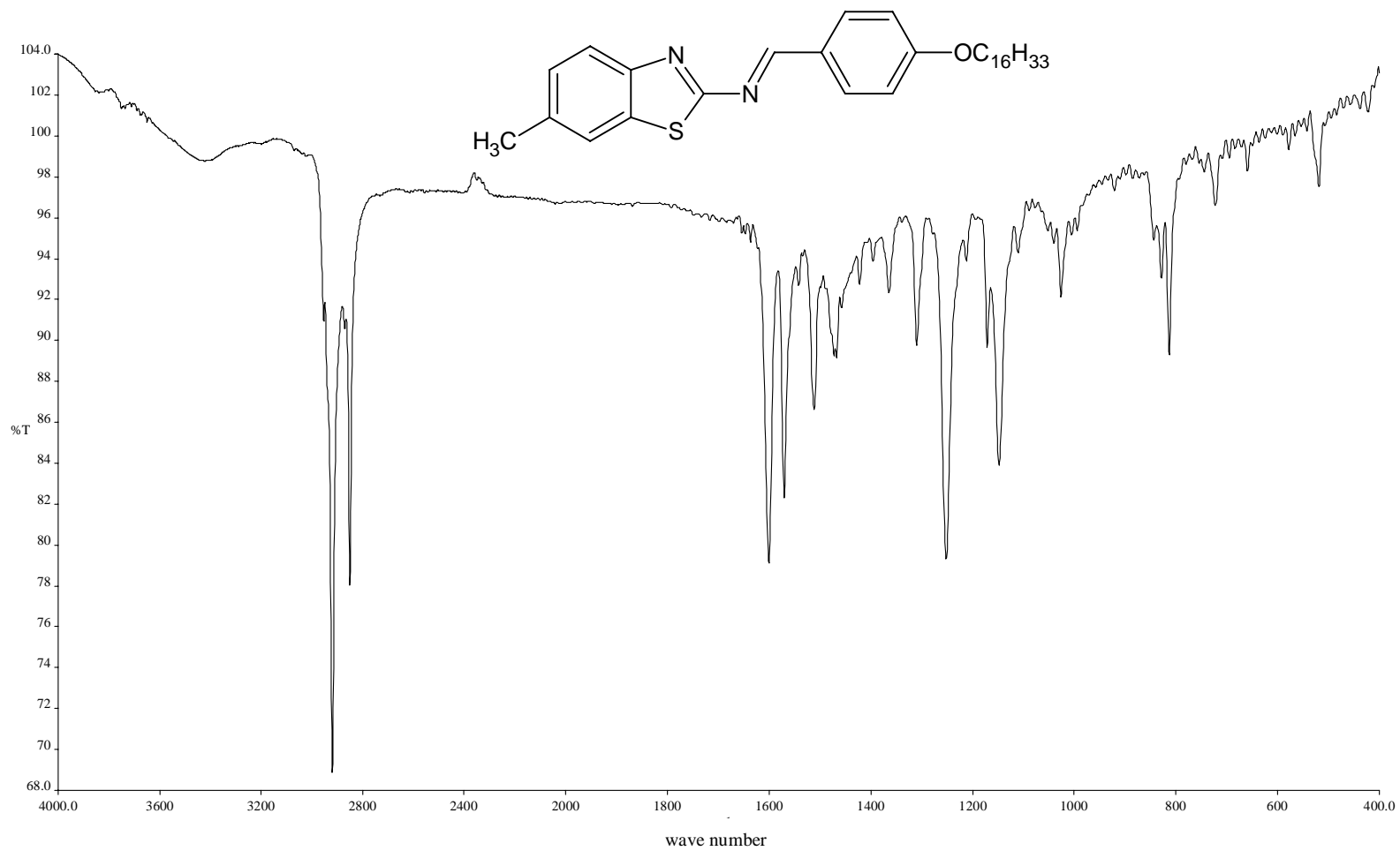


Figure 4.6: FT-IR spectrum of compound 16MeBTH.

Table 4.3: FT-IR spectral data of compounds nOMeBTH

Compound	IR ν (cm ⁻¹)				
	sp ² C-H Stretch (aromatic)	sp ³ C-H Stretch (aliphatic)	C=N (Schiff base)	C=N (benzothiazole)	Ar-O-R (ether)
2OMeBTH	3067	2928,2856	1600	1566	1261
3OMeBTH	3066	2939,2877	1597	1565	1261
4OMeBTH	3060	2954,2869	1598	1560	1264
5OMeBTH	3062	2946,2866	1598	1560	1251
6OMeBTH	3062	2928,2856	1602	1566	1261
7OMeBTH	3060	2919,2856	1595	1565	1259
8OMeBTH	3060	2920,2854	1596	1567	1258
9OMeBTH	3063	2940,2852	1597	1566	1258
10OMeBTH	3060	2919,2850	1598	1567	1257
12OMeBTH	3063	2923,2852	1589	1567	1254
14OMeBTH	3064	2918,2850	1603	1571	1253
16OMeBTH	3064	2919,2850	1604	1572	1254
18OMeBTH	3064	2918,2849	1603	1572	1253

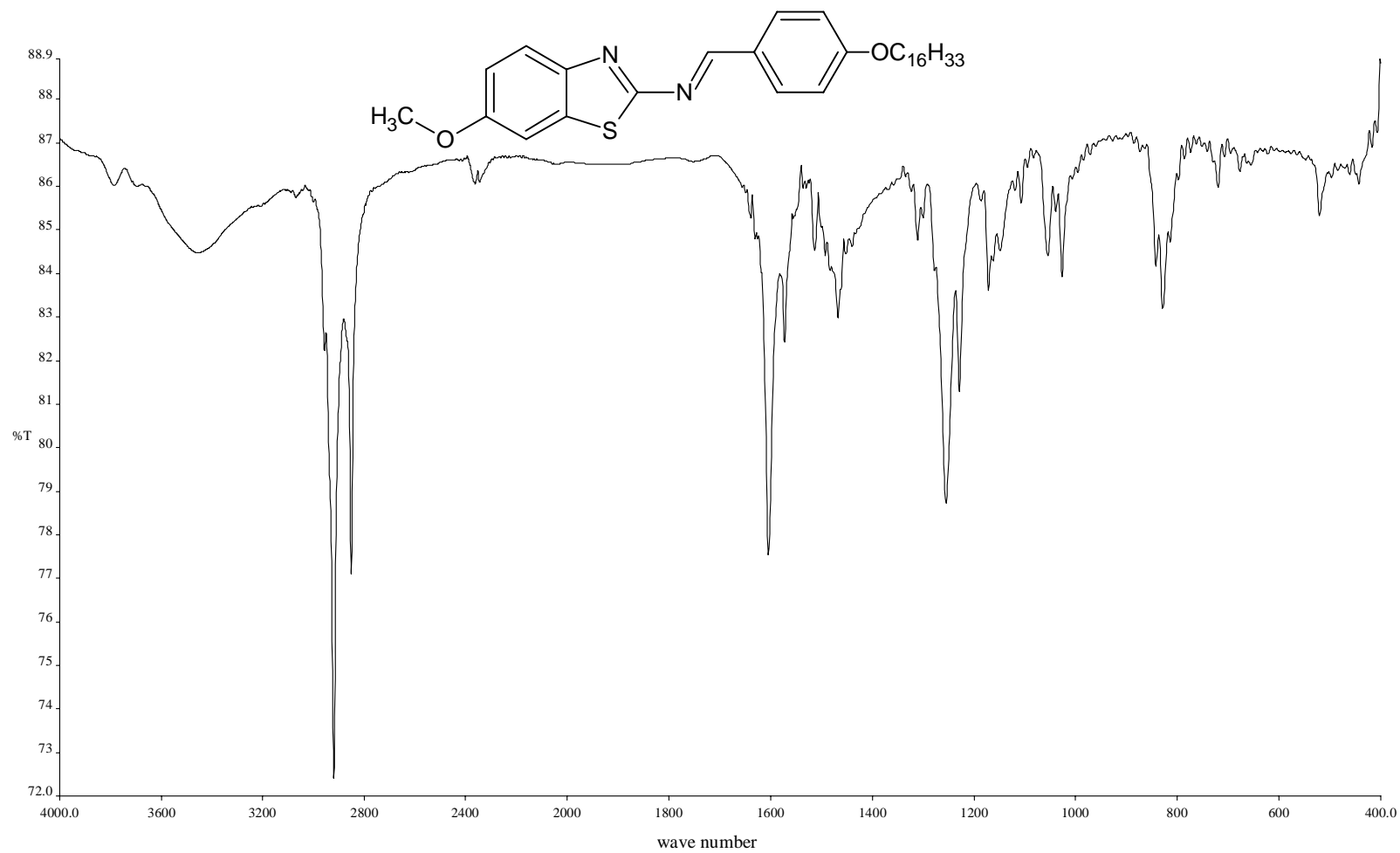


Figure 4.7: FT-IR spectrum of compound 16OMeBTH.

Table 4.4: FT-IR spectral data of compounds nOEtBTH

Compound	IR ν (cm ⁻¹)				
	sp ² C-H Stretch (aromatic)	sp ³ C-H Stretch (aliphatic)	C=N (Schiff base)	C=N (benzothiazole)	Ar-O-R (ether)
2OEtBTH	3065	2728,2882	1602	1575	1265
3OEtBTH	3063	2974,2878	1592	1561	1254
4OEtBTH	3064	2923,2868	1598	1563	1250
5OEtBTH	3063	2934,2866	1600	1557	1252
6OEtBTH	3064	2986,2858	1598	1568	1261
7OEtBTH	3064	2939,2857	1596	1566	1258
8OEtBTH	3064	2922,2854	1595	1565	1257
9OEtBTH	3064	2921,2851	1592	1567	1260
10OEtBTH	3064	2919,2850	1592	1567	1258
12OEtBTH	3064	2921,2849	1594	1563	1254
14OEtBTH	3064	2917,2847	1595	1563	1253
16OEtBTH	3064	2918,2850	1604	1573	1253
18OEtBTH	3064	2918,2850	1594	1563	1255

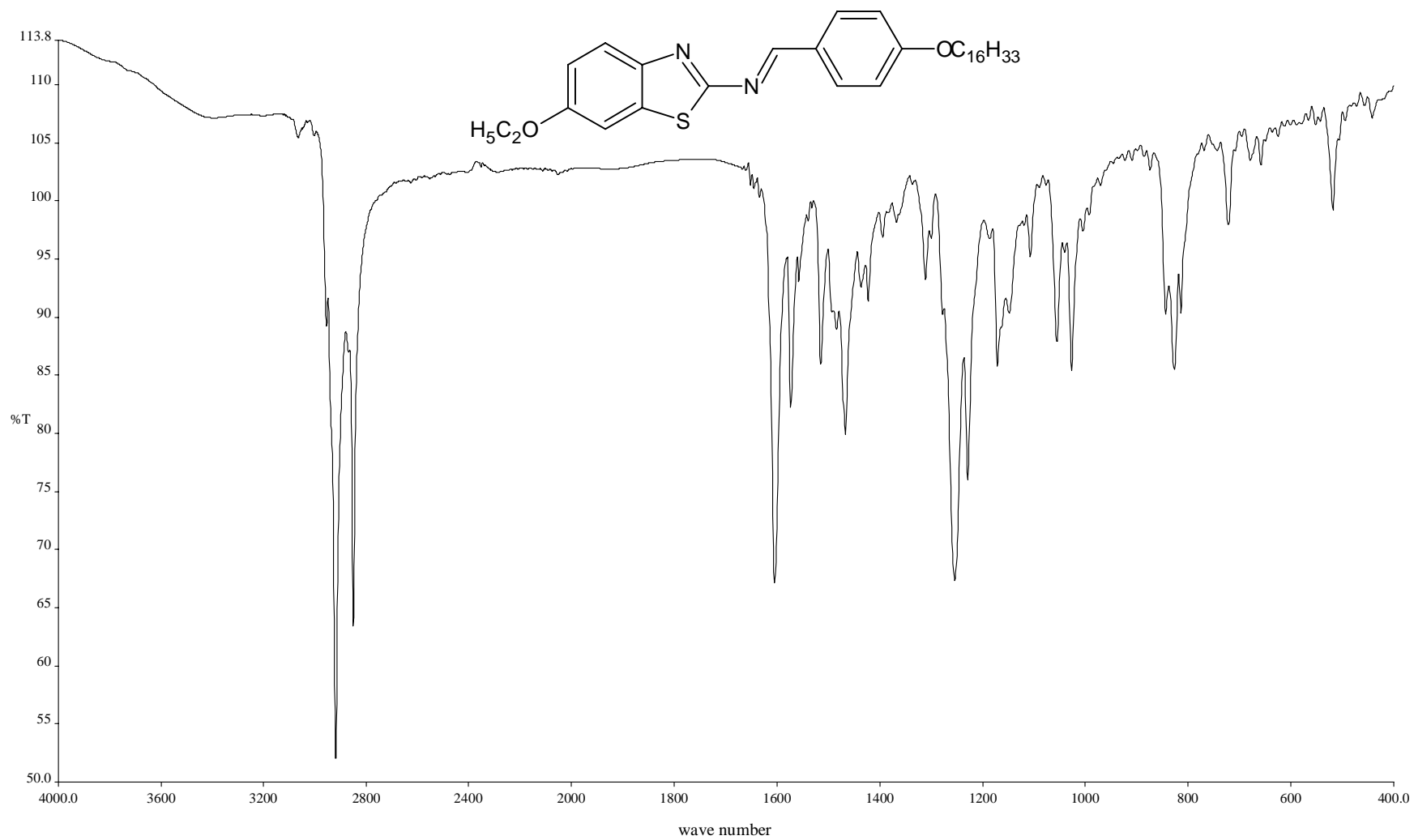


Figure 4.8: FT-IR spectrum of compound 16OEtBTH.

Table 4.5: FT-IR spectral data of compounds nHBZT

Compound	IR ν (cm ⁻¹)				
	sp ² C-H Stretch (aromatic)	sp ³ C-H Stretch (aliphatic)	C=N (Schiff base)	C=N (benzothiazole)	Ar-O-R (ether)
2HBZT	3067	2979,2860	1599	1566	1256
3HBZT	3051	2966,2874	1602	1566	1255
4HBZT	3055	2953,2867	1603	1565	1254
5HBZT	3055	2942,2867	1604	1563	1255
6HBZT	3056	2938,2849	1599	1564	1254
7HBZT	3056	2933,2855	1600	1567	1258
8HBZT	3055	2919,2855	1602	1566	1258
9HBZT	3056	2918,2848	1602	1567	1256
10HBZT	3056	2918,2848	1601	1567	1256
12HBZT	3056	2918,2847	1601	1567	1255
14HBZT	3057	2916,2850	1605	1570	1256
16HBZT	3058	2917,2849	1604	1571	1251
18HBZT	3056	2918,2849	1604	1573	1251

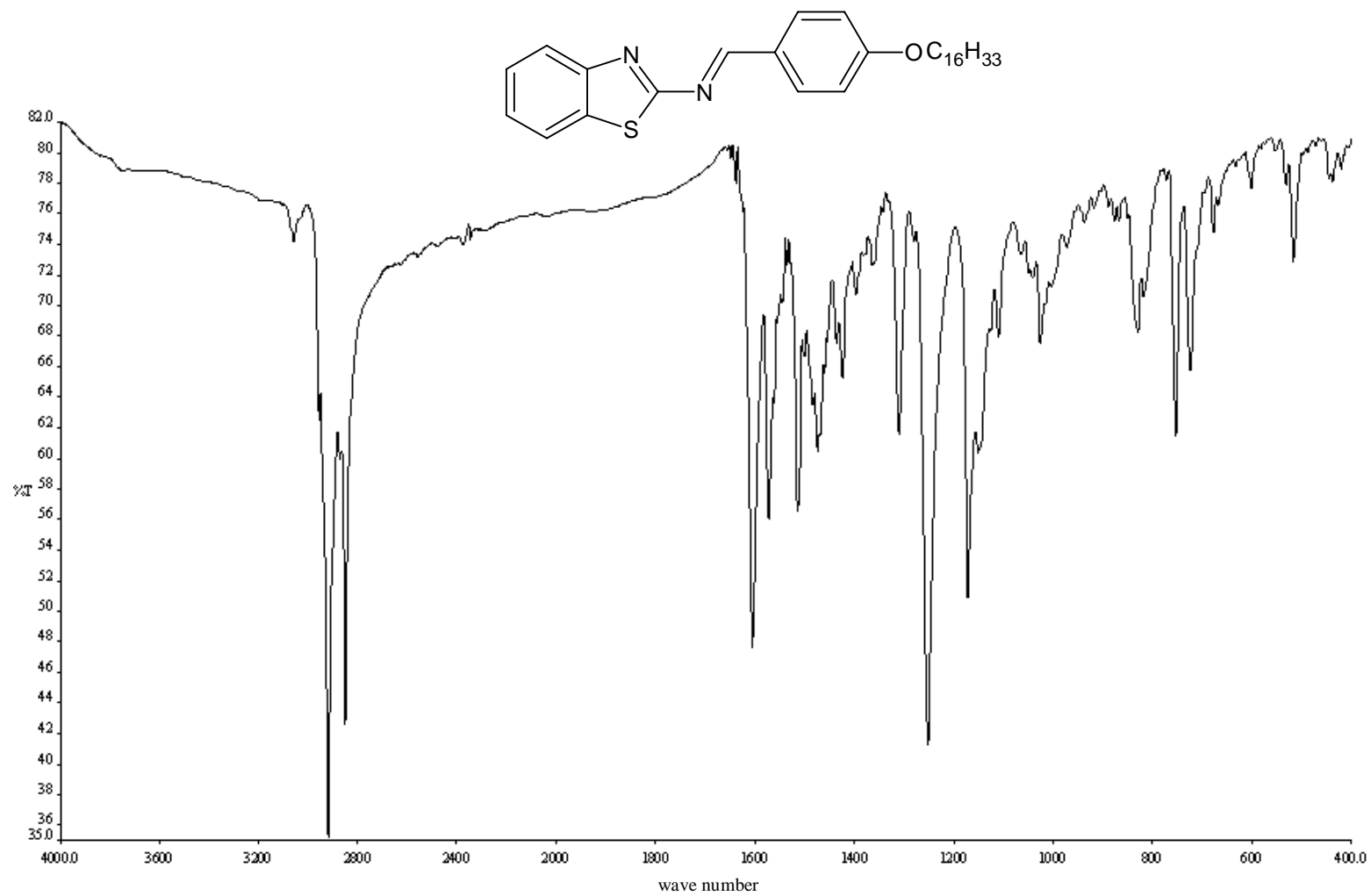


Figure 4.9: FT-IR spectrum of compound 16HBZT.

A NMR spectroscopic study was performed on the representative compounds **12MeBTH**, **12OMeBTH**, **12OEtBTH** and **12HBZT** for each series. The atomic numbering scheme of **12MeBTH**, **12OMeBTH**, **12OEtBTH** and **12HBZT** which are used to label the different types of protons and carbons are depicted in Figure 4.10.

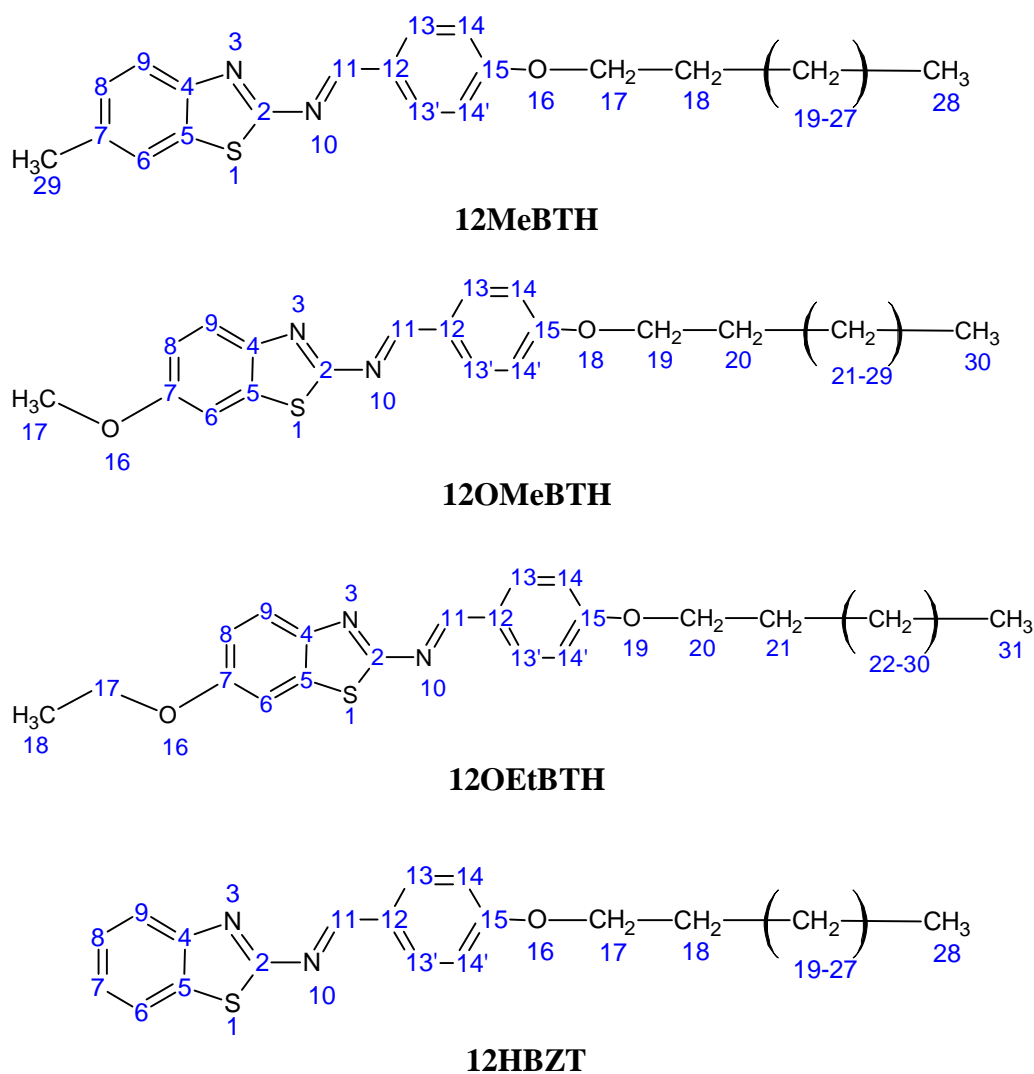


Figure 4.10: Structures with atomic numbering scheme for **12MeBTH**, **12OMeBTH**, **12OEtBTH** and **12HBZT**.

For compound **12MeBTH**, the 1D and 2D NMR spectral data are tabulated in the respective Tables 4.6-4.9 while the 1D and 2D NMR spectra of compound **12MeBTH** are depicted in Figures 4.11- 4.15, respectively.

In ^1H NMR spectrum of **12MeBTH**, a sharp singlet at $\delta = 8.91$ ppm corresponded to the azomethine proton ($-\text{N}=\text{CH}-$). This further supported the fact condensation reaction between 2-amino-6-methylbenzothiazoles with 4-hydroxybenzaldehyde has taken place. The characteristic resonance peaks for the rest of aromatic protons appeared as four doublets and a singlet were observed in relatively region at $\delta = 6.97$ to 7.84 ppm. Integration of ^1H NMR spectrum showed at Figure 4.11(a) and (b).

The aromatic protons of the compound appeared at more downfield region compared to those aliphatic protons. It is because they are deshielded by the large anisotropic field generated by the electrons in the ring's π system (Pavia *et al.*, 2001). These signals are assigned with the aid of the COSY experiment. Two doublets with an integration value corresponding to two protons at $\delta = 7.84$ and 6.97 ppm were assigned to H13/13' and H14/14', respectively. As for other doublets with an integration of one proton at $\delta = 7.38$ and 7.15 ppm were attributed to H9 and H8, respectively. H6 signal appeared as singlet in the spectrum at $\delta = 7.34$ ppm. A distinguishable peak was observed at $\delta = 4.00$ ppm in the spectrum of **12MeBTH**. It was due to the proton which attached to the carbon atom was directly bonded to the electronegativity oxygen atom in the ether linkage ($-\text{O}-\text{CH}_2-$).

The structures of the compounds were further substantiated by the ^{13}C NMR data. The ^{13}C NMR spectrum exhibited the different types of carbons including quaternary, methyl (CH_3), methylene (CH_2) and methane (CH) carbons. In the ^{13}C NMR spectrum of **12MeBTH**, the signals appeared at the range of $\delta = 114.83$ - 163.51 ppm indicated the twelve carbons in aromatic ring from C2 until C15 while the signals between $\delta = 68.51$ and 14.23 ppm belong to carbons in alkyl chain. The peak with the highest chemical shift was assigned to C2, $\delta = 171.46$ ppm which carbon centered by two electronegative atoms, nitrogen and sulfur atoms ($-\text{N}=\text{C}-\text{S}-$). The following resonance signal $\delta = 164.93$ ppm corresponded to C11 which is the carbon atom in Schiff base linkage. A significant peak observed at $\delta = 68.51$ ppm is assigned to C17 in the alkoxy chain. It is because the signal has the highest chemical shift among all the aliphatic carbon was directly bonded to the electronegativity oxygen atom in the ether linkage ($-\text{O}-\text{CH}_2-$). A peak at $\delta = 14.23$ ppm was assigned to the methylene ($-\text{CH}_3$) carbon for compound **12MeBTH**. This carbon was found away from those electronegativity atoms and thus showed a peak in the higher field region.

The structure of the compound is further substantiated by the ^{13}C NMR data. The HMQC spectrum of **12MeBTH** (Figure 4.14) also reveals the connectivity between the aromatic hydrogens and their corresponding carbons. From the plot, the peaks owing to the carbons at $\delta = 132.97$ and 114.83 ppm show correlation with the H13 (or H13') (refer to cross peak) and the H14 (or H14') (refer to cross peak) atoms, respectively. Thus, the peak at $\delta = 132.97$ and 114.83 ppm are associated with the C13 (or C13') and the C14 (or C14') atoms,

respectively. The spectrum also show the cross peak of the H9 atom with the C9 atom at $\delta = 129.84$ ppm, the cross peak of the H6 atom with the C6 atom at $\delta = 121.42$ ppm and the cross peak of the H8 atom with the C8 atom at $\delta = 118.69$ ppm.

The HMQC experiment also reveals that the H28 atom ($\delta = 0.87$ ppm) correlates with the C28 atom at $\delta = 14.23$ ppm and the H17 atom at $\delta = 4.00$ ppm correlates with the C17 atom at $\delta = 68.51$ ppm. A quintet at $\delta = 1.79$ ppm owing to the H18 atom correlates with the C18 atom at $\delta = 32.01$ ppm. The multiplets attributed to the H19-H27 atoms at the chemical shift range of $\delta = 1.26$ - 1.46 ppm are found to correlate with the C 19-C27 atoms at the chemical shift range of $\delta = 14.23$ - 29.73 ppm.

The quaternary carbons are assigned by using the HMBC experiment. The long range HMBC cross peaks of the H13 (or H13') atom with the C2 atom at $\delta = 171.46$ ppm, H14 (or H14') atom with the C6 atom at $\delta = 121.42$ ppm , H9 atom with the C13, C13' atom at $\delta = 132.97$ ppm, H6 atom with the C9 atom at $\delta = 129.84$ ppm and the H8 atom with the C6 atom at $\delta = 121.42$ ppm strongly support the positions of these atoms. The peak of the C17 ether atom at $\delta = 68.51$ ppm is assigned based on the heteronuclear connectivities with the methylene protons (H18 and H19).

The same NMR experiments have also been performed on the representative compounds (**12OMeBTH**, **12OEtBTH** and **12HBZT**). These

compounds show the similar NMR features as those observed for compounds **12MeBTH**. The NMR spectral data of compounds **12OMeBTH**, **12OEtBTH** and **12HBZT** included in Appendices 7A to C, respectively.

Table 4.6: ¹H NMR spectral data of compound 12MeBTH in CDCl₃

Proton Number	Chemical Shift, δ (ppm)	Integrals	Multiplicity*	Coupling Constant, J (Hz)
H11	8.91	1H	s	-
H13,H13'	7.84	2H	d	8.7
H9	7.38	1H	d	8.1
H6	7.34	1H	s	-
H8	7.15	1H	d	8.1
H14,H14'	6.97	2H	d	8.7
H17	4.00	2H	t	6.6
H29	2.34	3H	s	-
H18	1.79	2H	p	6.9
H19-H27	1.25-1.46	18H	m	-
H28	0.87	3H	t	6.9

Note:

TMS was used as an internal standard.

*s=singlet,

d=doublet

t=triplet

p=quintet

m=multiplet

Table 4.7: ^{13}C NMR spectral data of compound 12MeBTH in CDCl_3

Carbon number	Chemical Shift, δ (ppm)
C2	171.46
C11	164.93
C15	163.51
C7	149.84
C13,C13'	132.97
C4	132.49
C12	131.24
C9	129.84
C5	125.56
C6	121.42
C8	118.69
C14,C14'	114.83
C17	68.51
C18	32.01
C19-C25	29.73
	29.68
	29.65
	29.44
	29.19
	29.13
C26	26.04
C27	22.78
C29	21.33
C28	14.23

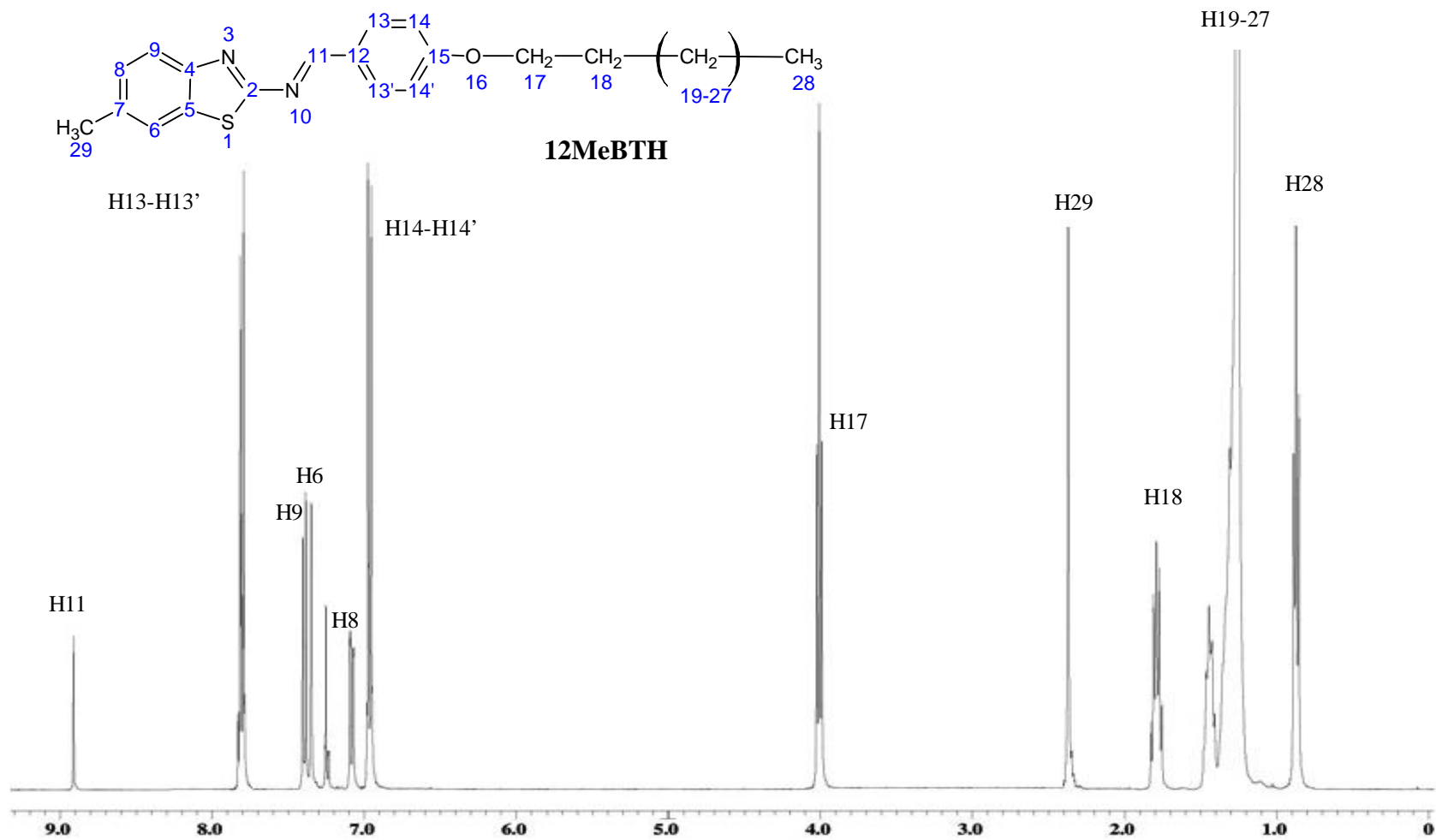


Figure 4.11: ¹H NMR spectrum of compound 12MeBTH.

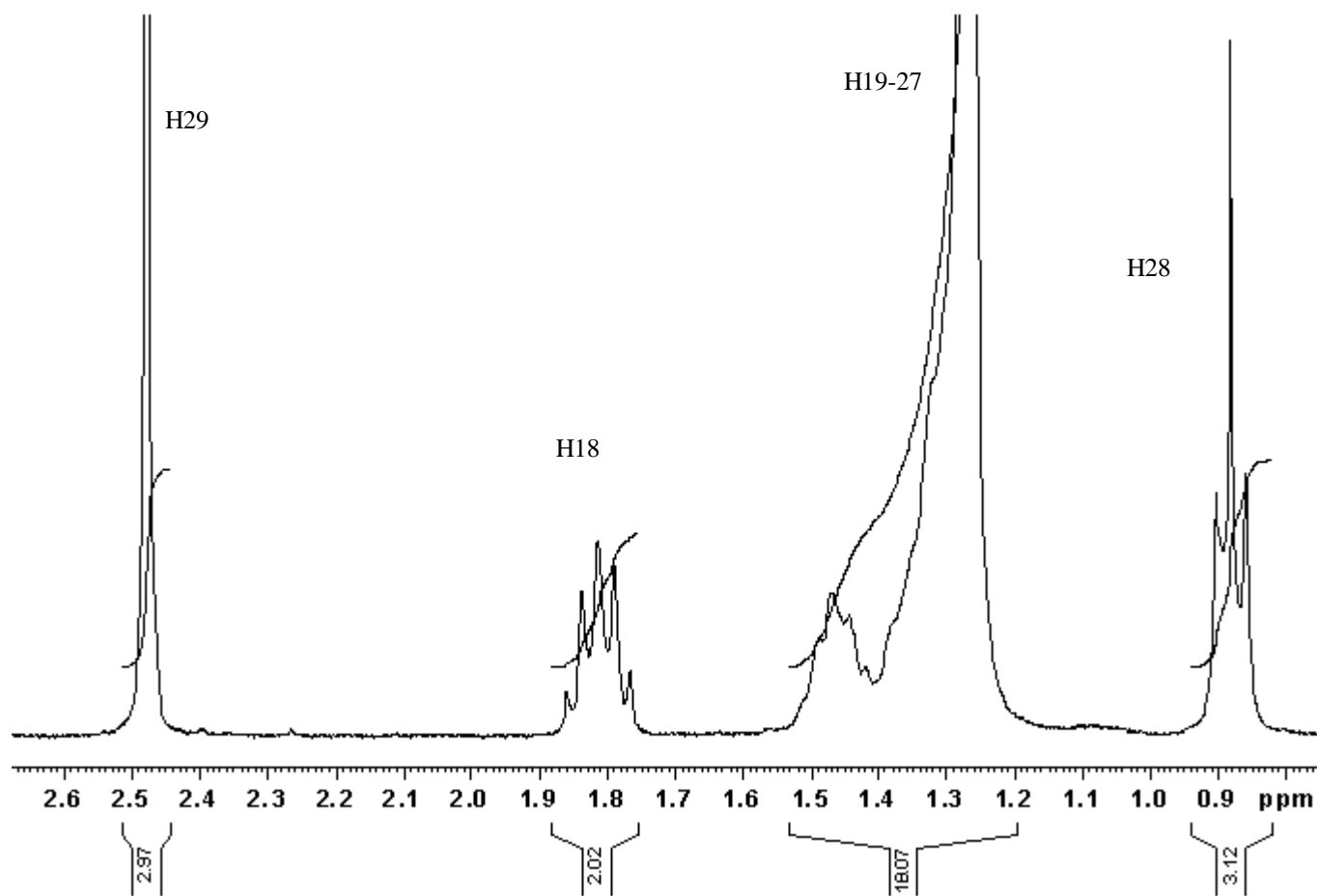


Figure 4.11(a): Integration of ^1H NMR spectrum of compound 12MeBTH, 1st part.

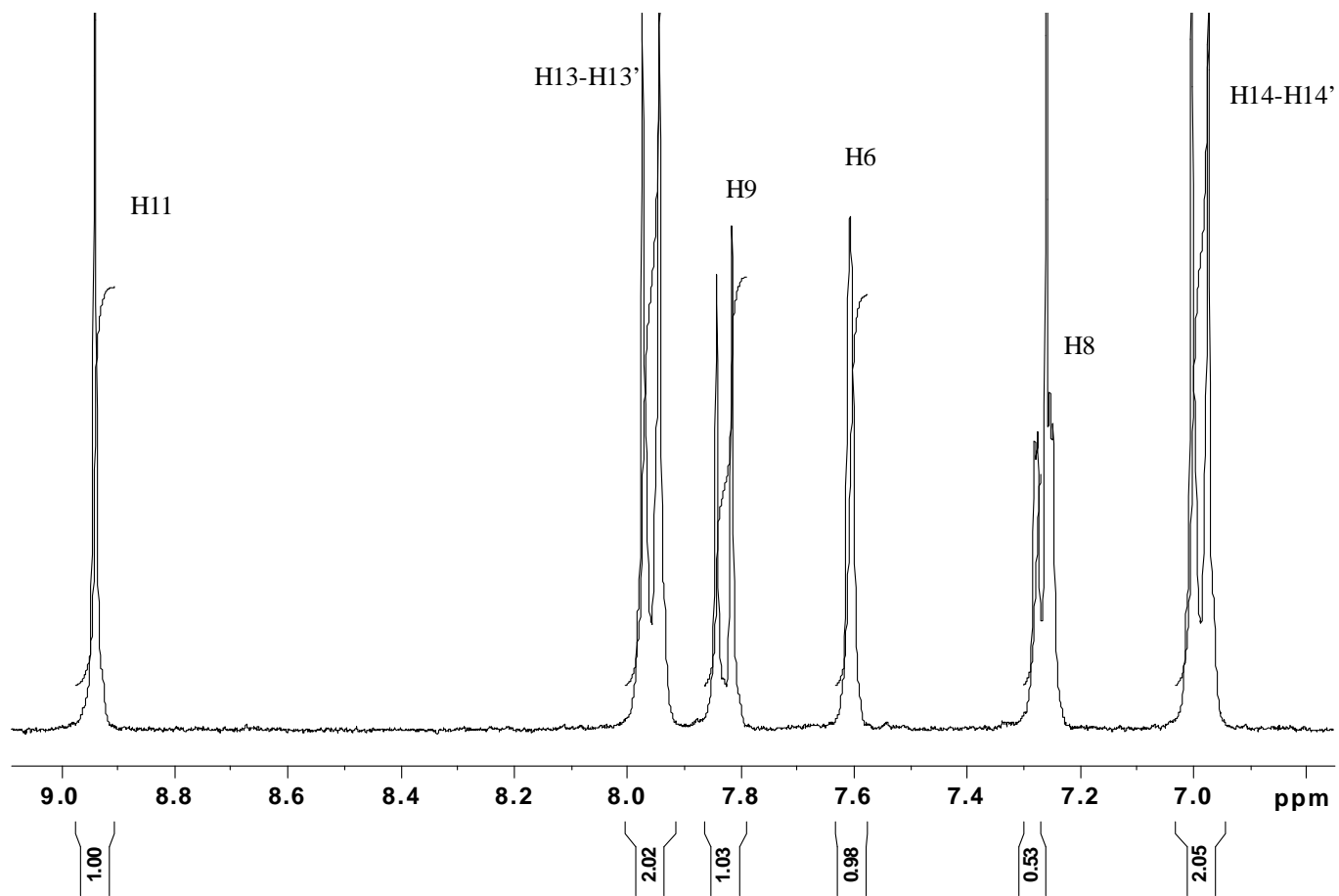


Figure 4.11(b): Integration of ^1H NMR spectrum of compound 12MeBTH, 2nd part.

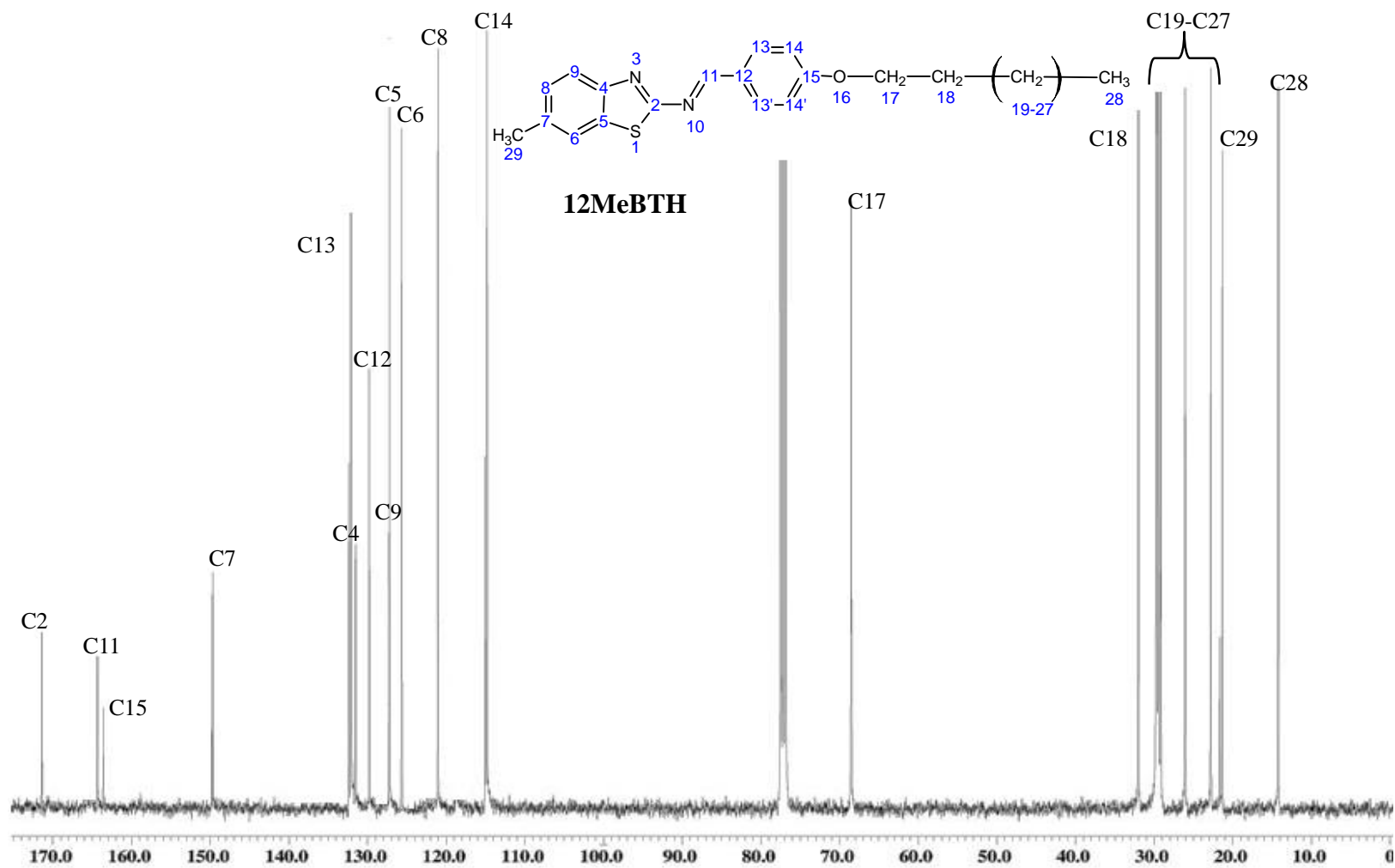


Figure 4.12: ¹³C NMR spectrum of compound 12MeBTH.

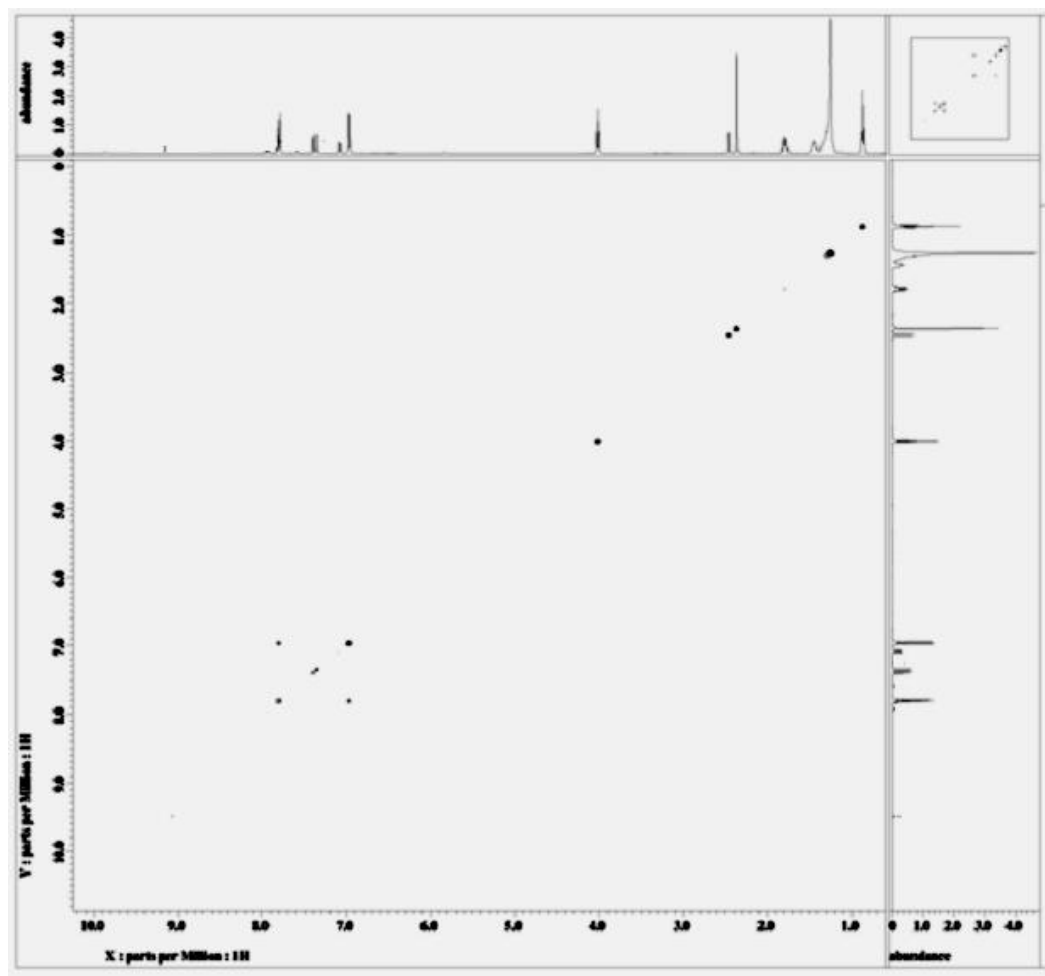


Figure 4.13: COSY spectrum of compound 12MeBTH.

Table 4.8: ^1H - ^1H correlations as deduced from the 2D COSY experiments for compound 12MeBTH

Atom No. ^a	^1H - ^1H COSY correlations
H11	---
H13,H13'	H14, H14'
H9	H8
H6	H9
H8	H9, H6
H14,H14'	H13, H13'
H17 ^b	H18
H29	-
H18 ^c	H17, H19-27
H28	H19-H27

TMS was used as internal standard.

^a Based on the numbering scheme in Figure 4.11.

^b The H17 atom correlates with the methylene protons (H19-H27) but their real positions could not be determined because the ^1H chemical shifts of the H19-H27 atoms were indistinguishable.

^c The H18 atom correlates with the methylene protons (H19-H27) but their real positions could not be determined because the ^1H chemical shifts of the H19-H27 atoms were indistinguishable.

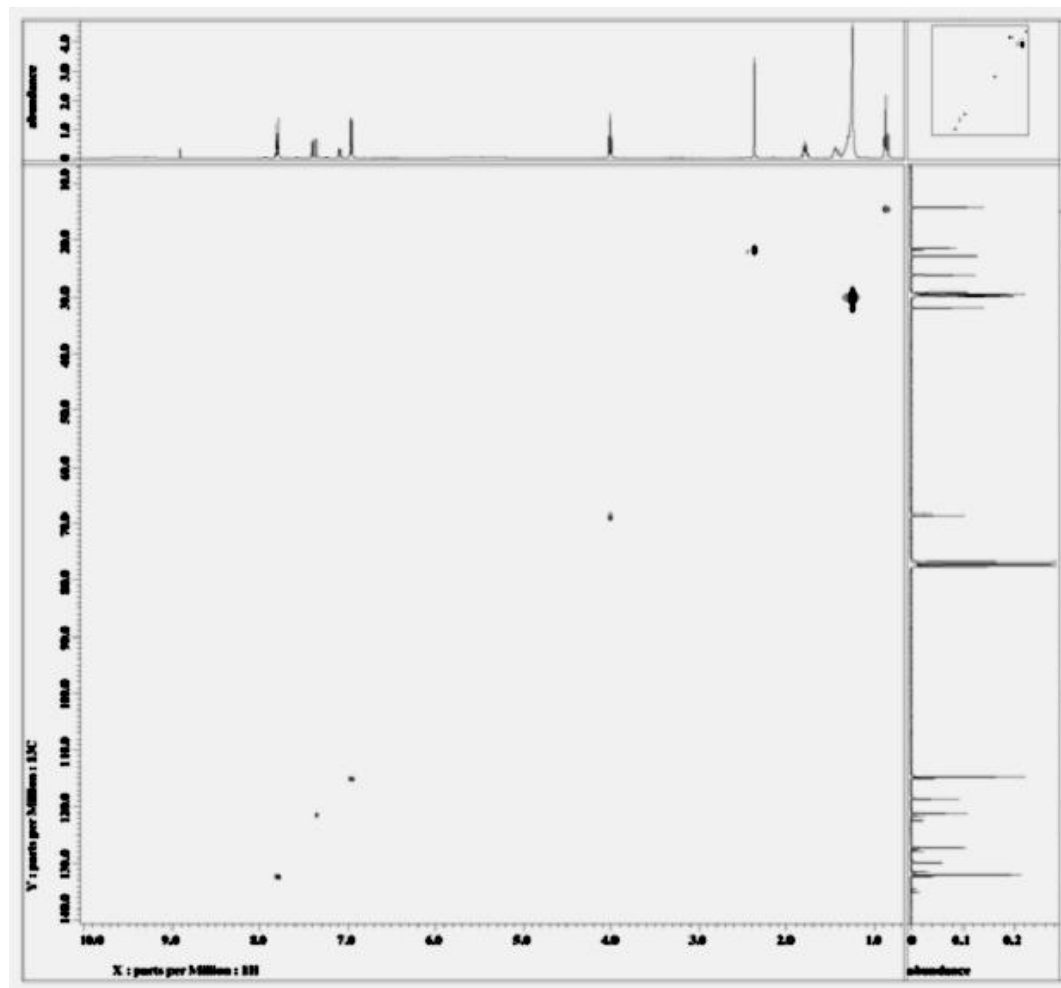


Figure 4.14: HMQC spectrum of compound 12MeBTH.

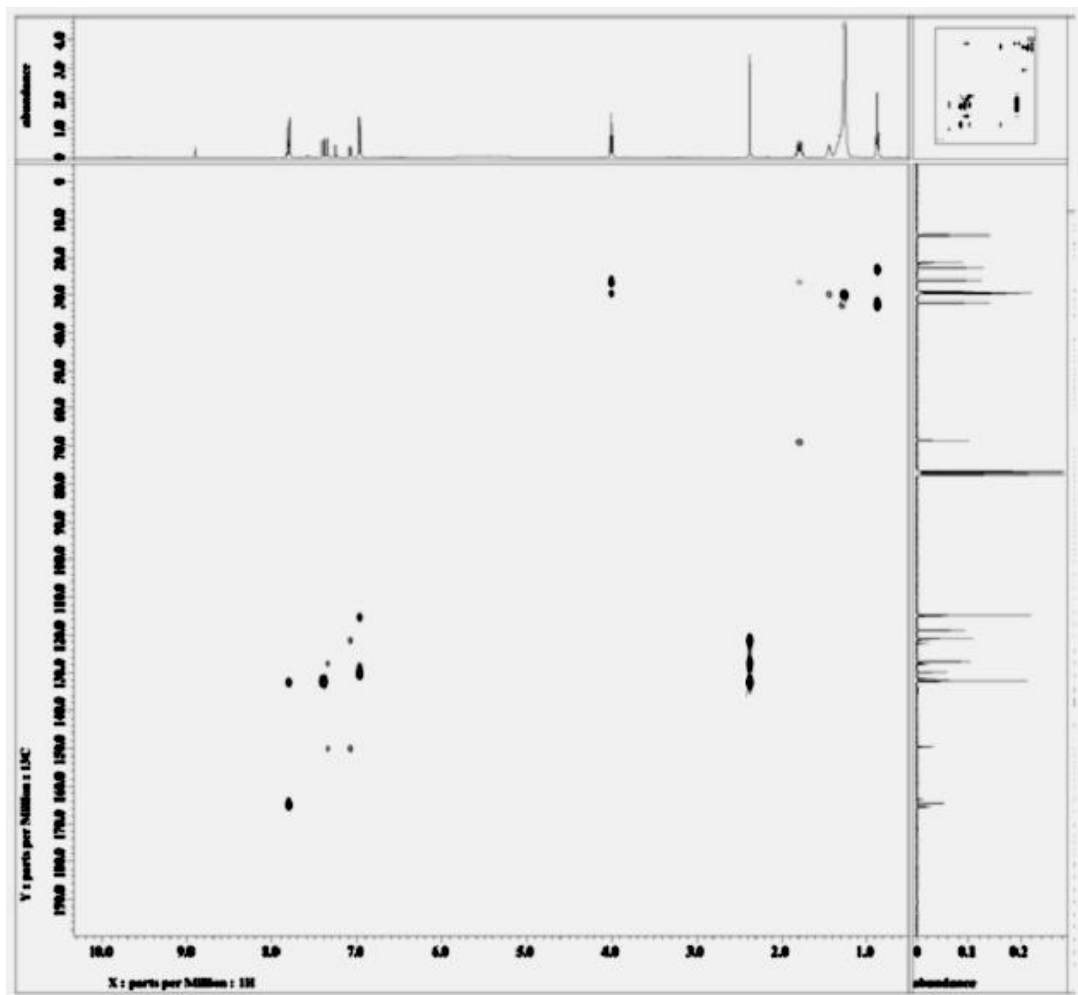


Figure 4.15: HMBC spectrum of compound 12MeBTH.

Table 4.9: ^{13}C - ^1H correlations as deduced from the 2D HMQC and HMBC experiments for compound 12MeBTH

Atom No. ^a	HMQC		HMBC [$J(\text{C,H})$]		
	1J	2J	3J	4J	bJ
H11	C11	C12	---	---	---
H13	C13	---	C11,C15	---	C2
H13'	C13'	---	C11,C15	---	C2
H9	C9	---	---	---	C13,C13'
H8	C8	---	---	C6	---
H6	C6	C7	---	C9	---
H14	C14	C15	C12	---	C6
H14'	C14'	C15	C12	---	C6
H17 ^c	C17	C18	C19	---	---
H29	C29	---	C6	C9	C13,C13'
H18 ^d	C18	C17,C19	---	---	---
H28	C28	C27	C26	---	---

TMS was used as internal standard.

^a Based on the numbering scheme in Figure 4.12.

^b Intramolecular interaction.

^c The C17 atom correlates with the methylene carbons (C19-C25) but their real [$J(\text{C,H})$] value could not be determined because the ^{13}C chemical shifts of the C19-C25) atoms were indistinguishable.

^d The C18 atom correlates with the methylene carbons (C19-C25) but their real [$J(\text{C,H})$] value could not be determined because the ^{13}C chemical shifts of the C19-C25) atoms were indistinguishable.

4.2 Series 2: Structural Elucidation of 6-Methyl-2-[4-(4-alkoxybenzoyloxy)benzylidenamino]benzothiazoles (nMe3R), 6-methoxy-2-[4-(4-alkoxybenzoyloxy)benzylidenamino]benzothiazoles (nOMe3R) and 2-[4-(4-alkoxybenzoyloxy)benzylidenamino]benzothiazoles (nHB3R)

The chemical structures of the title compounds are shown at Figure 4.16.

The percentage of yields are summarized in Table 4.10.

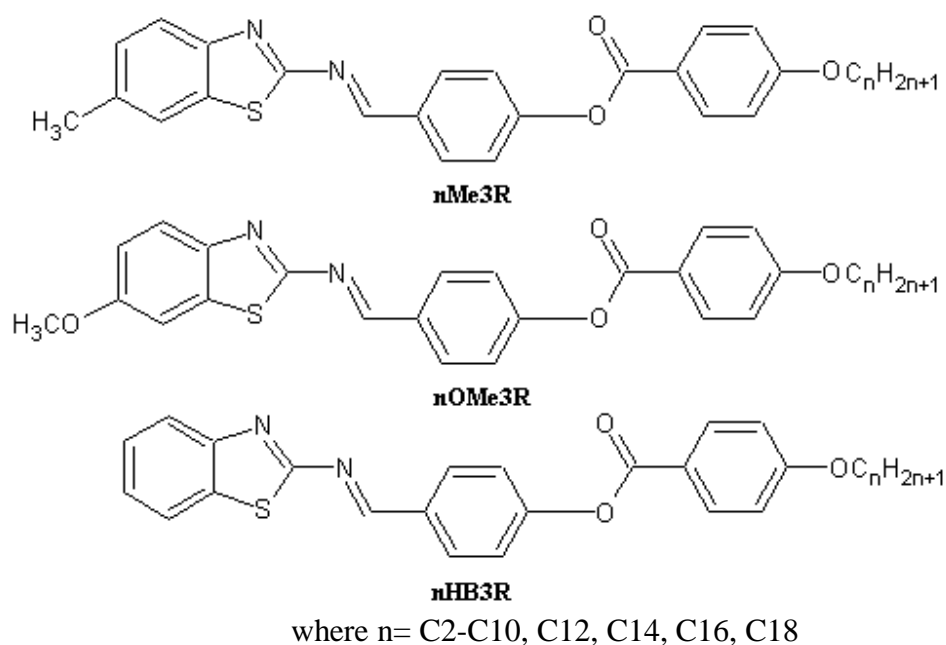


Figure 4.16: Chemical structures of nMeBTH, nOMeBTH, nOEtBTH and nHBZT.

Table 4.10: Percentage of yields of compounds nMe3R, nOMe3R and nHB3R.

<u>nMe3R</u>			<u>nOMe3R</u>	
Compound	Percentage	of	Compound	Percentage
	yield (%)			of yield (%)
2Me3R	25		2OMe3R	28
3Me3R	23		3OMe3R	25
4Me3R	31		4OMe3R	34
5Me3R	36		5OMe3R	39
6Me3R	40		6OMe3R	42
7Me3R	44		7OMe3R	46
8Me3R	46		8OMe3R	49
9Me3R	43		9OMe3R	44
10Me3R	51		10OMe3R	52
12Me3R	46		12OMe3R	47
14Me3R	59		14OMe3R	56
16Me3R	63		16OMe3R	62
18Me3R	68		18OMe3R	67

<u>nHB3R</u>	
Compound	Percentage
	of yield (%)
2HB3R	26
3HB3R	27
4HB3R	33
5HB3R	37
6HB3R	44
7HB3R	48
8HB3R	45
9HB3R	46
10HB3R	51
12HB3R	48
14HB3R	55
16HB3R	63
18HB3R	68

Structural elucidations of compounds **nMe3R**, **nOMe3R** and **nHB3R** were conclusively elucidated via spectroscopic methods (FT-IR, NMR and EI-MS). The purity of the compound was confirmed by using HPLC and TLC analysis. The HPLC chromatograms of the representative compounds, **16Me3R**, **14OMe3R** and **9HB3R** are shown in Appendix 2A. The TLC R_f data associated with compounds **nMe3R**, **nOMe3R** and **nHB3R** are listed in Appendix 2B and 2C, respectively. All the compounds gave a single spot on the TLC plate (Sharma *et al.*, 2003b).

A mass spectrometric study was carried out on **16Me3R**, **16OMe3R** and **16HB3R** as representative compounds for each series. EI mass spectrum of **16Me3R**, **16OMe3R** and **16HB3R** are shown in Figures 4.17, 4.18 and 4.19, respectively. Recognition of the molecular ion peak was based on the molecular mass of compound **16Me3R** found at 612.4 *m/z* with relative abundance of 4.09. The mass spectra of compounds **16OMe3R** and **16HB3R** confirmed the molecular mass based on the molecular ion peaks at 628.4 and 589.4 *m/z* with relative abundance of 7.58 and 1.87, respectively.

Selected FT-IR data associated with compounds **16Me3R**, **16OMe3R** and **16HB3R** are summarized in Tables 4.11, 4.12 and 4.13, respectively, while the FT-IR spectrum of the representative compound **16Me3R**, **16OMe3R** and **16HB3R** are shown in Figures 4.20, 4.21 and 4.22, respectively.

From the spectrum of compound **16Me3R**, the absorption bands at 2917 and 2848 cm⁻¹ represented C-H bond stretching in the long terminal carbon chains while

the other diagnostic band at 1261 cm^{-1} was ascribed to the aromatic C-O ether bond in the compound. Another major absorption band at 1737 cm^{-1} was indicated to the carbonyl group (C=O) of ester linkage, indicating the successful Steglich esterification. By referring to the chemical structure of **16Me3R**, the formation of benzothiazole ring can be traced by the appearance of absorption band at 1598 cm^{-1} and the band appeared at 1608 cm^{-1} was assigned to C=N for Schiff base linkage.

For compounds **16OMe3R** and **16HB3R**, it can be noticed that the absorption bands at range of 2900 to 2800 cm^{-1} represented C-H bond stretching in the long terminal carbon chains while the other diagnostic band around 1254 to 1255 cm^{-1} was ascribed to the aromatic C-O ether bond in the compound. Another major absorption band was observed within 1727 to 1729 cm^{-1} and this band assigned to the carbonyl group of ester (-COO-) linkage. The C=N for Schiff base linkage can be observed at 1607 cm^{-1} .

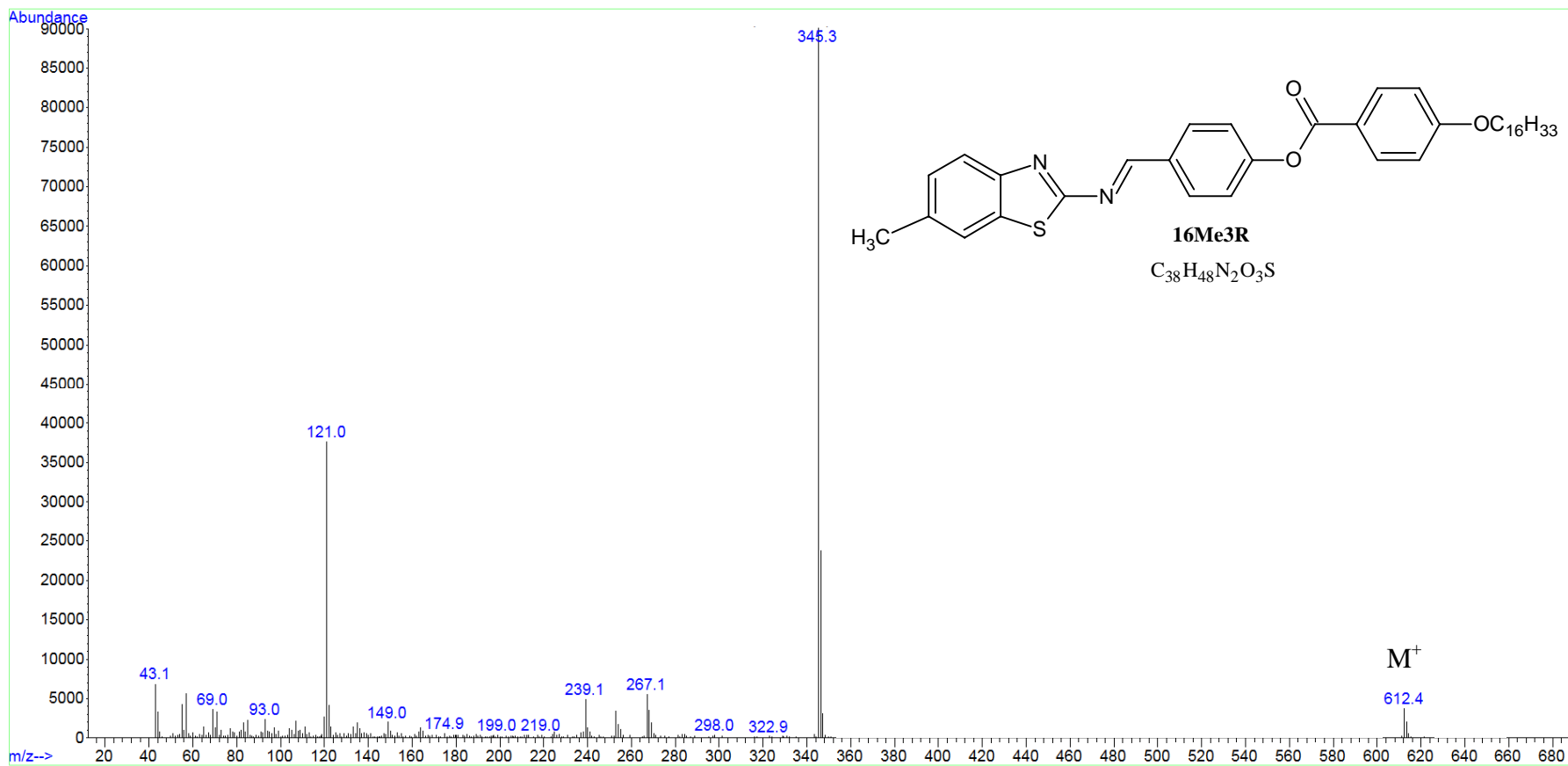


Figure 4.17: Mass spectrum of compound 16Me3R.

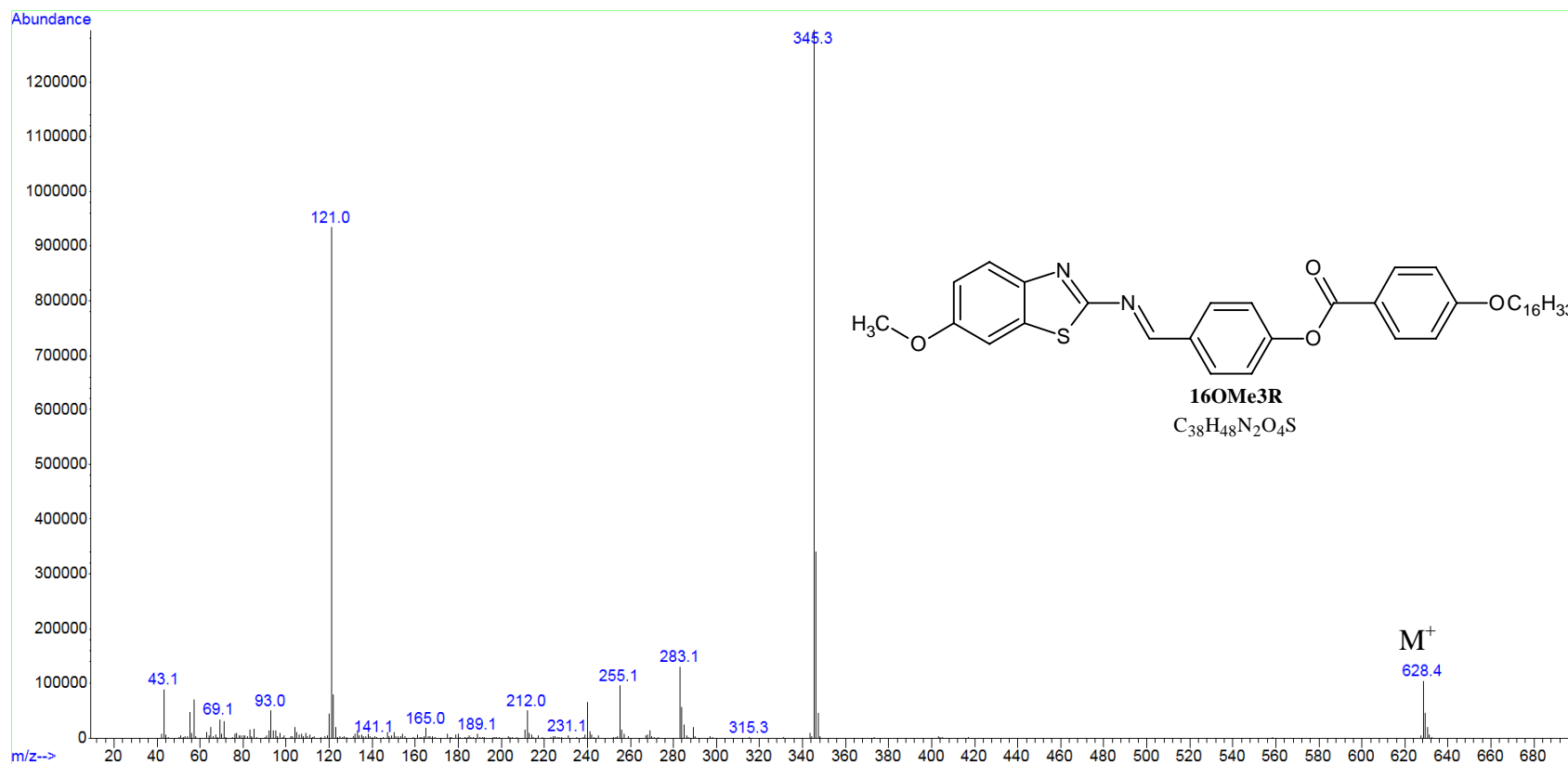


Figure 4.18: Mass spectrum of compound 16OMe3R.

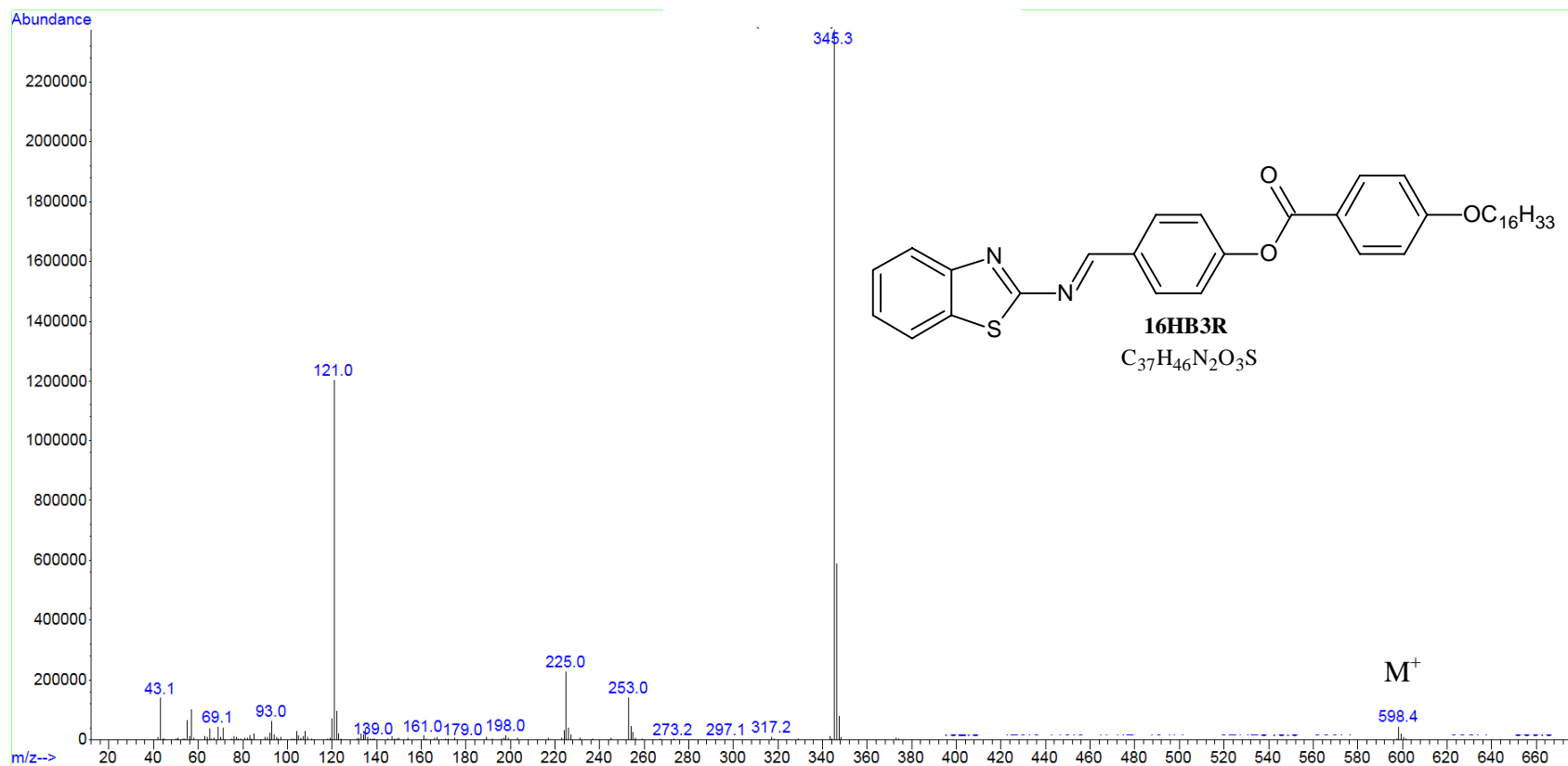


Figure 4.19: Mass Spectrum of compound 16HB3R.

Table 4.11: FT-IR spectral data of compounds nMe3R

Compound	IR ν (cm ⁻¹)					
	sp ² C-H Stretch (aromatic)	sp ³ C-H Stretch (aliphatic)	C=O (ester)	C=N (Schiff base)	C=N (Benzothiazole)	Ar-O-C (Ether)
2Me3R	3033	2934,2852	1731	1612	1598	1269
3Me3R	3023	2938,2878	1729	1607	1596	1256
4Me3R	3022	2934,2877	1726	1604	1592	1255
5Me3R	3063	2932,2850	1731	1599	1581	1256
6Me3R	3063	2930,2853	1731	1598	1581	1256
7Me3R	3054	2917,2854	1728	1607	1580	1260
8 Me3R	3055	2916,2853	1729	1606	1593	1259
9Me3R	3055	2920,2851	1731	1606	1598	1272
10Me3R	3028	2925,2847	1720	1607	1571	1275
12Me3R	3026	2918,2849	1728	1607	1594	1262
14Me3R	3017	2921,2851	1726	1601	1576	1252
16Me3R	3018	2917,2848	1737	1608	1598	1261
18Me3R	3055	2920,2850	1732	1608	1577	1257

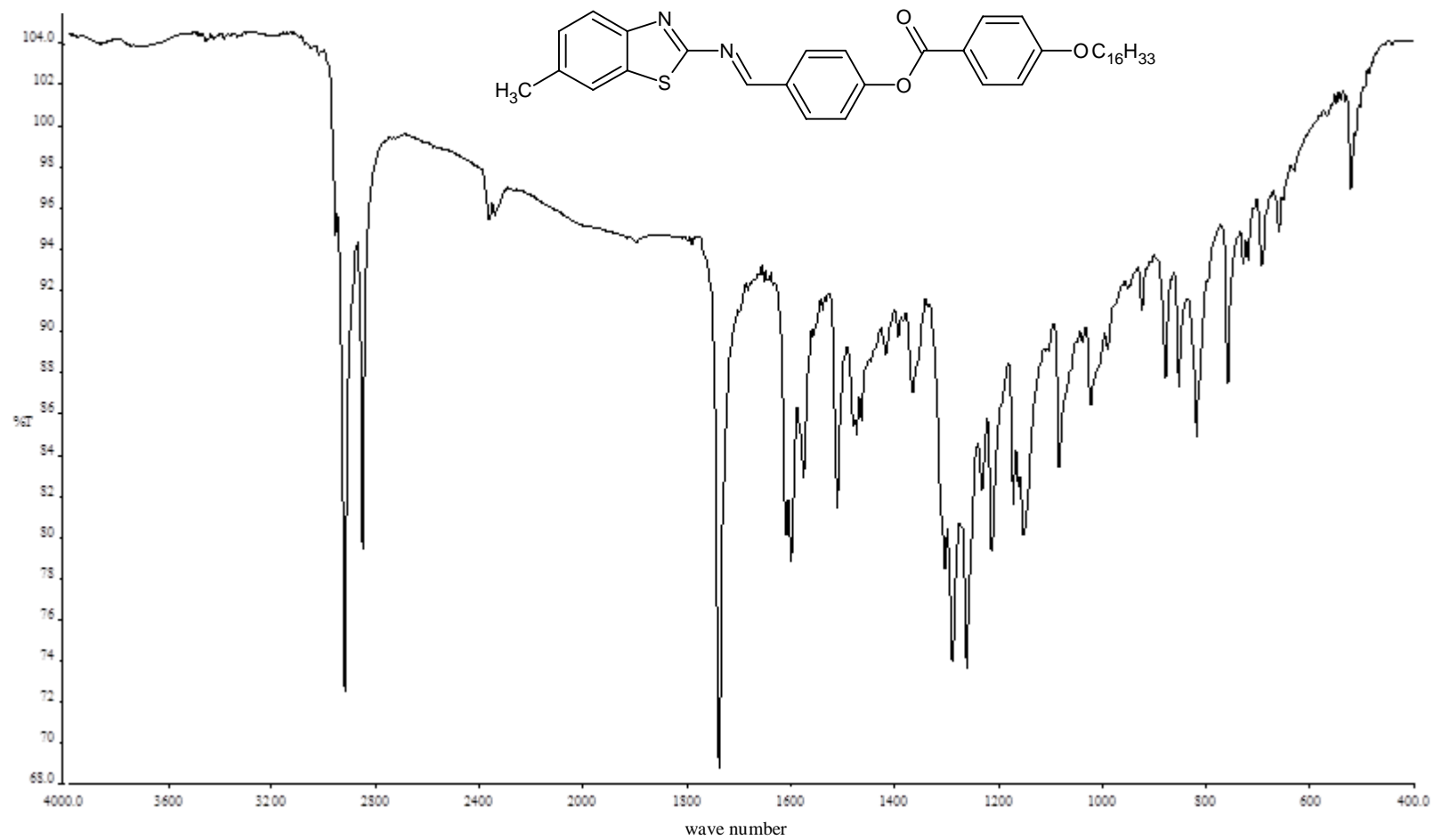


Figure 4.20: FT-IR spectrum of compound 16Me3R.

Table 4.12: FT-IR spectral data of compounds nOMe3R

Compound	IR ν (cm ⁻¹)					
	sp ² C-H Stretch (aromatic)	sp ³ C-H Stretch (aliphatic)	C=O (ester)	C=N (Schiff base)	C=N (Benzothiazole)	Ar-O-C (Ether)
2OMe3R	3059	2982,2826	1729	1611	1602	1272
3OMe3R	3057	2917,2849	1725	1601	1599	1268
4OMe3R	3073	2952,2869	1724	1605	1576	1258
5OMe3R	3053	2940,2857	1730	1598	1570	1252
6OMe3R	3064	2954,2853	1734	1607	1572	1264
7OMe3R	3070	2916,2849	1729	1607	1568	1264
8OMe3R	3000	2916,2854	1727	1607	1568	1264
9OMe3R	3016	2916,2852	1726	1607	1569	1264
10OMeR	3077	2916,2851	1728	1611	1574	1266
12OMe3R	3065	2923,2853	1735	1606	1580	1267
14OMe3R	3071	2918,2849	1729	1605	1574	1254
16OMe3R	3070	2918,2849	1729	1607	1578	1255
18OMe3R	3070	2916,2850	1725	1607	1579	1286

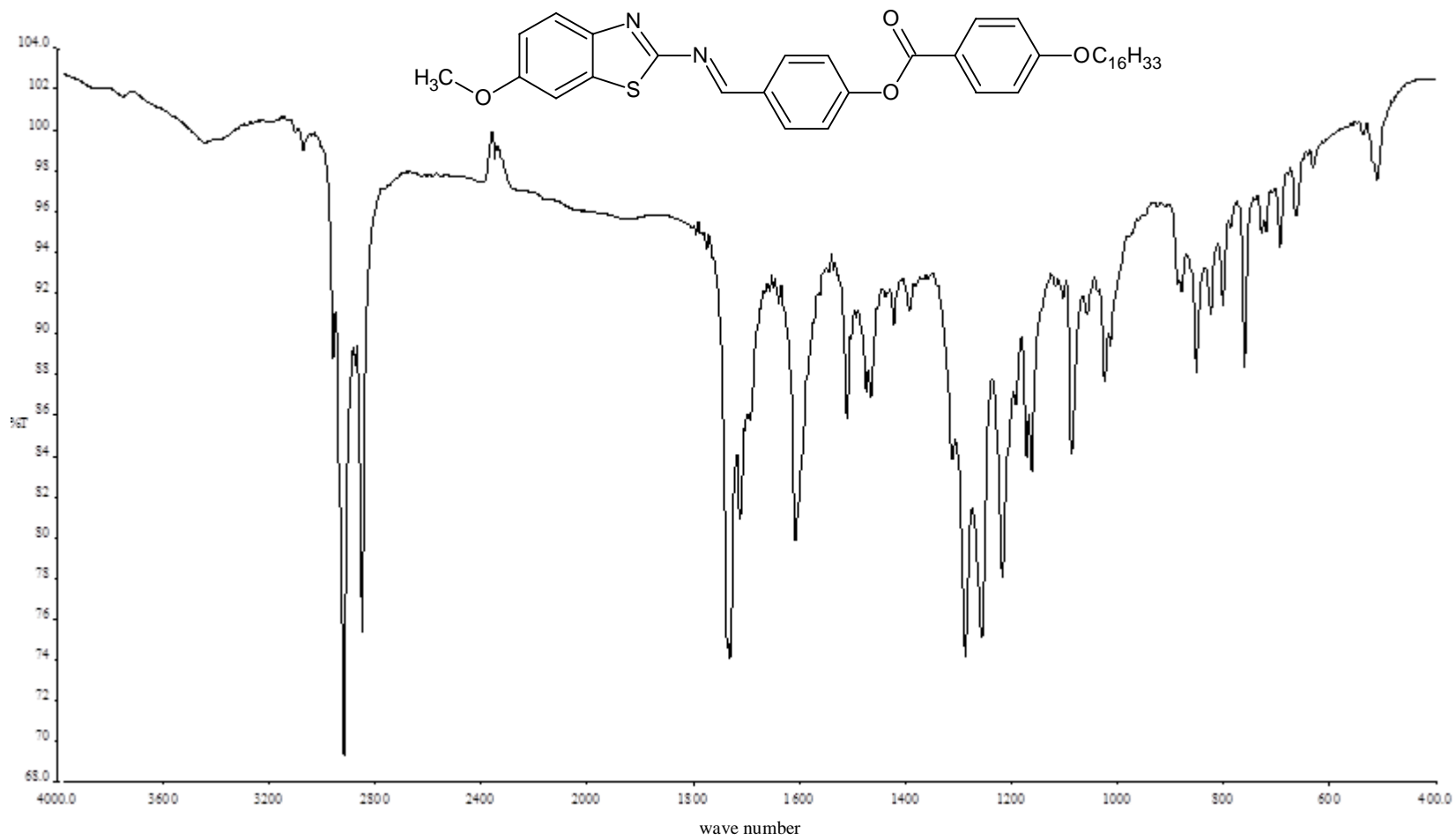


Figure 4.21: FT-IR spectrum of compound 16OMe3R.

Table 4.13: FT-IR spectral data of compounds nHB3R

Compound	IR ν (cm ⁻¹)					
	sp ² C-H Stretch (aromatic)	sp ³ C-H Stretch (aliphatic)	C=O (ester)	C=N (Schiff base)	C=N (Benzothiazole)	Ar-O-C (Ether)
2HB3R	3003	2917,2849	1726	1608	1590	1269
3HB3R	3063	2963,2878	1721	1616	1601	1266
4HB3R	3062	1961,2875	1721	1615	1600	1265
5HB3R	3061	2948,2867	1721	1615	1599	1270
6HB3R	3063	2947,2867	1730	1616	1601	1250
7HB3R	3062	2948,2847	1721	1602	1589	1270
8HB3R	3055	2919,2855	1726	1608	1577	1255
9HB3R	3054	2920,2850	1726	1601	1577	1257
10HB3R	3056	2919,2850	1726	1601	1578	1255
12HB3R	3056	2920,2851	1726	1602	1577	1255
14HB3R	3058	2917,2849	1727	1606	1579	1254
16HB3R	3061	2918,2849	1728	1607	1589	1254
18HB3R	3070	2916,2850	1724	1607	1578	1285

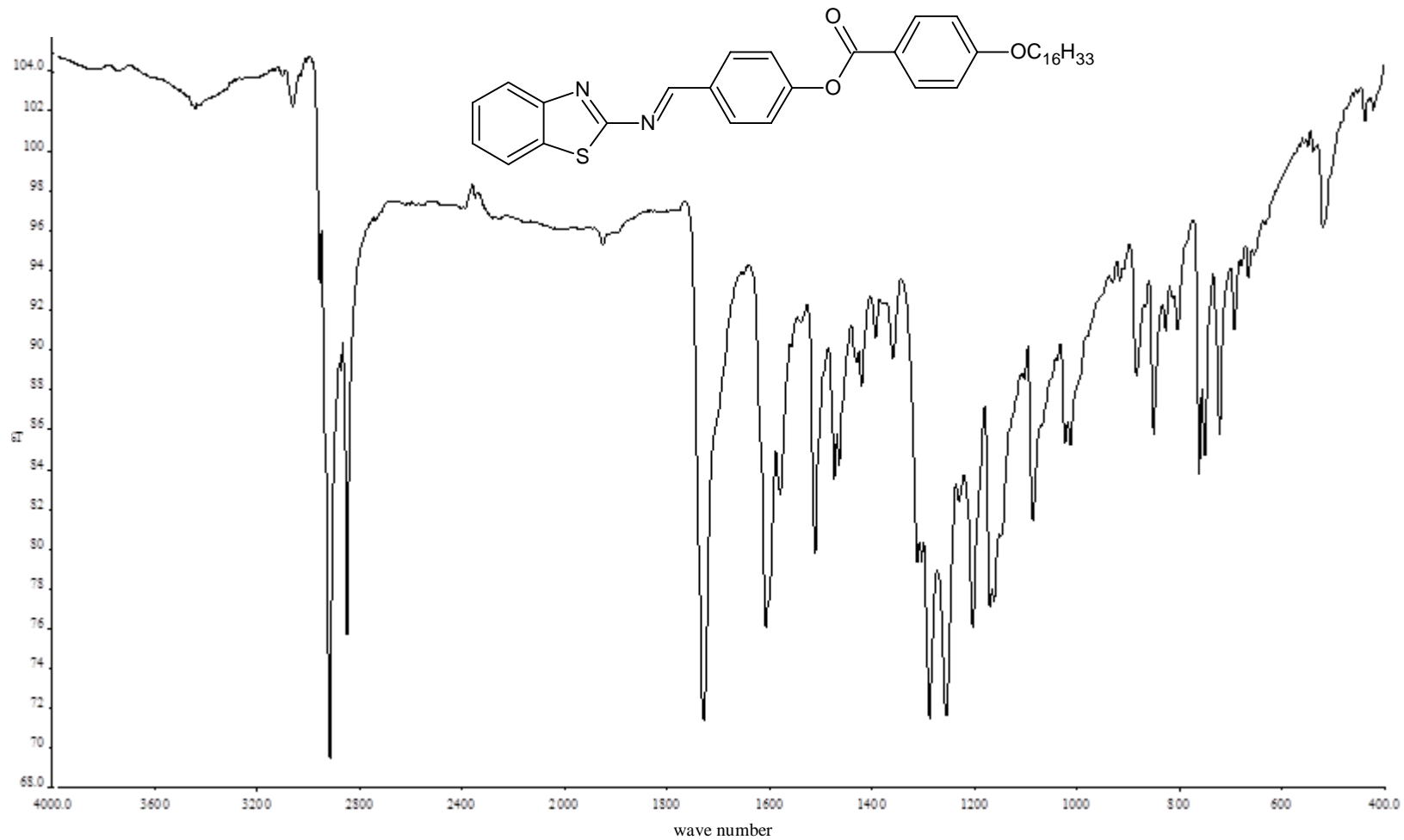


Figure 4.22: FT-IR Spectrum of compound 16HB3R.

NMR spectroscopy was performed on representative compounds **12Me3R**, **8OMe3R** and **16HB3R** for each series. The atomic number scheme of **12Me3R**, **8OMe3R** and **16HB3R** which is used to label the different types of protons and carbons are depicted in Figure 4.23.

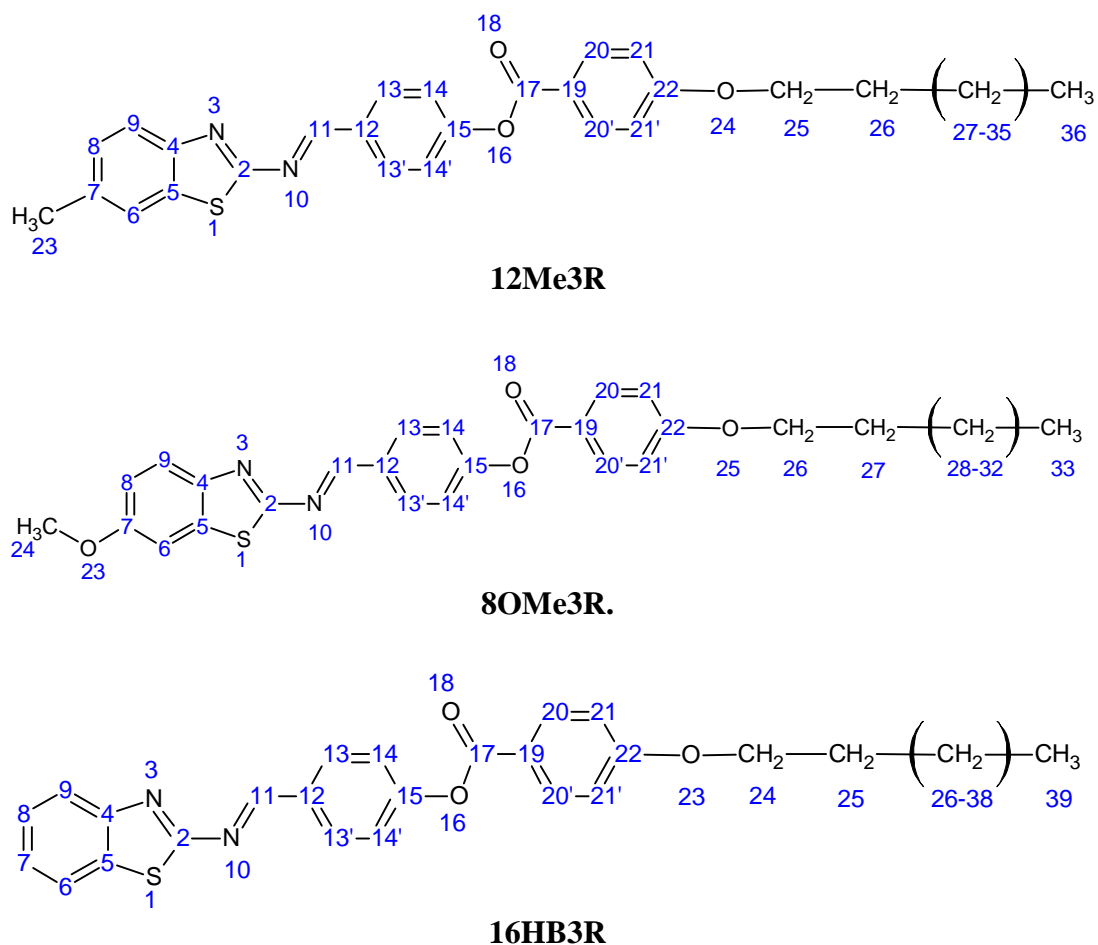


Figure 4.23: Structures with atomic numbering scheme for 12Me3R, 8OMe3R and 16HB3R.

For compounds **12Me3R**, the 1D and 2D NMR spectral data are tabulated in the respective Tables 4.14-4.17, and the 1D NMR and 2D NMR spectra of compounds **12Me3R** are shown in Figures 4.24- 4.28, respectively.

In the ^1H NMR of **12Me3R**, a signal was found at $\delta = 9.07$ ppm corresponded to the azomethine proton (-CH=N-) of **12Me3R** (Ha *et al.*, 2010a). In compound **12Me3R**, there is only one singlet signal was observed for aromatic proton corresponding to H6 at $\delta = 7.64$ ppm. The rest of the protons appeared as doublet within the chemical shift range of $\delta = 6.97$ to 8.13 ppm. Subsequently, the remaining aliphatic protons, H25 to H39, were ascribed to the resonance signals in highfield region of $\delta = 0.83$ to 4.03 ppm. Similar characteristics were shown in compounds **8OMe3R** and **16HB3R**. An additional singlet appeared at $\delta = 4.05$ ppm was assigned to the proton in the terminal methoxy (-OCH₃) of **8OMe3R**. It appeared at more downfield region than others aliphatic protons as it located nearer to the electronegative oxygen atom.

In ^{13}C NMR of **12Me3R**, the signal at highest chemical shift $\delta = 171.10$ ppm was attributed to the carbonyl carbon (-C=O-) of ester, C17. Carbon centered by two electronegative atoms nitrogen and sulfur atoms (-N=C-S-) in benzothiazole fragment, C2, was shifted to downfield region $\delta = 164.39$ ppm. The following resonance signal at $\delta = 163.84$ ppm corresponded to C11 which is the carbon atom in Schiff base linkage. The sixteen aromatic carbons appeared within the chemical shift range of $\delta = 114.44$ to 154.98 ppm. The remaining aliphatic carbons in ether group, C25-C35, give rise to the resonance signals within the chemical shift range of $\delta = 14.09$ to 68.41 ppm. Carbon in the terminal methyl group (-CH₃), C23, however, exhibited signal at lower chemical shift at $\delta = 21.59$ ppm. Similar patterns were observed for compounds **8OMe3R** and **16HB3R**. Additional two signals resonated at $\delta = 68.40$ and 58.40 ppm were assigned to C24

and C26, respectively, which proved that two carbons were bonded directly to the electronegativity oxygen atom at the terminal ether linkage for compound **8OMe3R**.

The HMQC spectrum of compound **12Me3R** confirms the presence of the azomethine carbon (C11) at $\delta = 163.84$ ppm based on the direct bond heteronuclear correlation with the azomethine proton (H11). The same ^1H NMR spectrum also shows the resonance owing to the aromatic protons. These signals are assigned with the aid of the COSY experiment. The doublets at $\delta = 7.84$ and 6.97 ppm can be ascribed to the H13 (or H13') and H14 (or H14') atoms, respectively. As for other doublets with an integration of one proton at $\delta = 7.38$ and 7.15 ppm were attributed to H9 and H8, respectively. H6 signal appeared as singlet in the spectrum at $\delta = 7.34$ ppm. A distinguishable peak was observed at $\delta = 4.00$ ppm in the spectrum of **12Me3R**. It was due to the proton which attached to the carbon atom was directly bonded to the electronegativity oxygen atom in the ether linkage (-O-CH₂-).

The HMQC spectrum (Figure 4.27) also reveals the connectivity between the aromatic hydrogens and their corresponding carbons. From the plot, the peaks owing to the carbons at $\delta = 132.41$ and 122.61 ppm showed correlation with the H13 (or H13') (refer to cross peak) and the H14 (or H14') (refer to cross peak) atoms, respectively. The spectrum also showed the cross peak of the H9 atom with the C9 atom at $\delta = 121.05$ ppm, the cross peak of the H6 atom with the C6 atom at $\delta = 131.43$ ppm and the cross peak of the H8 atom with the C8 atom at $\delta = 122.54$

ppm. The HMQC experiment also reveals that the H28 atom ($\delta = 0.87$ ppm) correlates with the C28 atom at $\delta = 14.23$ ppm and the H17 atom at $\delta = 4.00$ ppm correlates with the C17 atom at $\delta = 68.51$ ppm. A quintet at $\delta = 1.79$ ppm owing to the H18 atom correlates with the C18 atom at $\delta = 32.01$ ppm. The multiplets attributed to the H19-H27 atoms at the chemical shift range of $\delta = 1.26$ - 1.46 ppm are found to correlate with the C19-C27 atoms at the chemical shift range of $\delta = 14.23$ - 29.73 ppm.

The quaternary carbons are assigned by using the HMBC experiment. The long range HMBC cross peaks of the H13 (or H13') atom with the C15 atom at $\delta = 155.11$ ppm, H14 (or H14') atom with the C6 atom at $\delta = 131.43$ ppm, H6 atom with the C20 atom at $\delta = 134.81$ ppm and the H8 atom with the C22 atom at $\delta = 121.41$ ppm strongly support the positions of these atoms. The peak of the C17 ether atom at $\delta = 68.51$ ppm is assigned based on the heteronuclear connectivities with the methylene protons (H18 and H19).

The same NMR experiments have also been performed on the representative compounds (**8OMe3R** and **16HB3R**). These compounds show the similar NMR features as those observed for compounds **12Me3R**. The NMR spectral data of compounds **8OMe3R** and **16HB3R** included in Appendices 8A and 8B, respectively.

Table 4.14: ¹H NMR spectral data of compound 12Me3R in CDCl₃

Proton Number	Chemical Shift, δ ppm	Integrals	Multiplicity*	Coupling Constant, J (Hz)
H11	9.07	1H	s	-
H20,H20'	8.13	2H	d	9.0
H13,H13'	8.08	2H	d	8.7
H9	7.85	1H	d	8.4
H6	7.64	1H	s	-
H14,H14'	7.37	2H	d	8.7
H8	7.28	1H	d	8.4
H21,H21'	6.97	2H	d	9.0
H25	4.03	2H	t	6.6
H23	2.50	3H	t	6.6
H26	1.78	2H	p	6.9
H27-H35	1.28-1.48	26H	m	-
H36	0.83	3H	t	6.9

Note:

TMS was used as an internal standard.

*s=singlet,

d=doublet

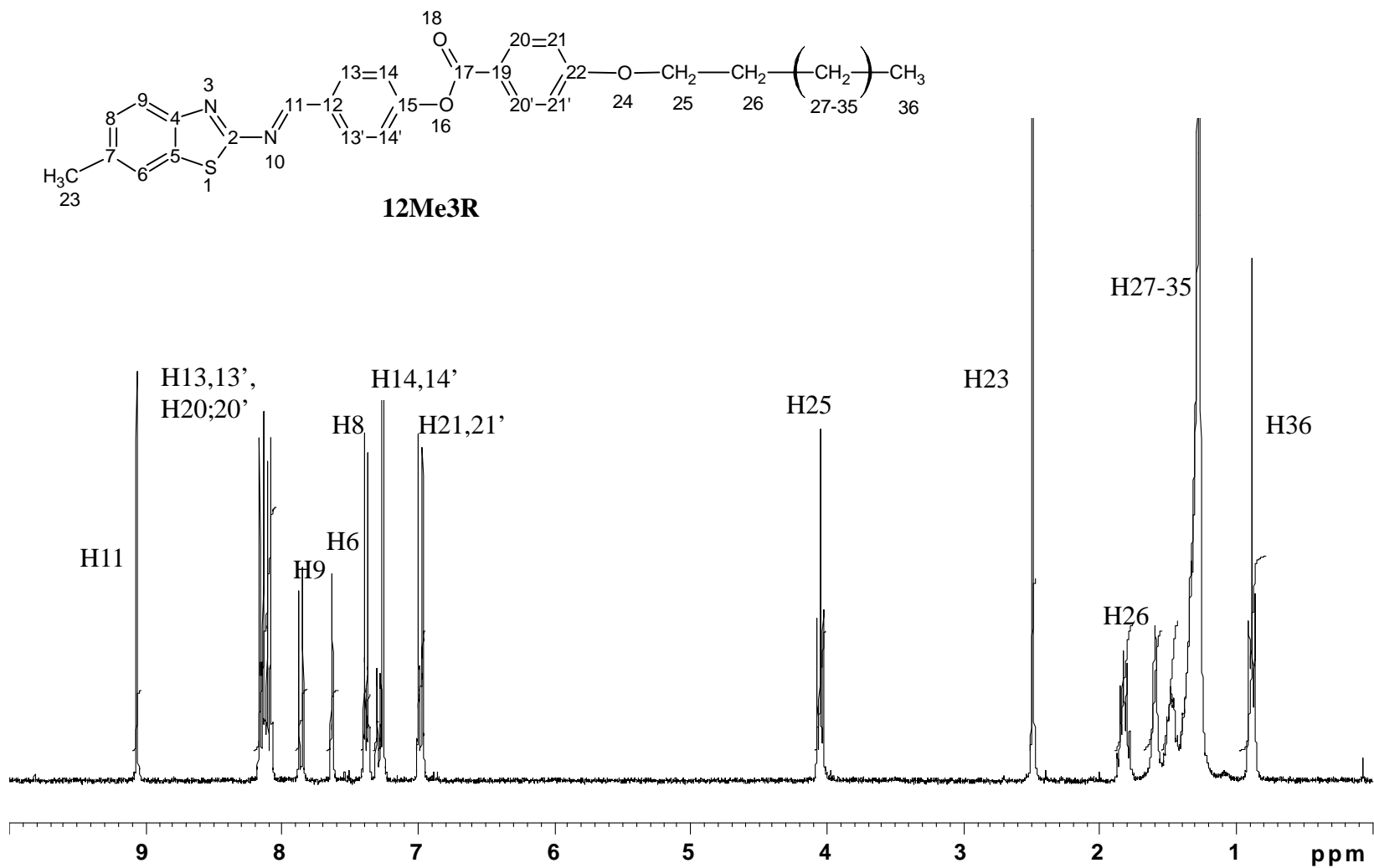
t=triplet

p=quintet

m=multiplet

Table 4.15: ^{13}C NMR spectral data of compound 12Me3R in CDCl_3

Carbon Number	Chemical Shift , δ (ppm)
C17	171.10
C2	164.39
C11	163.84
C15	155.11
C19	154.98
C17	149.19
C12	135.32
C20,C20'	134.81
C13,C13'	132.41
C5	132.43
C6	131.45
C7	128.03
C14,C14'	122.61
C8	122.54
C22	121.41
C9	121.05
C21,C21'	114.44
C25	68.41
C26	31.91
C28-C34	29.84
	29.62
	29.58
	29.54
	29.34
	29.09
C27	25.91
C35	22.68
C23	21.59
C36	14.09



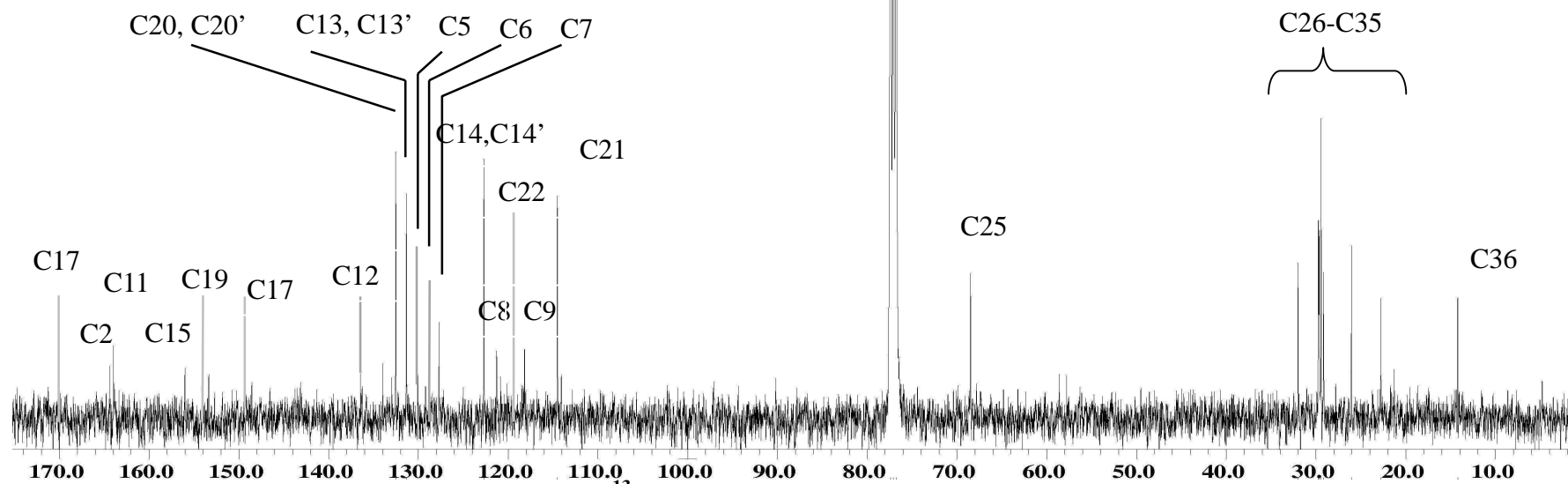
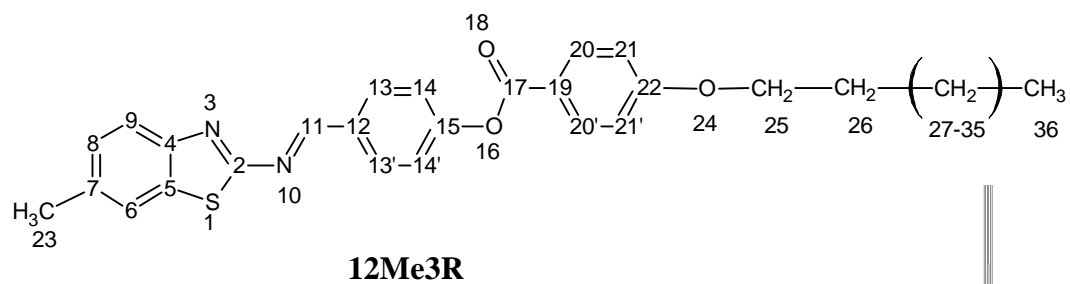


Figure 4.25: ^{13}C NMR spectrum of compound 12Me3R.

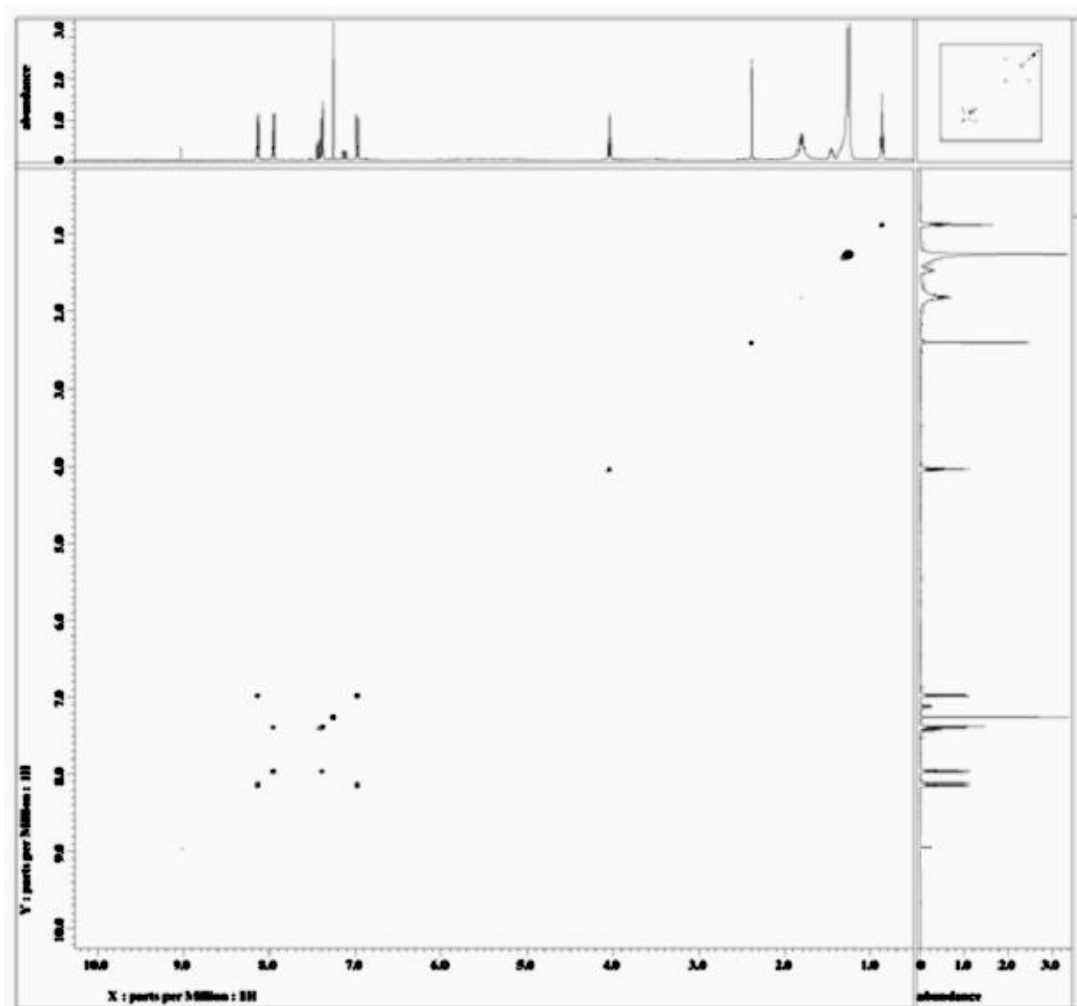


Figure 4.26: COSY spectrum of compound 12Me3R.

Table 4.16: ^1H - ^1H correlations as deduced from the 2D COSY experiments or compound 12Me3R

Atom No. ^a	^1H - ^1H COSY correlations
H20,H20'	H21,H21'
H13,H13'	H14,H14'
H9	H13,H13'
H14,H14'	H13,H13'
H21,H21'	H20, H20'
H25 ^b	H26
H26 ^c	H25, H27-H35
H36	H27-H35

TMS was used as internal standard.

^a Based on the numbering scheme in Figure 4.24.

^b The H25 atom correlates with the methylene protons (H27-H35) but their real positions could not be determined because the ^1H chemical shifts of the H27-H35 atoms were indistinguishable.

^c The H26 atom correlates with the methylene protons (H27-H35) but their real positions could not be determined because the ^1H chemical shifts of the H27-H35 atoms were indistinguishable.

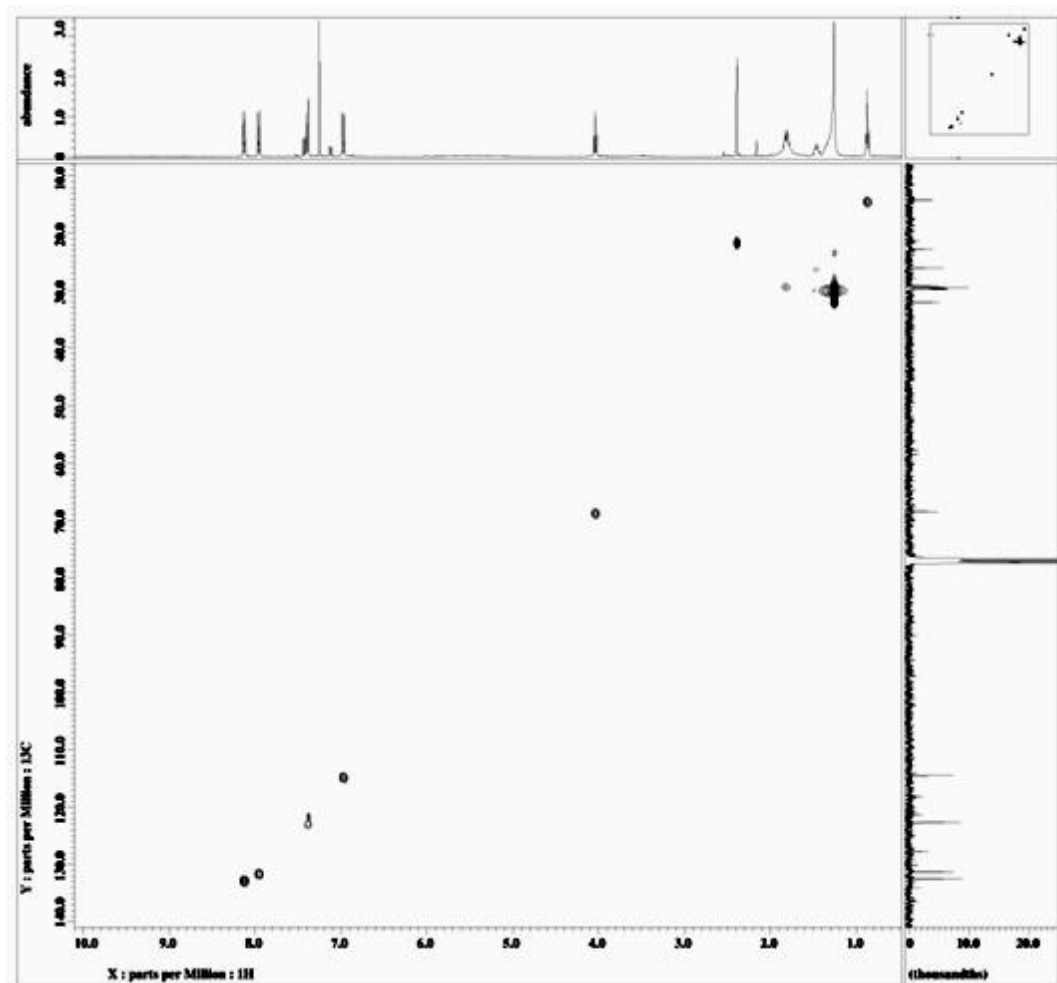


Figure 4.27: HMQC spectrum of compound 12Me3R.

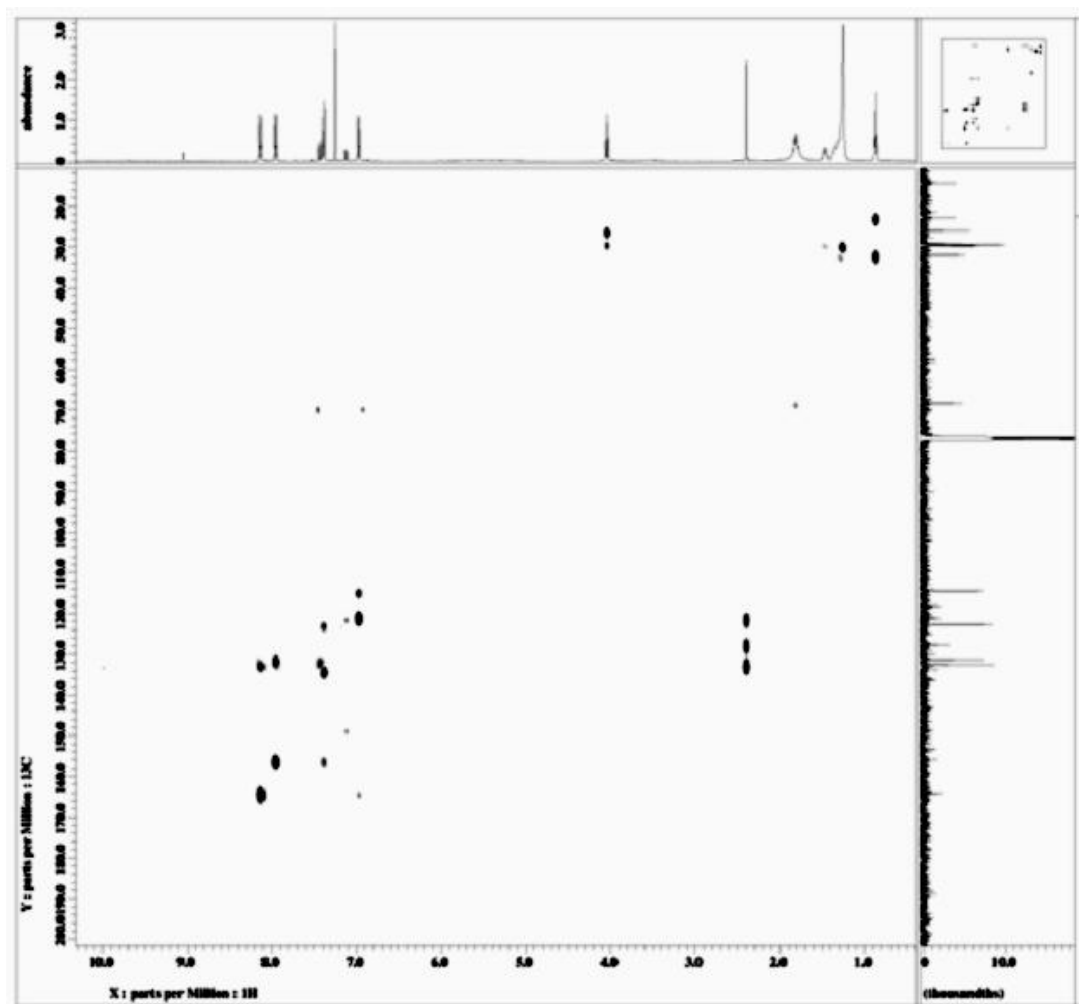


Figure 4.28: HMBC spectrum of compound 12Me3R.

Table 4.17: ^{13}C - ^1H correlations as deduced from the 2D HMQC and HMBC experiments for compound 12Me3R

Atom No. ^a	HMQC		HMBC [$J(\text{C,H})$]		
	1J	2J	3J	4J	bJ
H20	C20	---	C17,C22	---	---
H20'	C20'	---	C17,C22	---	---
H13	C13	---	C11,C15	---	---
H13'	C13'	---	C11,C15	---	---
H14	C14	C15	C12	---	C6
H14'	C14'	C15	C12	---	---
H6	C6	---	---	---	C20, C20'
H8	C8	C7	---	---	C22
H21	C21	C22	C17	---	C6
H21'	C21'	C22	C17	---	C6
H25 ^c	C25 ^b	C26, C27	---	---	---
H23	C23	C7	C6	---	C22
H26 ^d	C26 ^c	C25	C27	---	---
H36	C36	C35	C34	---	---

TMS was used as internal standard.

^a Based on the numbering scheme in Figure 4.25.

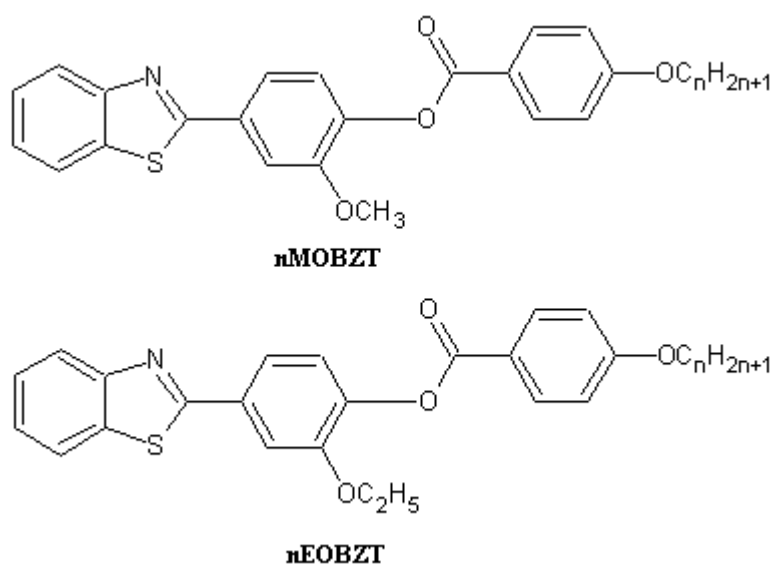
^b Intramolecular interaction.

^c The C25 atom correlates with the methylene carbons (C27-C33) but their real [$J(\text{C,H})$] value could not be determined because the ^{13}C chemical shifts of the C27-C33 atoms were indistinguishable.

^d The C26 atom correlates with the methylene carbons (C27-C33) but their real [$J(\text{C,H})$] value could not be determined because the ^{13}C chemical shifts of the C27-C33 atoms were indistinguishable.

4.3 Series 3: Structural Elucidation of 2-[3-Methoxy-(4-alkoxybenzoyloxy)phenyl]benzothiazoles (nMOBZT) and 2-[3-ethoxy-(4-alkoxybenzoyloxy)phenyl]benzothiazoles (nEOBZT)

2-[3-Methoxy-(4-alkoxybenzoyloxy)phenyl]benzothiazole (nMOBZT, where $n = 2$ to 10, 12, 14, 16, 18) and 2-[3-ethoxy-(4-alkoxybenzoyloxy)phenyl]benzothiazole (nEOBZT, where $n = 2$ to 10, 12, 14, 16, 18) were synthesized. Chemical structures of both series are shown at Figure 4.29. The percentage of yields are summarized in Table 4.18.



where $n = C2-C10, C12, C14, C16, C18$

Figure 4.29: Chemical structures of 2-[3-Methoxy-(4-alkoxybenzoyloxy)phenyl]benzothiazoles (nMOBZT) and 2-[3-ethoxy-(4-alkoxybenzoyloxy)phenyl]benzothiazoles (nEOBZT).

Table 4.18: Percentage of yields of compounds nMOBZT and nEOBZT

<u>nMOBZT</u>		<u>nEOBZT</u>	
Compound	Percentage of yield (%)	Compound	Percentage of yield (%)
2MOBZT	25	2EOBZT	27
3MOBZT	27	3EOBZT	31
4MOBZT	31	4EOBZT	33
5MOBZT	34	5EOBZT	36
6MOBZT	40	6EOBZT	41
7MOBZT	44	7EOBZT	49
8MOBZT	46	8EOBZT	50
9MOBZT	47	9EOBZT	51
10MOBZT	51	10EOBZT	54
12MOBZT	55	12EOBZT	52
14MOBZT	56	14EOBZT	55
16MOBZT	60	16EOBZT	56
18MOBZT	65	18EOBZT	59

The purity of the compound was confirmed by using HPLC and TLC analysis. The HPLC chromatograms of the representative compound **12MOBZT** and **12EOBZT** are shown in Appendix 3A. The TLC R_f data associated with compounds **nMOBZT** and **nEOBZT** are listed in Appendix 3B.

Mass spectrometry analysis was conducted on representative compounds, **12MOBZT** and **12EOBZT** in order to verify the molecular mass of the synthesized compound. EI mass spectrum of **12MOBZT** and **12EOBZT** is given in Figures 4.30 and 4.31, respectively. The molecular ion peak was observed at 545.3 and 559.3 *m/z* with relative abundance of 1.98 and 2.17, respectively.

Tables 4.19 and 4.20 summarized all the IR data of compounds **nMOBZT** and **nEOBZT**, respectively, while Figures 4.32 and 4.33 depicted the representative IR spectrum of **16MOBZT** and **16EOBZT**, respectively.

By referring the chemical structure of **16MOBZT**, the formation benzothiazole ring can be traced by appearance of absorption band at 1607 cm^{-1} and 1605 cm^{-1} for the compound **16EOBZT**. This band assigned to the C=N bond in the benzothiazole ring fragment. Upon successfully Steglich esterification, carbonyl ester C=O bond gave a rise to the absorption band at 1731 cm^{-1} for **16MOBZT** and **16EOBZT**, respectively. The absorption bands at the range of 2920 and 2850 cm^{-1} represented C-H bond stretching in the long terminal carbon chains($\text{-C}_{16}\text{H}_{33}$) of **16MOBZT** and **16EOBZT**. Another diagnostic band at 1256 cm^{-1} indicated the aromatic C-O ether bond in the compound. The absorption band at 1260 cm^{-1} was ascribed to the aromatic C-O ether bond in the compound.

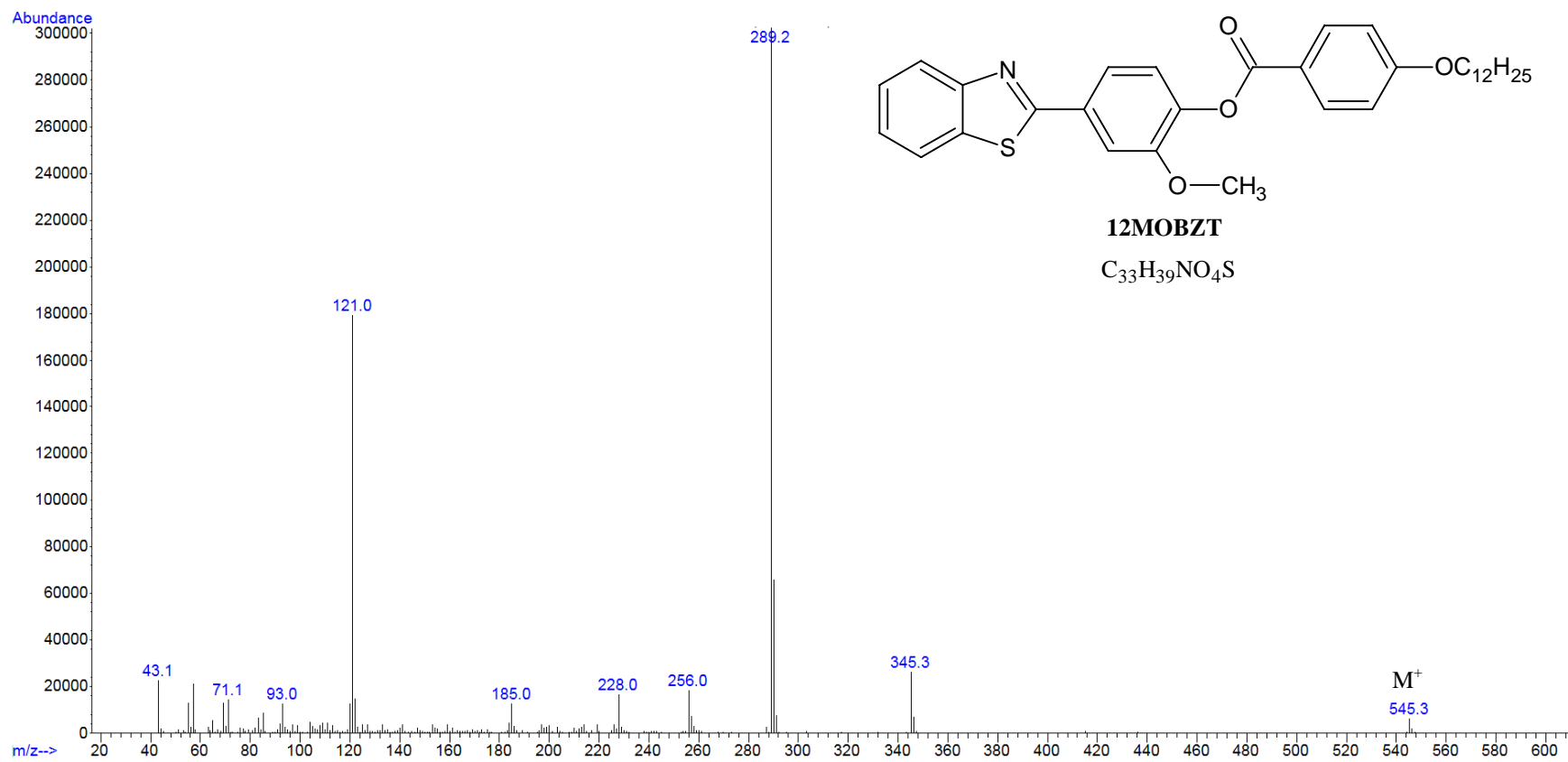


Figure 4.30: Mass Spectrum of compound 12MOBZT.

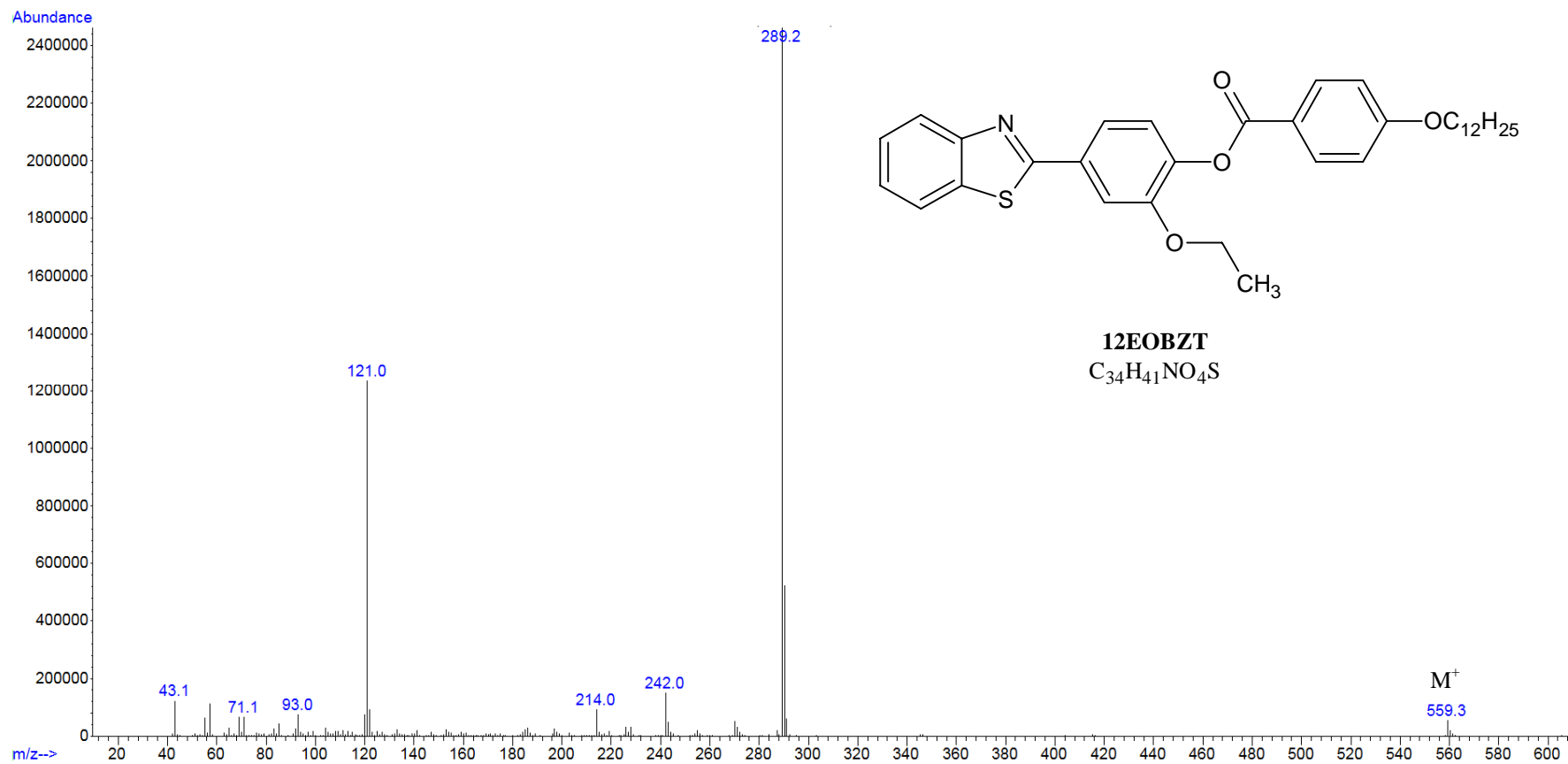


Figure 4.31: Mass Spectrum of compound 12EOBZT.

Table 4.19: FT-IR spectral data of compounds nMOBZT

Compound	IR ν (cm ⁻¹)				
	sp ² C-H Stretch (aromatic)	sp ³ C-H Stretch (aliphatic)	C=O (ester)	C=N (benzothizole)	Ar-O-C (Ether)
2MOBZT	3055	2728,2882	1721	1607	1259
3MOBZT	3059	2969,2875	1731	1606	1259
4MOBZT	3056	2953,2871	1736	1608	1259
5MOBZT	3061	2956,2871	1734	1607	1260
6MOBZT	3058	2937,2855	1734	1604	1248
7MOBZT	3065	2929,2856	1724	1603	1255
8MOBZT	3063	2924,2855	1734	1605	1252
9MOBZT	3065	2921,2852	1720	1605	1255
10MOBZT	3054	2922,2852	1731	1607	1256
12MOBZT	3054	2922,2852	1731	1607	1256
14MOBZT	3054	2921,2851	1732	1607	1257
16MOBZT	3054	2920,2850	1731	1607	1256
18MOBZT	3055	2920,2850	1732	1608	1257

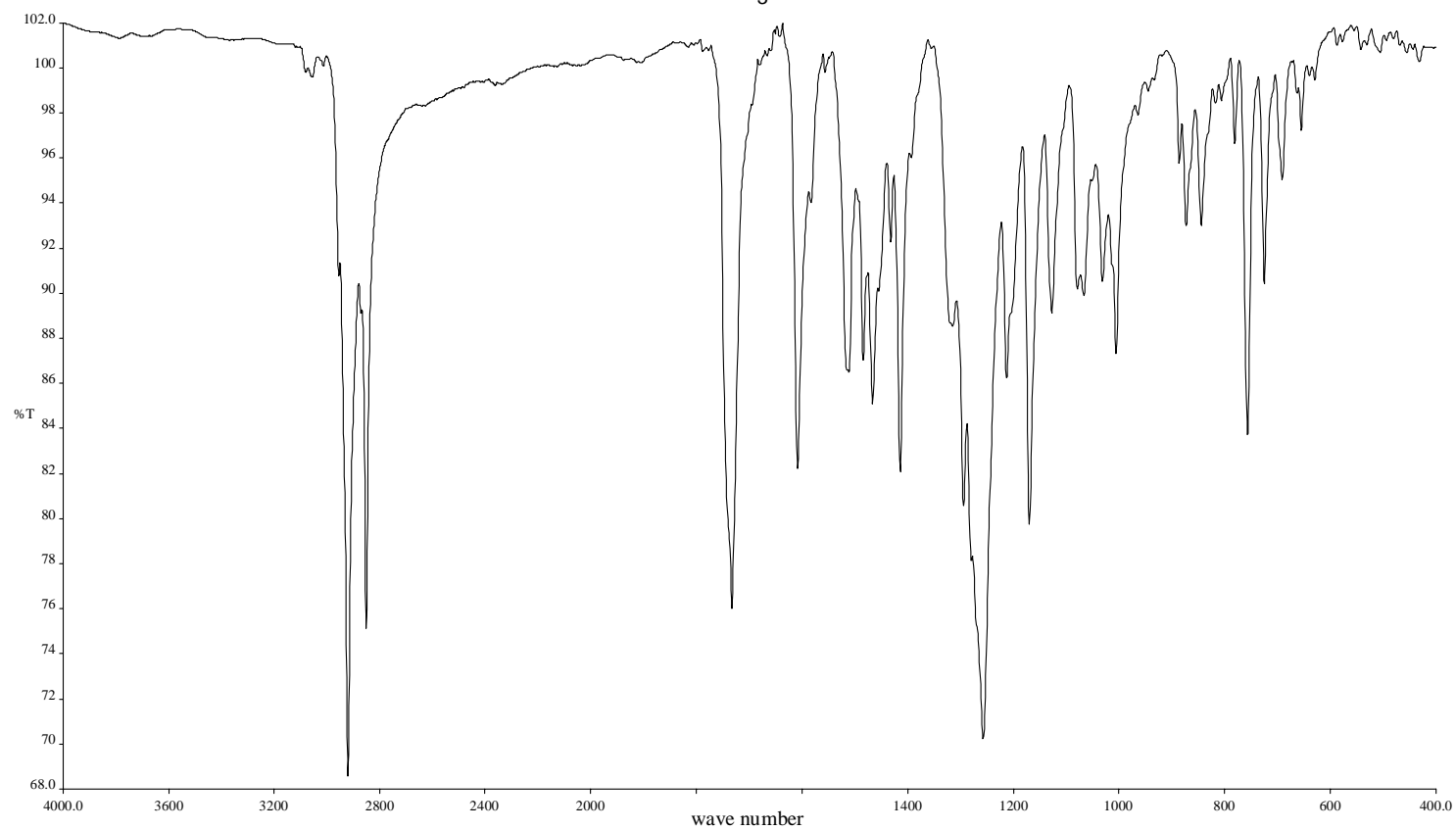
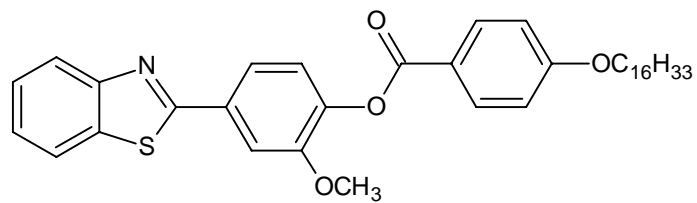


Figure 4.32: FT-IR spectrum of compound 16MOBZT.

Table 4.20: FT-IR spectral data of compounds nEOBZT

Compound	IR ν (cm ⁻¹)				
	sp ² C-H Stretch (aromatic)	sp ³ C-H Stretch (aliphatic)	C=O (ester)	C=N (benzothiazole)	Ar-O-C (ether)
2EOBZT	3075	2935,2886	1737	1607	1265
3EOBZT	3051	2932,2884	1729	1608	1259
4EOBZT	3051	2933,2872	1732	1607	1258
5EOBZT	3069	2942,2872	1736	1607	1257
6EOBZT	3064	2930,2869	1734	1604	1257
7EOBZT	3065	2930,2856	1723	1604	1256
8EOBZT	3077	2925,2855	1734	1604	1253
9EOBZT	3068	2923,2852	1723	1605	1258
10EOBZT	3064	2923,2852	1731	1604	1255
12EOBZT	3061	2917,2848	1731	1607	1255
14EOBZT	3066	2921,2852	1732	1605	1256
16EOBZT	3058	2919,2850	1731	1605	1260
18EOBZT	3055	2920,2850	1728	1607	1260

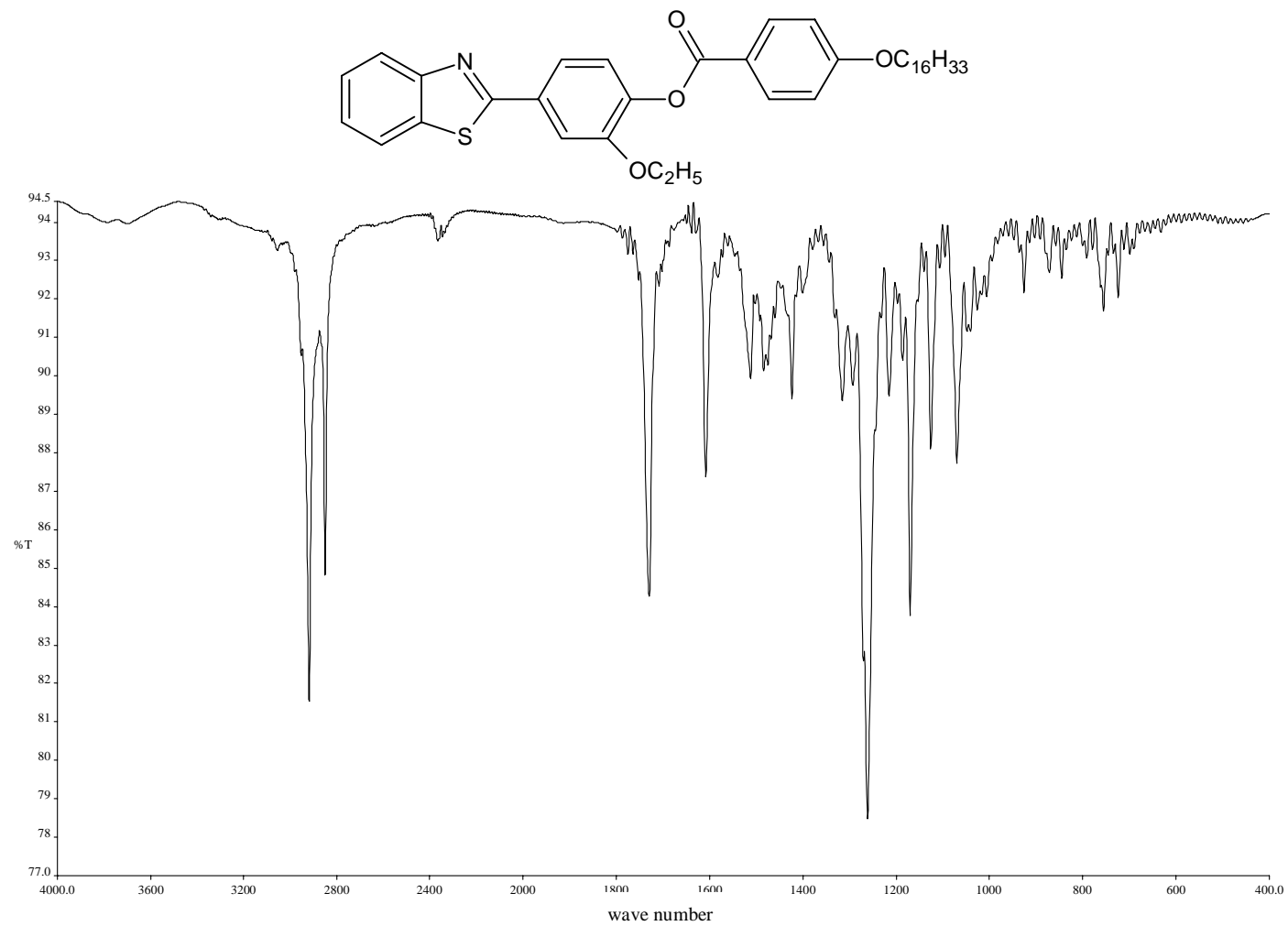


Figure 4.33: FT-IR Spectrum of compound 16EOBZT

Compounds **12MOBZT** and **16EOBZT** were selected as representative compounds for ^1H and ^{13}C NMR spectroscopy analysis. The atomic numbering scheme of **12MOBZT** and **16EOBZT** which is used to label the different types of protons and carbons are depicted in Figure 4.34.

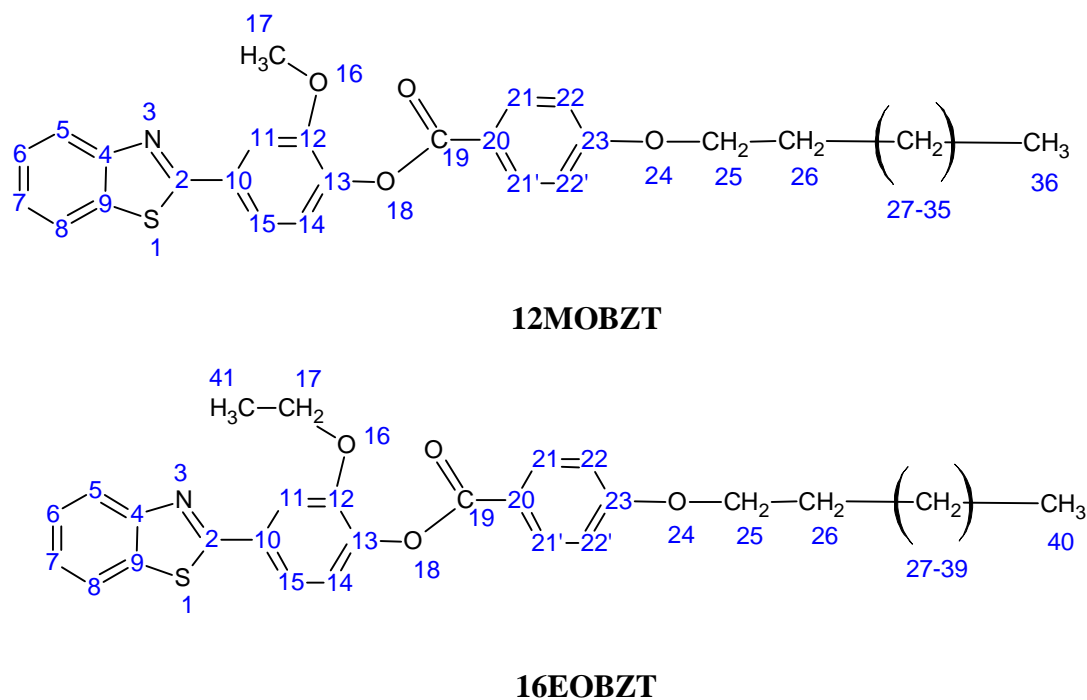


Figure 4.34: Structures with atomic numbering scheme for 12MOBZT and 16EOBZT.

Tables 4.21- 4.24 summarized the respective 1D and 2D NMR spectral data for compounds **12MOBZT** while the 1D NMR and 2D NMR spectra of compound **12MOBZT** are depicted in Figures 4.35 and 4.36, respectively.

Table 4.21: ¹H NMR spectral data of compound 12MOBZT in CDCl₃

Proton Number	Chemical Shift, δ ppm	Integrals	Multiplicity*	Coupling Constant, J (Hz)
H21,H21'	8.14	1H	d	8.8
H14	8.06	1H	d	8.4
H15	7.87	1H	d	7.6
H11	7.84	1H	s	-
H5	7.61	1H	d	7.9
H8	7.49	1H	d	7.6
H6	7.37	1H	s	7.6
H7	7.24	1H	d	8.4
H22,H22'	7.02	2H	d	8.8
H25	4.00	2H	t	6.4
H17	3.94	2H	s	-
H26	1.76	3H	t	6.8
H27-H35	1.25-1.45	26H	m	-
H36	0.85	3H	t	6.8

Note:

TMS was used as an internal standard.

*s=singlet,

d=doublet

t=triplet

p=quintet

m=multiplet

Table 4.22: ^{13}C NMR spectral data of compound 12MOBZT in CDCl_3 .

Carbon Number	Chemical Shift , δ (ppm)
C19	167.59
C2	164.41
C20	163.80
C14	154.04
C10	152.08
C4	142.75
C12	135.23
C21, C21'	132.68
C23	132.35
C8	126.61
C6	125.49
C7	123.81
C13	123.32
C15	121.25
C5	120.76
C22, C22'	114.49
C11	111.23
C25	68.51
C17	56.43
C26	31.12
C27-C34	29.90
	29.79
	29.77
	29.57
	29.29
	26.18
C35	22.89
C36	14.33

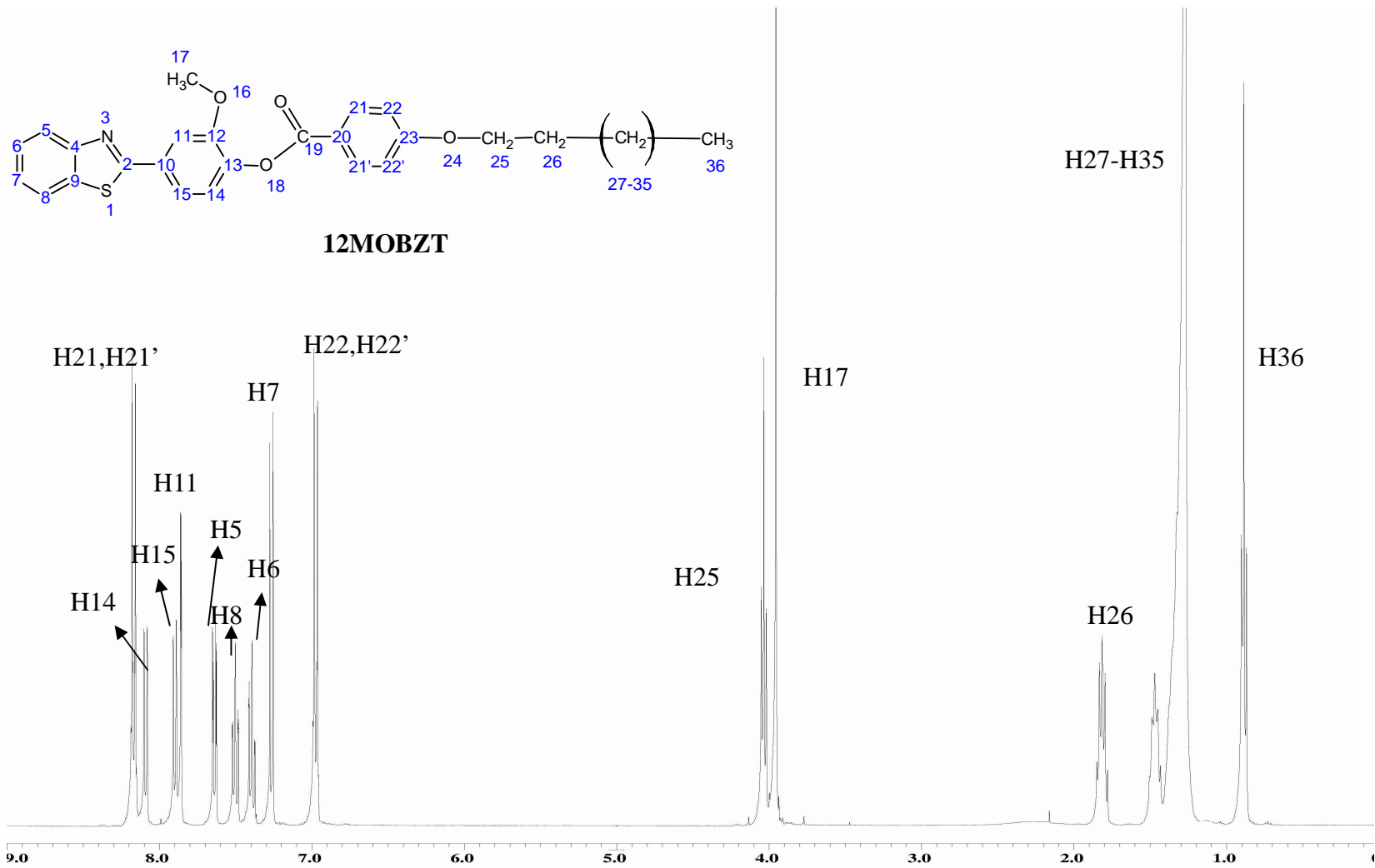


Figure 4.35: ¹H NMR spectrum of compound 12MOBZT.

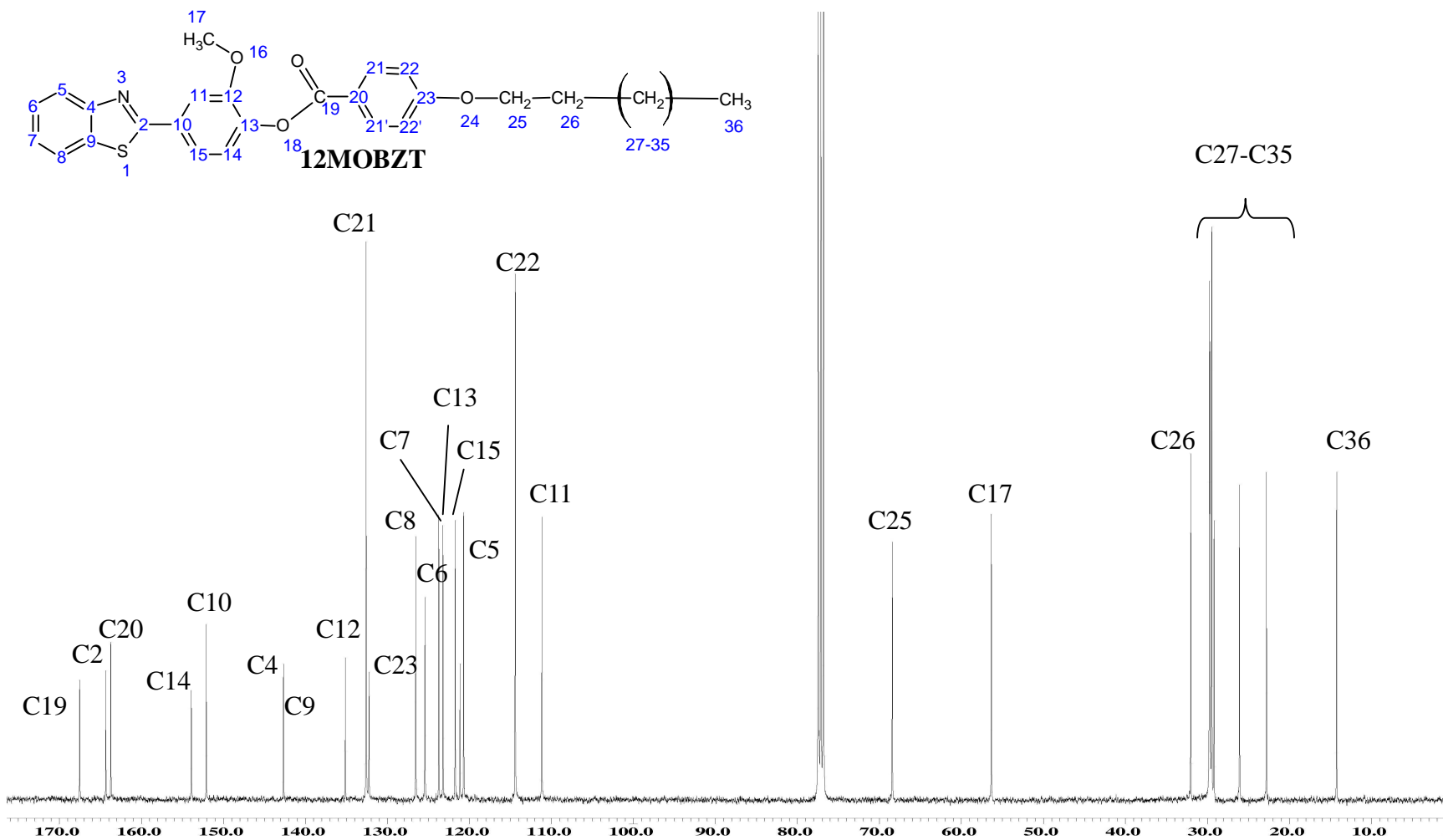


Figure 4.36: ¹³C NMR spectrum of compound 12MOBZT.

In ^1H NMR spectra, it was found that a doublet signals appeared at $\delta = 8.14$ ppm with the integrals of two protons was assigned to H22, H22'. Signals due to H11, H14 and H15 in aromatic ring gave rise to the resonance peaks within the respective chemical shift $\delta = 7.84, 8.06$ and 7.87 ppm. Meanwhile, signals due to H5, H8, H6 and H7 in benzothiazole fragment gave rise to the resonance peaks within the respective chemical shift $\delta = 7.63, 7.47, 7.37$ and 7.24 ppm. The aliphatic protons, H25 appeared at the downfield region of chemical shift $\delta = 4.00$ ppm due to the effect of electronegative oxygen atom. The remaining aliphatic protons H26 to H40 were observed within the chemical shift of $\delta = 0.85-1.87$ ppm. ^1H NMR spectrum of **16EOBZT** exhibited the similar pattern as discussed for **12MOBZT**. An additional signal at $\delta = 1.33$ ppm is due to the protons which attached at the lateral ethoxy group ($-\text{OCH}_2-\text{CH}_3$).

In the ^{13}C NMR spectrum, the highest chemical shift $\delta = 167.59$ and 167.40 ppm was attributed to the carbonyl carbon ($\text{C}=\text{O}$) of ester linkage for compound **12MOBZT** and **16EOBZT**, respectively. The carbon (C2) sandwiched between electronegative nitrogen and sulfur atoms ($-\text{N}=\text{C}-\text{S}-$) in benzothiazole fragment appeared at 164.29 and 164.41 ppm in the respective ^{13}C NMR spectra of **12MOBZT** and **16EOBZT**. Another downfield signal at $\delta = 163.59$ and 163.80 ppm corresponded to C23 which is attached to ether oxygen. The following signals at the chemical shift range of $\delta = 154.04$ to 111.23 ppm indicated the carbons in the remaining aromatic ring, C4-C9, C11-C15 and C20-C22. While the signals at $\delta = 68.36$ ppm were assigned to C25 which is relatively higher chemical shift than others aliphatic carbons. The signals appeared at $\delta = 56.43$ and 64.91 ppm were

ascribed to the lateral substituents carbon (C17). The downfield shift of these signals was due to the descreening effect of the electronegative oxygen atom. As for compound **16EOBZT**, the signals appeared at $\delta = 14.69$ ppm attributed to the carbon in ethoxy group, C41, while the signals between $\delta = 31.12$ to 14.09 ppm belong to the remaining carbons in alkyl chain. A peak at $\delta = 14.33$ and 14.09 ppm were assigned to the methylene ($-\text{CH}_2-$) carbon for compound **12MOBZT** and **16EOBZT**, respectively.

The structure of the compound is further substantiated by the ^{13}C NMR data. The HMQC spectrum (Figure 4.38) also reveals the connectivity between the aromatic hydrogens and their corresponding carbons. From the plot, the peaks owing to the carbons at $\delta = 114.49$ and 132.68 ppm show correlation with the H22 (or H22') (refer to cross peak) and the H21 (or H21') (refer to cross peak) atoms, respectively. Thus, the peak at $\delta = 114.49$ and 132.68 ppm are associated with the C22 (or C22') and the C21 (or C21') atoms, respectively. The spectrum also shows the cross peak of the H11 atom with the C11 atom at $\delta = 111.23$ ppm, the cross peak of the H14 atom with the C14 atom at $\delta = 154.04$ ppm and the cross peak of the H15 atom with the C15 atom at $\delta = 121.25$ ppm.

The HMQC experiment also reveals that the H36 atom correlates with the C36 atom at $\delta = 14.33$ ppm and the H25 atom at $\delta = 4.00$ ppm correlates with the C25 atom at $\delta = 68.51$ ppm. A quintet at $\delta = 1.76$ ppm owing to the H26 atom correlates with the C16 atom at $\delta = 31.12$ ppm. The multiplets attributed to the H27-35 atoms at $\delta = 1.26$ - 1.45 ppm are found to correlate with the C27-35 atoms

at $\delta = 22.89\text{-}29.90$ ppm.

The quaternary carbons are assigned by using the HMBC experiment. The long range HMBC cross peaks of the H21 (or H21') atom with the C2 atom at $\delta =$ ppm, H22 (or H22') atom with the C15 atom at $\delta = 121.25$ ppm, H14 (or H14') atom with the C6 atom at $\delta = 125.49$ ppm, H15 (or H) atom with the C8 atom at $\delta = 126.61$ ppm and the H11 and H7 atom with the C21 (or C21') atom at $\delta = 132.68$ ppm strongly support the positions of these atoms. The C15 signal at $\delta = 121.25$ ppm is assigned based on the correlation with its nearest proton, H14. The peak of the C25 ether atom at $\delta = 68.51$ ppm is assigned based on the heteronuclear connectivities with the methylene protons (H26 and H27). The C19 carbonyl atom at $\delta = 167.59$ ppm is confirmed via correlations with the aromatic H21 (or H21') and H22 (or H22') protons.

The same NMR experiments have also been performed on the remaining compounds. These compounds show the similar NMR features as those observed for compounds **12EOBZT**. The ^1H and ^{13}C NMR spectral data of compounds **16EOBZT** are included in Appendix 9A, respectively.

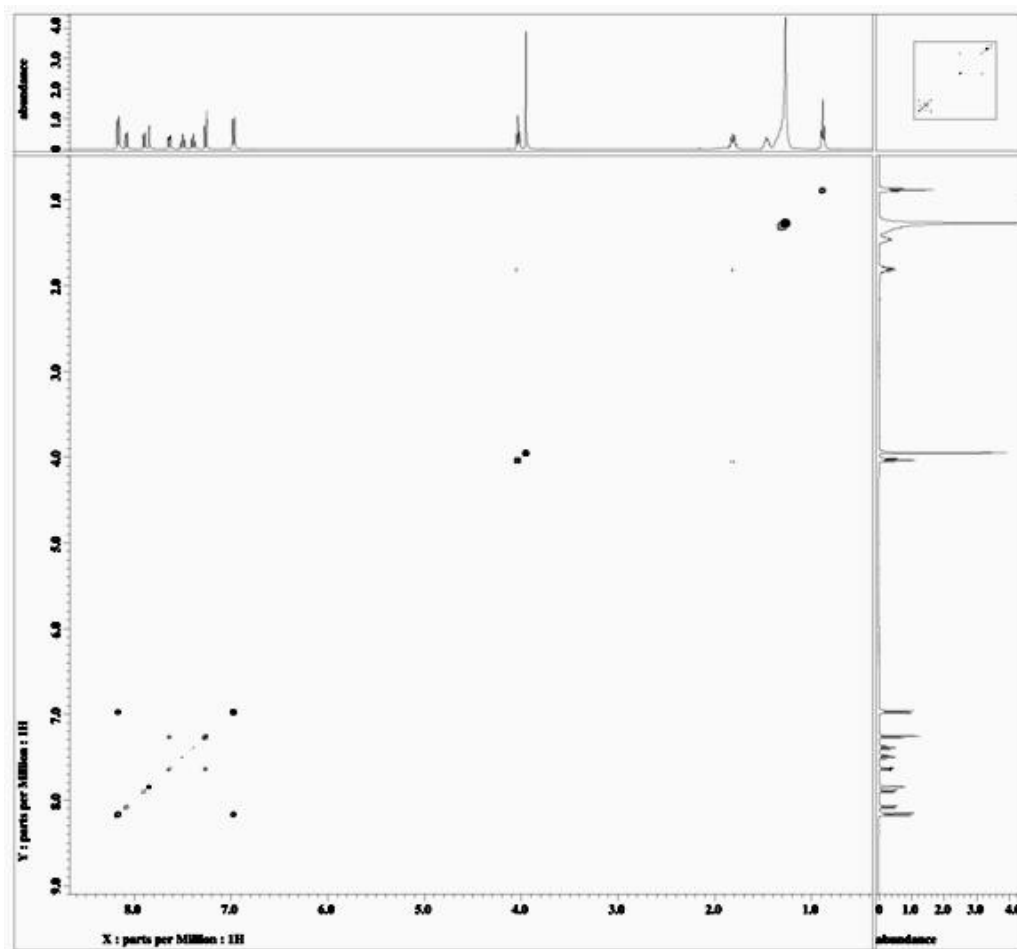


Figure 4.37: COSY spectrum of compound 12MOBZT.

Table 4.23: ^1H - ^1H correlations as deduced from the 2D COSY experiments for compound 12MOBZT

Atom No. ^a	^1H - ^1H COSY correlations
H21,H21'	H8
H14	H22, H22'
H15	H11
H11	H15
H5	H7
H8	H6, H21, H21'
H6	H8
H7	H5
H22,H22'	H14
H25 ^b	H26
H17	---
H26 ^c	H25, H27-H35
H36	H27-H35

TMS was used as internal standard.

^a Based on the numbering scheme in Figure 4.35.

^b The H25 atom correlates with the methylene protons (H27-H35) but their real positions could not be determined because the ^1H chemical shifts of the H27-H35 atoms were indistinguishable.

^c The H26 atom correlates with the methylene protons (H27-H35) but their real positions could not be determined because the ^1H chemical shifts of the H27-H35 atoms were indistinguishable.

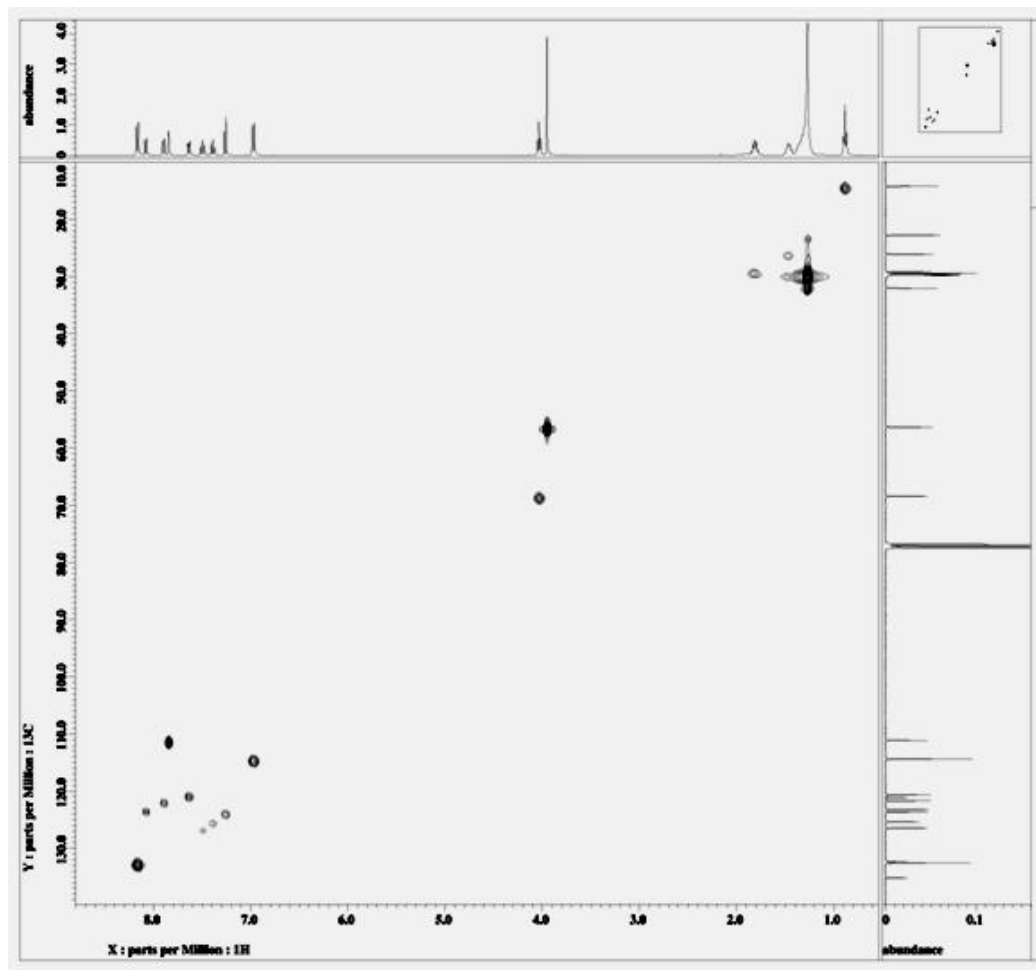


Figure 4.38: HMQC spectrum of compound 12MOBZT.

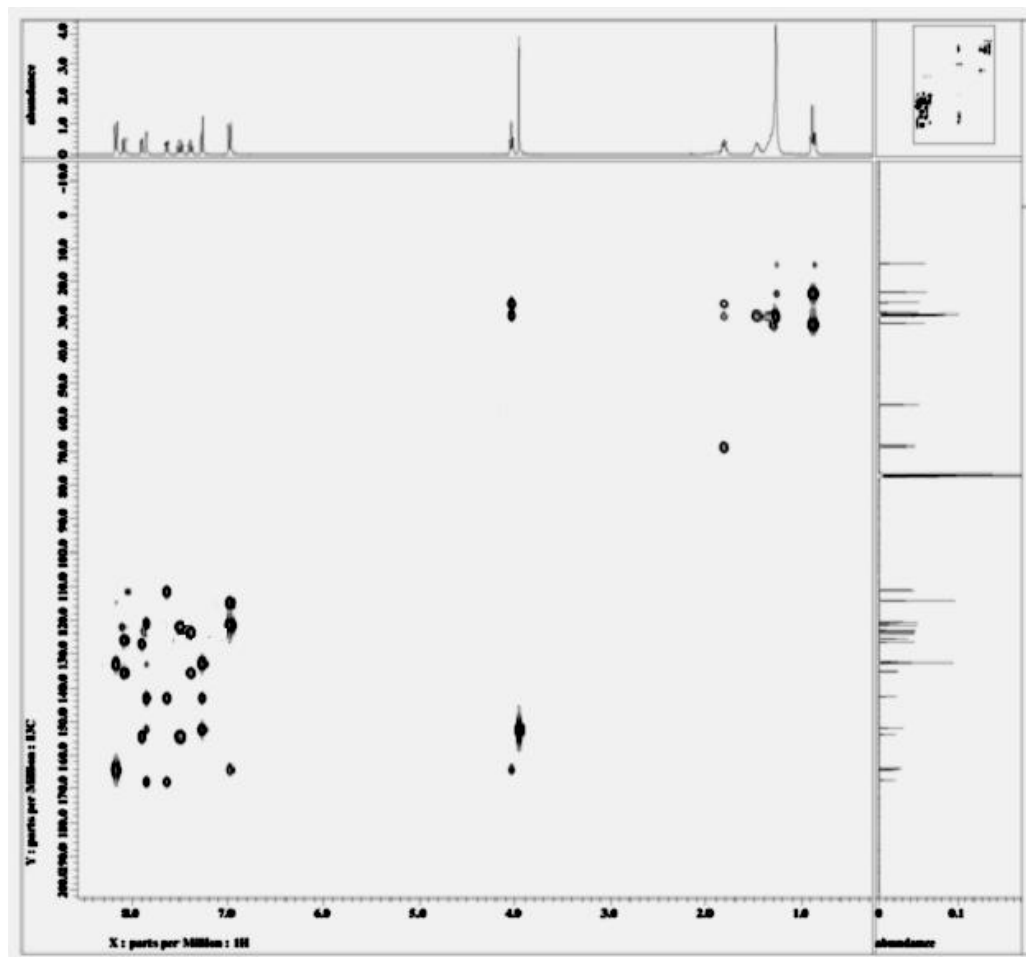


Figure 4.39: HMBC spectrum of compound 12MOBZT.

Table 4.24: ^{13}C - ^1H correlations as deduced from the 2D HMQC and HMBC experiments for compound 12MOBZT

Atom No. ^a	HMQC		HMBC [$J(\text{C,H})$]		
	1J	2J	3J	4J	bJ
H21	C21	C20	C19	---	C2
H21'	C21'	C20	C19	---	C2
H14	C14	C13, C15	---	---	C6
H15	C15	---	---	---	C8
H11	C11	C10	C2	---	C21, C21'
H5	C5	C4	---	C2	C11
H8	C8	C9	---	C5	---
H6	C6	C7	---	---	---
H7	C7	---	---	---	C21, C21'
H22	C22	C23	---	C19	C15
H22'	C22'	C23	---	C19	C15
H25 ^c	C25	C24, C26	----	---	---
H26 ^d	C26	C25	C27	---	---
H36	C36	C35	C34	---	---

TMS was used as internal standard.

^a Based on the numbering scheme in Figure 4.36.

^b Intramolecular interaction.

^c The C25 atom correlates with the methylene protons (C27-C33) but their real [$J(\text{C,H})$] value could not be determined because the ^{13}C chemical shifts of the C27-C33 atoms were indistinguishable.

^d The C26 atom correlates with the methylene protons (C27-C33) but their real [$J(\text{C,H})$] value could not be determined because the ^{13}C chemical shifts of the C27-C33 atoms were indistinguishable.

4.4 Series 4: Structural Elucidation of α,ω -bis[6-Methoxy-2-(4-alkoxybenzylidenamino)]benzothiazoles (nOMeD) and α,ω -bis[6-ethoxy-2-(4-alkoxybenzylidenamino)]benzothiazoles (nOEtD)

The chemical structures of the title compounds are shown at Figure 4.40.

The percentage of yields are tabulated in Table 4.25.

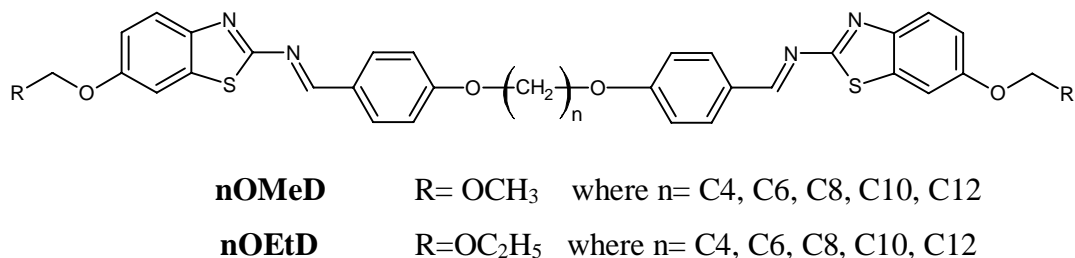


Figure 4.40: α,ω -bis[6-Methoxy-2-(4-alkoxybenzylidenamino)]benzothiazoles (nOMeD) and α,ω -bis[6-ethoxy-2-(4-alkoxybenzylidenamino)]benzothiazoles (nOEtD)

Table 4.25: Percentage of yields of compounds nOMeD and nOEtD

<u>nOMeD</u>		<u>nOEtD</u>	
Compound	Percentage of yield (%)	Compound	Percentage of yield (%)
4OMeD	50	4OEtD	55
6OMeD	59	6OEtD	64
8OMeD	65	8OEtD	68
10OMeD	68	10OEtD	70
12OMeD	66	12OEtD	65

The purity of the compound was confirmed by using HPLC and TLC analysis. The HPLC chromatograms of the representative compound **16OMeD** and **8OEtD** are shown in Appendix 4A. The TLC R_f data associated with compounds **nOMeD** and **nOEtD** are listed in Appendix 4B.

Mass spectrometry analysis was performed on the representative compounds, **8OMeD** and **8OEtD** in order to verify the molecular mass of the synthesized compounds. EI mass spectra of **8OMeD** and **8OEtD** are shown in Figures 4.41 and 4.42, respectively. The mass spectra of compounds **8OMeD** and **8OEtD** confirmed the molecular mass of each compound at 678.4 and 706.4 m/z with relative abundance of 12.31 and 11.18, respectively.

Selected FT-IR data of compounds **nOMeD** and **nOEtD** are listed in Tables 4.26 and 4.27, respectively, while the FT-IR spectra of the representative compounds **8OMeD** and **8OEtD** are shown in Figures 4.43 and 4.44, respectively.

Inspection of the FT-IR data has suggested that compound **8OMeD** and **8OEtD** were successfully synthesized through the Williamson's etherification. The presence of the alkyl groups was supported by the appearance of diagnostic bands within the frequency range of 2954 to 2849 cm^{-1} . Meanwhile, the strongest band is observed in the fingerprint region of 1253 cm^{-1} , which can attribute to the presence of two ether (O-CH₂) groups for every dimeric structure. The formation of Schiff base linkage between amino and aldehyde group can be represented by the diagnostic band of C=N at 1601 cm^{-1} while the thiazole C=N appeared at 1572 cm^{-1} (Ha *et al.*, 2010c).

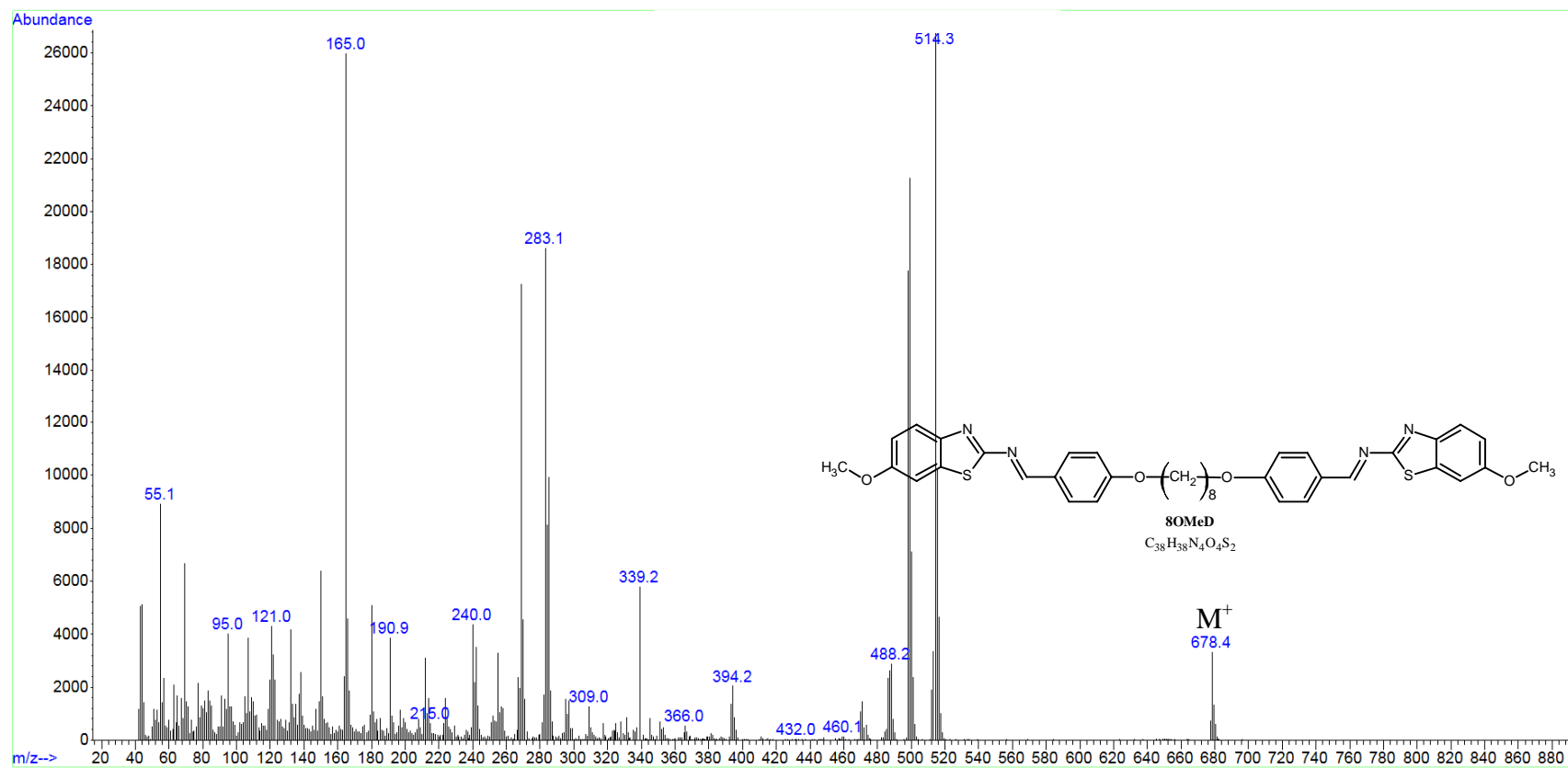


Figure 4.41: Mass spectrum of compound 8OMeD.

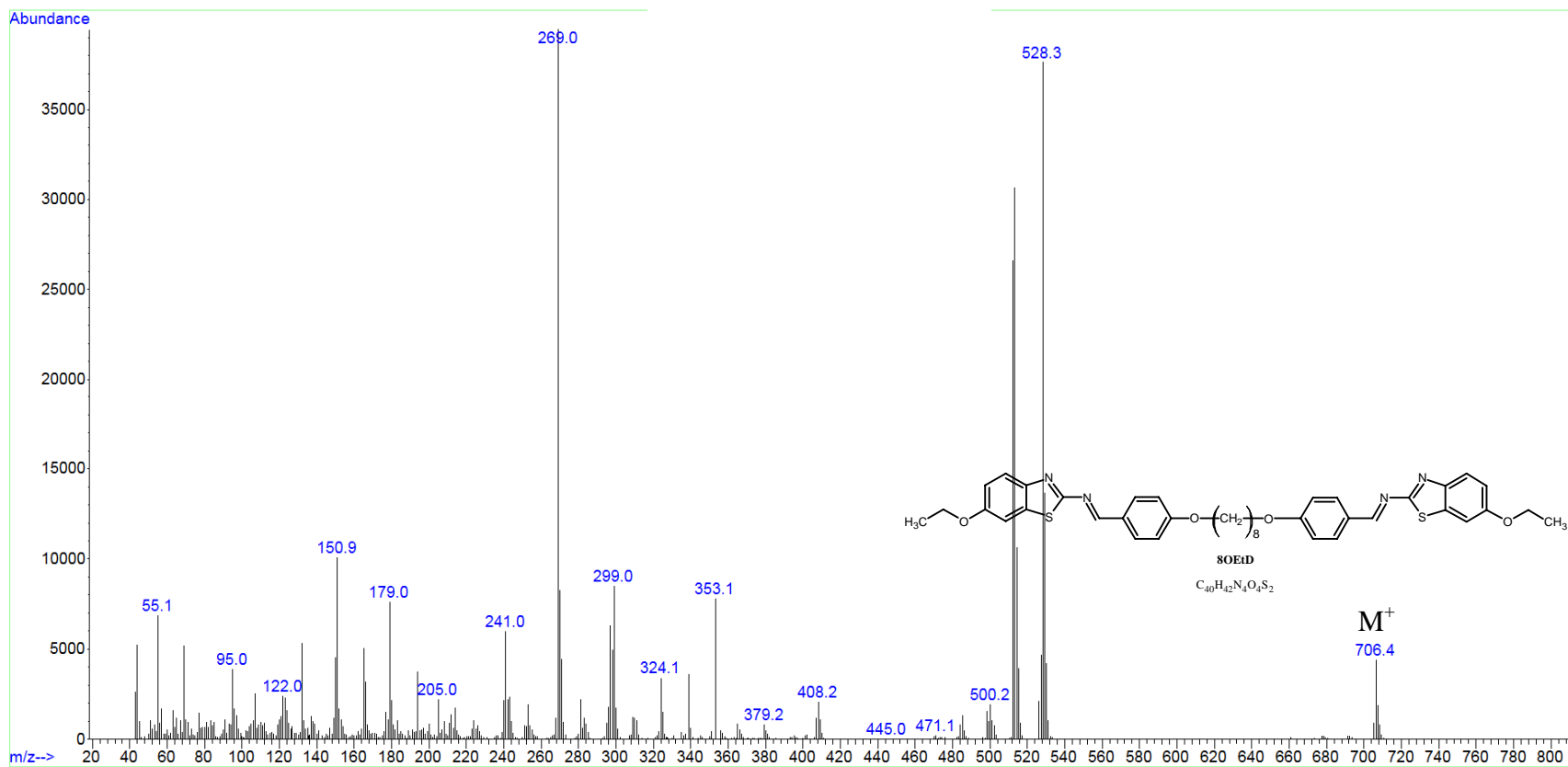


Figure 4.42: Mass spectrum of compound 8OEtD.

Table 4.26: FT-IR spectral data of compounds nOMeD

Compound	IR ν (cm ⁻¹)				
	sp ² C-H Stretch (aromatic)	sp ³ C-H Stretch (aliphatic)	C=N (Schiff base)	C=N (benzothiazole)	Ar-O-R (ether)
4OMeD	3066	2949,2876	1602	1565	1254
6OMeD	3058	2941,2870	1598	1570	1250
8OMeD	3067	2938,2852	1598	1570	1247
10OMeD	3067	2918,2851	1600	1567	1248
12OMeD	3067	2919,2850	1601	1569	1256

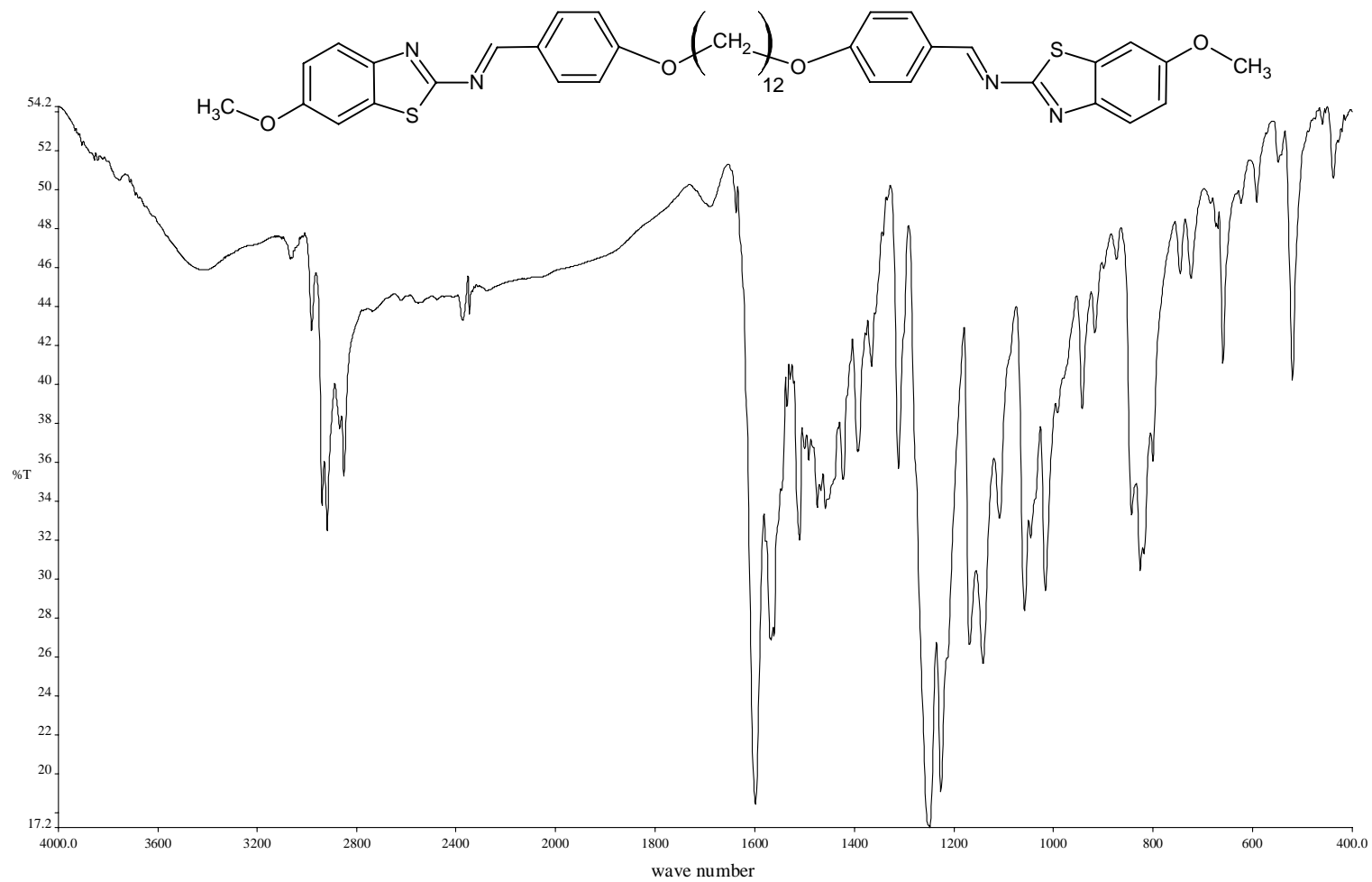


Figure 4.43 : FT-IR spectrum of compound 12OMeD

Table 4.27: FT-IR spectral data of compounds nOEtD

Compound	IR ν (cm ⁻¹)				
	sp ² C-H Stretch (aromatic)	sp ³ C-H Stretch (aliphatic)	C=N (Schiff base)	C=N (benzothiazole)	Ar-O-R (ether)
4OEtD	3059	2949,2873	1597	1560	1252
6OEtD	3066	2946,2879	1592	1560	1251
8OEtD	3066	2937,2852	1597	1560	1253
10OEtD	3066	2918,2851	1598	1560	1248
12OEtD	3059	2919,2850	1599	1569	1256

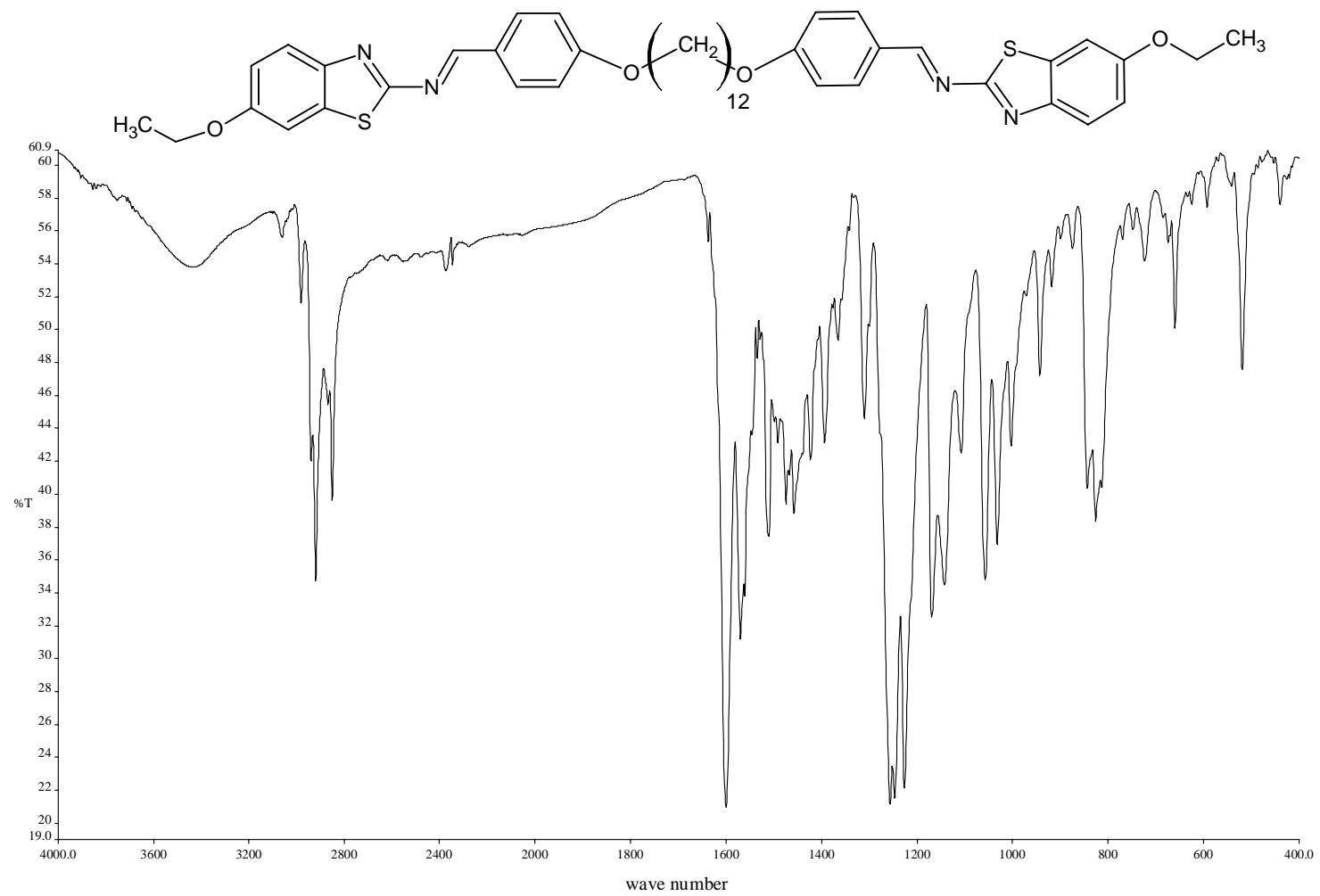


Figure 4.44 : FT-IR spectrum of compound 12OEtD.

A NMR spectroscopic study was performed on representative compounds **8OMeD** and **8OEtD** for each series. The atomic numbering scheme of **8OMeD** and **8OEtD** which is used to label the different types of protons and carbons are depicted in Figure 4.45.

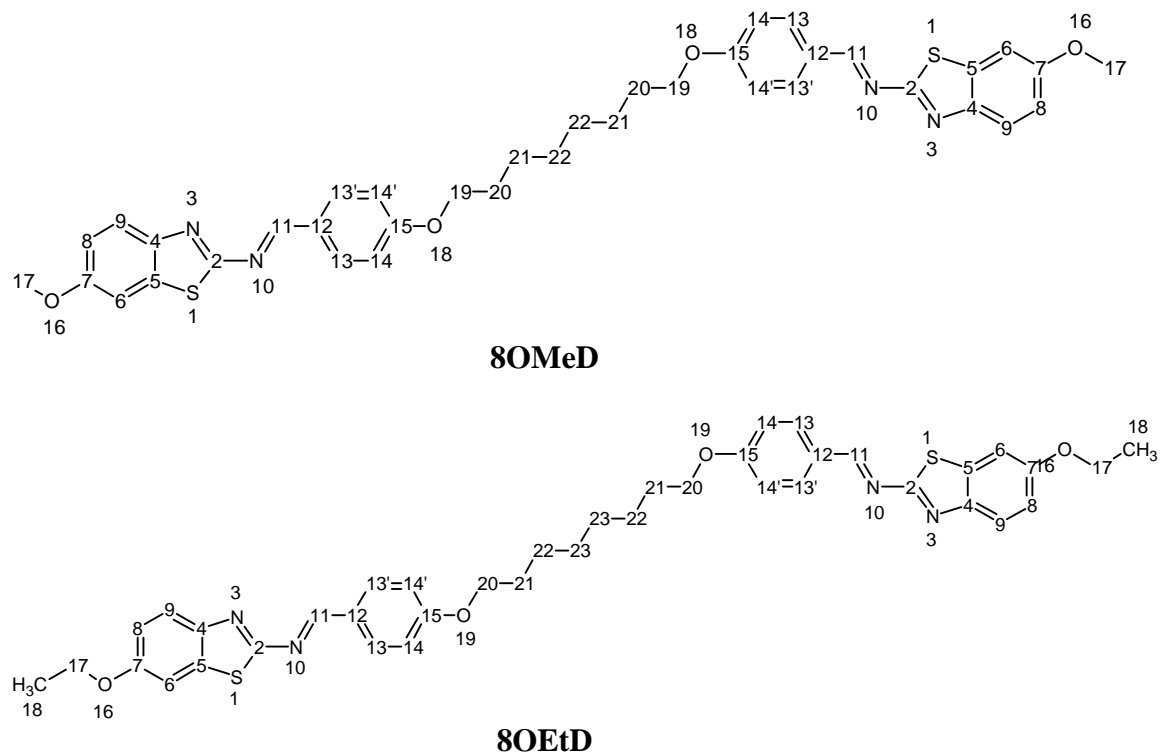


Figure 4.45: Structures with atomic numbering scheme for 8OMeD and 8OEtD.

For compound **8OMeD**, the 1D and 2D NMR spectral data are tabulated in the respective Tables 4.28- 4.31 while the 1D and 2D NMR spectra of compound **8OMeD** are shown in Figures 4.46-4.50, respectively.

Table 4.28: ¹H NMR spectral data of compound 8OMeD in CDCl₃

Proton Number		Chemical Shift, δ ppm	Integrals	Multiplicity*	Coupling Constant
H11	H11	8.89	2H	s	-
H13,H13'	H13,H13'	7.80	4H	d	9.0
H9	H9	7.42	2H	d	9.0
H6	H6	7.22	2H	s	-
H8	H8	7.08	2H	d	9.0
H14,H14'	H14,H14'	6.97	4H	d	8.7
H19	H19	4.03	4H	t	7.2
H17	H17	3.78	4H	s	-
H20	H20	1.79	4H	p	7.8
H21-22	H21-22	1.39-1.47	8H	m	-

Note:

TMS was used as an internal standard.

*s=singlet,

d=doublet

t=triplet

p=pentet

m=multiplet

Table 4.29: ^{13}C NMR spectral data of compound 8OMeD in CDCl_3

Carbon Number		Chemical Shift , δ (ppm)
C2	C2	169.90
C11	C11	164.31
C15	C15	164.13
C7	C7	155.79
C9	C9	145.62
C13,C13'	C13,C13'	132.56
C4	C4	132.10
C12	C12	129.83
C9	C9	119.70
C14,C14'	C14,C14'	115.05
C5	C5	114.81
C8	C8	113.79
C6	C6	105.43
C19	C19	68.42
C17	C17	55.96
C20	C20	29.32
C21	C21	29.11
C22	C22	26.00

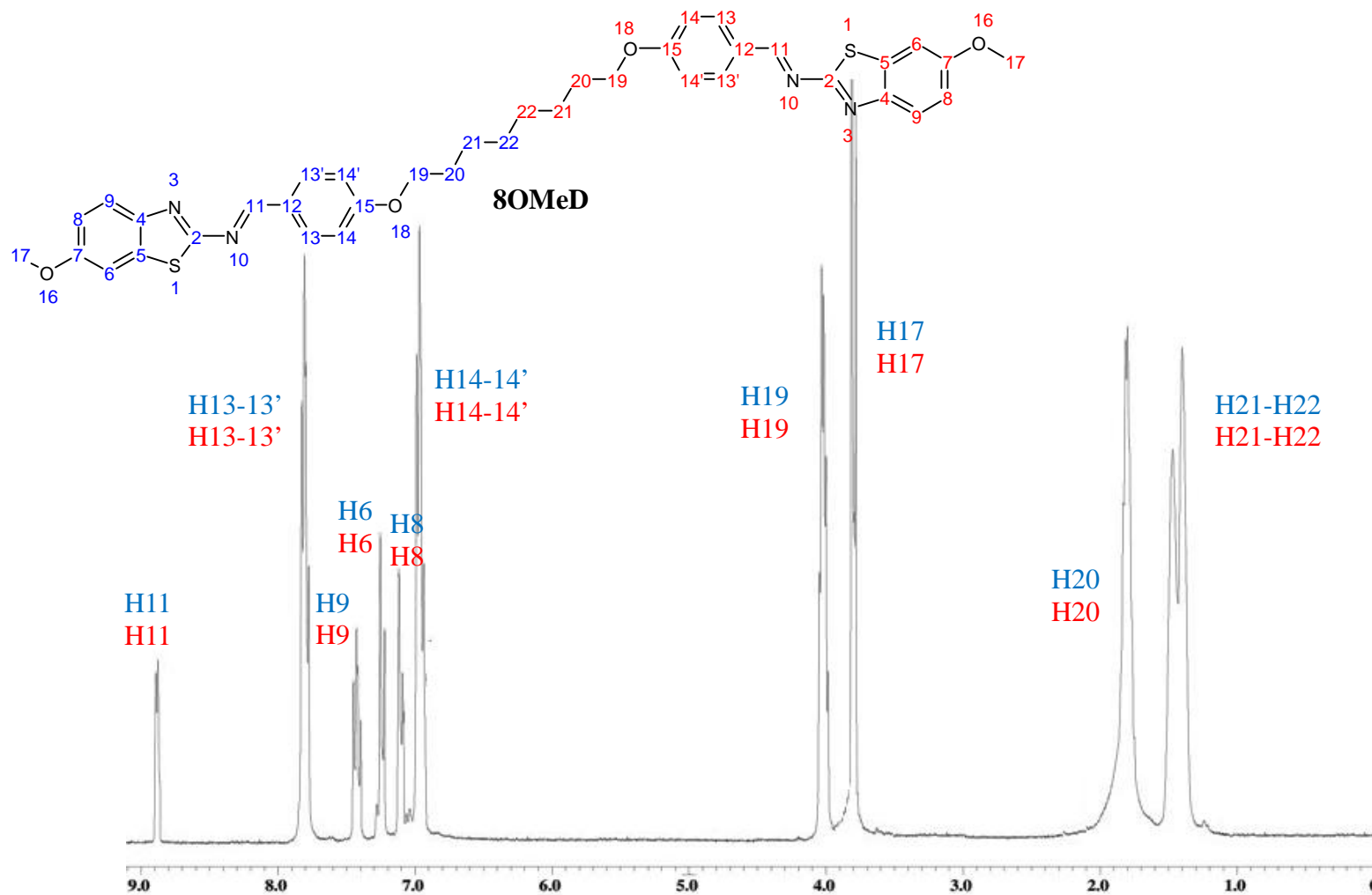


Figure 4.46: ¹H NMR spectrum of compound 8OMeD.

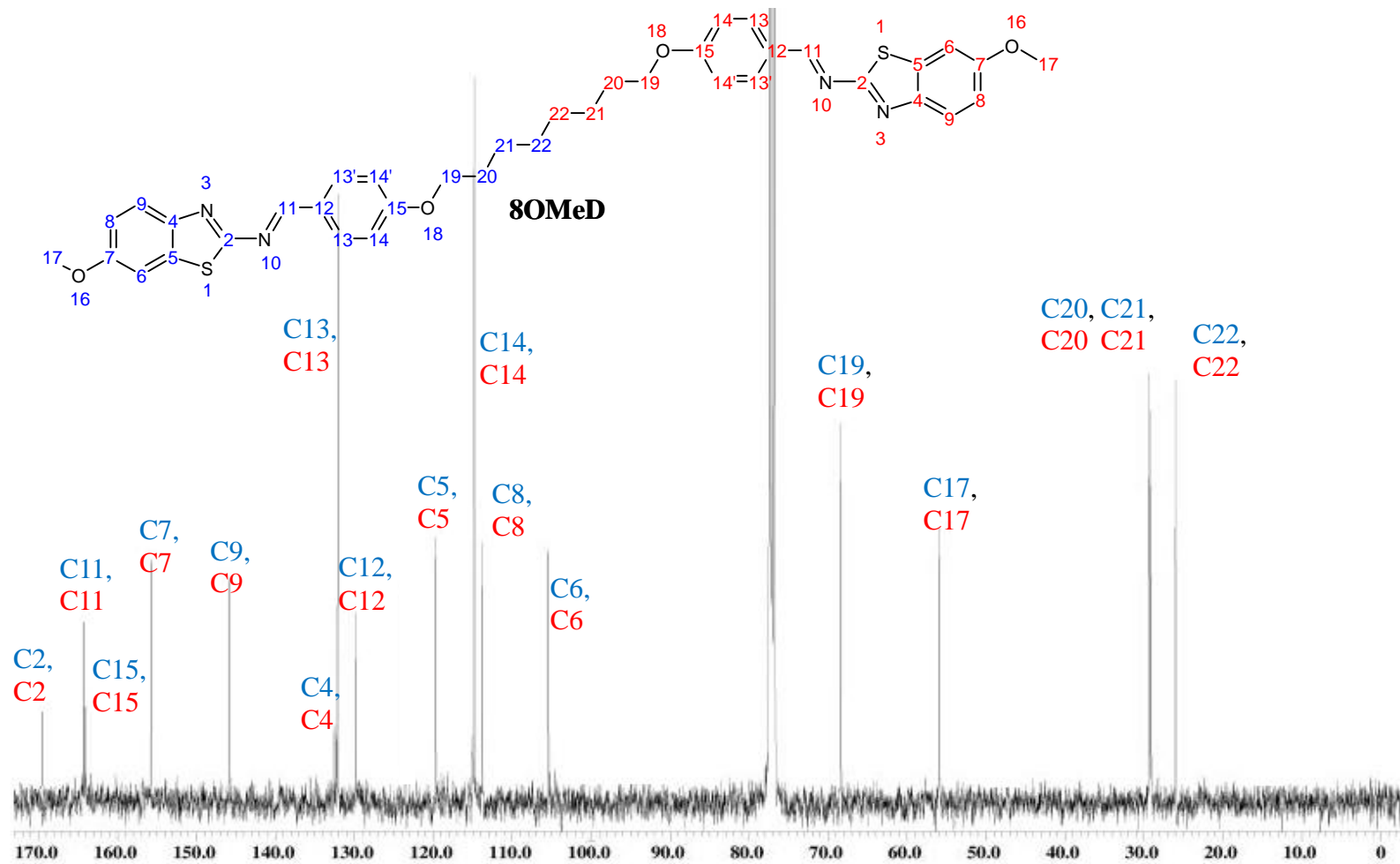


Figure 4.47: ^{13}C NMR spectrum of compound 8OMeD.

Due to its dimeric properties, half of the molecule will share the same chemical environment compared to another half (Venema *et al.*, 1994). In ^1H NMR spectra of **8OMeD** and **8OEtD**, a sharp singlet corresponding to the azomethine proton (-N=CH-) appeared at $\delta = 8.89$ and 8.90 ppm in respective spectrum. The HMQC spectrum of compound **8OMeD** confirms the presence of the azomethine carbon (C11) at $\delta = 164.31$ ppm based on the direct bond heteronuclear correlation with the azomethine proton (H11).

The ^1H NMR spectrum also showed the resonance owing to the aromatic protons. These signals are assigned with the aid of the COSY experiment. The doublets at $\delta = 7.80$ and 6.97 ppm can be ascribed to the H13 (or H13') and H14 (or H14') atoms, respectively. A sharp singlet (H17) appeared at $\delta = 3.78$ ppm in the spectra of **8OMeD** was assigned to the protons in the ether group (-OCH₂-) while a triplet appeared at $\delta = 4.03$ ppm was assigned to the terminal methoxy group (H19). Signals exhibiting quartet and triplet appeared at respective $\delta = 4.07$ and 4.03 ppm represent H17 and H20 of ether chain for **8OEtD**. It appeared at more downfield region than others aliphatic protons as it located nearer to the electronegativity oxygen atom. The rest of the aliphatic protons of **8OMeD** and **8OEtD** appeared within the chemical range of $\delta = 1.39$ - 1.47 ppm and 1.22 - 4.03 ppm, respectively.

The structure of the compound is further substantiated by the ^{13}C NMR data. The HMQC spectrum (Figure 4.49) also reveals the connectivity between the aromatic hydrogens and their corresponding carbons. From the plot, the peaks

owing to the carbons at $\delta = 132.56$ and 125.05 ppm show correlation with the H13 (or H13') (refer to cross peak) and the H14 (or H14') (refer to cross peak) atoms, respectively. Thus, the peak at $\delta = 132.56$ and 125.05 ppm are associated with the C13 (or C13') and the C14 (or C14') atoms, respectively. The spectrum also showed the cross peak of the H9 atom with the C9 atom at $\delta = 145.62$ ppm, the cross peak of the H6 atom with the C6 atom at $\delta = 105.43$ ppm and the cross peak of the H8 atom with the C8 atom at $\delta = 113.79$ ppm. In ^{13}C NMR, the signals appeared at $\delta = 164.13$ and 163.35 ppm in the respective spectrums of **8OMeD** and **8OEtD** were attributed to the carbon (C15) in the ether group (-C-O-C-). Another noticeable signal at $\delta = 164.31$ and 164.31 ppm for **8OMeD** and **8OEtD** were observed corresponding to the azomethine carbon (C11) linkage. In compound **8OMeD**, carbon in the terminal methoxy group (-OCH₃-), C17, appeared at $\delta = 68.42$ ppm. The downfield shift of these signals was due to the descreening effect of the electronegativity oxygen atom. For compound **8OEtD**, the aromatic carbons appeared within the chemical shift range $\delta = 105.27$ to 156.89 ppm. Two carbons resonance signals at $\delta = 64.13$ and 68.29 ppm were assigned to C20 and C17, respectively. The remaining aliphatic carbons in the ether group, C18 and C21-C23, give rise to the resonance signals within the chemical shift range of $\delta = 14.83$ to 29.21 ppm.

The quaternary carbons are assigned by using the HMBC experiment. The long range HMBC cross peaks of the H13 (or H13') atom with the C11 atom at $\delta = 16$ ppm, H14 (or H14') atom with the C15 atom at $\delta = 164.13$ ppm, H19 atom with the C20 atom at $\delta = 29.32$ ppm strongly support the positions of these atoms. The

C11 signal at $\delta = 164.31$ ppm is assigned based on the correlation with its nearest proton, H13 (or H13').

The same NMR experiments have also been performed on the representative compounds (**8OEtD**). These compounds show the similar NMR features as those observed for compounds **8OMeD**. The ^1H and ^{13}C NMR spectral data of compounds **8OEtD** are included in Appendices 10A, respectively.

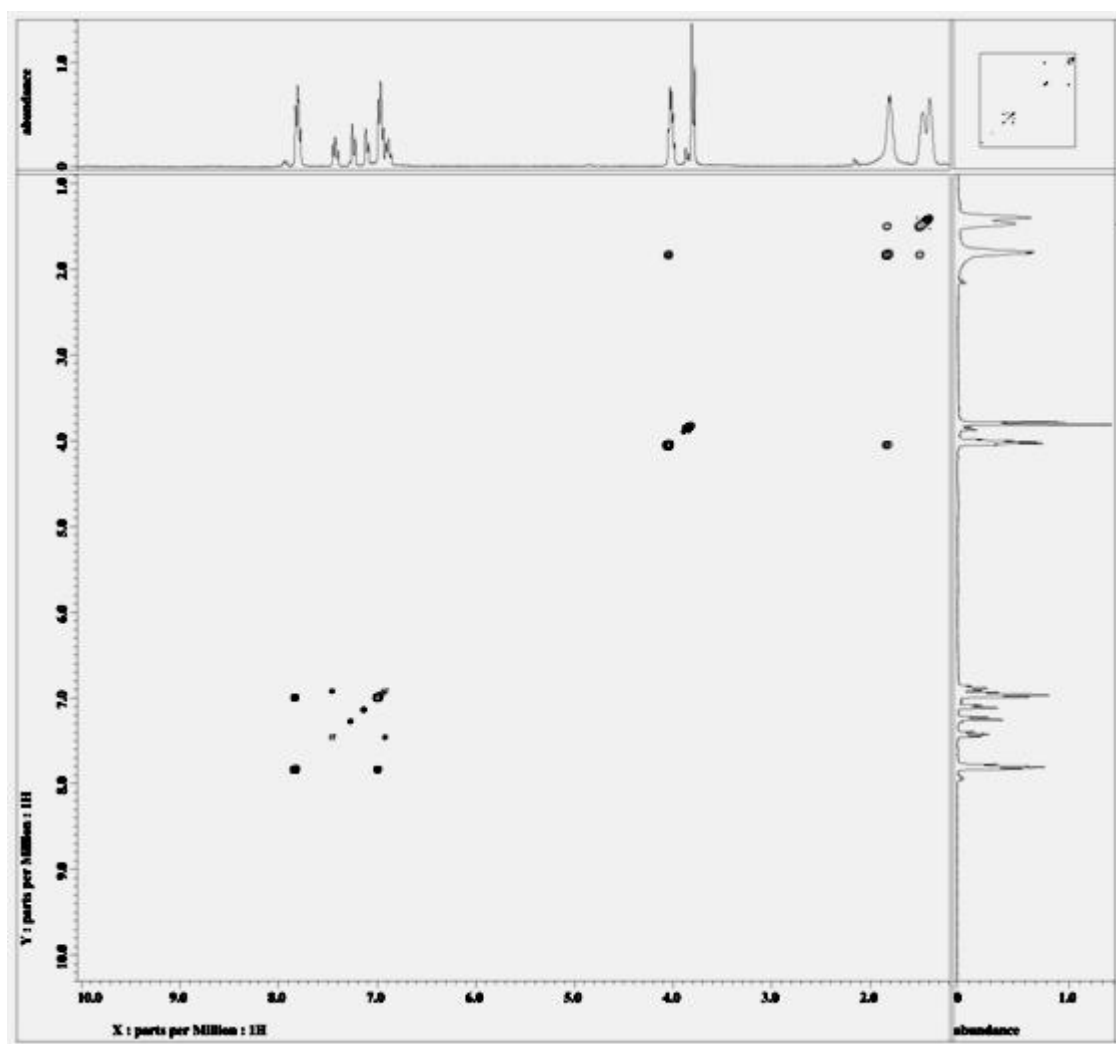


Figure 4.48: COSY spectrum of compound 8OMeD.

Table 4.30: ^1H - ^1H correlations as deduced from the 2D COSY experiments for compound 8OMeD

Atom No. ^a	^1H - ^1H COSY correlations
H11	---
H13,H13'	H14, H14'
H9	H14, H14'
H6	---
H8	---
H14,H14'	H13, H13'
H17	---
H19	H20, H21, H22
H20	H21, H22
H21-H22	H20

TMS was used as internal standard.

^a Based on the numbering scheme in Figure 4.46.

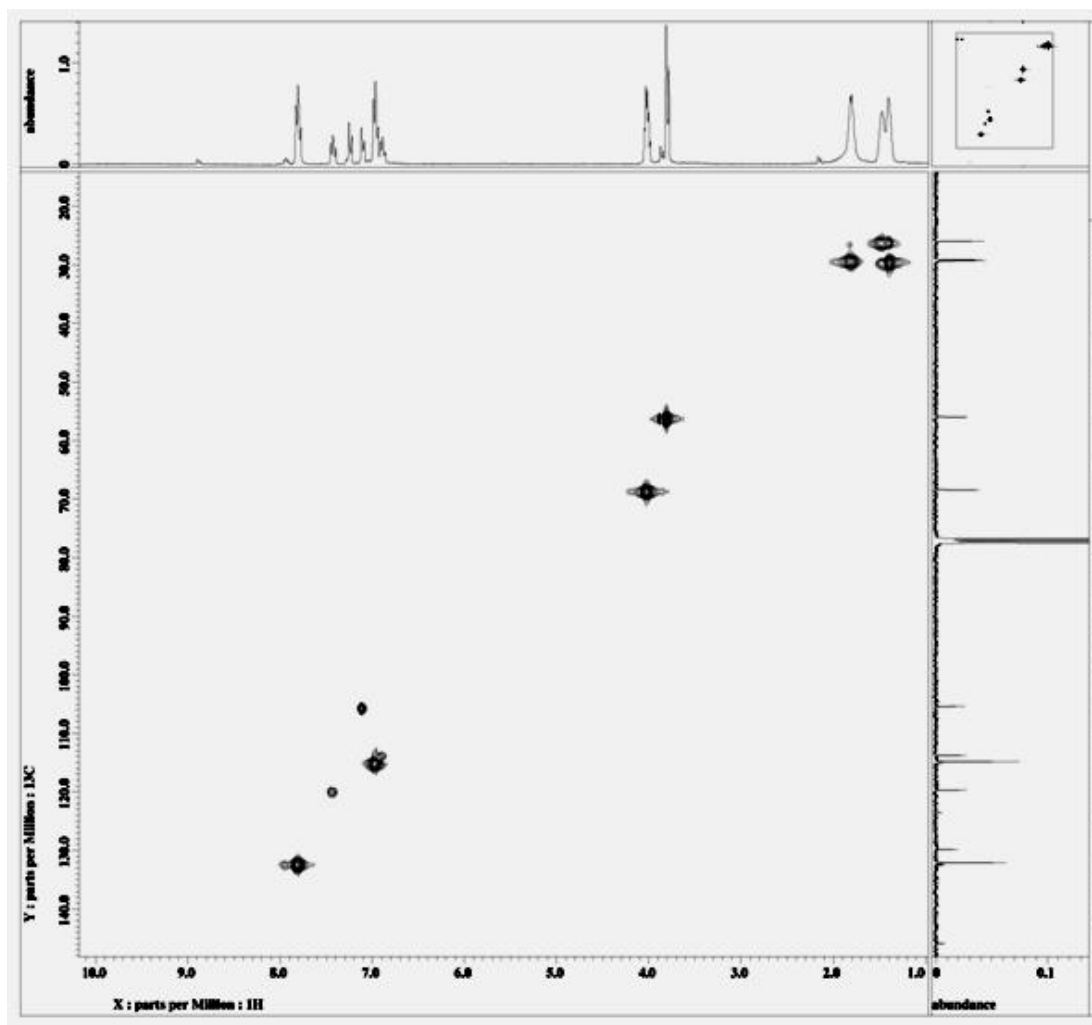


Figure 4.49: HMQC spectrum of compound 8OMeD.

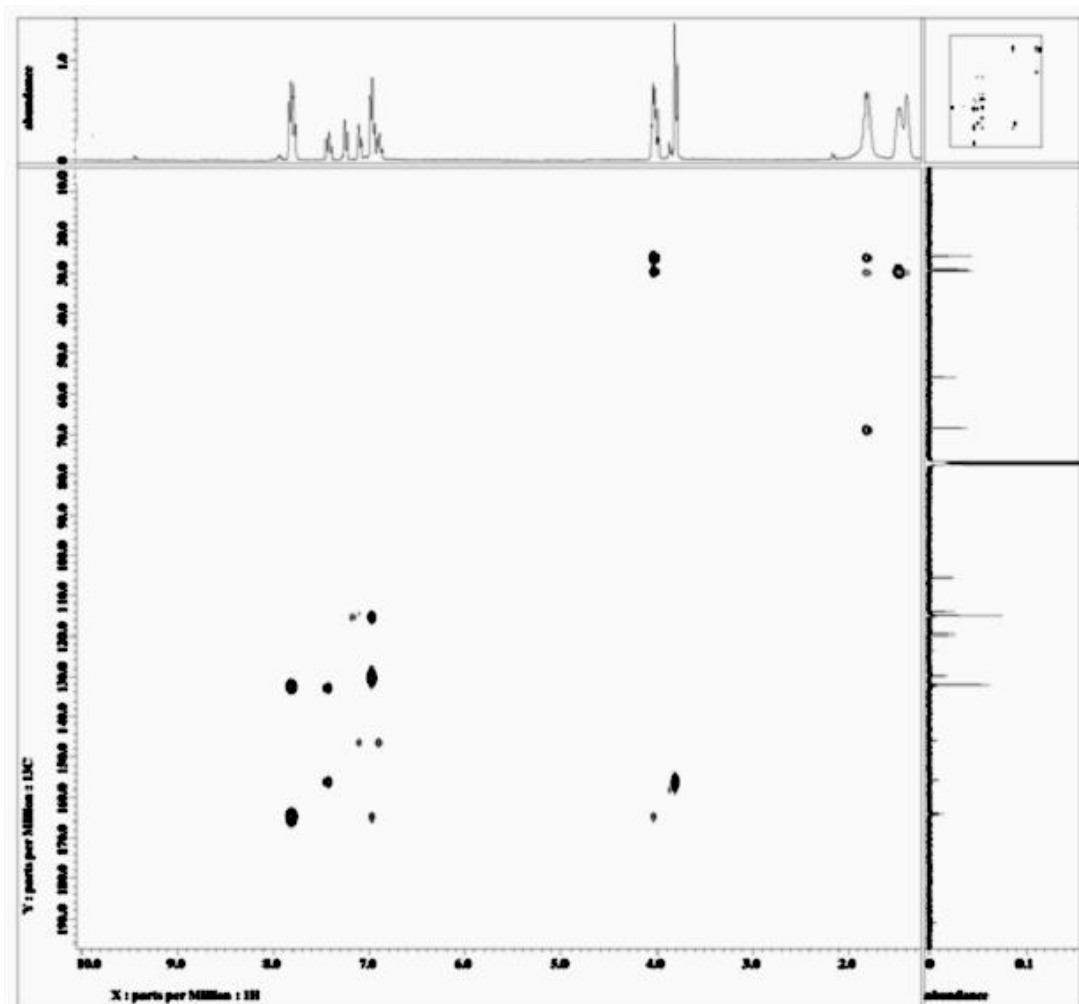


Figure 4.50: HMBC spectrum of compound 8OMeD.

Table 4.31: ^{13}C - ^1H correlations as deduced from the 2D HMQC and HMBC experiments for compound 8OMeD

Atom No. ^a	HMQC		HMBC [$J(\text{C,H})$]		
	1J	2J	3J	4J	bJ
H11	C11	C12	C13,C13'	---	---
H13	C13	---	C11	C15	---
H13'	C13'	---	C11	C15	---
H9	C9	---	C7	---	C13,C13'
H14	C14	C15	C12	---	---
H14'	C14'	C15	C12	---	---
H17	C17	---	---	---	C15
H19	C19	C20	C21	---	---
H20	C20	C19	---	---	---
H21	C21	C20,C22	---	---	---
H22	C22	C21	---	---	---

TMS was used as internal standard.

^a Based on the numbering scheme in Figure 4.47.

^b Intramolecular interaction.

4.5 Series 5: Structural Elucidation of 5-Methyl-2-[4-(4-alkyloxy-benzoyloxy)benzylidenamino]-2-pyridine s(nPM5B)

A homologous series of 5-methyl-2-[4-(4-alkyloxy-benzoyloxy)benzylidenamino]pyridines (**nPM5B**, where n = 2 to 10, 12, 14, 16, 18) were synthesized (Figure 4.51). The percentage of yields are tabulated in Table 4.32.

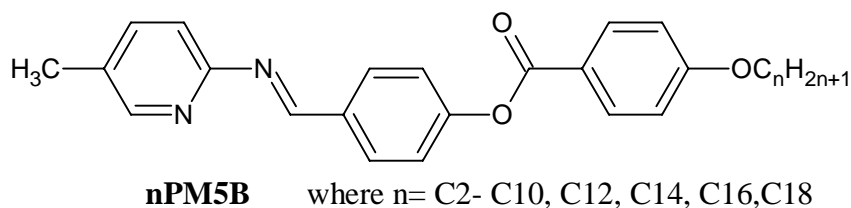


Figure 4.51: Chemical structure of 5-Methyl-2-[4-(4-alkyloxy-benzoyloxy)benzylidenamino]-2-pyridine s (nPM5B)

Table 4.32: Percentage of yields of compounds nPM5B

Compound	Percentage of yield (%)
2PM5B	30
3PM5B	36
4PM5B	40
5PM5B	45
6PM5B	46
7PM5B	48
8PM5B	47
9PM5B	48
10PM5B	54
12PM5B	52
14PM5B	59
16PM5B	66
18PM5B	70

The HPLC chromatogram of the representative compound **8PM5B** is shown in Appendix 5A. The TLC data associated with compounds **nPM5B** was listed in Appendix 5A. All the compounds gave a single spot on the TLC plate (Sharma *et al.*, 2003b).

A mass spectrometry was carried out on **12PM5B**, as representative compound for the series. EI mass spectrum of **12PM5B** is shown in Figure 4.52. The molecular ion peak showed at 502.4 m/z (relative abundance of 3.18) are in good agreement with the theoretical values.

Selected FT-IR data associated with compounds **nPM5B** are given in Table 4.32. The FT-IR spectrum of the representative compound **16PM5B** is shown in Figure 4.53. The presence of alkyl groups is supported by the appearance of characteristic bands within the frequency range of 2850 to 2918 cm^{-1} . The band assigned to the C=N bond at 1607 cm^{-1} . A distinct absorption band showed at 1253 cm^{-1} ascribed to the aromatic C-O ether bond. Absorption band observed at 1581 cm^{-1} assigned to the C=N for pyridyl ring (Thaker *et al.*, 2007). While the strongest absorption band of carbonyl group of ester linkage in **16PM5B** was found to be 1726 cm^{-1} .

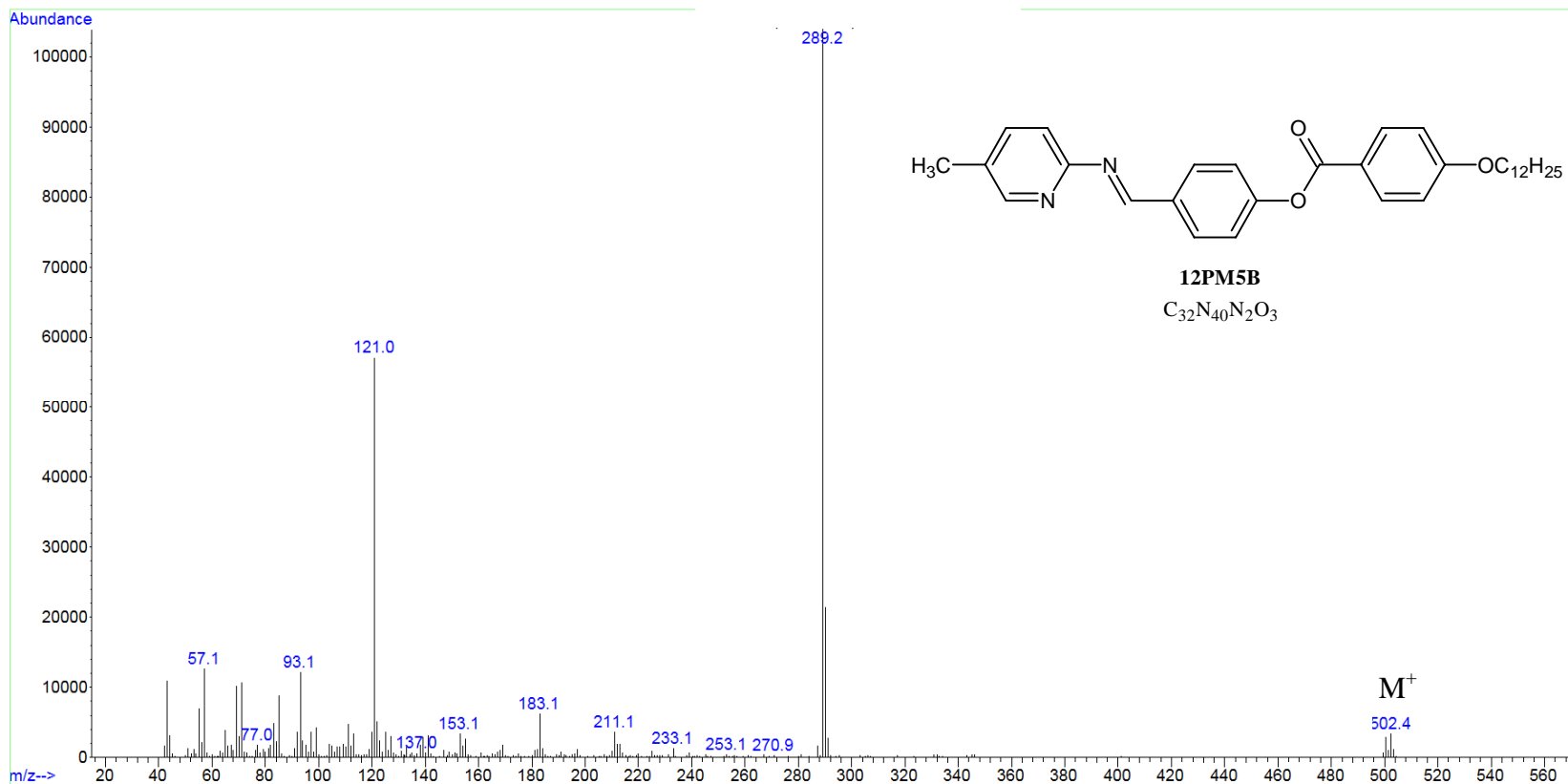


Figure 4.52: Mass Spectrum of compound 12PM5B.

Table 4.33: FT-IR spectral data of compounds nPM5B

Compound	IR ν (cm ⁻¹)					
	sp ² C-H Stretch	sp ³ C-H Stretch	C=O	C=N	C=N	Ar-O-R
	(aromatic)	(aliphatic)	(ester)	(Schiff base)	(pyridyl)	(ether)
2PM5B	3056	2985,2888	1729	1609	1590	1273
3PM5B	3055	2968,2831	1730	1604	1577	1257
4PM5B	3070	2964,2874	1726	1606	1579	1276
5PM5B	3062	2954,2869	1726	1602	1581	1256
6PM5B	3072	2926,2865	1723	1604	1575	1257
7PM5B	3039	2949,2867	1733	1608	1574	1261
8PM5B	3040	2938,2852	1736	1608	1581	1258
9PM5B	3040	2938,2852	1736	1608	1574	1258
10PM5B	3047	2940,2851	1723	1600	1581	1253
12PM5B	3070	2919,2849	1720	1608	1573	1262
14PM5B	3070	2918,2849	1725	1605	1575	1255
16PM5B	3069	2918,2850	1730	1607	1581	1257
18PM5B	3072	2915,2850	1724	1608	1593	1271

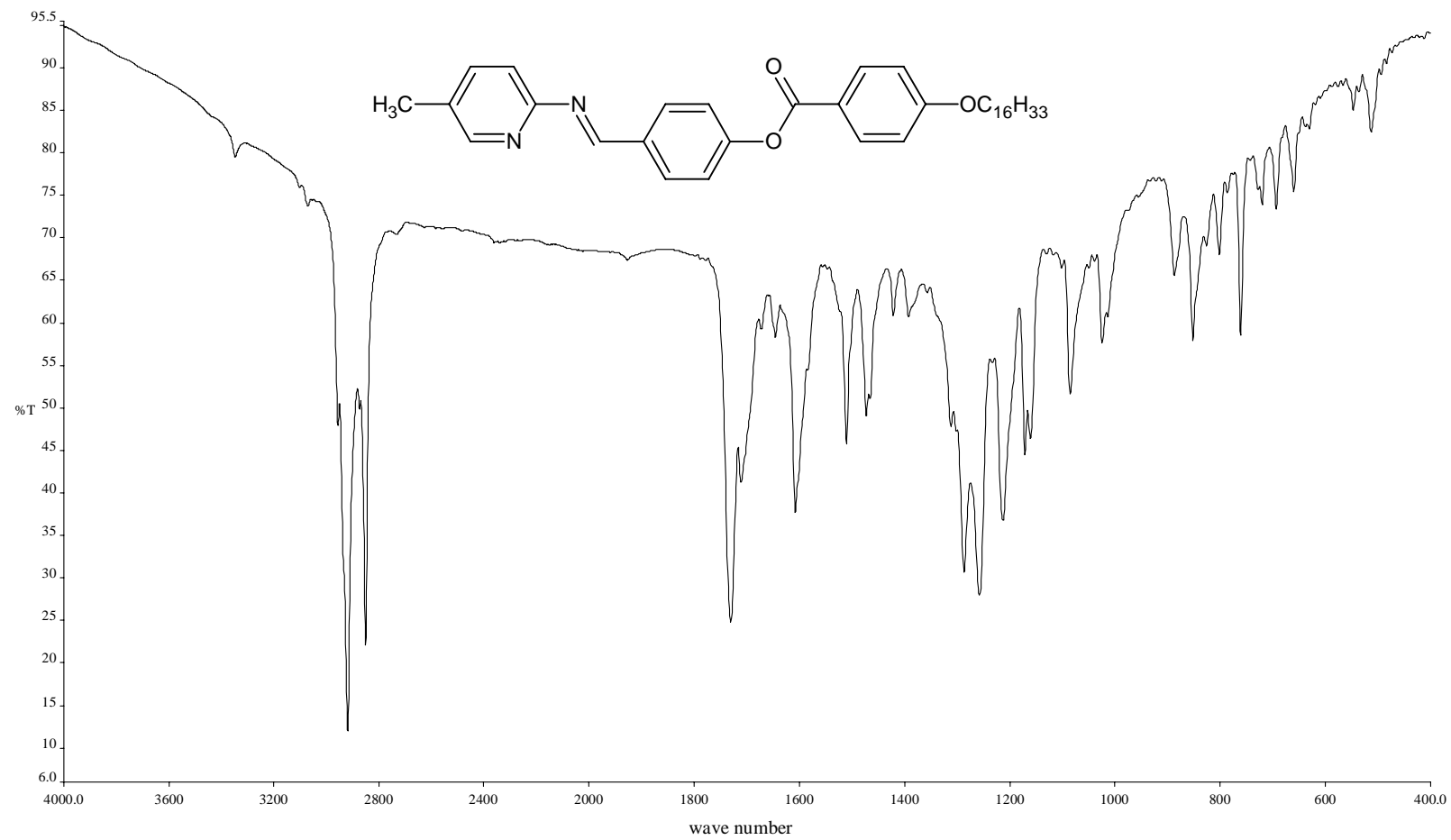


Figure 4.53: FT-IR spectrum of compound 16PM5B.

Compound **12PM5B** was selected as representative compound for ^1H and ^{13}C NMR spectroscopy analysis. Figure 4.54 shows the structure of **12PM5B** with the atomic numbering.

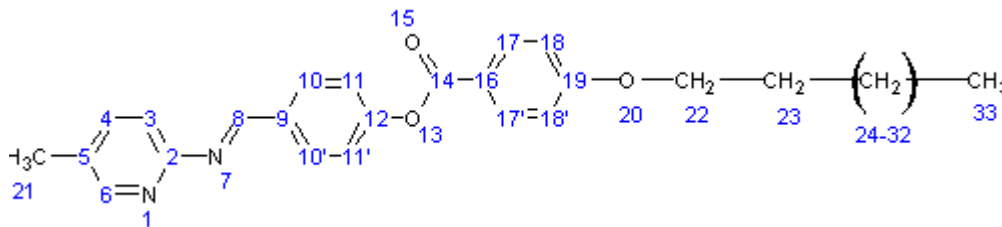


Figure 4.54: Structure with atomic numbering scheme for 12PM5B.

Tables 4.34-4.37 summarized the respective 1D and 2D NMR spectral data for compound **12PM5B**. The 1D and 2D NMR spectra of compound **12PM5B** are depicted in Figures 4.55- 4.59, respectively.

In the ^1H NMR, it was found that aromatic protons appeared at low field region as doublet within the chemical shift range of $\delta = 6.99$ to 8.15 ppm. A singlet at respective $\delta = 9.19$ ppm corresponded to the azomethine ($-\text{N}=\text{CH}-$) of **12PM5B**. Another singlet was observed at $\delta = 8.34$ ppm which attributed the aromatic proton attached to the electronegative nitrogen atom of pyridine ring. Aliphatic protons, H22 appeared at the downfield region $\delta = 4.04$ ppm due to the effect of electronegative oxygen atom. The rest of the aliphatic protons appeared within the chemical shift range of $\delta = 0.91$ to 2.39 ppm.

Table 4.34: ¹H NMR spectral data of compound 12PM5B in CDCl₃

Proton Number	Chemical Shift, δ ppm	Integrals	Multiplicity*	Coupling Constant
H8	9.19	1H	s	-
H6	8.34	1H	s	-
H17,H17'	8.15	2H	d	9.0
H10,H10'	8.05	2H	d	8.7
H3	7.57	1H	d	8.4
H11,H11'	7.34	2H	d	8.4
H4	7.28	1H	d	8.1
H18,H18'	6.99	2H	d	8.7
H22	4.04	2H	t	6.6
H21	2.39	2H	t	6.6
H23	1.77	2H	p	6.9
H24-H32	1.29-1.50	26H	m	-
H33	0.91	3H	t	6.9

In ¹³C NMR spectrum, the resonance signal at the highest chemical shift δ = 164.54 ppm was attributed to the carbonyl carbon (-C=O-) of ester linkage, C14. A noticeable signal at δ = 160.8 ppm for **12PM5B** was observed corresponding to the azomethine (-CH=N-) linkage. The following signals at the chemical shift range δ = 114.39 to 153.83 ppm were assigned to the remaining of aromatic carbons, C3-C7, C9-C12 and C16-C19. Next, C22 appeared at δ = 68.38 ppm which is relatively higher chemical shift than other aliphatic carbons. Other carbons in the alkoxy chains, C23 to C34, give rise to the signals in lower chemical shift range of δ = 14.09 to 31.91 ppm.

The HMQC spectrum (Figure 4.58) reveals the connectivity between the aromatic hydrogens and their corresponding carbons. From the plot, the peaks owing to the carbons at $\delta = 130.59$ and 114.39 ppm show correlation with the H10 (or H10') (refer to cross peak) and the H11 (or H11') (refer to cross peak) atoms, respectively. Thus, the peak at $\delta = 130.59$ and 114.39 ppm are associated with the C10 (or C10') and the C11 (or C11') atoms, respectively. The spectrum also show the cross peak of the H17 (or H17') atom with the C17 (or C17') atom at $\delta = 131.54$ ppm and the cross peak of the H18 (or H18') atom with the C18 (or C18') atom at $\delta = 108.64$ ppm. The HMQC experiment also reveals that the H33 atom correlates with the C33 atom at $\delta =$ ppm and the H22 atom at $\delta = 4.04$ ppm correlates with the C22 atom at $\delta = 68.38$ ppm. A quintet at $\delta = 1.77$ ppm owing to the H23 atom correlates with the C23 atom at $\delta = 31.91$ ppm. The multiplets attributed to the H24-32 atoms at the chemical shift range of $\delta = 1.29$ to 1.50 ppm are found to correlate with the C24-32 atoms at the chemical shift range of $\delta = 22.68$ to 29.64 ppm.

The quaternary carbons are assigned by using the HMBC experiment. The long range HMBC cross peaks of the H17 (or H17') atom with the C14 atom at $\delta = 164.54$ ppm, H18 (or H18') atom with the C3 atom at $\delta = 120.86$ ppm and H10 (or H10') atom with the C17 atom at $\delta = 131.54$ ppm strongly support the positions of these atoms. The C8 signal at $\delta = 160.83$ ppm is assigned based on the correlation with its nearest proton, H10 (or H10'). The C14 carbonyl atom at $\delta =$ ppm is confirmed via correlations with the aromatic H11 and H17 protons.

Table 4.35: ^{13}C NMR spectral data of compound 12PM5B in CDCl_3

Carbon Number	Chemical Shift , δ (ppm)
C14	164.54
C2	163.72
C8	160.83
C9	153.83
C8	149.03
C5	138.72
C4	133.63
C6	132.36
C17, C17'	131.54
C10, C10'	130.59
C16	122.21
C19	121.27
C3	120.86
C12	119.49
C11, C11'	114.39
C18, C18'	108.64
C22	68.38
C23	31.91
C24-C32	29.64
	29.54
	29.34
	29.09
	25.98
	22.68
C21	18.04
C33	14.09

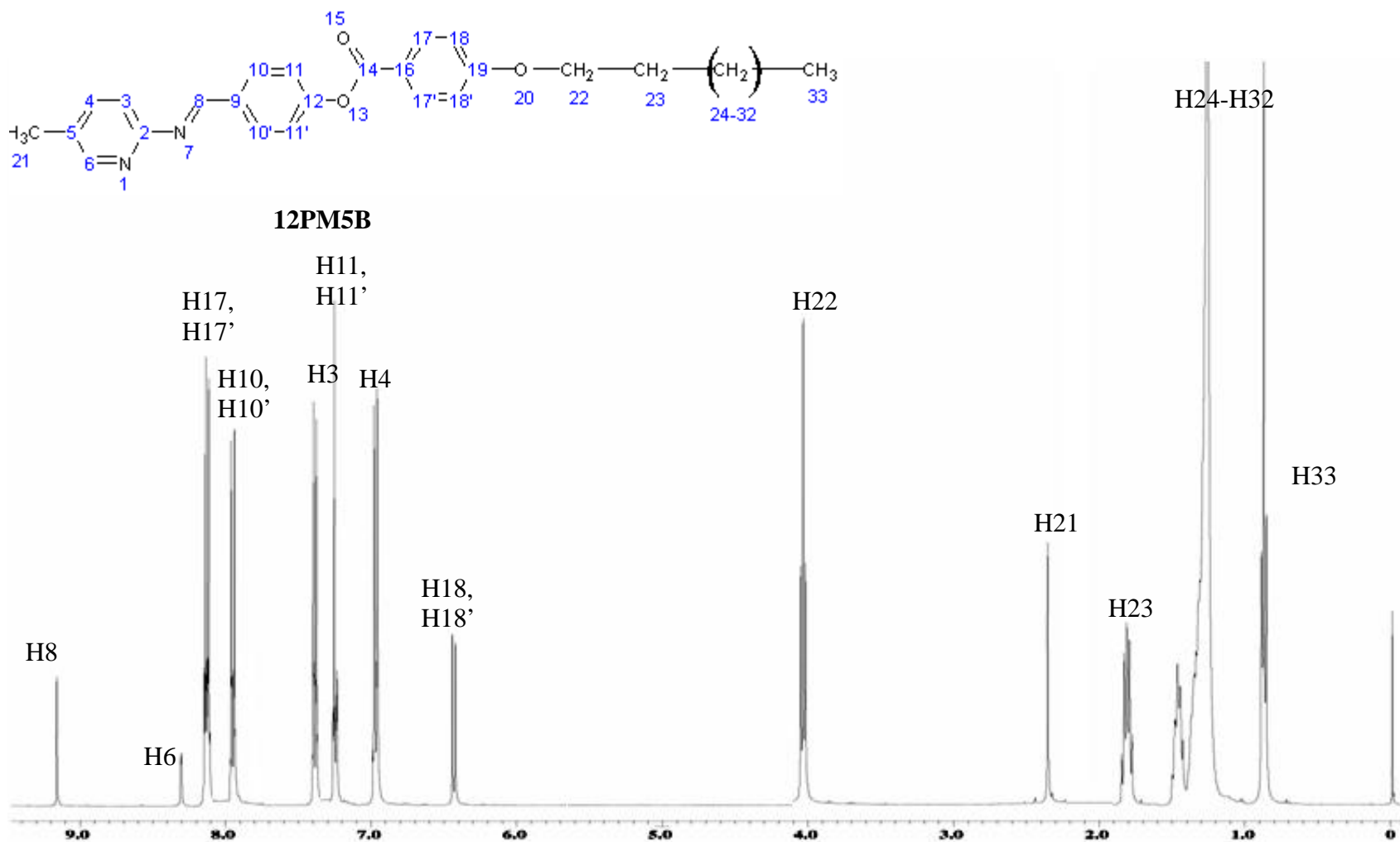


Figure 4.55: ¹H NMR spectrum of compound 12PM5B.
168

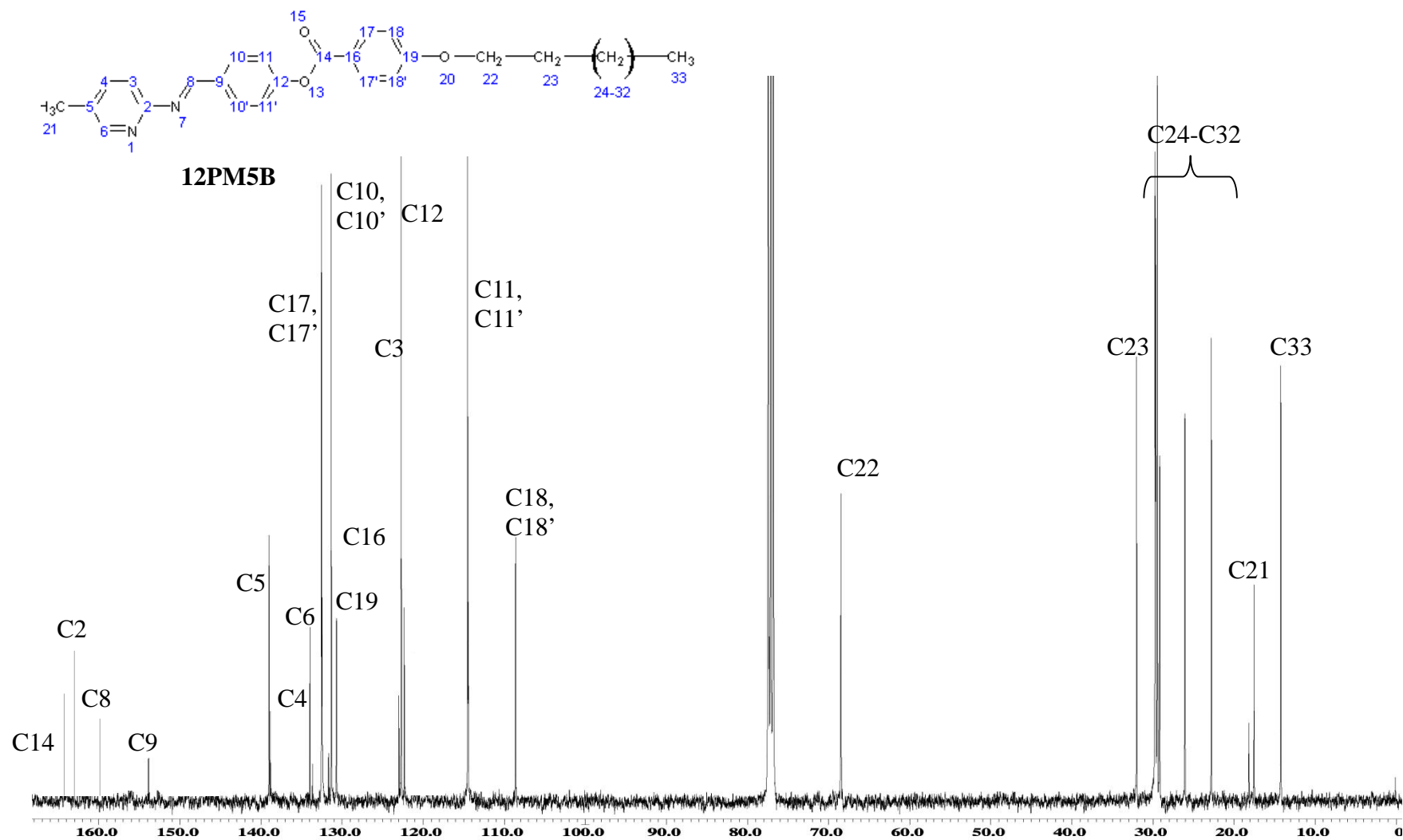


Figure 4.56: ¹³C NMR spectrum of compound 12PM5B.

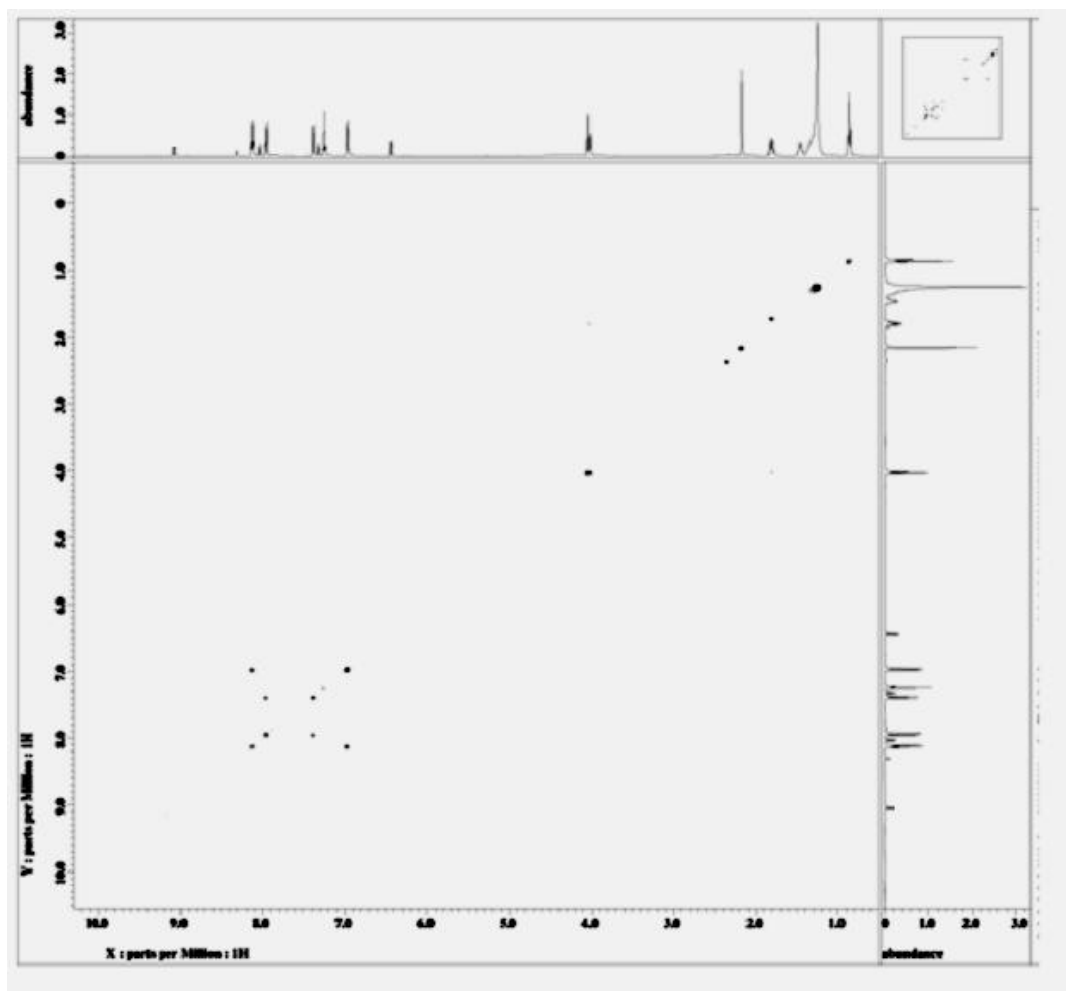


Figure 4.57: COSY spectrum of compound 12PM5B.

Table 4.36: ^1H - ^1H correlations as deduced from the 2D COSY experiments for compound 12PM5B

Atom No. ^a	^1H - ^1H COSY correlations
H8	---
H6	---
H17,H17'	H4, H4'
H10,H10'	H3
H3	H10, H10'
H11,H11'	H18,H18'
H4	H17, H17'
H18,H18'	H11, H11'
H22 ^b	H23
H21	---
H23 ^c	H22, H24-H32
H33	H24-H32

TMS was used as internal standard.

^a Based on the numbering scheme in Figure 4.55.

^b The H22 atom correlates with the methylene protons (H24-H32) but their real positions could not be determined because the ^1H chemical shifts of the H24-H32 atoms were indistinguishable.

^c The H23 atom correlates with the methylene protons (H24-H32) but their real positions could not be determined because the ^1H chemical shifts of the H24-H32 atoms were indistinguishable.

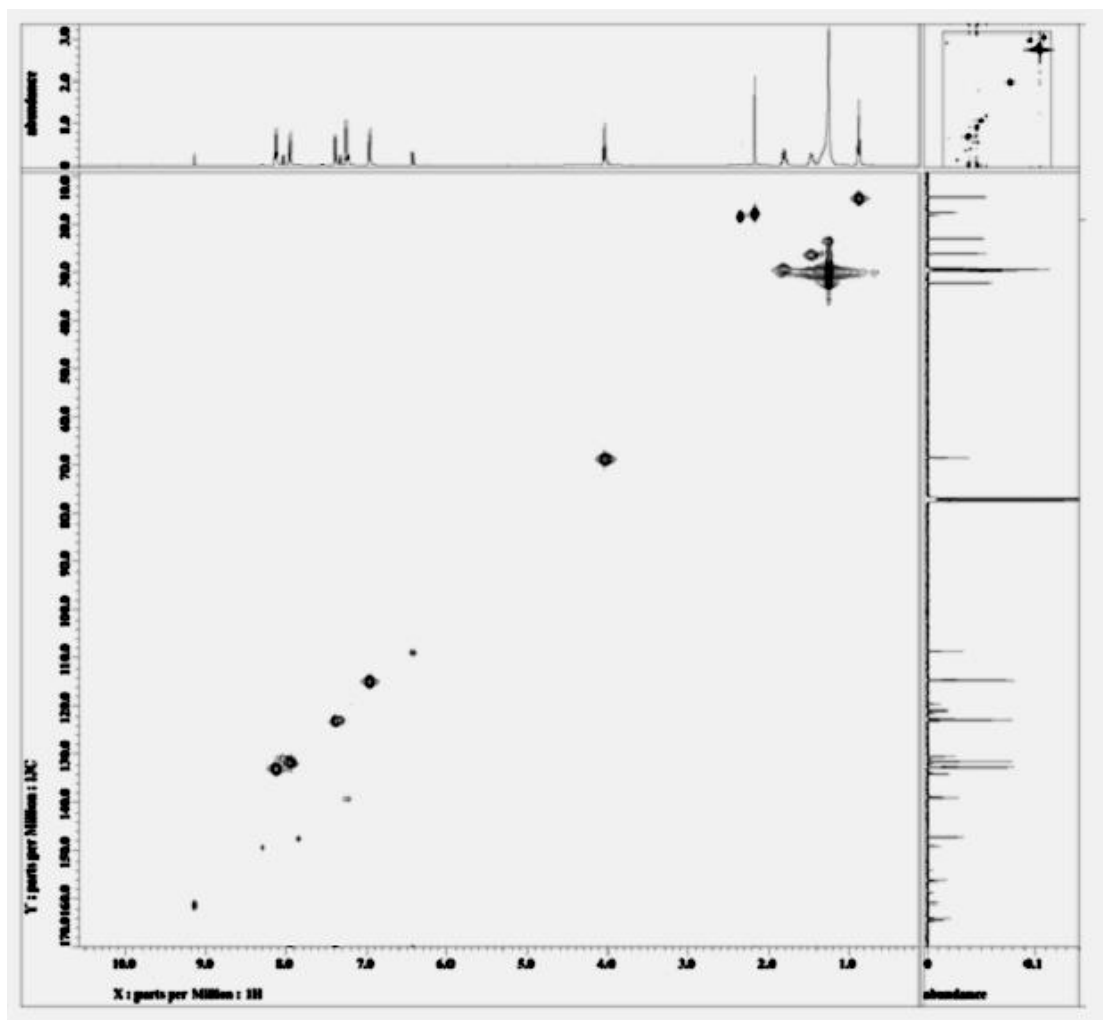


Figure 4.58: HMQC spectrum of compound 12PM5B.

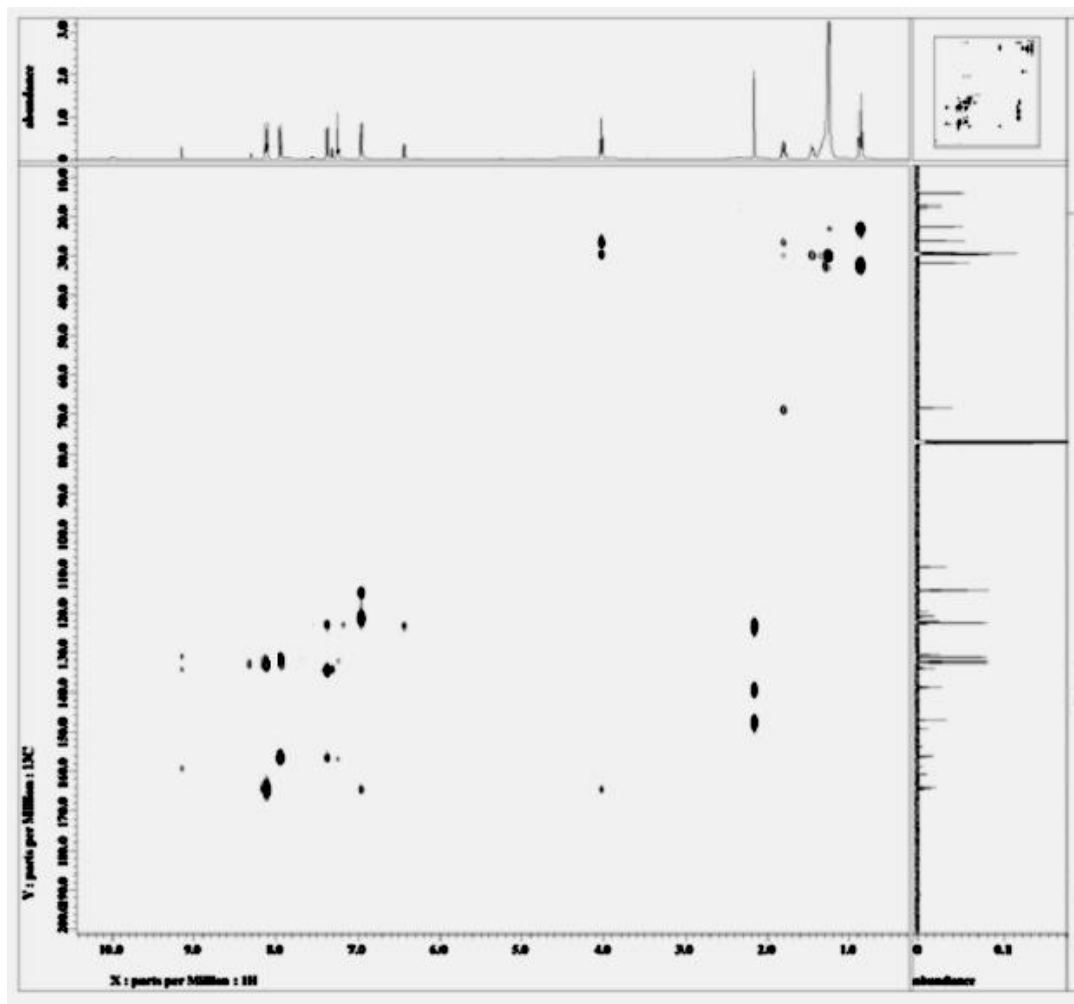


Figure 4.59: HMBC spectrum of compound 12PM5B.

Table 4.37: ^{13}C - ^1H correlations as deduced from the 2D HMQC and HMBC experiments for compound 12PM5B

Atom No. ^a	HMQC		HMBC [$J(\text{C,H})$]		
	1J	2J	3J	4J	bJ
H8	C8	C9	C10,C10'	---	C6
H6	C6	---	---	---	C17,C17'
H17	C17	---	C14,C19	---	---
H17'	C17'	---	C14,C19	---	---
H10	C10	C9	C8	---	C17,C17'
H10'	C10'	C9	C8	---	C17,C17'
H3	C3	C18	---	C6,C8	---
H11	C11	C12	---	C14	---
H11'	C11'	C12	---	C14	---
H4	C4	---	C6	---	---
H18	C18	C19	C16	---	---
H18'	C18'	C19	C16	---	---
H22 ^c	C22 ^b	C23	C24	---	---
H21	C21	C5	C4	C3	---
H23 ^d	C23 ^c	C22	C24	---	---
H33	C33	C32	C31	---	---

TMS was used as internal standard.

^a Based on the numbering scheme in Figure 4.56.

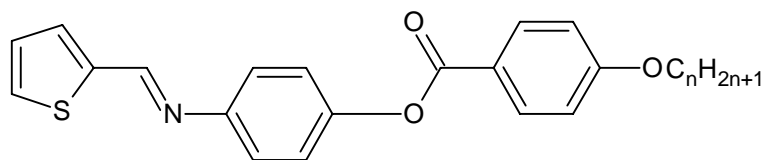
^b Intramolecular interaction.

^c The C22 atom correlates with the methylene carbons (C24-C32) but their real [$J(\text{C,H})$] value could not be determined because the ^{13}C chemical shifts of the C24-C30 atoms were indistinguishable.

^d The C23 atom correlates with the methylene carbons (C24-C32) but their real [$J(\text{C,H})$] value could not be determined because the ^{13}C chemical shifts of the C24-C30 atoms were indistinguishable.

4.6 Series 6: Structural Elucidation of 2-[4-(4-Alkoxybenzoyloxy)benzylidenaniline]thiophenes (nTAP)

A homologous series of 2-[4-(4-Alkoxybenzoyloxy)benzylidenanilines]thiophenes (**nTAP**, where $n = 2$ to 10, 12, 14, 16, 18) were synthesized (Figure 4.60). The percentage of yields are tabulated in Table 4.38.



nTAP where $n = 2, 10, 12, 14, 16, 18$

Figure 4.60: Structure of 2-[4-(4-Alkoxybenzoyloxy)benzylidenaniline]-thiophenes (nTAP).

Table 4.38: Percentage of yields of compounds nTAP

Compound	Percentage of yield (%)
2TAP	30
3TAP	36
4TAP	40
5TAP	45
6TAP	46
7TAP	48
8TAP	47
9TAP	48
10TAP	54
12TAP	52
14TAP	59
16TAP	66
18TAP	70

The purity of the compound was confirmed by using HPLC and TLC analysis. The highest purity of the compound migrated as single peak on HPLC chromatogram and the TLC data associated with compounds **nTAP** is listed in Appendix 6A.

Mass spectrometry was carried out on **16TAP** as representative compound for series **nTAP**. EI mass spectrum of **16TAP** is shown in Figure 4.61. The mass spectrum of compound **16TAP**, confirmed the molecular ion peak at 547.4 m/z with relative abundance of 2.80.

Selected FT-IR data associated with compounds **nTAP** are given in Table 4.39. The FT-IR spectrum of the representative compound **16TAP** is given in Figure 4.62. From the spectrum, the C=N bond showed at 1607 cm^{-1} (Parra *et al.*, 2005). A distinct absorption band showed at 1253 cm^{-1} ascribed to the aromatic C-O ether bond. Strong and intense absorption bands due to the long alkyl chain showed at 2917 and 2849 cm^{-1} are assigned to the stretching of C-H aliphatic bonds. While the absorption band of carbonyl group of ester linkage C=O in **16TAP** was found to be 1726 cm^{-1} , indicating the successful of Steglich esterification. Absorption band assigned to C-S-C thiophene ring was found to be 1468 cm^{-1} (Marin *et al.*, 2009).

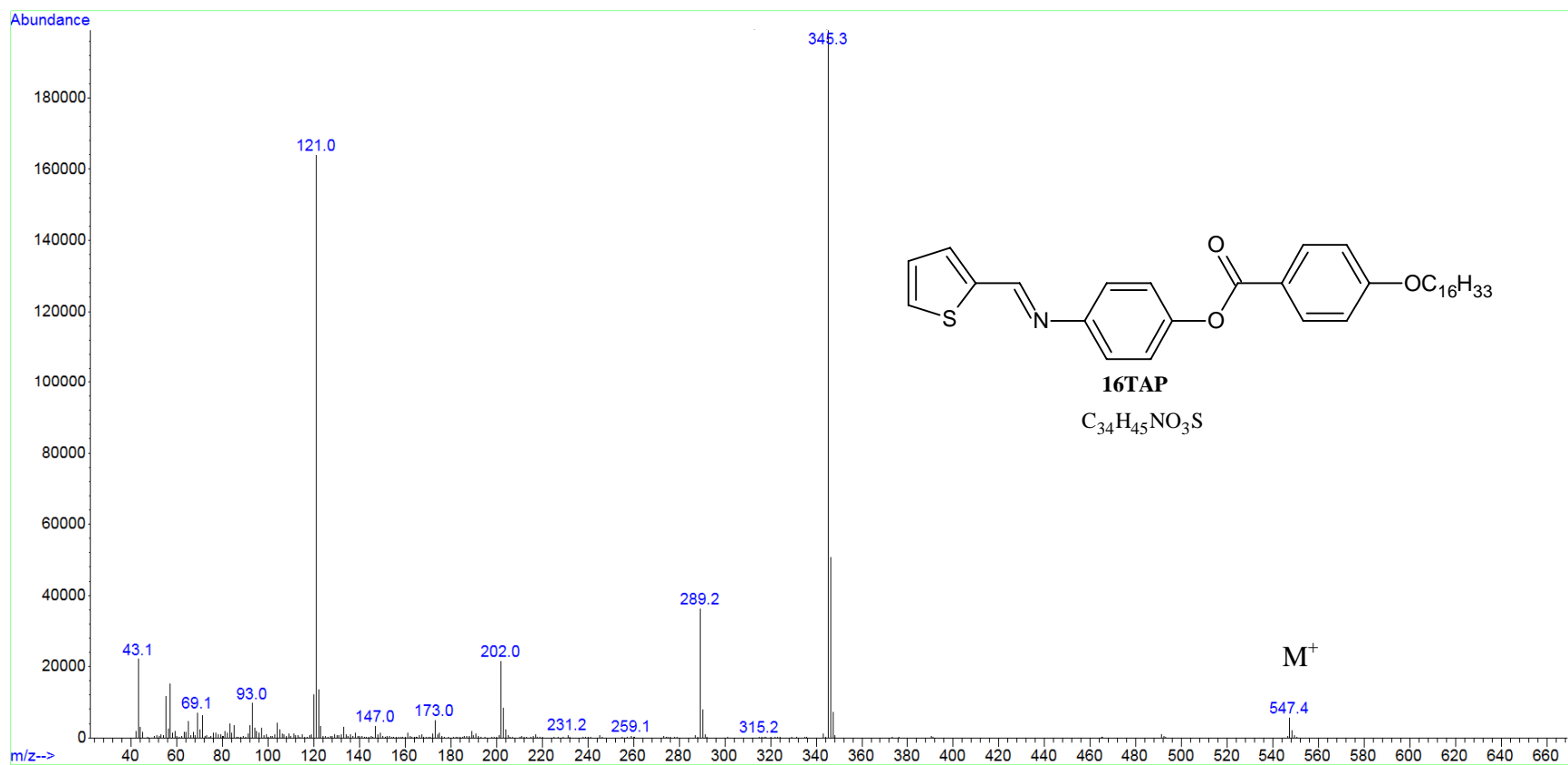


Figure 4.61: Mass Spectrum of compound 16TAP.

Table 4.39: FT-IR spectral data of compounds nTAP

Compound	IR ν (cm ⁻¹)					
	sp ² C-H Stretch (aromatic)	sp ³ C-H Stretch (aliphatic)	C=O (ester)	C=N (Schiff base)	C-S-C (thiophene)	Ar-O-R (ether)
2TAP	3079	2926,2876	1723	1608	1474	1263
3TAP	3078	2974,2878	1561	1592	1463	1254
4TAP	3078	2917,2849	1732	1604	1463	1253
5TAP	3071	2918,2873	1716	1606	1466	1257
6TAP	3072	2926,2865	1723	1604	1469	1257
7TAP	3071	2927,2869	1723	1604	1468	1261
8TAP	3071	2924,2852	1723	1603	1469	1262
9TAP	3071	2923,2849	1723	1604	1468	1261
10TAP	3070	2918,2850	1723	1608	1469	1260
12TAP	3070	2919,2850	1723	1608	1469	1262
14TAP	3070	2918,2849	1725	1605	1468	1255
16TAP	3070	2917,2849	1726	1607	1468	1253
18TAP	3070	2918,2850	1725	1607	1463	1255

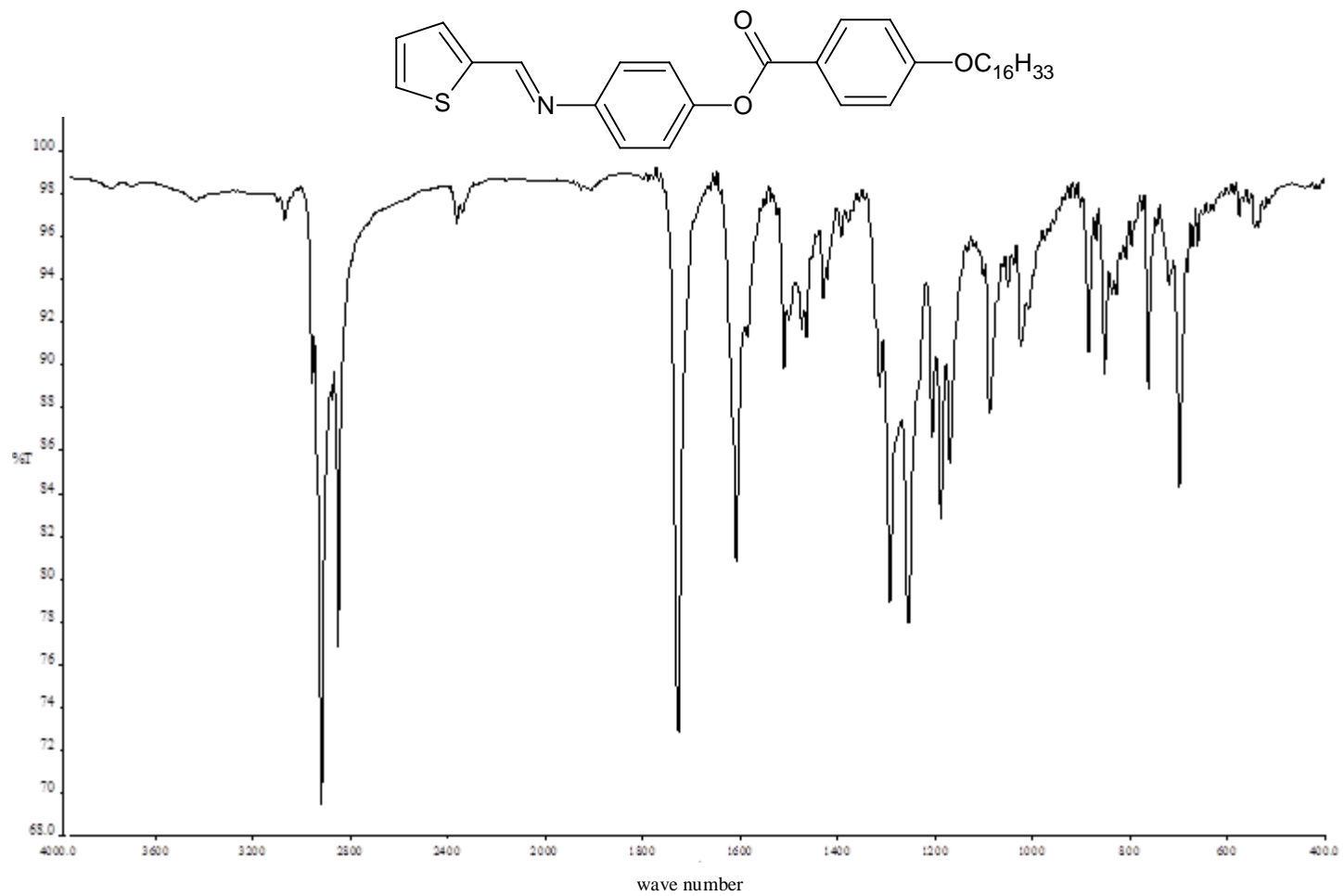


Figure 4.62: FT-IR spectrum of compound 16TAP.

Compound **10TAP** was chosen as representative compound for ^1H and ^{13}C NMR spectroscopy analysis. The atomic numbering scheme of **10TAP** which is used to label the different types of protons and carbons are shown in Figure 4.63.

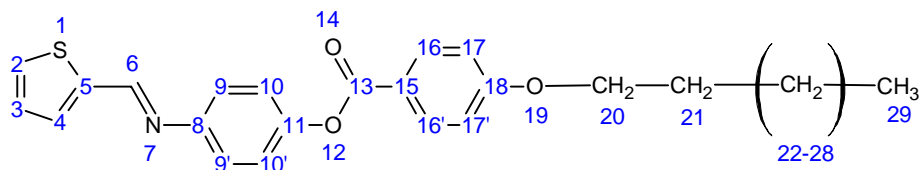


Figure 4.63: Structure with atomic numbering scheme for 10TAP.

The 1D and 2D NMR spectral data are tabulated in the representative Tables 4.40-4.43 while the 1D and 2D NMR spectral data of compound **10TAP** are shown in Figures 4.64- 4.68, respectively.

In the ^1H NMR, a signal appeared at $\delta = 8.59$ ppm corresponded to the azomethine proton ($-\text{CH}=\text{N}-$) of **10TAP**. The aromatic protons appeared as doublet within the chemical shift range of $\delta = 6.96$ to 8.16 ppm. All the signals within $\delta = 6.96$ to 8.16 ppm were assigned to the aromatic protons accordingly. The thiophene protons appeared as doublets and showed within $\delta = 7.20$ to 7.28 ppm. Subsequently, the remaining aliphatic proton (H21 to H34) was ascribed to the resonance signals in highfield region of $\delta = 1.27$ to 4.03 ppm. A triplet signal appeared at $\delta = 0.86$ ppm in the spectra of **10TAP** was assigned to the protons in the terminal methyl group ($-\text{CH}_3$).

Table 4.40: ¹H NMR spectral data of compound 10TAP in CDCl₃

Proton Number	Chemical Shift, δ ppm	Integrals	Multiplicity*	Coupling Constant
H6	8.59	1H	s	-
H16,H16'	8.11	2H	d	9.0
H9,H9'	7.49	2H	d	8.7
H2	7.28	1H	d	8.1
H4	7.22	1H	d	8.1
H3	7.20	1H	t	8.4
H10,H10'	7.13	2H	d	8.7
H17,H17'	6.96	2H	d	9.0
H20	4.03	2H	t	6.6
H21	1.78	2H	p	7.8
H22-H28	1.27-1.53	26H	m	-
H29	0.86	3H	t	6.9

Note:

TMS was used as an internal standard.

*s=singlet,

d=doublet

t=triplet

p=quintet

m=multiplet

Table 4.41: ^{13}C NMR spectral data of compound 10TAP in CDCl_3

Carbon Number	Chemical Shift , δ (ppm)
C13	165.02
C5	164.39
C6	153.03
C8	149.31
C15	148.97
C18	142.83
C17, C17'	132.28
C9, C9'	132.24
C3	130.39
C2	127.75
C4	122.41
C11	121.89
C16, C16'	121.56
C10, C10'	114.35
C20	68.38
C21	31.93
C22-C27	29.70
	29.66
	29.59
	29.56
	29.36
	26.00
C28	22.68
C29	14.10

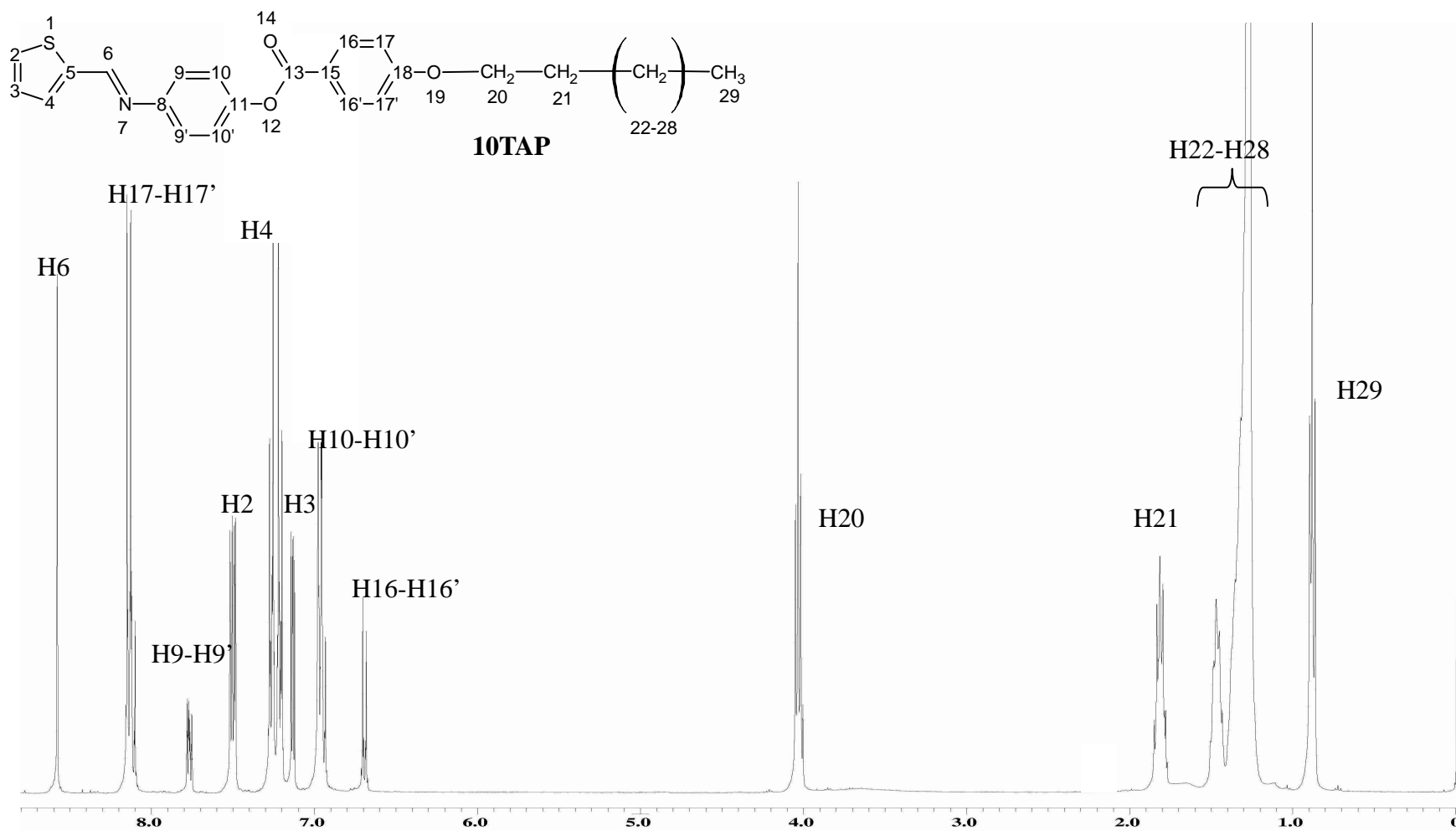


Figure 4.64: ¹H NMR spectrum of compound 10TAP.

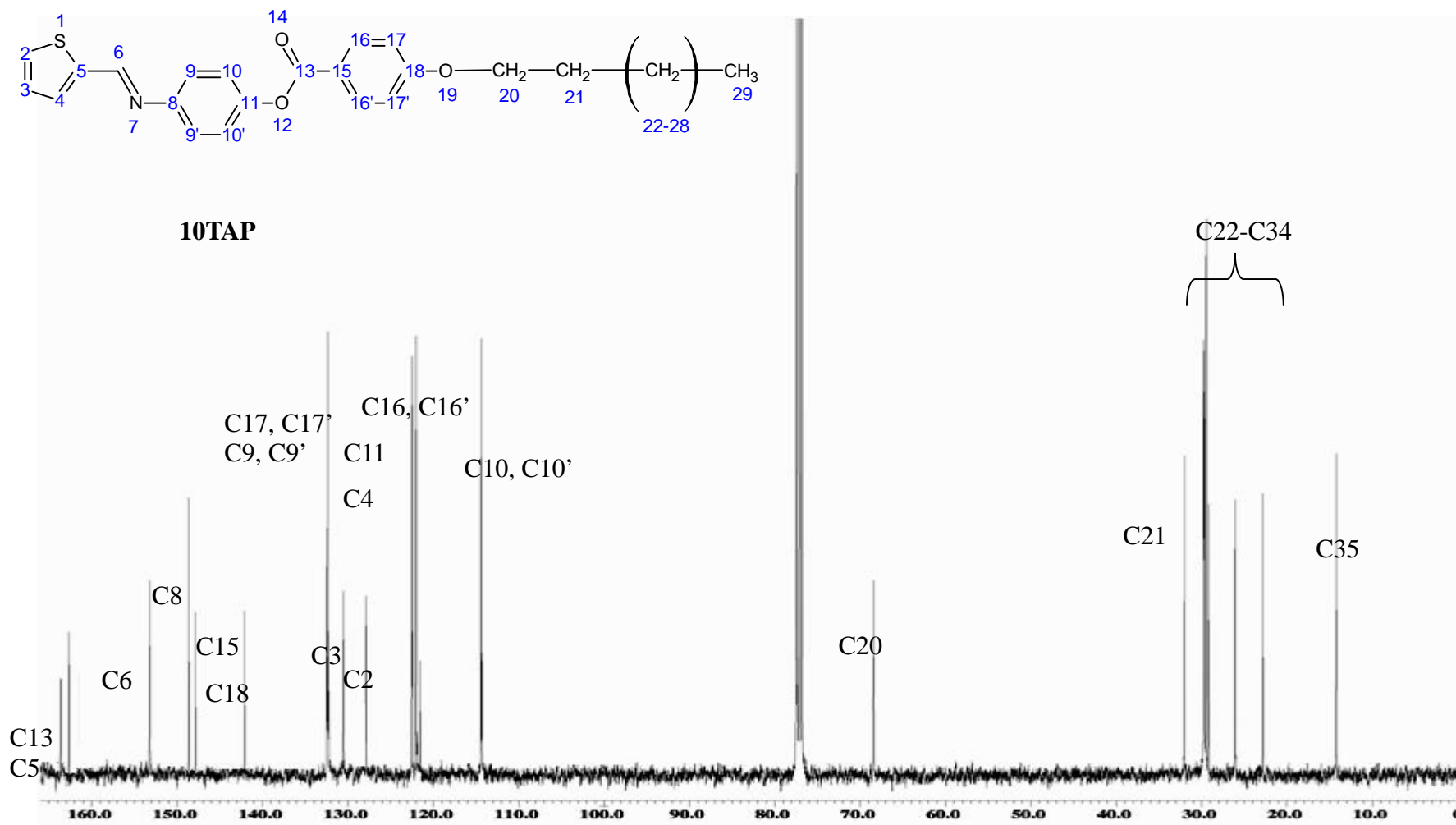


Figure 4.65: ¹³C NMR spectrum of compound 10TAP.

In the ^{13}C NMR, the signal at highest chemical shift $\delta = 165.02$ ppm was attributed to the carbon in the ester group (-COO-), C13. Carbon which directly attached to the sulfur atoms (-C-S-C-) in thiophene fragment was shifted to downfield region $\delta = 164.39$ ppm. The following resonance signal at $\delta = 163.60$ ppm corresponded to C6 which is the carbon atom in Schiff base linkage. The aromatic carbons appeared within the chemical shift range of $\delta = 114.35$ to 153.03 ppm. The remaining aliphatic carbons in ether group, C20-C35, give rise to the resonance signals within the chemical shift range at $\delta = 68.38, 31.93, 29.70, 29.66, 29.59, 29.36, 26.00, 22.68$ and 14.10 ppm.

The same ^1H NMR spectrum also showed the resonance owing to the aromatic protons. These signals are assigned with the aid of the COSY experiment. The doublets at $\delta = 7.49$ and 7.13 ppm can be ascribed to the H9 (or H9') and H10 (or H10') atoms, respectively. The signal owing to the H16 (or H16') and H17 (or H17') atoms are observed at the respective chemical shifts of $\delta = 8.11$ and 6.96 ppm.

The structure of the compound is further substantiated by the ^{13}C NMR data. The HMQC spectrum (Figure 4.67) also reveals the connectivity between the aromatic hydrogens and their corresponding carbons. From the plot, the peaks owing to the carbons at $\delta = 132.24$ and 114.35 ppm show correlation with the H9 (or H9') (refer to cross peak) and the H10 (or H10') (refer to cross peak) atoms, respectively. Thus, the peak at $\delta = 132.24$ and 114.35 ppm are associated with the C9 (or C9') and the C10 (or C10') atoms, respectively. The spectrum also show

the cross peak of the H16 (or H16') atom with the C16 (or C16') atom at $\delta = 121.56$ ppm and the cross peak of the H17 (or H17') atom with the C17 (or C17') atom at $\delta = 132.28$ ppm.

The HMQC experiment also reveals that the H31 atom at $\delta = 0.86$ ppm correlates along the C31 atom at $\delta = 14.10$ ppm. A quintet at chemical shift, $\delta = 1.78$ ppm owing to the H21 atom correlates with the C21 atom at $\delta = 31.93$ ppm. The multiplets attributed to the H22-30 atoms at the chemical shift range of $\delta = 1.27$ - 1.53 ppm are found to correlate with the C22-30 atoms at the chemical shift range of $\delta = 22.68$ - 29.70 ppm.

The quaternary carbons are assigned by using the HMBC experiment. The long range HMBC cross peaks of the H16 (or H16') atom with the C15 atom at $\delta = 148.97$ ppm, H17 (or H17') atom with the C5 atom at $\delta = 164.39$ ppm and H10 (or H10') atom with the C4 atom at $\delta = 122.41$ ppm, H4 atom with the C8 atom at $\delta = 149.31$ ppm strongly support the positions of these atoms. The peak of the C20 ether atom at $\delta = 68.38$ ppm is assigned based on the heteronuclear connectivities with the methylene protons (H21 and H22).

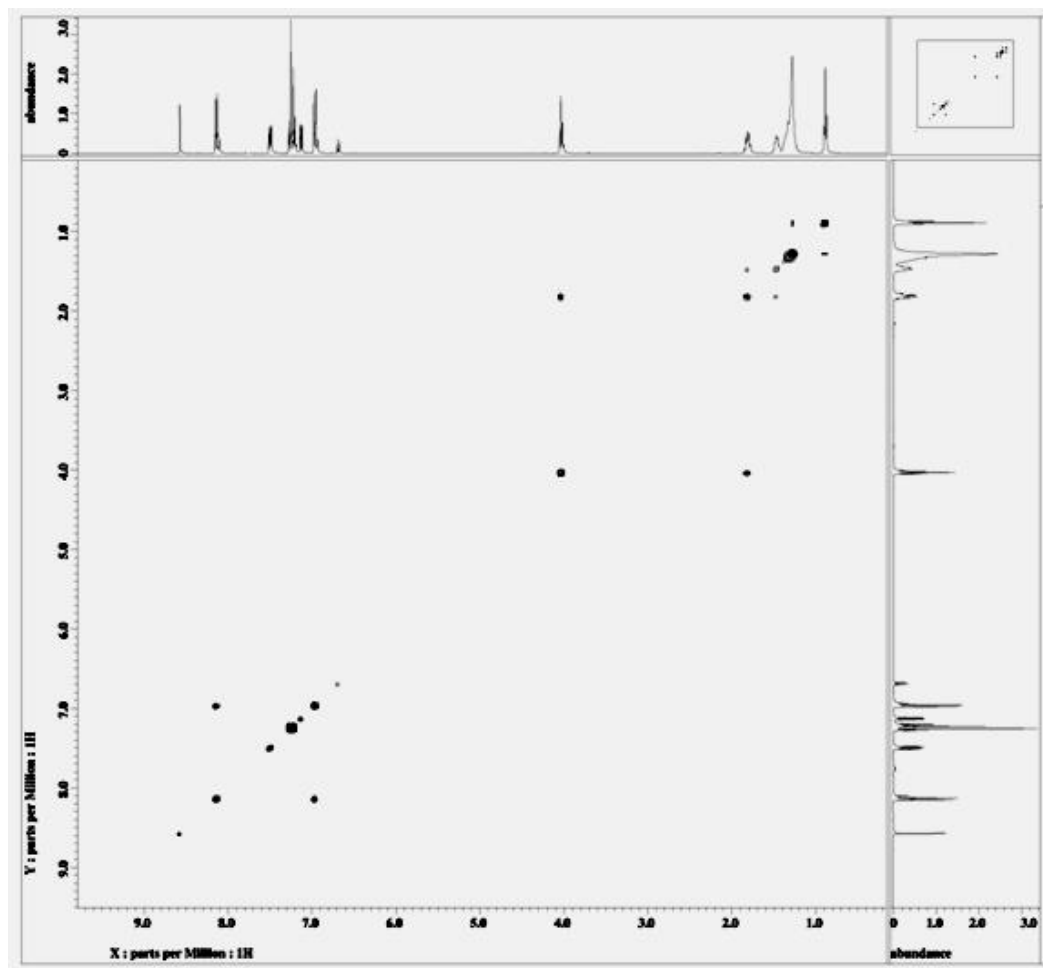


Figure 4.66: COSY spectrum of compound 10TAP.

Table 4.42: ^1H - ^1H correlations as deduced from the 2D COSY experiments for compound 10TAP

Atom No. ^a	^1H - ^1H COSY correlations
H6	---
H16,H16'	H10, H10'
H9,H9'	---
H2	H3
H4	H3
H3	H2
H10,H10'	H17, H17'
H17,H17'	H10, H10'
H20	H21
H21	H20, H22-H28
H29	H22-H28

TMS was used as internal standard.

^a Based on the numbering scheme in Figure 4.64.

^b The H20 atom correlates with the methylene protons (H22-H28) but their real positions could not be determined because the ^1H chemical shifts of the H22-H28 atoms were indistinguishable.

^c The H21 atom correlates with the methylene protons (H22-H28) but their real positions could not be determined because the ^1H chemical shifts of the H22-H28 atoms were indistinguishable.

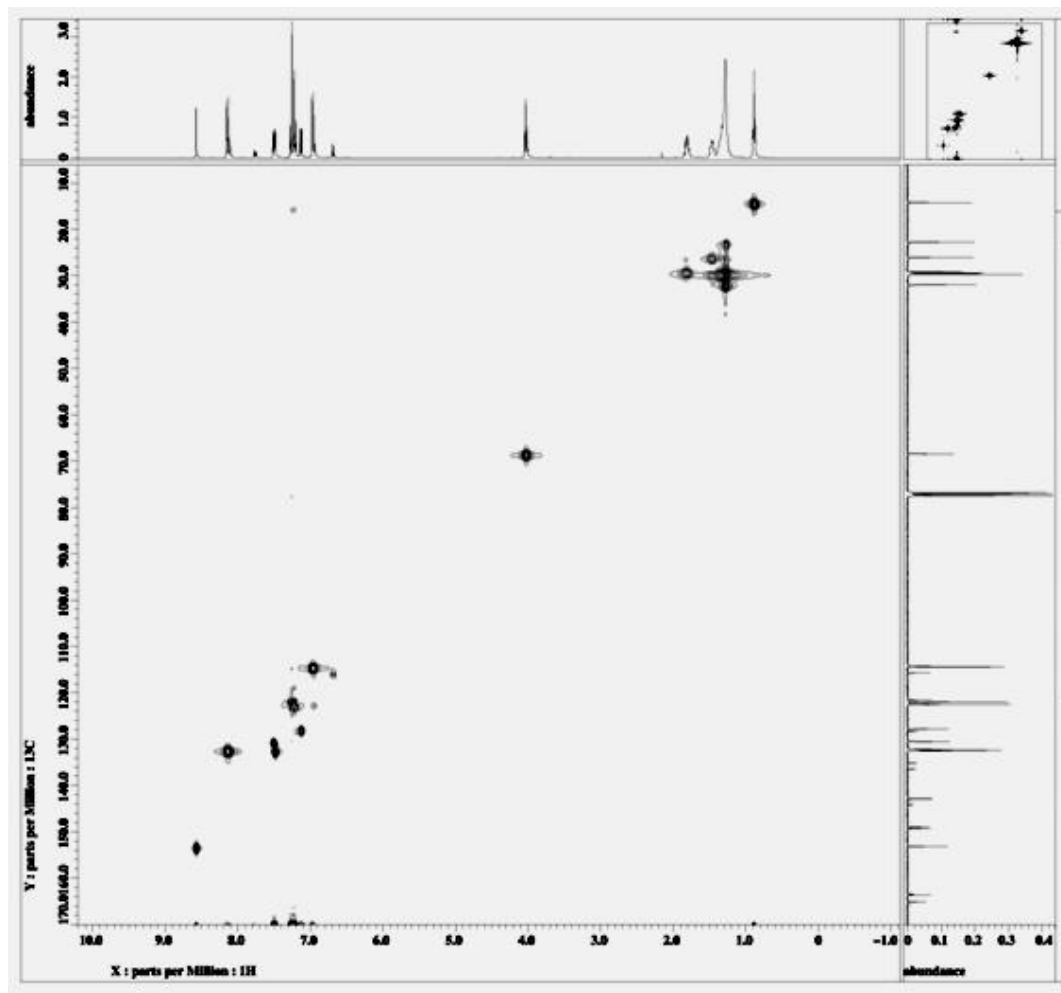


Figure 4.67: HMQC spectrum of compound 10TAP.

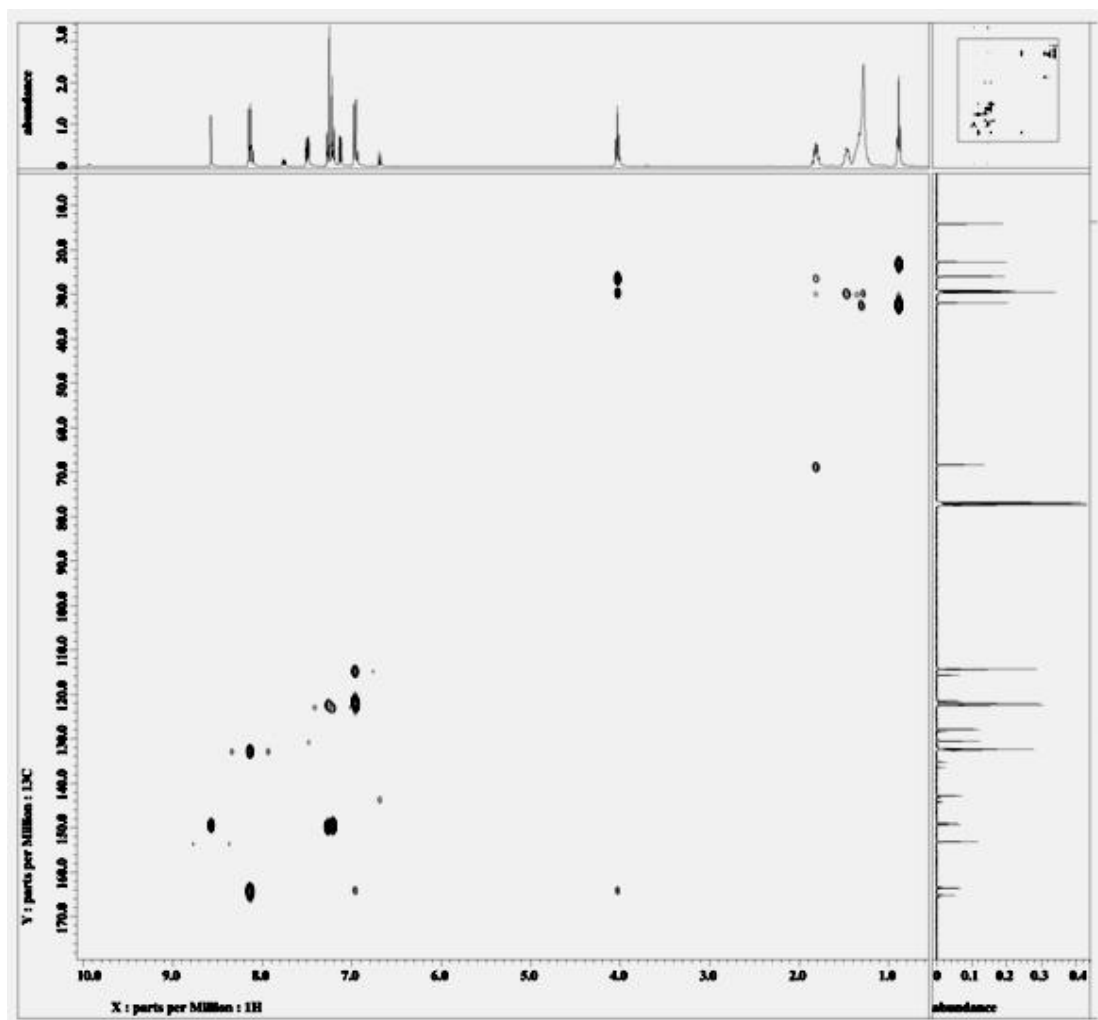


Figure 4.68: HMBC spectrum of compound 10TAP.

Table 4.43: ^{13}C - ^1H correlations as deduced from the 2D HMQC and HMBC experiments for compound 10TAP

Atom No. ^a	HMQC		HMBC [$J(\text{C},\text{H})$]		
	1J	2J	3J	4J	bJ
H6	C6	C8	---	---	---
H16	C16	---	C13,C18	---	---
H16'	C16'	---	C13,C18	---	---
H9	C9	---	C11	---	C15
H9'	C9'	---	C11	---	C15
H2	C2	C4	---	---	---
H4	C4	C2	---	---	---
H10	C10	C11	C8	---	C4
H10'	C10'	C11	C8	---	C4
H17	C17	C18	C15	---	C5
H17'	C17'	C18	C15	---	C5
H20 ^c	C20	C18,C21	---	---	C5
H21 ^d	C21	C20	---	---	---
H29	C29	C28	C27	---	---

TMS was used as internal standard.

^a Based on the numbering scheme in Figure 4.65.

^b Intramolecular interaction.

^c The C20 atom correlates with the methylene carbons (C22-C28) but their real positions could not be determined because the ^1H chemical shifts of the C22-C28 atoms were indistinguishable.

^d The C21 atom correlates with the methylene carbons (C22-C28) but their real positions could not be determined because the ^1H chemical shifts of the C22-C28 atoms were indistinguishable.

CHAPTER 5.0

RESULTS AND DISCUSSION 2: PHASE TRANSITION TEMPERATURES AND MESOMORPHIC PROPERTIES

5.1 Series 1: Mesomorphic Properties of 6-Methyl-2-(4-alkoxybenzylidenamino)benzothiazoles (nMeBTH), 6-methoxy-2-(4-alkoxybenzylidenamino)benzothiazoles (nOMeBTH), 6-ethoxy-2-(4-alkoxybenzylidenamino)benzothiazoles (nOEtBTH) and 2-(4-alkoxybenzylidenamino)benzothiazoles (nHBZT)

5.1.1 Optical and Thermal Studies

The liquid crystalline of the synthesized compounds have been characterized by using DSC and POM methods. The phase transition temperatures and associated enthalpy changes (ΔH) obtained from DSC analysis during heating and cooling cycles of series **nMeBTH**, **nOMeBTH**, **nOEtBTH** and **nHBZT** were determined and the results are summarized in Tables 5.1, 5.2, 5.3 and 5.4, respectively.

Representative DSC thermograms of **10MeBTH** and **10OMeBTH** are depicted in Figure 5.1. It can be noticed that **10MeBTH** exhibited enantiotropic mesophases. Total of three transition peaks can be observed in each scan which are due to the transition of Cr-SmA, SmA-N and N-I. For **10OMeBTH**, there is an additional exothermic peak occurred in the cooling scan compared to the heating scan.

The compound exhibited monotropic smectic A phase. The first peak represents the crystal-smectic A transition and the second peak reflects the transition from smectic A to nematic phase and the last peak indicates the nematic to isotropic liquid transition.

Representative of DSC thermogram of **8OEtBTH** and **8HBZT** are depicted in Figure 5.2. For **8OEtBTH**, there is an additional exothermic peaks occurred from isotropic liquid during cooling scan indicating that the compound exhibited monotropic smectic C phase. The first peak (Figure 5.2) represents the crystal-smectic C transition and the second peak reflects the transition from smectic C to nematic phase and the last peak indicates the nematic to isotropic liquid transition. Compound **8HBZT** monotropic mesophase where the SmA mesophase stability (76.34 °C) is lower than the melting point (79.57 °C).

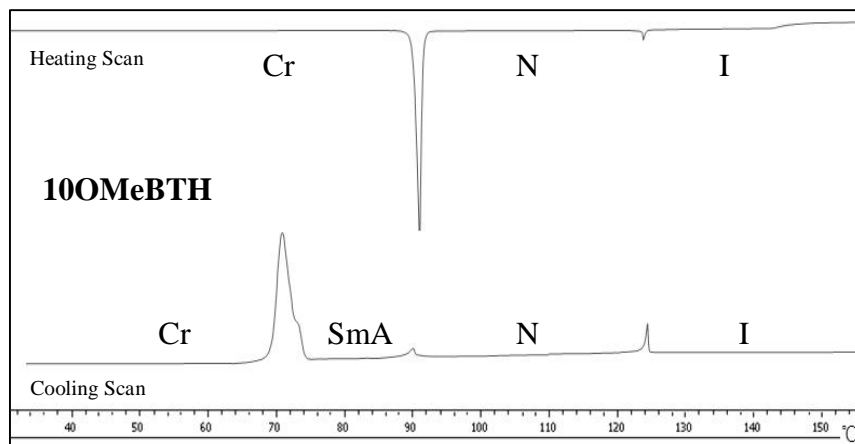
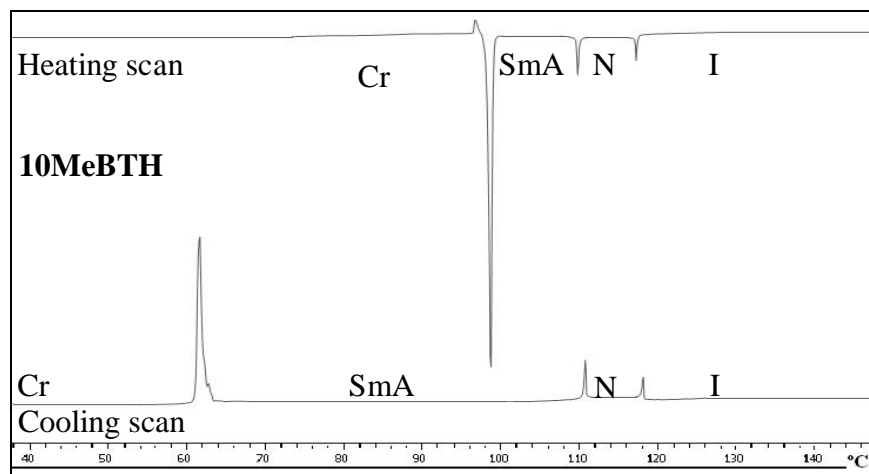


Figure 5.1: DSC thermogram of 10MeBTH and 10OMeBTH during heating and cooling cycles.

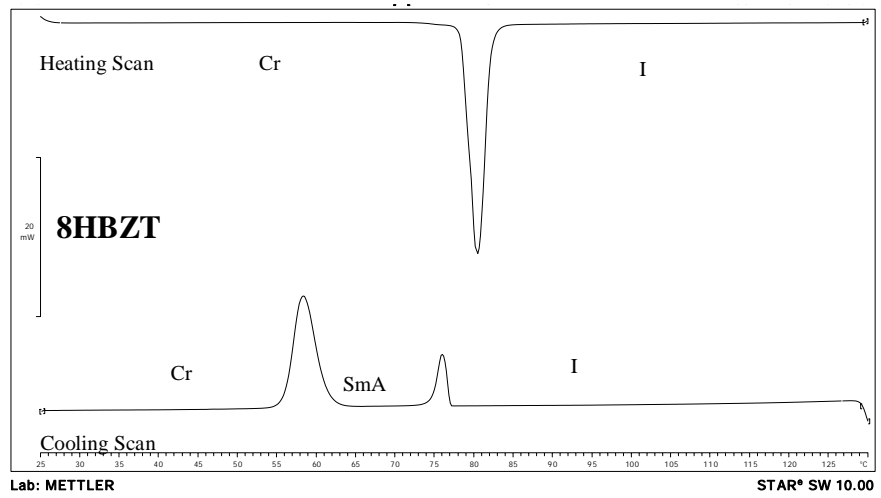
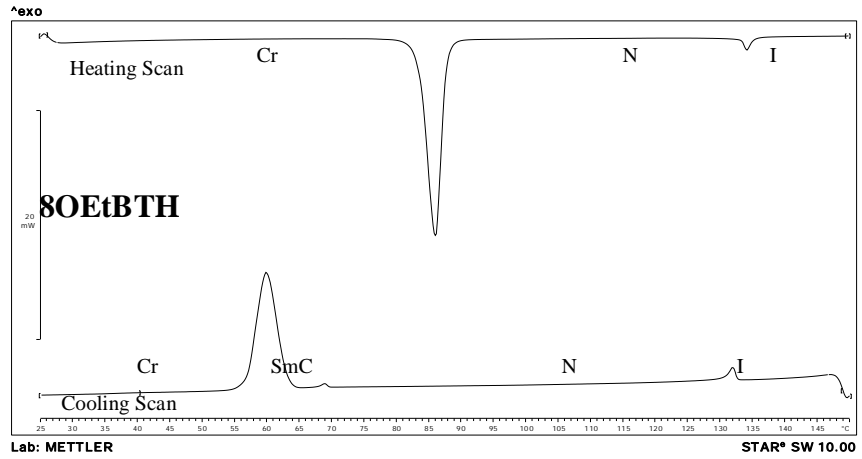


Figure 5.2: DSC thermograms of 8OEtBTH and 8HBZT during heating and cooling cycles.

Table 5.1: Phase transition temperatures and associated enthalpy changes of series nMeBTH

Compound	Transition Temperatures, °C (ΔH , kJ mol ⁻¹)	Heating Cooling
2MeBTH	Cr 117.0 (35.27) N 140 (1.12) I <i>Cr₁ 70.0 (1.45) Cr₂ 86.5 (29.64) N 139.8 (1.11) I</i>	
3MeBTH	Cr 94.2 (31.64) N 105.4 (0.49) I <i>Cr 66.2 (27.59) N 102.8 (0.68) I</i>	
4MeBTH	Cr 99.6 (31.02) N 125.3 (1.13) I <i>Cr 63.8 (26.38) N 125.1 (1.15) I</i>	
5MeBTH	Cr 93.6 (36.82) N 114.7 (0.57) I <i>Cr 80.4 (35.59) N 112.8 (0.73) I</i>	
6MeBTH	Cr 105.4 (39.83) N 119.4 (1.03) I <i>Cr 83.2 (35.60) N 119.3(1.47) I</i>	
7MeBTH	Cr 102.5 (36.87) N 116.5 (0.96) I <i>Cr 72.8 (24.37) SmA 81.5 (0.56) N 114.3(0.98) I</i>	
8MeBTH	Cr 108.1 (49.10) N 118.2 (1.33) I <i>Cr 70.3 (33.94) SmA 96.2 (1.43) N 118.1 (1.84) I</i>	
9MeBTH	Cr 92.9 (33.15) SmA 104.5 (2.21) N 117.1 (1.22) I <i>Cr 57.8 (23.63) SmA 102.8 (2.30) N 115.3 (1.40) I</i>	
10MeBTH	Cr 99.1 (49.84) SmA 110.8 (3.41) N 118.3 (1.79) I <i>Cr 61.2 (37.42) SmA 110.9 (3.13) N 118.2 (1.94) I</i>	
12MeBTH	Cr 81.5 (44.98) SmA 116.2 (8.25) I <i>Cr 68.8 (41.13) SmA 116.6 (8.90) I</i>	
14MeBTH	Cr 83.1 (48.79) SmA 113.5 (8.6) I <i>Cr 69.6 (47.86) SmA 115.0 (8.97) I</i>	
16MeBTH	Cr 88.4 (61.10) SmA 115.8 (10.45) I <i>Cr 81.3 (58.64) SmA 115.5 (10.94) I</i>	
18MeBTH	Cr ₁ 55.6 (1.21) Cr ₂ 91.2 (67.18) SmA 109.6 (10.83) I <i>Cr₁ 54.7 (1.28) Cr₂ 86.6 (57.81) SmA 112.1 (8.7) I</i>	

Table 5.2: Phase transition temperatures and associated enthalpy changes of series nOMeBTH

Compound	Transition Temperatures, °C (ΔH , kJmol ⁻¹)	Heating Cooling
2OMeBTH	Cr 85.2 (42.48) N 130.2 (1.16) I Cr 71.1 (33.43) N 129.9 (0.87) I	
3OMeBTH	Cr 102.2 (27.48) N 130.4 (1.16) I Cr 127.02 (18.24) N 33.8 (0.74) I	
4OMeBTH	Cr 132.1 (43.92) N 139.9 (0.85) I Cr 80.8 (31.32) N 139.2 (0.92) I	
5OMeBTH	Cr 102.2 (28.71) N 123.7 (0.63) I Cr 43.3 (18.90) N 121.3 (0.61) I	
6OMeBTH	Cr 84.7 (48.64) N 128.8 (0.96) I Cr 70.0 (38.69) N 128.3 (0.92) I	
7OMeBTH	Cr 91.4 (36.16) N 123.1 (0.92) I Cr 46.9 (27.63) N 121.1 (0.92) I	
8OMeBTH	Cr 95.6 (49.17) N 125.3 (1.27) I Cr 49.7 (30.14) SmC 56.5 (0.76) N 126.1 (1.31) I	
9OMeBTH	Cr 86.5 (39.19) N 123.7 (1.15) I Cr 37.9 (25.92) SmC 78.6 (0.76) N 121.9 (1.05) I	
10OMeBTH	Cr 91.2 (54.77) N 124.5 (1.53) I Cr 41.2 (30.15) SmA 90.4 (1.27) N 124.2 (1.53) I	
12OMeBTH	Cr 84.1 (61.56) SmA 101.8 (1.49) N 121.9 (1.58) I Cr 51.3 (42.55) SmA 101.9 (2.08) N 121.6 (2.26) I	
14OMeBTH	Cr 77.9 (54.8) SmA 107.8 (2.31) N 118.8 (2.12) I Cr 62.6 (49.99) SmA 107.8 (1.77) N 118.5 (2.26) I	
16OMeBTH	Cr 84.5 (57.98) SmA 110.6 (2.90) N 116.1 (3.26) I Cr 64.1 (53.93) SmA 110.7 (3.31) N 116.0 (3.36) I	
18OMeBTH	Cr 86.9 (53.68) SmA 108.4 (6.98) I Cr 73.6 (67.1) SmA 110.9 (7.52) I	

Table 5.3: Phase transition temperatures and associated enthalpy changes of series nOEtBTH

Compound	Transition Temperatures, °C (ΔH , kJmol ⁻¹)	Heating Cooling
2OEtBTH	Cr 136.2 (35.44) N 168.1 (1.16) I <i>Cr 107.6 (25.20) N 164.5 (0.94) I</i>	
3OEtBTH	Cr 106.8 (25.47) N 145.7 (0.87) I <i>Cr 66.8 (18.57) N 142.8(0.94) I</i>	
4OEtBTH	Cr 105.0 (26.77) N 151.9 (1.24) I <i>Cr 68.6 (21.33) N 147.5 (1.29) I</i>	
5OEtBTH	Cr 75.5 (31.25) N 139.3 (0.93) I <i>Cr 60.1 (26.61) N 138.1 (1.02) I</i>	
6OEtBTH	Cr 94.57 (38.34) N 116.33 (1.04)I <i>Cr 35.35 (15.08) N 112.79 (0.84) I</i>	
7OEtBTH	Cr 76.8 (32.36) N 133.0 (1.07) I <i>Cr 56.8 (31.88) N 133.1 (1.15) I</i>	
8OEtBTH	Cr 85.4 (34.75) N 134.1 (1.24) I <i>Cr 60.2 (27.96) SmC 68.9 (0.30) N 132.1 (1.11) I</i>	
9OEtBTH	Cr 82.0 (35.66) N 130.2 (1.07) I <i>Cr 35.8 (13.07) SmC 81.3 (0.26) N 127.7 (1.36) I</i>	
10OEtBTH	Cr 88.7 (45.52) SmA 95.6 (0.25) N 131.2 (1.58) I <i>Cr 57.0 (19.34) *SmC 91.2 SmA 93.9 (0.21) N 129.5 (1.76) I</i>	
12OEtBTH	Cr 90.3 (50.11) SmC 97.7 (2.07) SmA 109.1(1.26) N 126.9 (1.87) I <i>Cr 65.9 (45.38) *SmC 92.0 SmA 107.66 (1.02) N 125.4 (2.22) I</i>	
14OEtBTH	Cr 91.3 (51.43) SmA 113.2 (1.65) N 121.8 (1.67) I <i>Cr 69.4 (46.98) SmA 111.6 (1.39) N 120.3 (1.86) I</i>	
16OEtBTH	Cr 96.5 (62.28) SmA 116.1 (1.46) N 120.1 (1.40) I <i>Cr 67.2 (53.60) SmA 114.5 (1.31) N 118.5 (1.63)I</i>	
18OEtBTH	Cr 98.8 (83.73) SmA 116.0 (7.55) I <i>Cr 81.1 (75.46) SmA 117.7 (7.99) I</i>	

*POM data

Table 5.4: Phase transition temperatures and associated enthalpy changes of series nHBZT

Compound	Transition Temperatures, °C (ΔH , kJmol ⁻¹)	Heating Cooling
2HBZT	Cr 85.0(26.23) I Cr 20.34 (16.78) I	
3HBZT	Cr 83.97 (26.51) I Cr 34.02 (15.47) I	
4HBZT	Cr 86.46 (24.29) I Cr 56.48 (19.98) I	
5HBZT	Cr 82.76 (26.19) I Cr 51.34 (22.78) I	
6HBZT	Cr ₁ 74.18 (1.10) Cr ₂ 90.69(41.74) I Cr 61.2 (32.83) I	
7HBZT	Cr 76.73 (37.44) I Cr 35.98 (5.16) SmA 64.46 (23.04) I	
8HBZT	Cr 79.57 (46.75) I Cr 58.73 (6.74) SmA 76.34 (32.74) I	
9HBZT	Cr 79.14 (41.39) I Cr 40.08 (5.73) SmA 75.86 (21.62) I	
10HBZT	Cr 82.52 (35.80) SmA 84.62 (0.56) I Cr 38.43 (6.16) SmA 80.6 (22.94) I	
12HBZT	Cr 81.88 (45.42) SmA 90.1 (7.60) I Cr 46.27 (7.79) SmA 86.14 (36.84) I	
14HBZT	Cr 77.65 (45.60) SmA 91.93 (8.85) I Cr 47.57 (8.60) SmA 89.0 (36.09) I	
16HBZT	Cr 84.69 (48.08) SmA 90.75 (6.28)I Cr 61.3 (9.89) SmA 87.83 (43.91) I	
18HBZT	Cr 83.78 (37.79) SmA 90.36 (5.57) I Cr 61.16 (9.87) SmA 87.35 (51.72) I	

In optical study, the mesophase of entire synthesized compounds were identified using polarizing optical microscope (POM) with heating and cooling cycles.

The optical photomicrographs of compounds **12MeBTH** and **16MeBTH** are shown in Figures 5.3 and 5.4, respectively. Upon cooling for **12MeBTH**, SmA phase emerged with fan-shaped texture (Figure 5.3). During cooling cycle, the isotropic liquid phase of **16MeBTH** appeared as *bâtonnet* texture (Figure 5.4a) and then coalesced to SmA mesophase with fan-shaped texture (Figure 5.4b).

Optical photomicrographs of **8OMeBTH** and **12OMeBTH** are shown in Figures 5.5 and 5.6 as the representative illustration. Nematic phase with *Schlieren* texture (Figure 5.5a) and SmC with *Schlieren* texture (Figure 5.5b) were observed during cooling cycle for **8OMeBTH**. During cooling scan of **12OMeBTH**, nematic mesophase was appeared as droplets and then coalesced to form nematic with marble-like texture (Figure 5.6a). Further cooling, nematic phase was transformed to SmA with fan-shaped (elliptical) texture (Figure 5.6b).

The optical photomicrographs of **8OEtBTH** are illustrated in Figure 5.7. Similarly, by cooling from isotropic liquid phase, nematic mesophase emerged and coalesced to form nematic mesophase with marble-liked texture. By further cooling, nematic mesophase transformed to SmC phase with *Schlieren* texture. For compound **12OEtBTH**, nematic mesophase with *Schlieren* texture was observed during cooling cycle from isotropic liquid. Upon cooling, SmA phase with homeotropic (dark area) textures were observed. When further cooling, SmC with *Schlieren* texture was

formed before crystallization (Figure 5.8). Figure 5.9(a) shows the optical photomicrographs of **16OEtBTH**. Further cooling of nematic phase, a change in texture from nematic to SmA phase with fan-shaped (elliptical) texture was observed before crystallization. As for **18OEtBTH**, smectic A mesophase exhibited focal-conic texture was observed (Figure 5.9b).

Figure 5.10 shows the optical photomicrographs of **10HBZT** and **14HBZT** obtained during cooling cycle. During cooling the isotropic liquid of **10HBZT**, the SmA mesophase appeared as *bâtonnet* (Figure 5.10a) texture. As for **14HBZT**, the SmA mesophase with fan-shaped texture (Figure 5.10b) was observed.

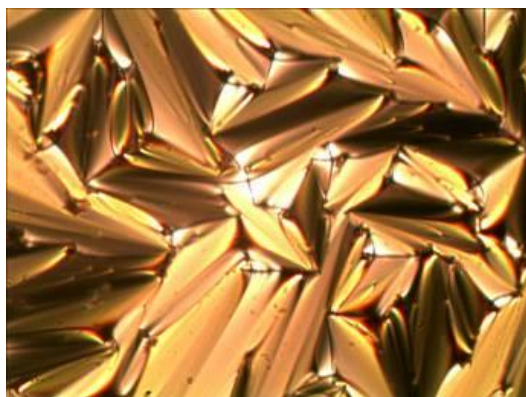


Figure 5.3: Optical photomicrographs of 12MeBTH taken during cooling cycle. SmA phase appeared with fan-shaped texture.

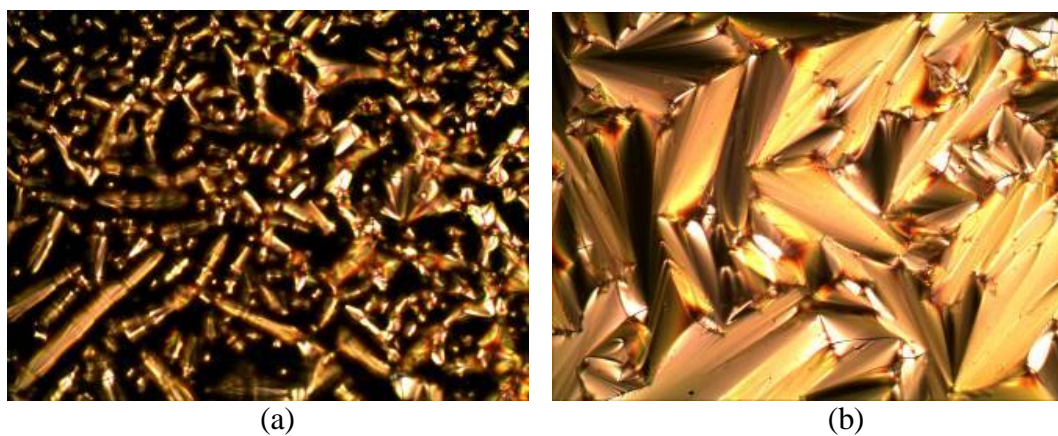


Figure 5.4: (a) Optical photomicrographs of 16MeBTH where *batonnet* texture can be observed upon cooling cycle from isotropic liquid to formed SmA phase.(b) SmA phase with fan-shaped texture.

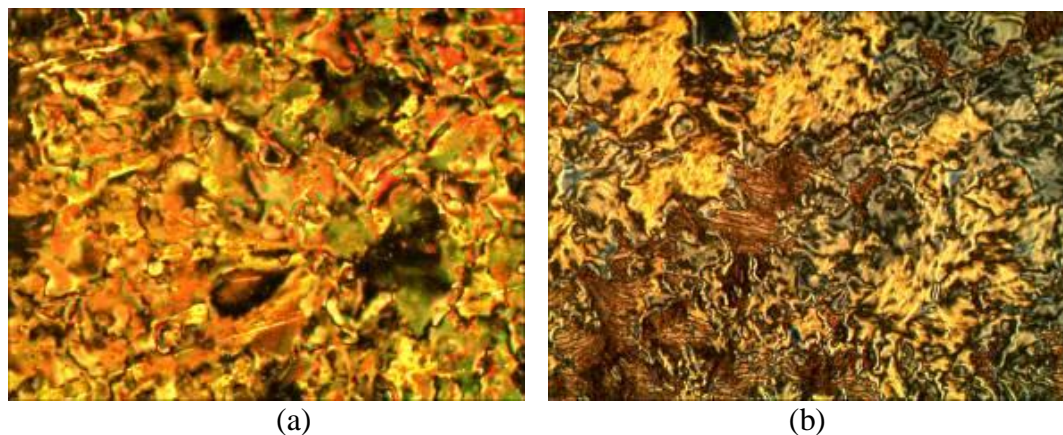


Figure 5.5: Optical photomicrographs of 8OMeBTH during cooling cycle exhibited nematic *Schlieren* texture (a). On further cooling, SmC phase with *Schlieren* texture (b) was observed.

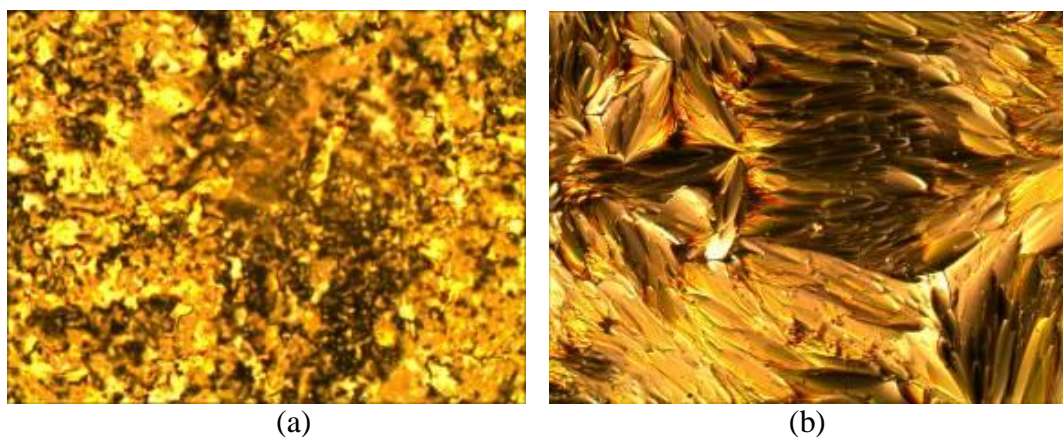
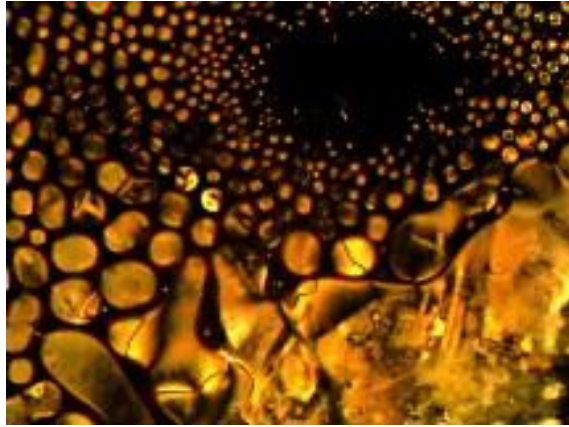
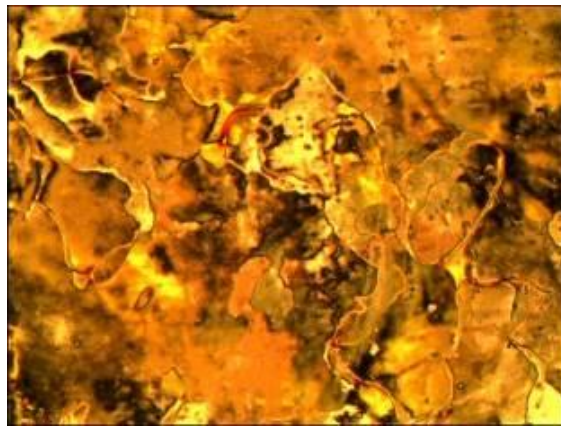


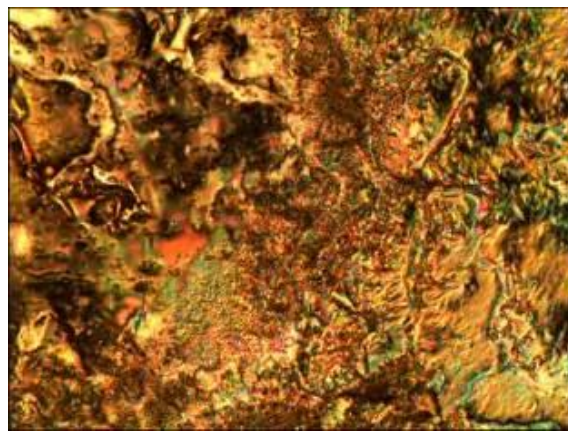
Figure 5.6: Optical photomicrographs of 12OMeBTH during cooling cycle exhibited (a) nematic marble-like texture. On further cooling, SmA phase with focal conic texture (elliptical) was observed.



(a)

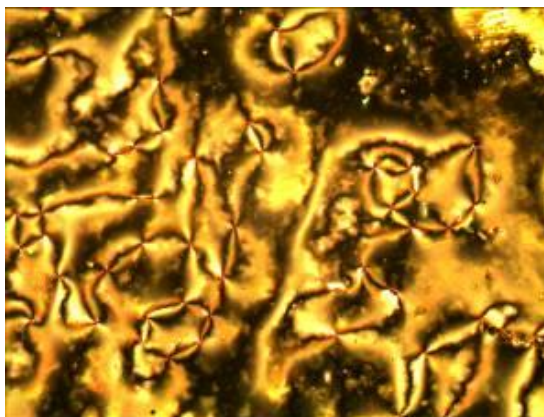


(b)



(c)

Figure 5.7: Liquid crystal textures of 8OEtBTH upon cooling. The nematic droplets (a) appeared and coalesced to form nematic phase with marble-like texture (b). Further cooling, transition of nematic (left) to SmC (right) phase was observed.



(a)



(b)



(c)

Figure 5.8: Optical photomicrographs of 12OEtBTH exhibiting (a) nematic phase with *Schlieren* texture, (b) Upon further cooling, SmA phase with fan-shaped and homeotropic (dark area) textures was observed and (c) SmC phase with *Schlieren* (grey) texture.

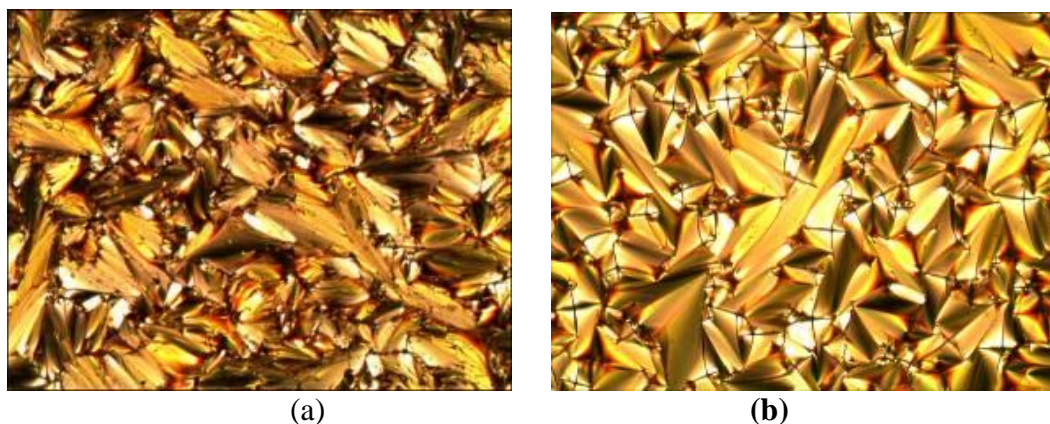


Figure 5.9: (a) Optical photomicrographs of 16OEtBTH. Upon cooling, SmA phase with fan-shaped (elliptical) texture was observed. (b) Optical photomicrographs of 18OEtBTH. Upon cooling from isotropic, SmA with focal conic fan shaped texture was observed.

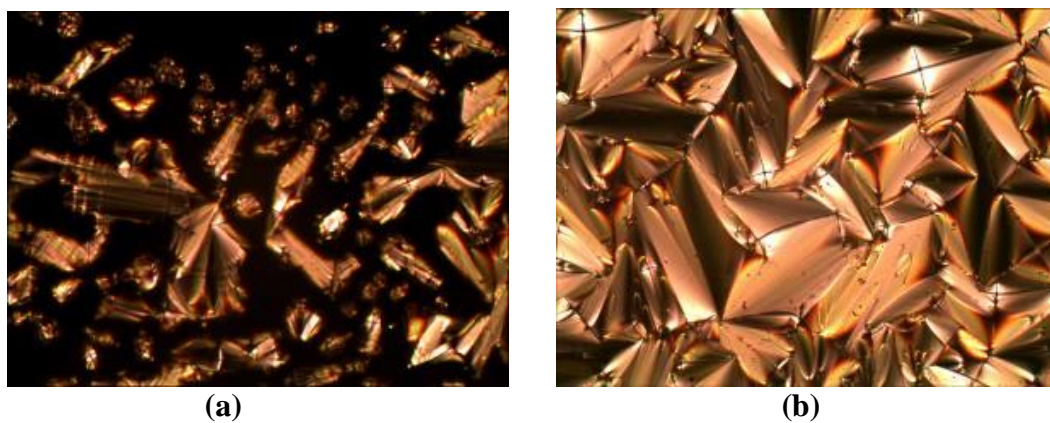


Figure 5.10: (a) Optical photomicrographs of 10HBZT exhibiting SmA phase with *bâtonnet* textures. (b) Optical photomicrographs of 14HBZT exhibiting SmA phase with fan-shaped textures.

A plot which discusses the mesomorphic properties, transition temperatures and the influences of number of carbons in the alkoxy chains for series **nMeBTH**, **nOMeBTH**, **nOEtBTH** and **nHBZT** was studied (Figures 5.11, 5.12, 5.13 and 5.14).

Series **nMeBTH**, **nOMeBTH** and **nOEtBTH** exhibited liquid crystal properties where the terminal chain lengths are sufficient for exhibiting mesophase formation. Generally, compounds with short carbon chains ($n = 2$ to 6) exhibit wider nematic temperature ranges than compounds with longer alkoxy chains ($n = 7$ to 18) (Majumdar *et al.*, 2009). Smectogenic properties were observed as the chain length increased. In general, a metastable smectic phase commenced from C_7 or C_8 member as monotropic phase and become a stable enantiotropic smectic phase from C_{10} member and persistent till the end of the series. The odd-even effect on the transition temperature was observed from C_2 to C_{10} members, it can be obviously inferred that the terminal chains length can majorly affect the mesomorphic properties of the compounds (Collings and Hird, 1997b). The azomethine ($C=N$) linkage which given a step like structure caused in the thickening effect which in turn heighten the nematic phase for short to medium chain compounds (Ha *et al.*, 2012).

From the plots, the clearing temperature showed descending trends when the carbon chain length increased. The flexible terminal alkoxy chain acts as a diluent to the mesogenic core rings system, hence, depressed the clearing

temperature of compounds **nMeBTH**, **nOMeBTH** and **nOEtBTH**. The descending direction was in agreement with the series of 6-methoxy-2-(2-alkanoyloxybenzyliden-amino)benzothiazoles in which the homologous with the longest chain owned the lowest thermal stability (Ha *et al.*, 2010b). As can be seen from the graphs, the nematic mesophase range (Δ_N) is narrowed and disappeared while the smectic mesophase range (Δ_{SmA}) is raised as increase the chain length. The increasing *Van der Waals* forces resulted from the lengthening of alkyl chain that plays an important role in stabilizing the smectic mesophase by facilitating the lamellar packing; on the other hand, it inhibited the nematic mesophase range (Fisch and Kumar, 2001). In addition, the elongation of the carbon chain which been intertwined and attracted, in turn stimulates the packing ability and reduce the nematic mesophase range (Yeap *et al.*, 2006a). As the carbon chain increase, the smectic mesophase range (Δ_{SmA}) showed an increased trend from C₁₂ to C₁₈ members.

For series **nOEtBTH**, a metastable SmC phase commenced from C₈ member as monotropic phase. It became a stable enantiotropic SmC phase from C₁₀ to C₁₂ and exhibited narrow temperature range of the nematic phase. However, a monotropic SmC phase with dark area (homeotropic) emerged from C₈ derivatives and then replaced by specific *schlieren* texture (Godwon *et al.*, 2006), become a stable enantiotropic SmC phase from C₁₂ members.

Based on the plot of series **nHBZT**, the shorter chain members ($n = 2$ to 6) in the series did not exhibit liquid crystal phase. It could be due to the shorter terminal alkoxy chains, gave rise to higher melting point and suppressed the liquid crystal phase. High molecular rigidity in shorter chain member is another barrier for the meso phase formation. Nevertheless, mesophase starts to appear from C_7 derivatives as monotropic (metastable) SmA mesophase. Hence, it was believed that the flexible chains (C_7 for **nHBZT** series) is prerequisite to promote liquid crystal phases.

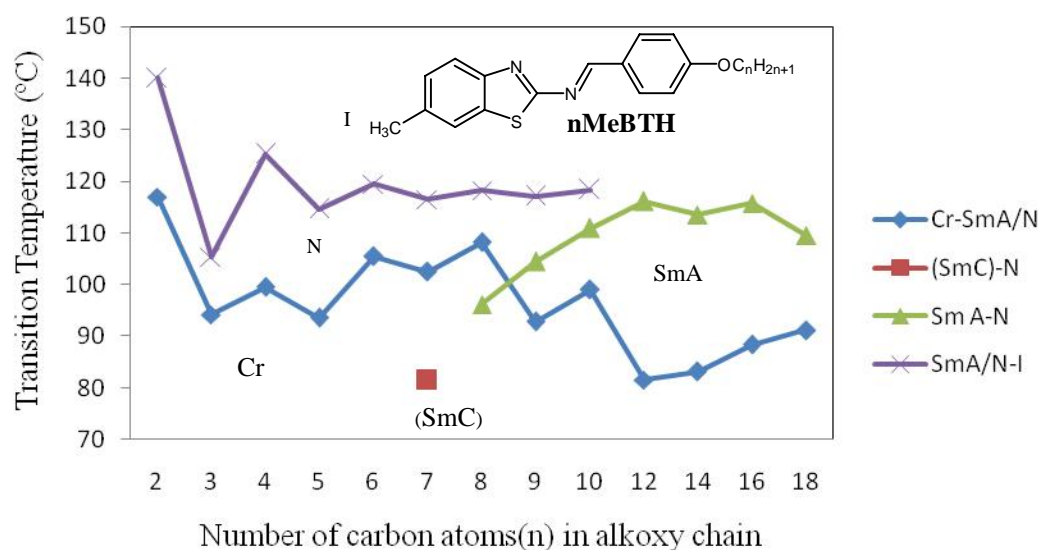


Figure 5.11: Plot of clearing temperature (°C) versus the carbon atoms (n) in alkoxy chain of homologous series nMeBTH.

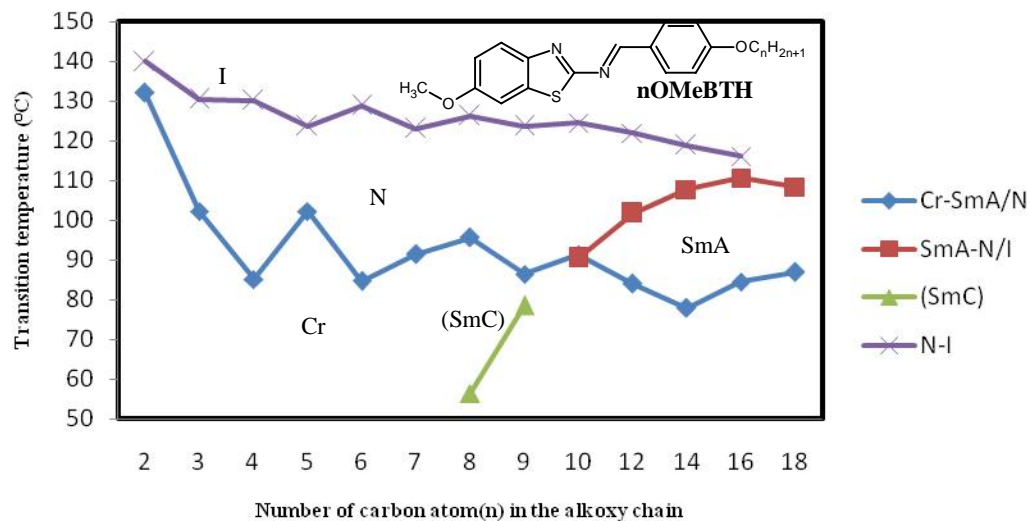


Figure 5.12: Plot of clearing temperature (°C) versus the carbon atoms (n) in alkoxy chain of homologous series nOMeBTH.

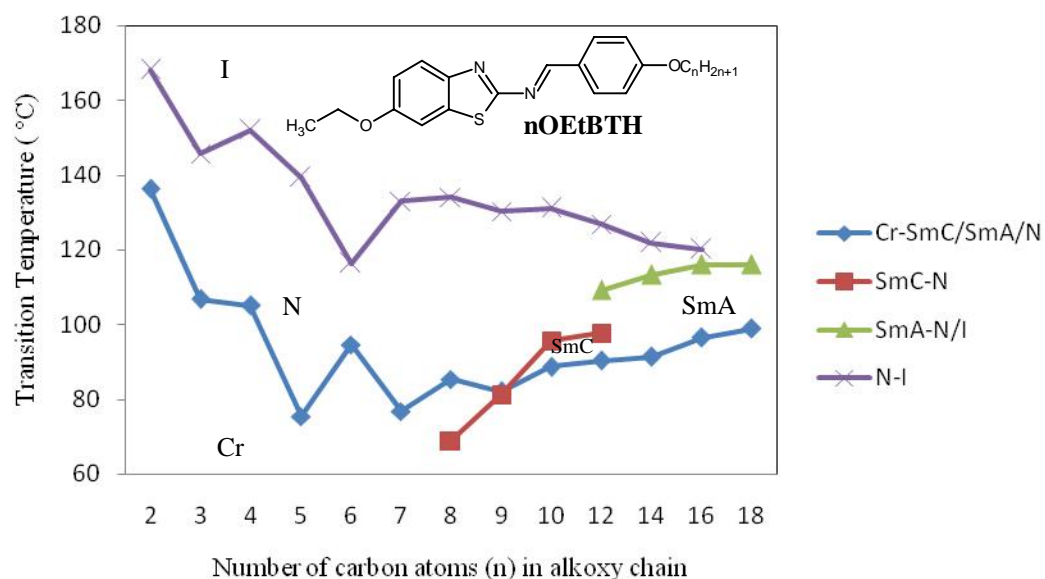


Figure 5.13: Plot of clearing temperature (°C) versus the carbon atoms (n) in alkoxy chain of homologous series nOEtBTH.

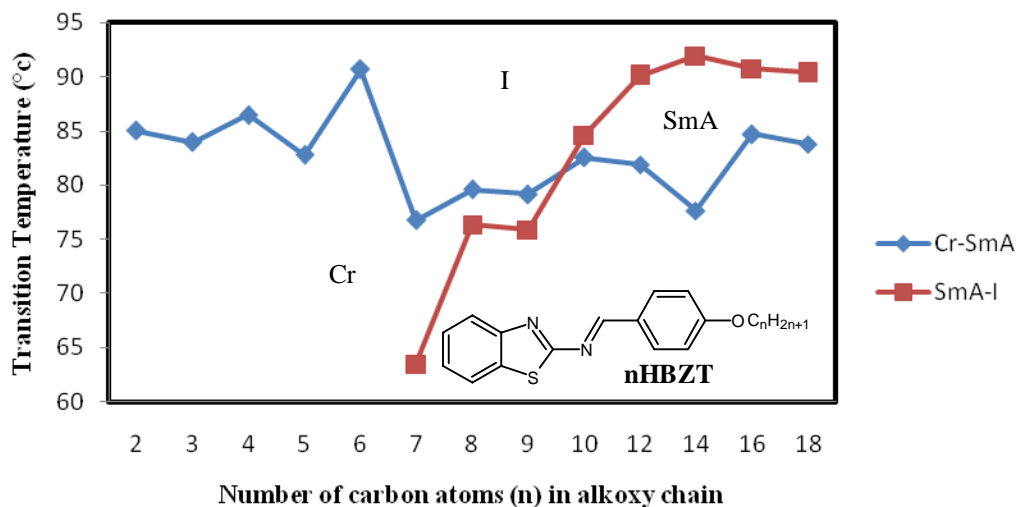


Figure 5.14: Plot of clearing temperature ($^{\circ}\text{C}$) versus the carbon atoms (n) in alkoxy chain of homologous series nHBZT.

5.1.2 XRD Study

5.1.2.1 XRD Study of nMeBTH, nOMeBTH, nOEtBTH and nHBZT

XRD analysis was conducted on **16MeBTH**, **18OMeBTH**, **14OEtBTH** and **18HBZT** in order to further identify the presence of SmA phase in the compounds. The XRD diffractograms of **16MeBTH**, **18OMeBTH**, **14OEtBTH** and **18HBZT** are depicted in Figures 5.15, 5.16, 5.17 and 5.18, respectively, while the XRD data was summarized in Tables 5.5, 5.6, 5.7 and 5.8, respectively.

Generally, a smectic, nematic or cholesteric structure has a broad peak associated with lateral packing at $2\theta \approx 16\text{-}21^{\circ}$ in a wide angle XRD curve. A sharp and strong peak at a low angle ($1^{\circ} < 2\theta < 6^{\circ}$) in a small angle X-ray scattering

curve can be observed for smectic structures, but it cannot be seen for nematic and cholesteric structures (Wang *et al.*, 2007).

From XRD pattern of **16MeBTH**, it has been revealed that the single sharp diffraction peak appeared at 1.605° indicating the presence of layered structure of smectic phase. When the reflection between the SmA layer corresponds to d approximate to L , the SmA arrangement is known as monolayer (Liao *et al.*, 2008). However, if the d -layer spacing is in between L and $2L$ then it is known as partial bilayer phase (Majumdar *et al.*, 2009). According to XRD data, the d -layer spacing was found to be 37.90 \AA . The layer spacing is much smaller than the molecular length and the d/L ratio was found to be 1.12. By combining the data from POM and XRD, it is confirmed that compound **16MeBTH** exhibited SmA phase (Wang *et al.*, 2008). It can be seen that the layer spacing d , is significantly larger than the calculated molecular length. This proved that the partial bilayer structure occurred between smectic layers (Reddy and Sadashiva, 2004).

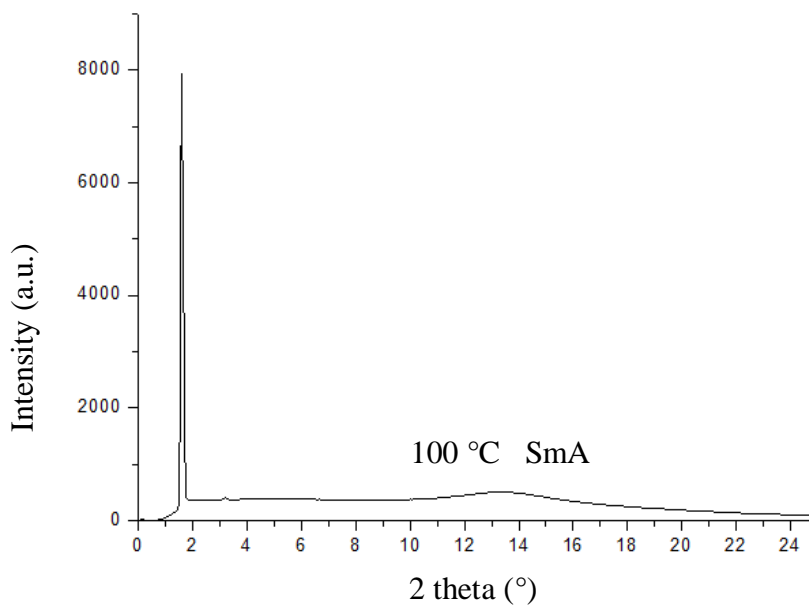


Figure 5.15: XRD diffractogram of compound 16MeBTH.

Table 5.5: Powder XRD data of 16MeBTH

2 theta (°)	1.605
d-spacing	37.9Å
<i>L</i>	33.579Å
<i>d/L</i>	1.12
Phase	SmA
Arrangement	Partial bilayer arrangement

From XRD pattern of **18OMeBTH**, the single sharp diffraction peak appeared at 1.52° indicating the presence of layered structure of smectic phase. According to XRD data, the *d*-layer spacing was found to be 41.49 Å, where the molecular length is 37.612 Å. The *d/L* ratio was found to be 1.10. Hence, SmA phase in **18OMeBTH** was suggested to afford partial bilayer arrangement. The presence of the SmA phase is concluded and supported by the texture studies (Wang *et al.*, 2008).

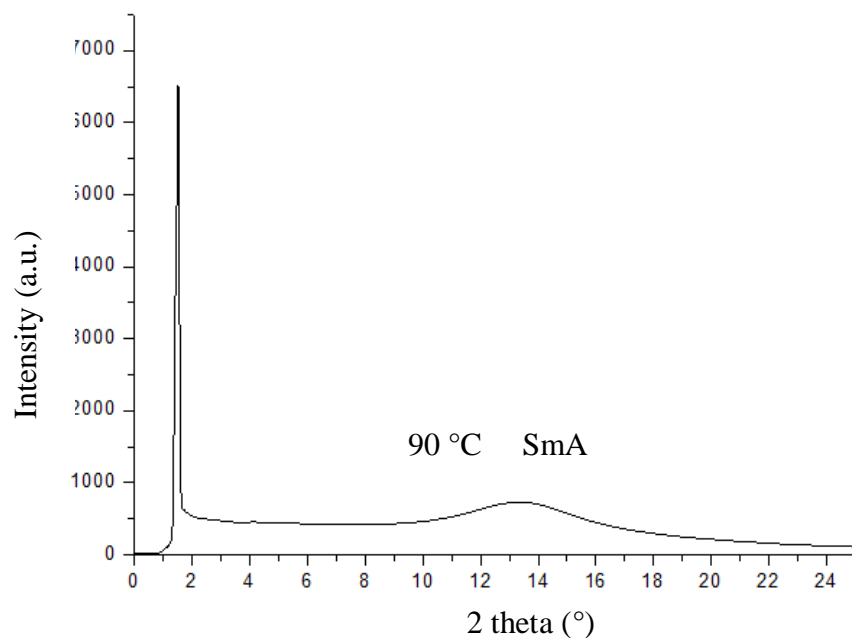


Figure 5.16: XRD diffractogram of compound 18OMeBTH.

Table 5.6: Powder XRD data of 18OMeBTH

2 theta (°)	1.52
<i>d</i> -spacing	41.49Å
<i>L</i>	37.612Å
<i>d/L</i>	1.10
Phase	SmA
Arrangement	Partial bilayer arrangement

The X-ray diffraction pattern of **14OEtBTH** in the mesophase at 121 °C on heating consists of one sharp peak at 1.74 Å. In higher-angle region a broad diffuse scattering indicates the liquid-like order of the molecules within the layers (Huang and Ma, 2010). The *d*-spacing (33.7 Å) is approximate to the calculated molecular length, *L* (33.89 Å). Since the *d/L* ratio is lower to 1, thus, it was said to correspond to the monolayer arrangement of the smectic A phase in compound **14OEtBTH** (Liao *et al.*, 2008).

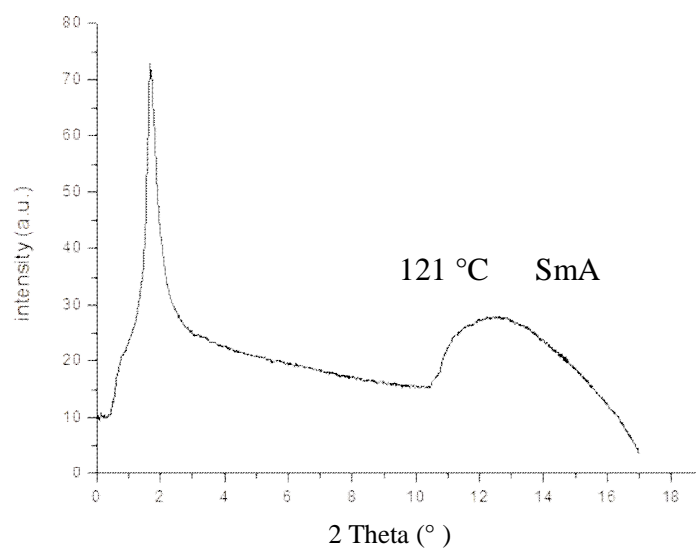


Figure 5.17: XRD diffractogram of compound 14OEtBTH.

Table 5.7: Powder XRD data of 14OEtBTH

2 theta (°)	1.74
d-spacing	33.7 Å
<i>L</i>	33.89 Å
<i>d/L</i>	0.98
Phase	SmA
Arrangement	monolayer arrangement

From XRD diffraction pattern of **18HBZT**, a single sharp diffraction peak was formed at 1.05° indicating the layered structure for liquid crystal phase (Zhang *et al.*, 1997). The *d/L* ratio was found to be 1.09. SmA phase in **18HBZT** was confirmed to afford partial bilayer arrangement.

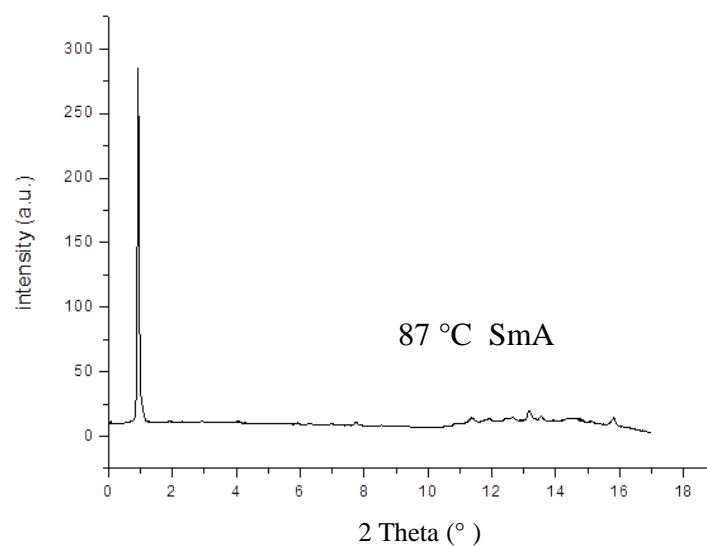


Figure 5.18: XRD diffractogram of compound 18HBZT.

Table 5.8: Powder XRD data of 18HBZT

2 theta (°)	1.05
d-spacing	32.25 Å
<i>L</i>	29.57 Å
<i>d/L</i>	1.09
Phase	SmA
Arrangement	Partial bilayer arrangement

5.2 Series 2: Mesomorphic Properties of 6-Methyl-2-[4-(4-alkoxybenzoyloxy)benzylidenamino]benzothiazoles (**nMe3R**), 6-methoxy-2-[4-(4-alkoxybenzoyloxy)benzylidenamino]benzothiazoles (**nOMe3R**) and 2-[4-(4-alkoxybenzoyloxy)benzylidenamino]benzothiazoles (**nHB3R**)

5.2.1 Optical and Thermal Studies

The associated enthalpy changes and transition temperatures during heating and cooling scans of series **nMe3R**, **nOMe3R** and **nHB3R** were determined using DSC analysis and the results are summarized in Tables 5.9, 5.10 and 5.11, respectively.

All compounds of **nMe3R** and **nOMe3R** in cooling cycle showed no different exothermic peaks during cooling scan. It is resulting from the partial decomposition of the compounds, thus, no cooling data can be obtained (Marin *et al.*, 2009). The decomposition temperatures were further verified by thermogravimetric analysis (TGA). For compound **14Me3R**, the first peak should be resulted of transition from one crystal (Cr_1) to another crystal form (Cr_2) because its enthalpy is smaller than that of the second peak (Figure 5.19). Figure 5.20 illustrates the TGA curves for compound **14Me3R**. It was found that the onset value (239.32 °C) and is relatively close to the clearing point obtained from DSC analysis (216.53 °C). Therefore, it is believed that partial decomposition occurred and no exothermic peak can be detected on cooling scan (Ha *et al.*, 2010a).

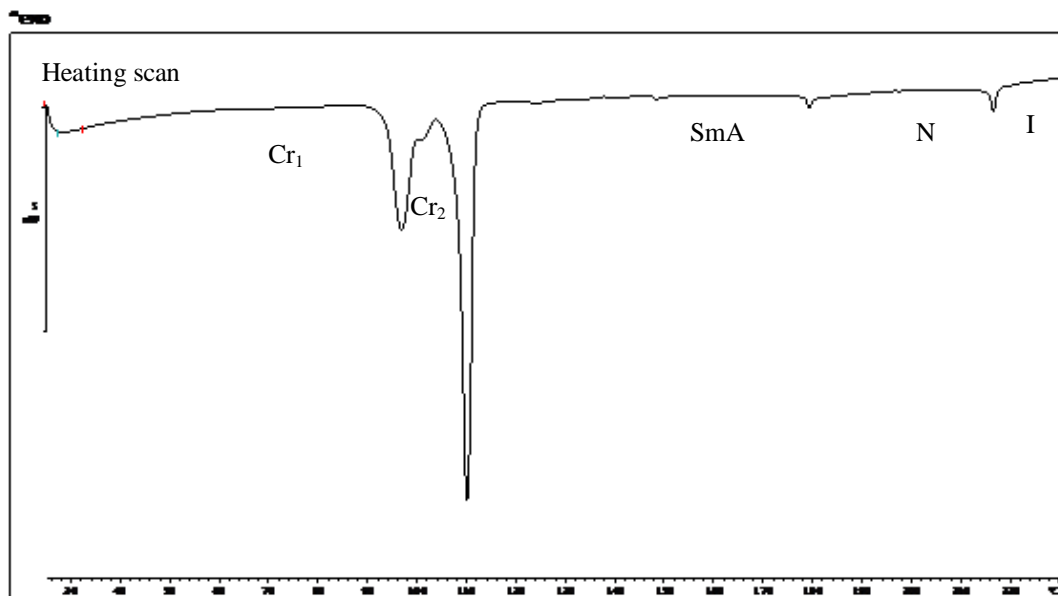


Figure 5.19: DSC thermogram of compound 14Me3R.

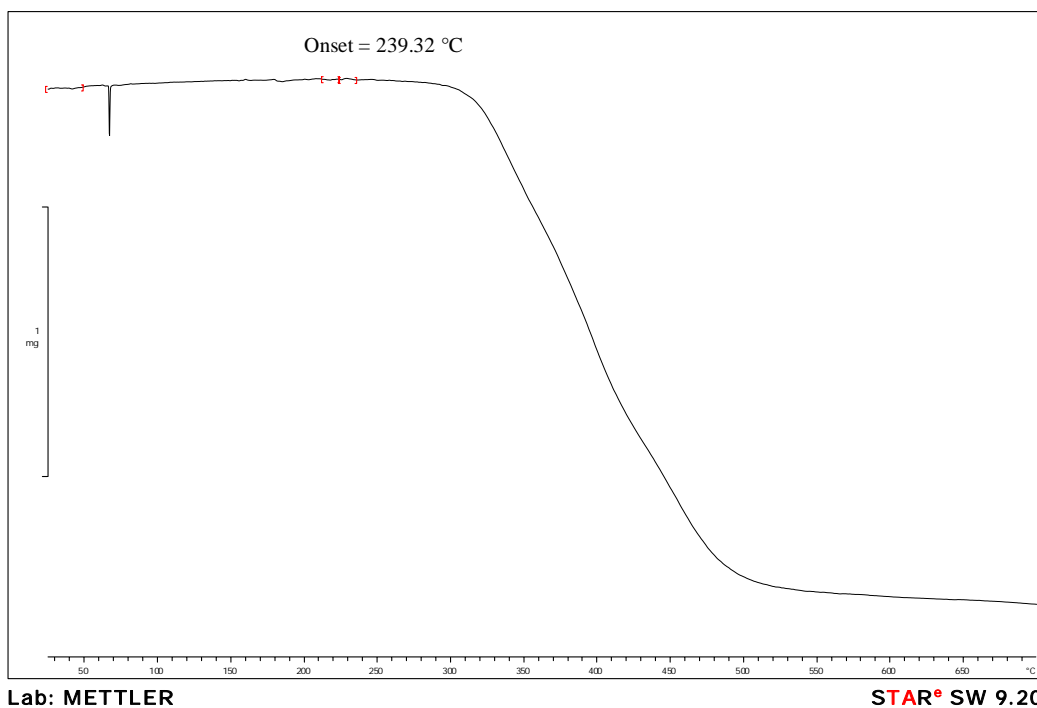


Figure 5.20: Thermogravimetric analysis curves of 14Me3R.

Figures 5.21 and 5.22 illustrate the DSC thermogram and TGA curves for compound **10OMe3R**. It was found that the onset value (244.90 °C) and is

relatively close to the clearing point obtained from DSC analysis (225.88 °C). Therefore, the partial decomposition occurred and no exothermic peak can be detected on cooling scan (Ha *et al.*, 2010a).

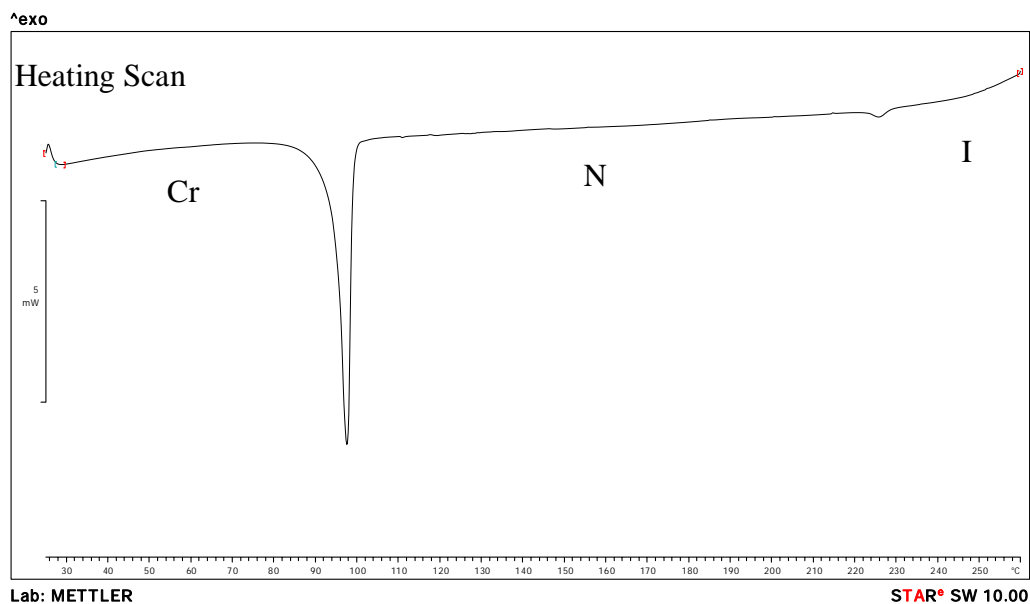


Figure 5.21: DSC thermogram of compound 10OMe3R.

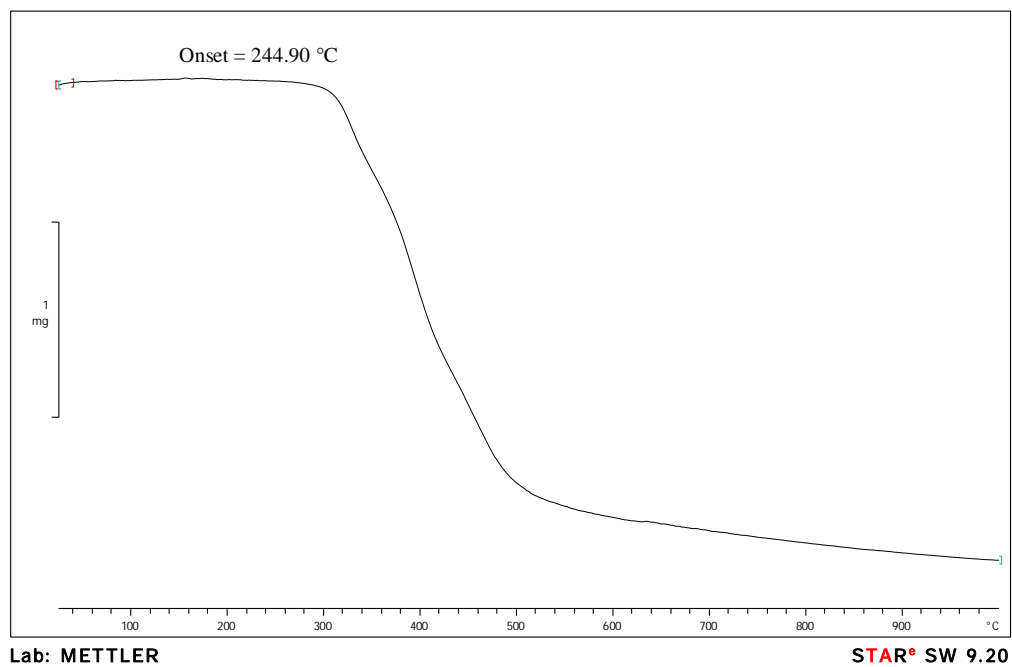
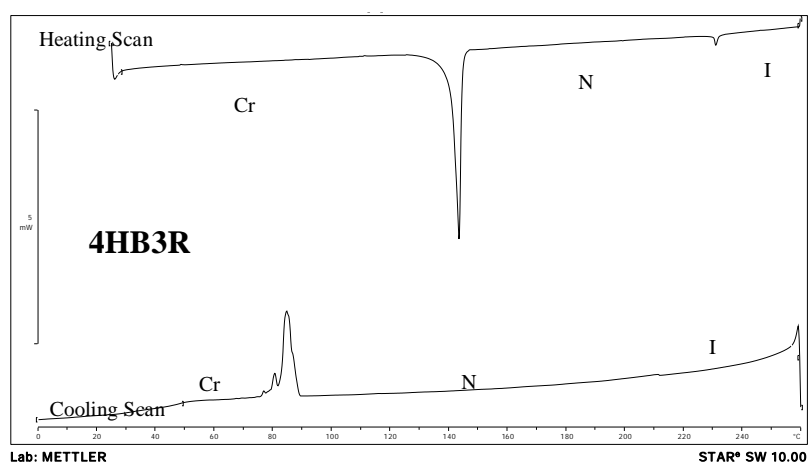
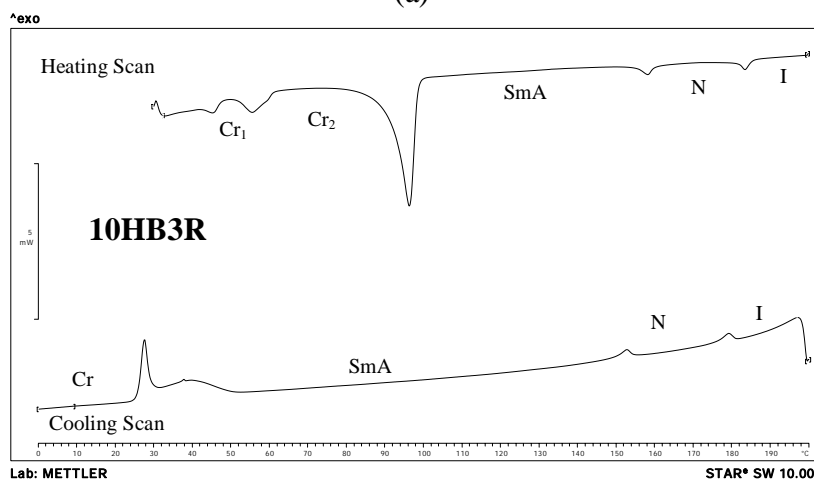


Figure 5.22: Thermogravimetric analysis curves of 10OMe3R.

The DSC thermograms of **4HB3R** and **10HB3R** are display in Figure 5.23. Both compounds exhibited enantiotropic liquid crystal properties. For **4HB3R**, due to the baseline is relatively flat, there is total of three transition peaks can be observed in each scan which are the transition of Cr-SmA, SmA-N and N-I. Besides, the smectogenic compound **10HB3R** only exhibited two transition peaks which are Cr-SmA, SmA-N and N-I in its DSC thermograms.



(a)



(b)

Figure 5.23: DSC thermogram of 4HB3R (a) and 10HB3R (b) during heating and cooling scan.

Table 5.9: Phase transition temperatures and associated enthalpy changes of series nMe3R[#]

Compound	Transition Temperatures, °C (ΔH , kJmol ⁻¹)	Heating Cooling
2Me3R	Cr ₁ 38.80 (2.57) Cr ₂ 168.04 (34.96) I	
3Me3R	Cr ₁ 121.99 (3.31) Cr ₂ 154.44 (46.17) I	
4Me3R	Cr 136.91 (43.93) I	
5Me3R	Cr ₁ 122.91 (5.46) Cr ₂ 142.54 (27.70) N 243.41 (3.94) I	
6Me3R	Cr ₁ 121.73 (30.02) Cr ₂ 140.84 (35.18) N 255.14 (26.97) I	
7Me3R	Cr ₁ 116.99 (12.56) Cr ₂ 146.41 (41.89) N 241.53 (25.78) I	
8Me3R	Cr ₁ 98.45 (2.95) Cr ₂ 129.69 (32.74) N 226.23 (1.67) I	
9Me3R	Cr ₁ 97.25 (7.77) Cr ₂ 131.60(29.99) N 219.29 (8.98) I	
10Me3R	Cr ₁ 94.09 (17.88) Cr ₂ 123.78 (26.85) N 221.68 (0.64) I	
12Me3R	Cr ₁ 81.53 (8.18) Cr ₂ 111.08 (29.10) SmC 162.98 (0.65) N 218.08 (1.16) I	
14Me3R	Cr ₁ 96.66 (12.36) Cr ₂ 109.79 (25.42) SmC 179.48 (0.36) N 216.53 (0.86) I	
16Me3R	Cr ₁ 86.43 (27.34) Cr ₂ 104.24 (32.48) SmA 179.2 (1.26) N 198.71 (1.23) I	
18Me3R	Cr ₁ 77.74 (6.50) Cr ₂ 108.01 (28.69) I	

[#]No cooling data

Table 5.10: Phase transition temperatures and associated enthalpy changes of series nOMe3R[#]

Compound	Transition Temperatures, °C (ΔH , kJmol ⁻¹)	Heating Cooling
2OMe3R	Cr 116.5 (29.79)	I
3OMe3R	Cr 179.2 (30.30)	I
4OMe3R	Cr ₁ 82.62 (4.80) Cr ₂ 136.9(29.79) N 257.99 (0.47)	I
5OMe3R	Cr 129.06 (27.13) N 246.20 (1.01)	I
6OMe3R	Cr 118.75 (41.14) N 243.44 (25.87)	I
7OMe3R	Cr ₁ 60.04 (7.54) Cr ₂ 124.51 (27.08) N 238.16 (14.35)	I
8OMe3R	Cr ₁ 87.47 (7.73) Cr ₂ 126.97 (29.01) N 233.77 (1.67)	I
9OMe3R	Cr 116.82 (36.31) N 237.95 (1.10)	I
10OMe3R	Cr 97.34 (45.77) N 225.88 (0.99)	I
12OMe3R	Cr 75.69 (36.83) SmC 126.75 (0.18) N 205.65 (0.55)	I
14OMe3R	Cr ₁ 42.75 (8.44) Cr ₂ 80.76 (29.52) SmC 139.72 (0.58) N 183.22 (0.93)	I
16OMe3R	Cr 67.98 (68.43) SmA 101.33 (5.46)	I
18OMe3R	Cr 66.61 (50.66) SmA 92.32 (2.13)	I

[#]No cooling data

Table 5.11: Phase transition temperatures and associated enthalpy changes of series nHB3R

Compound	Transition Temperatures, °C (ΔH , kJmol ⁻¹)	Heating Cooling
2HB3R	Cr ₁ 56.51 (10.17) Cr ₂ 167.01 (37.07) N 216.85 (1.35) I <i>Cr₁ 55.02 (8.84) Cr₂ 104.30 (15.25) N 116.21 (0.45) I</i>	
3HB3R	Cr 134.79 (35.57) N 234.14 (0.82) I <i>Cr 91.90 (24.03) N 220.10* I</i>	
4HB3R	Cr 143.38 (31.14) N 231.10 (0.77) I <i>Cr 84.88 (19.80) N 211.24 (0.39) I</i>	
5HB3R	Cr 113.47 (32.64) N 222.01 (0.73) I <i>Cr 74.77 (24.34) SmA 86.75 (0.40) N 218.54 (0.80) I</i>	
6HB3R	Cr 110.04 (43.74) SmA 123.86 (2.30) N 209.25 (0.85) I <i>Cr 56.00 (18.84) SmA 152.01* N 197.49 (0.42) I</i>	
7HB3R	Cr 107.16 (35.53) SmA 139.88 (0.36) N 212.28 (0.70) I <i>Cr 72.97 (20.79) SmA 136.52 (0.29) N 209.80 (0.90) I</i>	
8HB3R	Cr ₁ 50.23 (2.66) Cr ₂ 95.36 (21.94) SmA 128.43 (0.47) N 171.78 (0.81) I <i>Cr 16.26 (3.34) SmA 105.09 (0.44) N 141.05 (0.18) I</i>	
9HB3R	Cr 97.25 (26.75) SmA 145.75 (1.14) N 176.92 (0.89) I <i>Cr 23.93 (12.57) SmA 139.19 (0.93) N 173.83 (0.71) I</i>	
10HB3R	Cr ₁ 56.70 (3.50) Cr ₂ 96.99 (28.99) SmA 157.83 (1.57) N 182.01 (1.25) I <i>Cr 26.59 (17.44) SmA 150.50 (1.32) N 176.78 (1.00) I</i>	
12HB3R	Cr 95.75 (40.17) SmA 164.63 (1.60) N 179.64 (1.13) I <i>Cr 47.29 (26.02) SmA 159.08 (1.13) N 173.41 (1.01) I</i>	
14HB3R	Cr 94.23 (43.06) SmA 173.89 (1.31) N 179.70 (0.64) I <i>Cr 49.14 (27.69) SmA 167.61 (1.08) N 173.53 (0.57) I</i>	
16HB3R	Cr ₁ 63.12 (7.49) Cr 94.77 (43.13) SmA 163.37 (3.81)I <i>Cr 65.55 (37.50) SmA 154.46 (3.27) I</i>	
18HB3R	Cr 70.80 (68.02) SmA 112.15(0.41) I <i>Cr 40.61 (56.66) SmA 91.27(6.16) I</i>	

*POM data

In optical study, the mesophase of all the compounds were identified under an optical polarizing microscope (POM) during heating and cooling cycles. For series **nMe3R**,

Compounds C₂-C₄, C₁₈ = non-mesomorphic

Compounds C₅-C₁₀ = Nematic phase

Compounds C₁₂-C₁₄ = SmC and nematic phases (Figure 5.24)

Compounds C₁₆ = SmA and nematic phases (Figure 5.25)

For series **nOMe3R**,

Compounds C₂-C₃ = non-mesomorphic

Compounds C₄-C₁₀ = Nematic phase (Figures 5.26).

Compound C₁₂-C₁₄ = SmC and nematic phases (Figures 5.27 and 5.28)

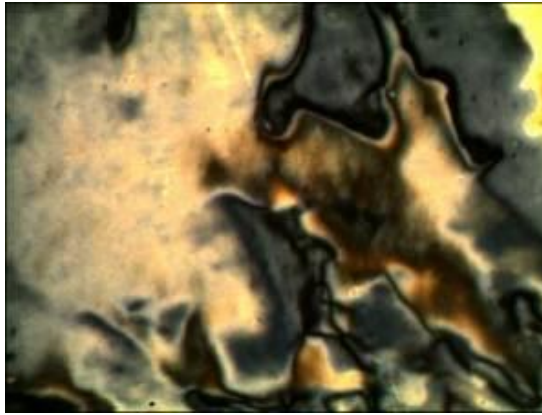
Compound C₁₆-C₁₈ = Sm A and nematic phases

For series **nHB3R**,

Compounds C₂-C₄ = Nematic phase

Compounds C₅-C₁₈ = SmA and nematic phases (Figures 5.29 and 5.30)

For **14Me3R**, a typical type of transition bars of SmC phase was observed during transition from nematic phase to *Schlieren* SmC phase. For **14OMe3R**, SmC phase with *Schlieren* texture was observed at lower temperature. When cooling from isotropic liquid phase of **16HB3R**, SmA phase was showed as *bâtonnet* texture (Figure 5.30a).



(a)



(b)



(c)

Figure 5.24: Optical photomicrographs of 14Me3R. (a) nematic phase with *Schlieren* texture and (b) typical transition bar of SmC phase during the transition from nematic to SmC phase. (c) SmC phase with *Schlieren* texture.

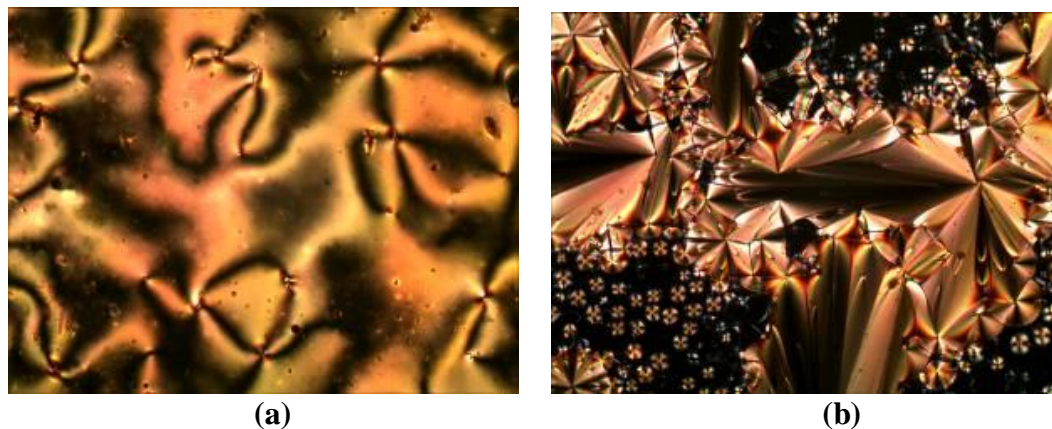


Figure 5.25: Optical photomicrographs of 16Me3R exhibiting (a) nematic phase with *Schlieren* texture with two and four-brushes defect during cooling cycle. On further cooling, (b) SmA phase with polygonal fan shaped texture was observed together with homeotropic area (dark area).

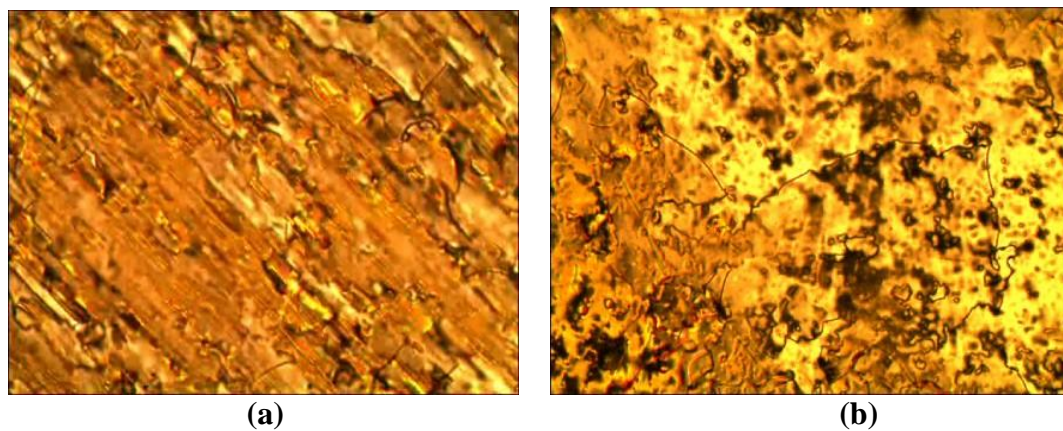


Figure 5.26: Optical photomicrographs of typical marble texture of nematic phase exhibited by (a) 6OMe3R and (b) 8OMe3R.

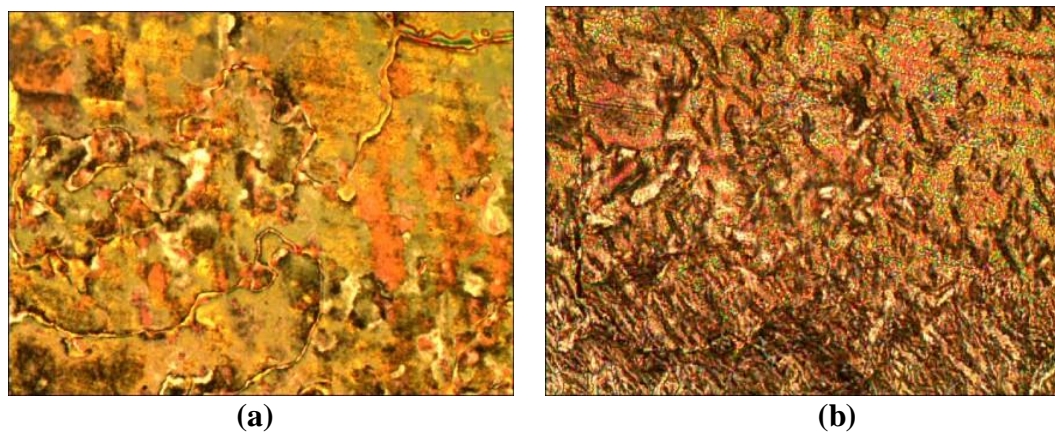


Figure 5.27: Optical photomicrographs of 12OMe3R exhibiting (a) marble texture and (b) transition bar of SmC phase appeared from bottom to top during the transition from nematic to SmC phase.

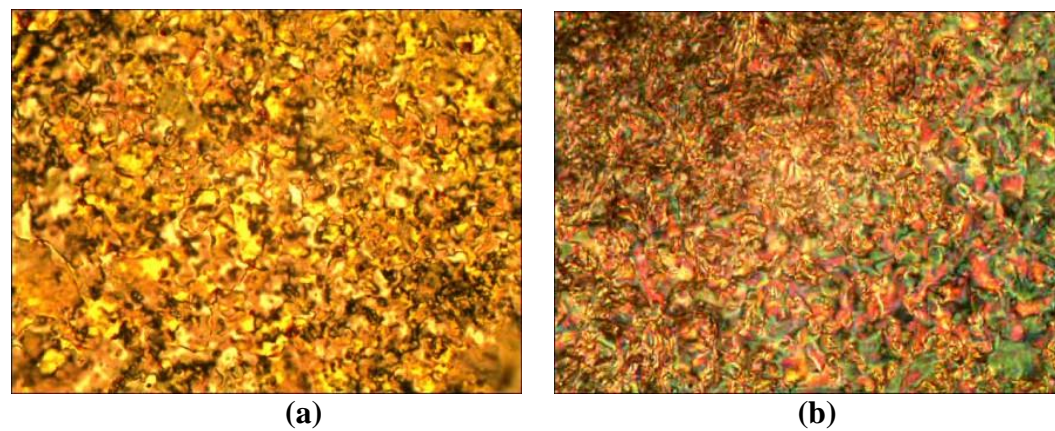


Figure 5.28: Optical photomicrographs of 14OMe3R exhibiting (a) *Schlieren* texture and (b) transition bar of SmC phase appeared from right to left during the transition from nematic to SmC phase.

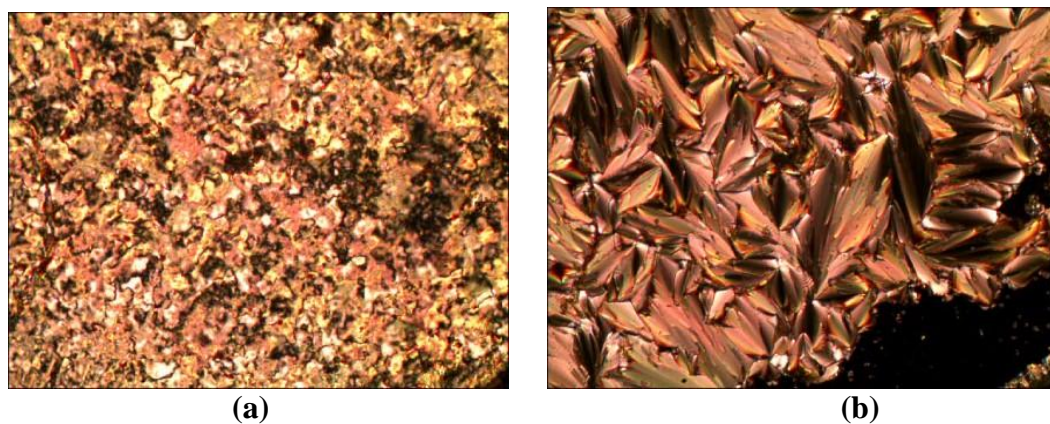


Figure 5.29: Optical photomicrographs of 10HB3R exhibiting (a) nematic phase with thread-like texture and (b) SmA phase with fan-shaped and a homeotropic (dark area) texture was observed.

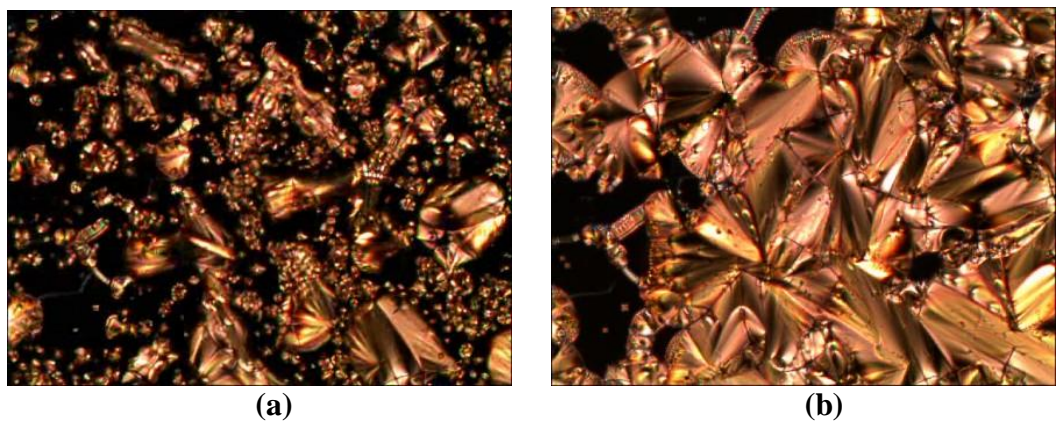


Figure 5.30: Optical photomicrographs of SmA phase emerged as *bâtonnet* upon cooling from isotropic liquid exhibited by 16HB3R (b) SmA phase with fan-shaped and homeotropic (dark area) textures was observed.

A plot which discusses the mesomorphic properties, transition temperatures and the influences of number of carbons in the alkoxy chains for series **nMe3R**, **nOMe3R** and **nHB3R** are given in Figures 5.31, 5.32 and 5.33, respectively.

For series **nMe3R** and **nOMe3R**, it is clearly noticed that no odd-even effect was observed. The short chain members ($n = 2, 3, 4$) are non-mesogen due to the high rigidity in their molecules structure thus there are not favouring to mesophase formation (Colling and Hird, 1997b). However, the odd-even effect on melting temperature of series **nHB3R** was clearly observed for short carbon chains compounds ($n = 2, 3, 4$). For series **nMe3R**, when the terminal chain increased from C_5 to C_{10} members, the lengths of the carbons are available for exhibiting nematic phase. As the carbon chain increased further from C_{12} to C_{16} members, the enantiotropic liquid crystal (smectic phase) was induced. This phenomenon is similar to the analogues reported by Yeap *et al.* (2006a).

In series **nMe3R** and **nOMe3R**, the smectic C phase range showed increased from C_{12} to C_{14} members which is because of the increasing of *van der Waals* forces resulted from the lengthening of alkoxy chain. For series **nHB3R**, as the carbon chain length increased to C_5 member, monotropic (metastable) SmA mesophase was noticeable during cooling scan. When the carbon chains reached a certain length, ($n \geq 6$), enantiotropic SmA mesophase which followed the nematic mesophase at higher temperature was prompted. A wide range nematic phase ($131.79\text{ }^\circ\text{C}$) is shown by C_5 derivative and this stability of the nematic phase is the highest of all compounds in series **nHB3R**. The SmA mesophase range ascending

from C₁₂ member (159.08 °C) to C₁₄ member (167.61 °C) and then reduced from C₁₆ (163.37 °C) to C₁₈ (112.15 °C). If the carbon chain length keeps increasing, it may produce a monotropic mesophase or even totally diminished the liquid crystalline formation (Ha *et al.*, 2009b)

The melting temperature of compounds **nMe3R**, **nOMe3R** and **nHB3R** decreased steadily with increasing carbon chains. However, the clearing temperature showed similar trend as melting temperature which is decreased with the raise in the carbon chain length. The falling trend of clearing temperatures has also been encountered by three-ring benzothiazole mesogen (Prajapati and Bonde, 2006b).

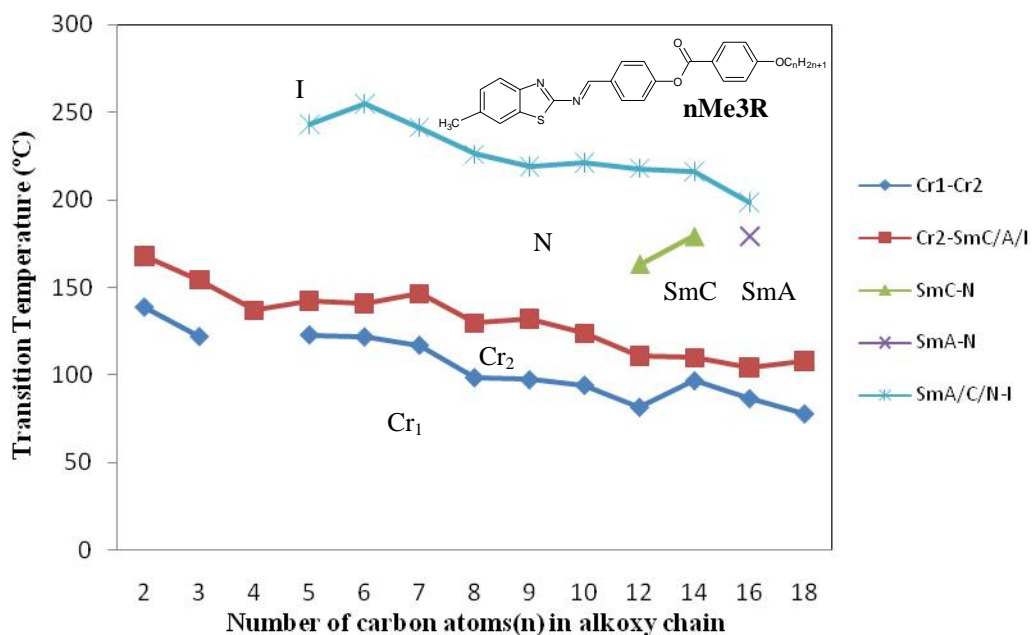


Figure 5.31: Plot of clearing temperature (°C) versus the carbon atoms (n) in alkoxy chain of homologous series **nMe3R**.

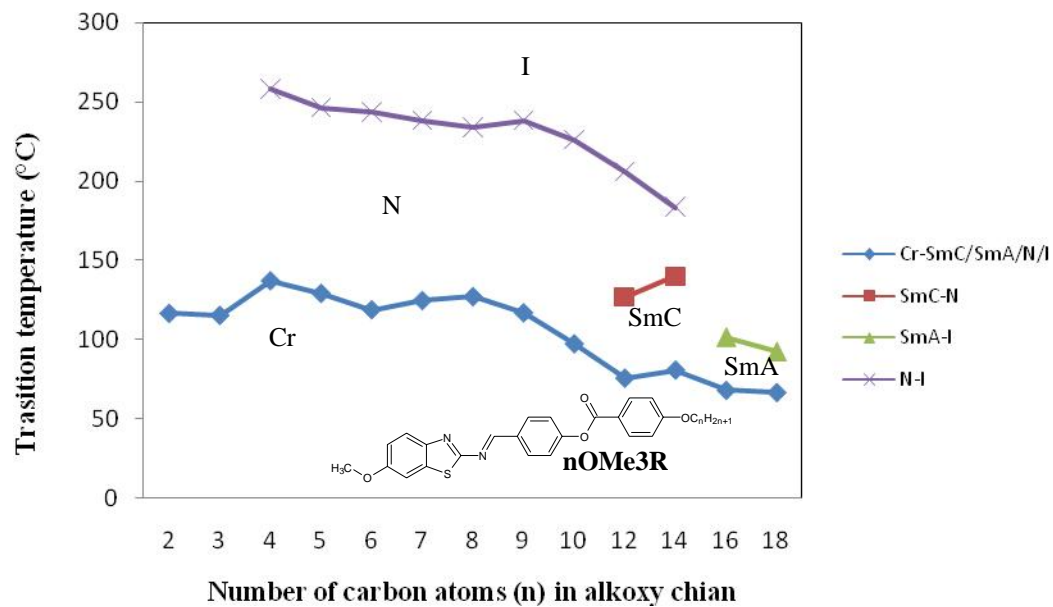


Figure 5.32: Plot of clearing temperature ($^{\circ}\text{C}$) versus the carbon atoms (n) in alkoxy chain of homologous series nOMe3R.

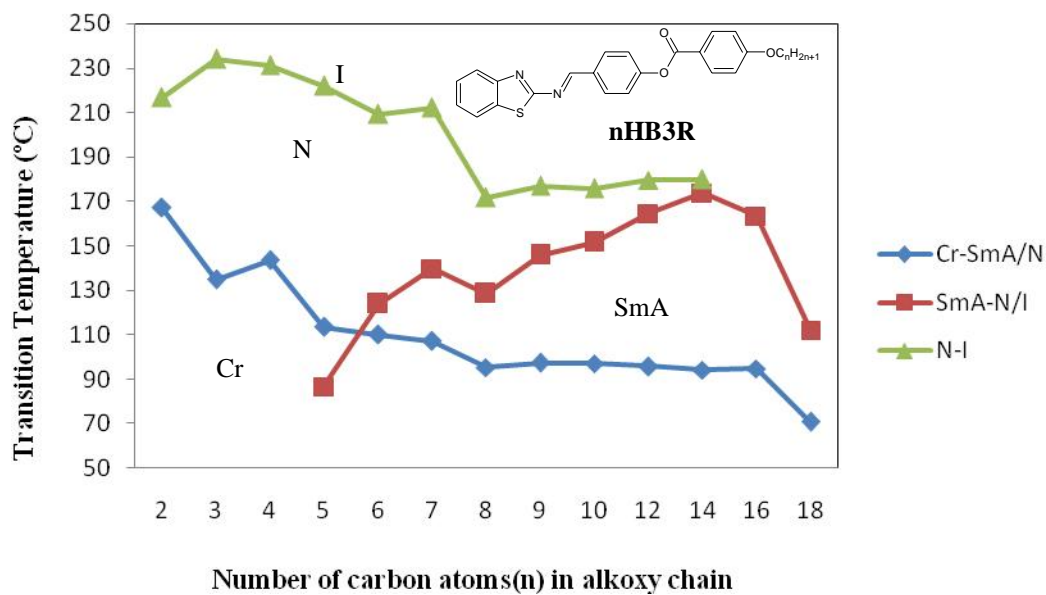


Figure 5.33: Plot of clearing temperature ($^{\circ}\text{C}$) versus the carbon atoms (n) in alkoxy chain of homologous series nHB3R.

5.2.2 XRD study

5.2.2.1 XRD Study of nMe3R, nOMe3R and nHB3R

XRD pattern of the representative compounds **16Me3R**, **14OMe3R** and **8HB3R** are shown in Figures 5.34, 5.35 and 5.36, respectively. The XRD data is summarized in Tables 5.12, 5.13 and 5.14, respectively.

In Figure 5.34, the diffraction pattern displays one intensity peak at lower region angle and a weak broad peak at wider angle. This diffraction pattern is typically characteristic of layer structure noticed for smectic phase (Wang *et al.*, 2007). The broad diffuse scattering maxima in the wide-angle region indicated a fluid like in-plane order with no long-range positional order within the smectic layers (Rao *et al.*, 2009). The XRD patterns of **16Me3R** shows a diffraction peak at 1.35° which implies the formation of a layered structure. In addition, wide angle diffuse peaks corresponding to a spacing value of 43.1 \AA in Figure 5.35 indicates that similar liquid-like in-plane orders with average intermolecular distances around 39.34 \AA are prevalent inside the smectic layers of compound **16Me3R** (Yang and Lin, 2006).

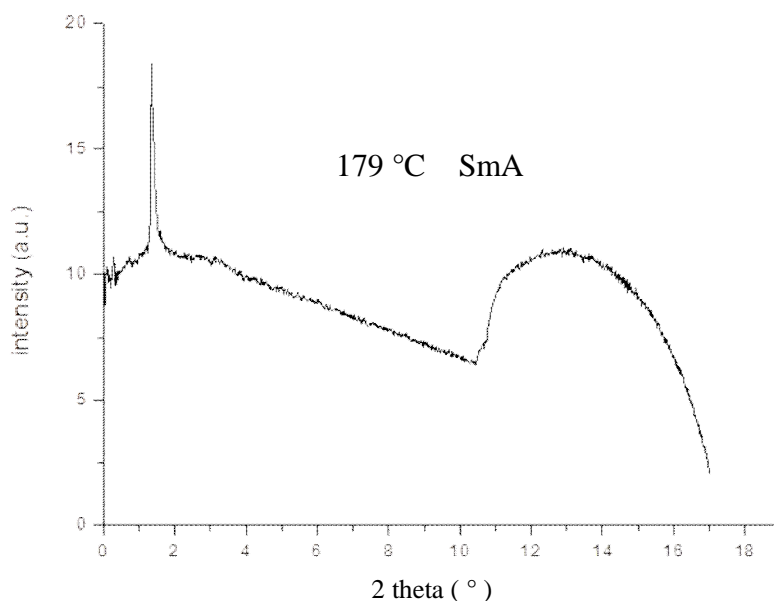


Figure 5.34: XRD diffractogram of compound 16Me3R.

Table 5.12: Powder XRD data of 16Me3R

2 theta (°)	1.35
<i>d</i> -spacing	43.1 Å
<i>L</i>	39.34 Å
<i>d</i> / <i>L</i>	1.10
Phase	SmA
Arrangement	Partial bilayer arrangement

In Figure 5.35, the existence of one sharp peak at lower region angle (1.43 °) has proved that the lamellar layer is present in the mesophase structure. The weak broad peak at wide angle region showed the liquid state of the mesophase (Yamaguchi *et al.*, 2004). Normally, *d*-layer spacing should be smaller than the molecular length *L* due to the tilted layer in the structural arrangement (Liao *et al.*, 2008). From the X-ray diffraction data, the *d*-layer spacing was found to be 41.2 Å

and it is much larger than the molecular length (37.51 Å) achieved by MM2 molecular calculation. The d/L ratio was calculated to be 1.10 and this verifies a tilted SmC phase is being noticed for **14OMe3R**. In addition, the presence of the SmC phase can be concluded by combining the observation of texture under POM analysis in which *Schlieren* texture of SmC phase was observed.

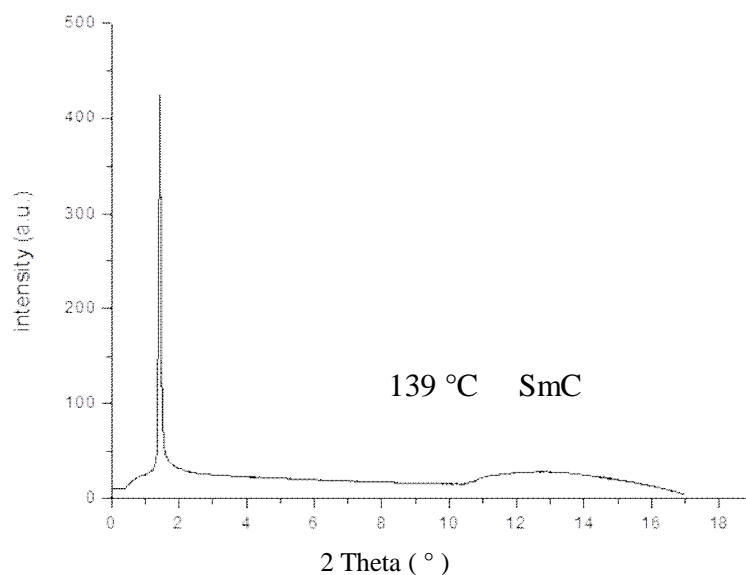


Figure 5.35: XRD diffractogram of compound 14OMe3R.

Table 5.13: Powder XRD data of 14OMe3R

2 theta (°)	1.43
d-spacing	41.2 Å
L	37.51 Å
d/L	1.10
Phase	SmC

The X-ray diffraction pattern obtained for **8HB3R** at 105 °C exhibited a sharp reflection with d -spacing in the SmA phase of about 31.5 Å in a low-angle region and a diffuse one in the wide-angle region was obtained for compound **8HB3R**. Molecular length was estimated from MM2 models, to be 29.52 Å for the compound. The small-angle region and a diffuse peak in the wide-angle region suggesting a tilted organization of molecules within the smectic layer (Yelamaggad *et al.*, 2006). The diffuse peak shows at high-angle region related to the short-range correlations between neighbouring molecules in each layer which is consistent with the liquid-like arrangement of the molecules within the smectic layers (Gallardo *et al.*, 2009).

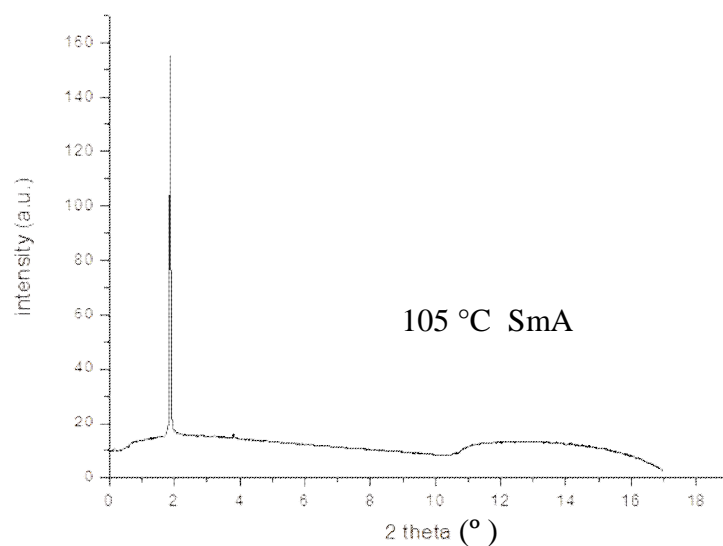


Figure 5.36: XRD diffractogram of compound 8HB3R.

Table 5.14: Powder XRD data of 8HB3R

2 theta (°)	1.87
d-spacing	31.5 Å
<i>L</i>	29.52 Å
<i>d/L</i>	1.07
Phase	SmA
Arrangement	monolayer arrangement

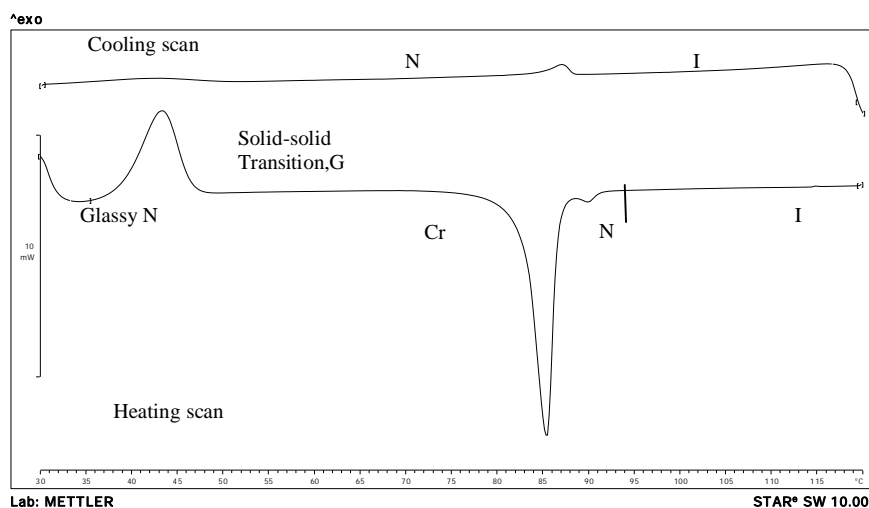
5.3 Series 3: Mesomorphic properties of 2-[3-Methoxy-(4-alkoxybenzoyloxy)phenyl]benzothiazoles (nMOBZT) and 2-[3-ethoxy-(4-alkoxybenzoyloxy)phenyl]benzothiazoles (nEOBZT)

5.3.1 Optical and Thermal studies

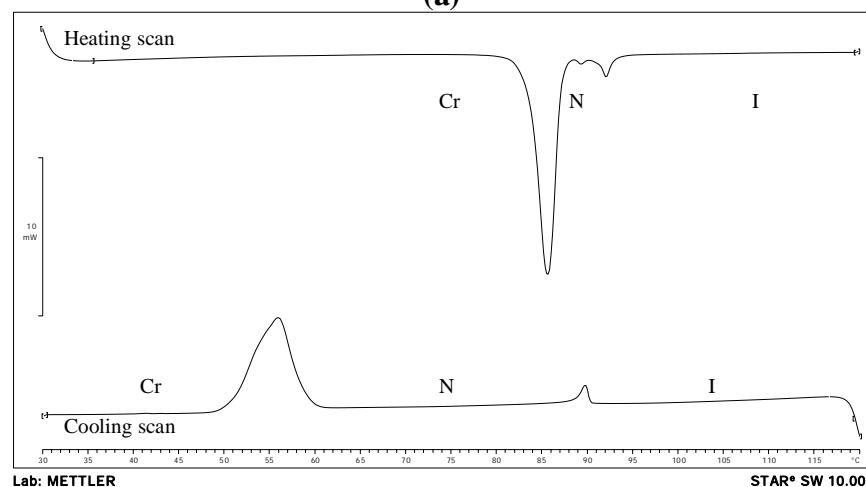
Associated enthalpy changes and transition temperature during heating and cooling scans of **nMOBZT** and **nEOBZT** are summarized in Tables 5.15 and 5.16, respectively.

The DSC thermograms shown in Figures 5.37 and 5.38 confirm the liquid crystalline transition temperatures of compounds **10MOBZT**, **14MOBZT**, **10EOBZT** and **16EOBZT**, respectively. For compounds **10MOBZT** and **10EOBZT**, the baseline of the thermogram during cooling scan is flat and a small sharp transition peak is observed with no thermal degradation. The relatively small isotropic–nematic peak is the characteristic of a nematic mesophase. A second order transition peak is observed on heating and cooling which are characterized of a glass transition temperature at 39 °C (**10MOBZT**) and 0 °C (**10EOBZT**) due to

a shift in the baseline. Crystallization occurs at 43.55 °C (**10MOBZT**) and 31.69 °C (**10EOBZT**), respectively during heating indicated to the solid-solid transition temperature is higher than glass transition temperatures (Aldred *et al.*, 2005a). The above phenomenon was also known as supercooling. This is usually attributed to the fact that the mesophase has the lowest transition temperature and so is easily frozen in a glassy state. Supercooling is a common, if not universal, feature of mesomorphic transition, particularly in case of the transition related to the crystal phase (Lu and Yang, 1991).

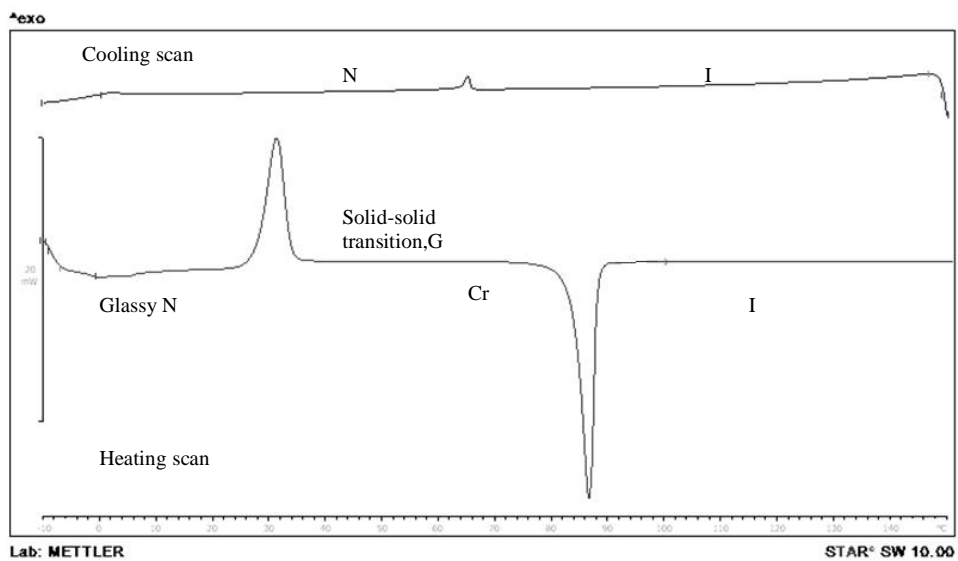


(a)

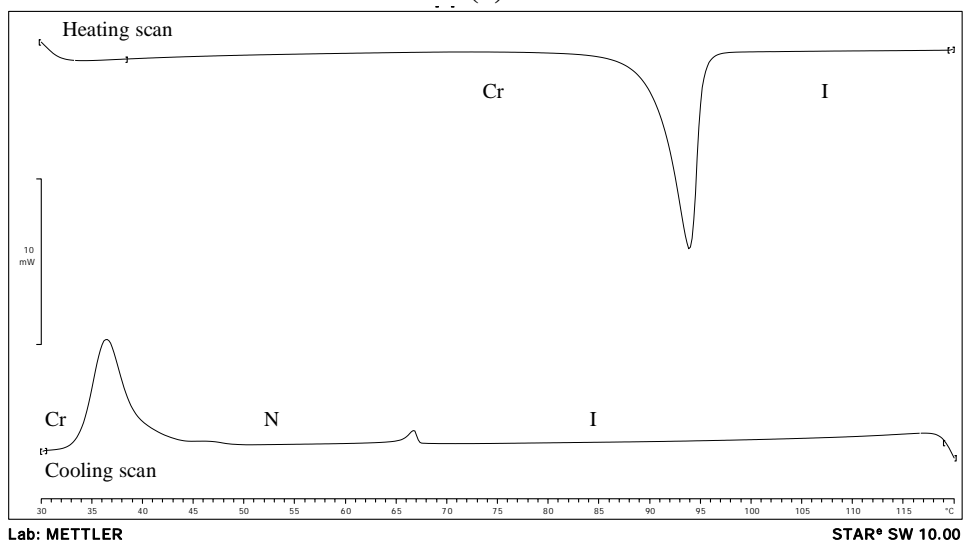


(b)

Figure 5.37: DSC thermogram of (a) 10MOBZT and (b) 14MOBZT during heating and cooling scans.



(a)



(b)

Figure 5.38: DSC thermogram of (a) 10EOBZT and (b) 16EOBZT during heating and cooling scans.

Table 5.15: Phase transition temperatures and associated enthalpy changes of series nMOBZT

Compound	Transition Temperatures, °C (ΔH , kJmol ⁻¹)	Heating Cooling
2MOBZT	Cr 141.16 (39.64) I Cr 118.90 (35.68) I	
3MOBZT	Cr 129.08 (44.33) I G 60.31 (2.88) N 93.31(0.81) I	
4MOBZT	Cr 124.69 (43.61) I G 53.85 (15.72) N 109.66 (1.08) I	
5MOBZT	Cr 103.23 (37.58) I G 64.29 (27.14) N 85.71 (0.86) I	
6MOBZT	Cr 91.36 (11.10) N 96.34 (0.16) I G 59.64 (19.85) N 93.68 (0.90) I	
7MOBZT	Cr 89.59 (19.07) I G 73.26 (18.99) N 87.31 (0.78) I	
8MOBZT	Cr 87.02 (41.74) N 95.83(4.10) I G 40.09 (12.78) N 87.91 (0.84) I	
9MOBZT	Cr 85.58 (57.33) I G 45.39 (19.94) N 86.17(1.27) I	
10MOBZT	Cr 83.73 (27.06) N 88.34 (1.14) I G 43.55 (9.19) N 87.87 (1.02) I	
12MOBZT	Cr 86.80 (28.35) N 92.88 (0.72) I G 37.02 (5.77) N 90.69 (1.21) I	
14MOBZT	Cr 86.80 (31.18) N 91.99 (1.33) I Cr 55.92 (28.37) N 89.77 (1.54) I	
16MOBZT	Cr 94.81 (41.42) I Cr 41.8 (32.82) N 89.24 (1.82) I	
18MOBZT	Cr 98.14 (47.56) I Cr 49.4 (40.50) N 85.64 (2.16) I	

G = Glassy state

Table 5.16: Phase transition temperatures and associated enthalpy changes of series nEOBZT

Compound	Transition Temperatures, °C (ΔH , kJmol ⁻¹)	Heating Cooling
2EOBZT	Cr 142.35 (35.10) I Cr 81.85 (21.14) I	
3EOBZT	Cr 140.93(47.79) I G 55.77 (17.81) N 51.06 (0.73) I	
4EOBZT	Cr 132.12 (38.09) I G 39.46 (15.32) N 68.34 (1.11) I	
5EOBZT	Cr 123.76 (52.70) I G 58.57 (35.67) N 49.69 (0.44) I	
6EOBZT	Cr 122.86 (38.55) I G 35.32 (20.27) N 64.69 (0.75) I	
7EOBZT	Cr 110.44 (37.62) I G 34.24 (18.84) N 60.83 (0.69) I	
8EOBZT	Cr 101.97 (50.17) I G 47.22 (20.74) N 56.27 (2.89) I	
9EOBZT	Cr 103.15 (37.04) I G 47.84 (33.59) N 59.80 (0.63) I	
10EOBZT	Cr 86.24 (39.04) I G 31.69 (26.98) N 65.24 (0.95) I	
12EOBZT	Cr 99.02 (42.46) I G 23.56 (17.96) N 68.67 (1.25) I	
14EOBZT	Cr 96.63 (38.25) I Cr 34.52 (26.15) N 66.91 (1.24) I	
16EOBZT	Cr 93.58 (62.26) I Cr 36.54 (39.71) N 66.57(1.59) I	
18EOBZT	Cr 96.71 (53.21) I Cr 50.76 (44.25) N 62.48 (1.30) I	

G = Glassy state

In optical study, the mesophase of entire synthesized compounds were identified under polarizing optical microscope (POM) during heating and cooling cycles. For series **nMOBZT**,

Compounds C₂ = non-mesomorphic

Compounds C₃-C₁₈ = Nematic phase (Figure 5.39)

Upon cooling the isotropic liquid of **6MOBZT** and **14MOBZT**, the nematic phase appeared as droplets and then coalesced to a nematic phase with disclination line and *Schlieren* texture.

For series **nEOBZT**,

Compounds C₂ = non-mesomorphic

Compounds C₃-C₁₈ = Nematic phase (Figure 5.40).

Upon cooling of **6EOBZT** and **12EOBZT**, nematic phase was also appeared as droplets nematic texture before coalesced to form *Schlieren* texture and nematic phase with disclination lines.

For short carbon members ($n \leq 12$), further cooling of the monotropic nematic phase does not result in crystallization, but to freeze the mesophase into a glass (glass transition state) (Six *et al.*, 2001). However, when the glassy mesophase is heated again, the remaining glass completely transformed to the crystalline state.

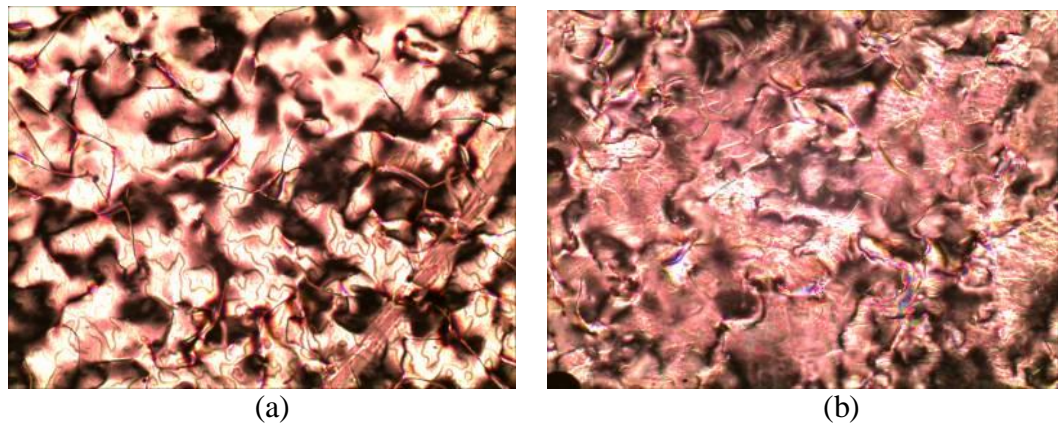


Figure 5.39: (a) Optical photomicrographs of nematic phase with disclination lines for 6MOBZT and (b) nematic phase with *Schlieren* texture upon cooling from isotropic liquid exhibited by 14MOBZT was observed.

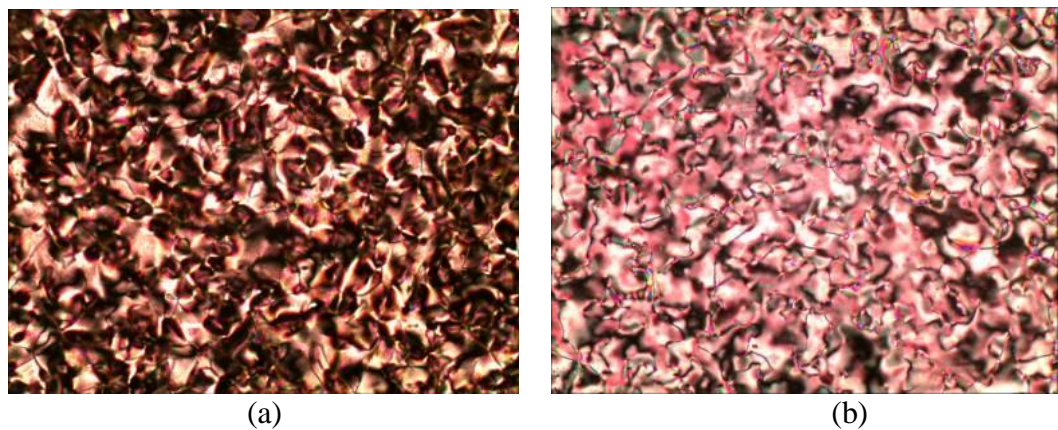


Figure 5.40: (a) Optical photomicrographs of nematic phase with *Schlieren* texture for 6EOBZT and (b) nematic phase with disclination lines upon cooling from isotropic liquid exhibited by 12EOBZT was observed.

A plot which discusses the mesomorphic properties, transition temperatures and the influences of number of carbons in the alkoxy chains for series **nMOBZT** and **nEOBZT** (Figures 5.41 and 5.42) enables the influences of the terminal chain on the mesomorphic properties to be studied.

First, it can be noticed that the odd-even effects influenced were distinct in this series but most of the compounds exhibited monotropic behaviours. All the compounds exhibited nematic mesophase except C_2 derivative is non-mesogen. For series **nMOBZT**, as the chain length increased to C_{10} member, an enantiotropic nematic phase was observed. This phenomenon only continued until C_{14} member. When the carbon chain length increased from C_{16} to C_{18} members, monotropic (metastable) nematic phase was observed.

Glass transition state was occurred in this series from C_3 until C_{12} members. Glassy state benzothiazole, which was prepared by cooling from the melt, did not recrystallize. However, it start transformed the remaining glass completely to the crystalline state when heat provided. Exothermic peak appeared during heating scan on DSC analysis. Given the fact that this transition was irreversible and decreased in enthalpy as a function of time, it is suggested that a monotropic solid-solid transition takes place (Six *et al.*, 2001). C_{10} member was found to stabilize the nematic phase (increased from 4.5 °C) to C_{12} member. By increased the flexibility to a certain lengths are necessary for promoting mesophase; however, keeps on increasing carbon chains length will lead to the molecule become too flexible, hence, reduced the stability or even completely diminish the mesophase.

Based on the graph of series **nEOBZT**, the liquid crystalline behaviours were strongly affected by the lateral ethoxyl group. The melting points show a decreasing trend from C₂ to C₁₀ and then increasing from the C₁₀ to C₁₂ derivatives. Gray has emphasized that an increased in molecular breadth reduces the length-to-breadth ratio, and the rod-like molecule has moved at least some way towards becoming a spherical system which is structurally unsuitable for liquid crystalline behaviour (Gray, 1962). The thermal stabilities of the compounds in series **nEOBZT** were likely to be low due to the ethoxy group occur along the side of the molecules and lead to any significant increase in the molecular breadth. The lateral ethoxyl group is generally known attribute to low liquid crystalline temperatures and the suppression of smectic phases due to the intermolecular forces of attraction, such as *van der Waals* interaction (Aldred *et al.*, 2005a). This direction was in good consensus with the homologous series of 4-n-alkoxy-2-hydroxybenzylidene-2'-naphthylamines reported by Prajapati and Bonde (2010b).

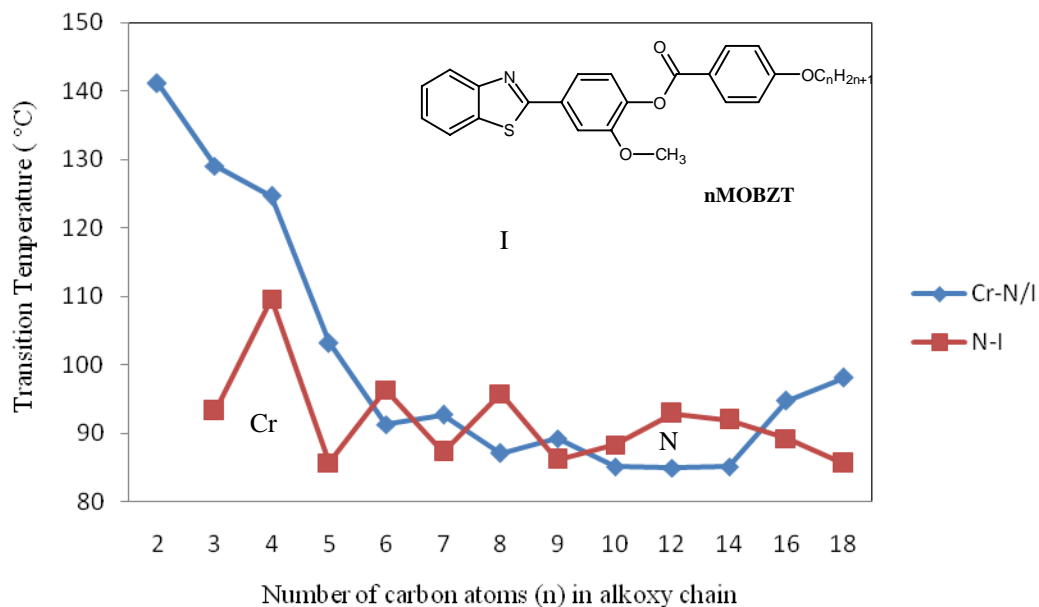
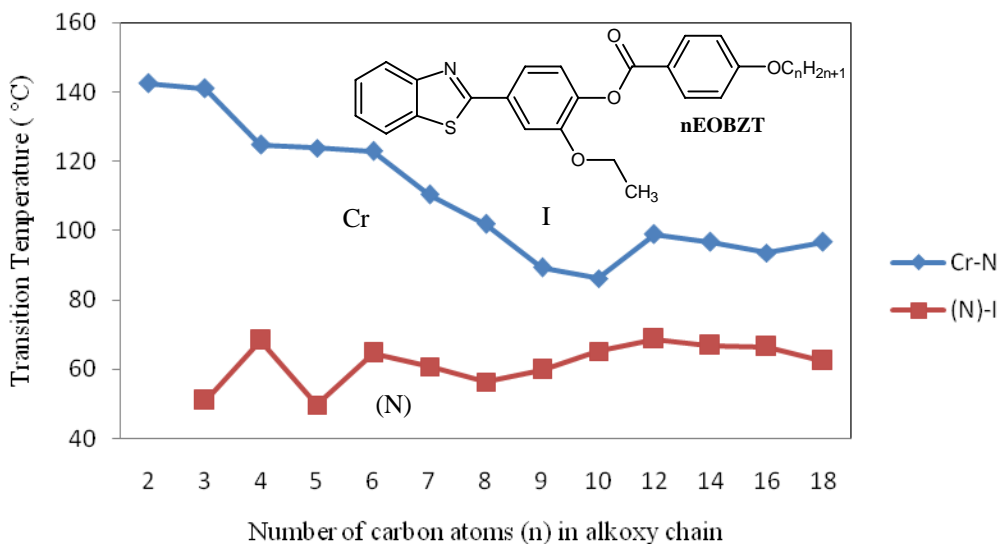


Figure 5.41: Plot of clearing temperature (°C) versus the carbon atoms (n) in alkoxy chain of homologous series nMOBZT.



(N) = monotropic nematic phase

Figure 5.42: Plot of clearing temperature (°C) versus the carbon atoms (n) in alkoxy chain of homologous series nEOBZT.

5.4 Series 4: Mesomorphic Properties of α,ω -bis[6-Methoxy-2-(4-alkoxybenzylidenamino)]benzothiazoles (**nOMeD**) and α,ω -bis[6-ethoxy-2-(4-alkoxybenzylidenamino)]benzothiazoles (**nOEtD**)

5.4.1 Optical and Thermal Studies

In thermal study, transition temperatures and associated enthalpy changes of **nOMeD** and **nOEtD** are summarized in Tables 5.17 and 5.18, respectively.

The DSC thermograms of **8OMeD** and **8OEtD** are shown in Figures 5.43 and 5.44, respectively. Both compounds exhibited liquid crystal properties. For **8OMeD**, there is total of two phase transitions can be observed in cooling scan which are due to the transition of I-N and N-Cr. However, for **8OEtD**, there are two endo- and exothermic peaks on its heating and cooling scans indicating the Cr-N, N-I transition and vice versa.

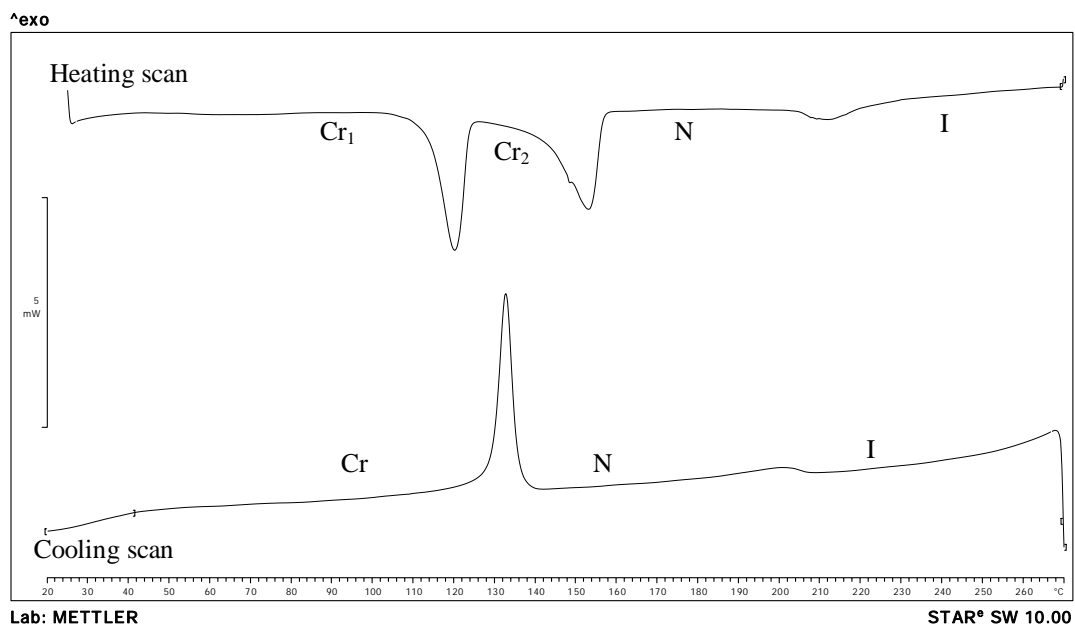


Figure 5.43: DSC thermogram of 8OMeD during heating and cooling scans.

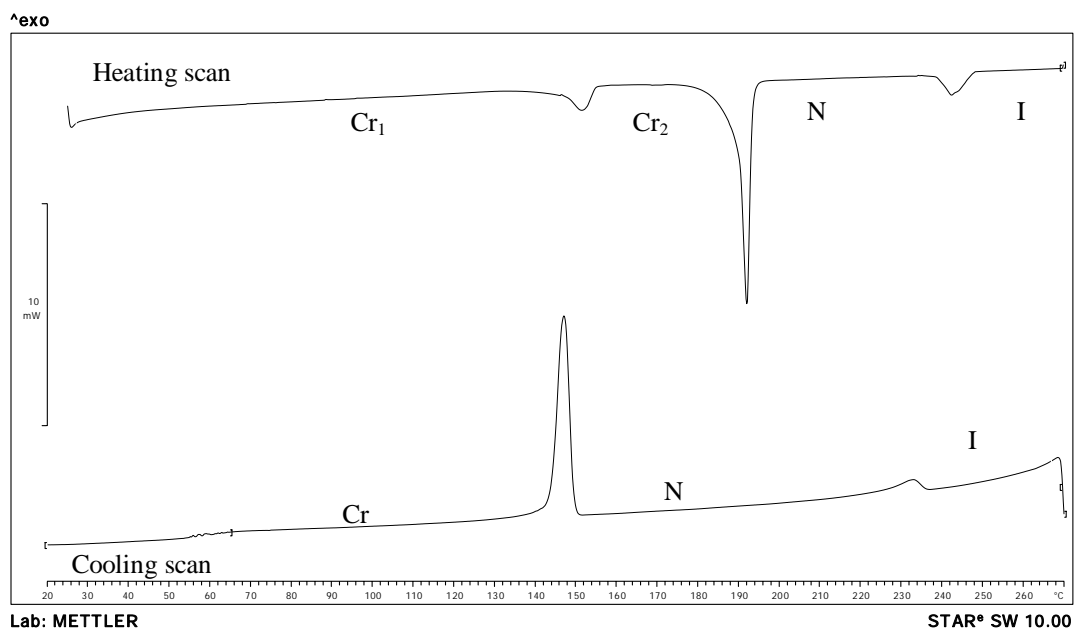


Figure 5.44: DSC thermogram of 8OEtD during heating and cooling scans.

Table 5.17: Phase transition temperatures and associated enthalpy changes of series nOMeD

Compound	Transition Temperatures, °C (ΔH , kJmol ⁻¹)	Heating Cooling
4OMeD	Cr 191.4 (22.92) I Cr 160.4 (23.11) I	
6OMeD	Cr 201.1 (48.64) I Cr 155.3 (38.69) I	
8OMeD	Cr 163.75 (32.33) N 201.8* I Cr 133.0 (29.92) N 200.8 (3.01) I	
10OMeD	Cr 120.9 (37.95) N 192.9 (3.49) I Cr 166.6 (32.12) N 180.9 (1.75) I	
12OMeD	Cr 119.1 (66.38) N 148.1 (4.91) I Cr 102.22(19.17) N 147.5 (3.69) I	

*POM data

Table 5.18: Phase transition temperatures and associated enthalpy changes of series nOEtD

Compound	Transition Temperatures, °C (ΔH , kJmol ⁻¹)	Heating Cooling
4OEtD	Cr 217.6 (1.24) I Cr 168.2 (1.29) I	
6OEtD	Cr 199.5 (38.34) N 264.8 (1.04) I Cr 146.8 (15.08) N 247.7 (0.84) I	
8OEtD	Cr 191.6 (44.75) N 242.8 (1.15) I Cr 147.6 (37.14) N 233.3 (1.42) I	
10OEtD	Cr 170.2 (55.27) N 190.1 (1.51) I Cr 145.3(48.69)) N 185.9 (1.67) I	
12OEtD	Cr 165.3 (36.35) N 203.6 (1.64) I Cr 141.6 (56.00) N 198.7 (1.64) I	

For series **nOMeD**,

Compounds C₄-C₆ = non-mesomorphic

Compounds C₈-C₁₂ = Nematic phase (Figure 5.45)

By cooling from isotropic liquid phase, nematic phase with marble-liked texture can be observed for compound **8OMeD** and *thread-liked* texture was observed for compound **12OMeD**.

For series **nOEtD**,

Compounds C₄ = non-mesomorphic

Compounds C₆-C₁₂ = Nematic phase (Figure 5.46)

For compound **8OEtD** and **12OEtD**, the nematic mesophase emerged upon cooling from isotropic liquid phase and then amalgamated with each other to form a typical thread-like nematic texture.

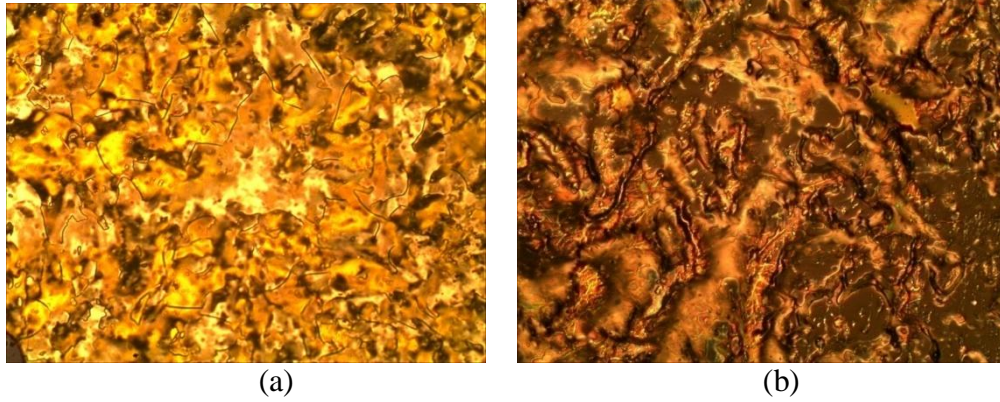


Figure 5.45: (a) Liquid crystal textures of 8OMeD upon cooling. The nematic droplets appeared and coalesced to form nematic phase *thread-liked* texture with disclination lines. (b) Optical photomicrographs of 12OMeD exhibiting nematic phase with *Schlieren* texture.

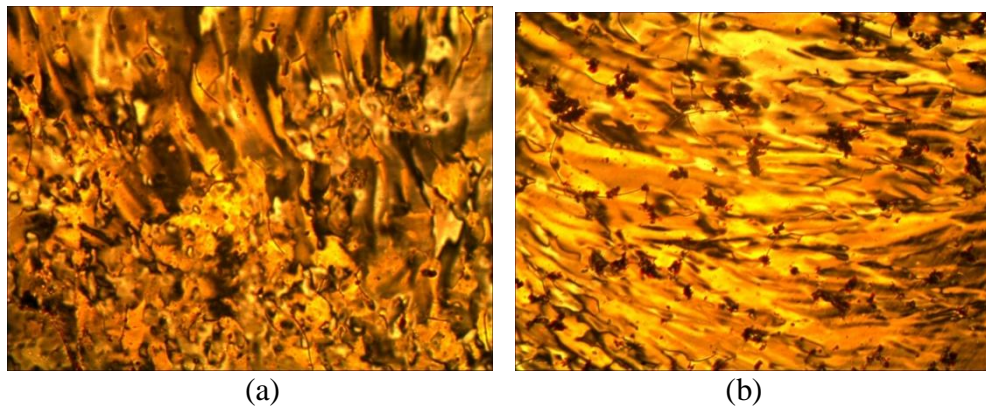


Figure 5.46: (a) Optical photomicrographs of (a) 6OEtD and (b) 12OEtD. Upon cooling, nematic droplets appeared and coalesced to form nematic phase with *thread-liked* texture.

For series **nOMeD**, a chart of transition temperatures versus the number of carbons in the alkoxy spacer chain is shown in Figure 5.47. There are three compounds exhibited enantiotropic mesomorphic properties which were C₈, C₁₀ and C₁₂ members. When the length of spacer chain increase from C₄ to C₁₂ derivatives, the spacer chain lengths are sufficient for exhibiting nematic mesophase.

The melting temperatures show a decreasing trend from C₆ to C₁₂. However, clearing temperature descended with the increase in the carbon chain length due to the dilution of the mesogenic core resulting from the flexibility provided by the spacer alkoxy chain. From the graph, the nematic mesophase range (Δ_N) seemingly decreased when the length of the terminal chain increased when comparing C₈ and C₁₂ members. The inspected activity is in good agreement with the predictions which done by Henderson (2005) where the even-numbered and alkoxy dimers consist higher clearing temperature.

For series **nOEtD**, a plot of the transition temperatures versus the number of carbons in the alkoxy chain enables the effect of the spacer chains on the mesomorphic properties to be studied (Figure 5.48). The clearing points show a marked alternation on changing the number of carbon in which the even members have the higher values.

The melting temperatures decreased when the length of the spacer alkoxy chain of the derivatives increased from C₄ to C₁₂ members. The featured shown by

C₄ to C₁₂ could be explained in term of the rigidity of the long molecular axis which will often be reduced owing to grow in the flexibility of the spacer alkoxy chain which suppressed the anisotropy of the molecules (Kelker and Hatz, 1980). Besides that, clearing temperatures decreased as the number of carbon atom increased due to the dilution of the core. The increasing *Van der Waals* forces tend to increase the clearing temperature from C₁₀ to C₁₂ derivatives. An obvious decreased of nematic mesophase range is observed when the carbon chain length increases. This shows that with elongating at the length of the spacer carbon chain, nematogenic properties declined and it may due to attraction between the long alkoxy spacer chains leading to their intertwining, facilitating the lamellar pack (Yeap *et al.*, 2004).

Both series exhibited purely nematogens which may due to the existence of azomethine group which conferred a stepped core structure in which linearity is maintained, resulting in thicken effect which in turn heightened the nematic mesophase stability (Collings and Hird, 1997b).

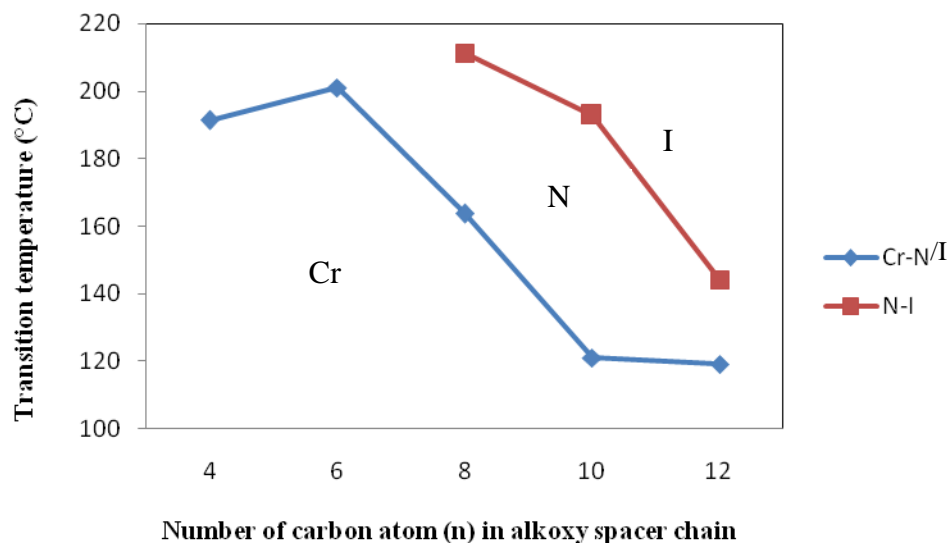


Figure 5.47: Plot of clearing temperature (°C) versus the carbon atoms (n) alkoxy chain of homologous series nOMeD.

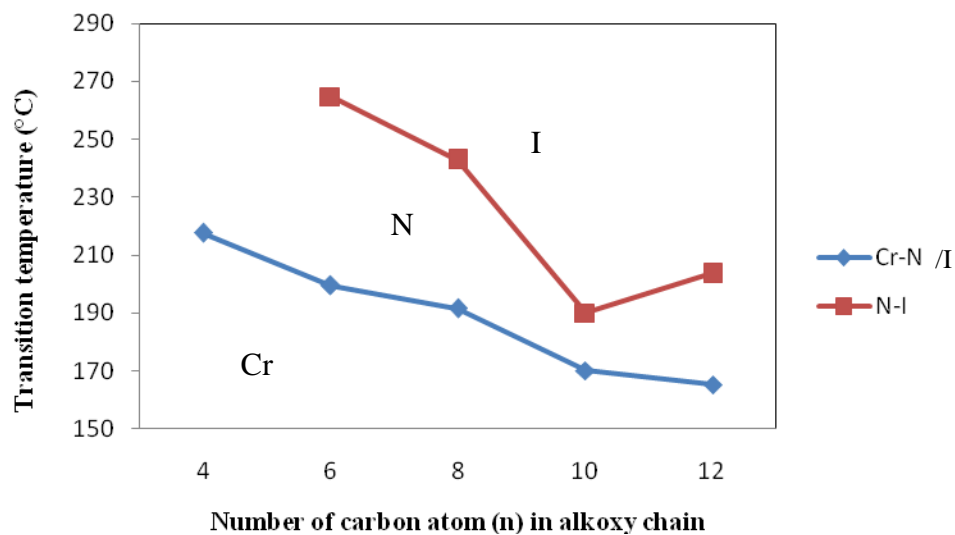


Figure 5.48: Plot of clearing temperature (°C) versus the carbon atoms (n) in alkoxy chain of homologous series nOEtD.

5.5 Series 5: Mesomorphic properties of 5-Methyl-2-[4-(4-alkoxybenzoyloxy)benzylideneamino]-2-pyridines (nPM5B)

5.5.1 Optical and Thermal Studies

The phase transition temperatures and associated enthalpy changes (ΔH) obtained from DSC analysis during heating and cooling cycles of **nPM5B** are summarized in Table 5.19.

The DSC thermogram of **14PM5B** during heating and cooling scans is depicted in Figure 5.49. It can be noticed that **14PM5B** exhibited enantiotropic liquid crystal phase as the liquid crystal phase (three transition peaks) can be observed during heating and cooling scans which are due to the transition of Cr-SmA, SmA-N and N-I.

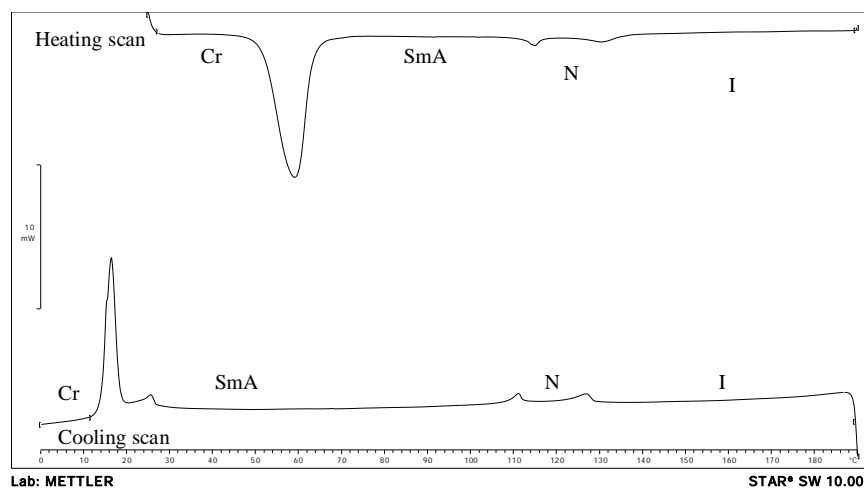


Figure 5.49: DSC thermogram of 14PM5B during heating and cooling scans.

Table 5.19: Phase transition temperature and associated enthalpy changes of series nPM5B

Compound	Transition Temperature, °C (ΔH , kJmol ⁻¹)	Heating Cooling
2PM5B	Cr 123.0 (39.90) I Cr 88.74 (27.05) I	
3PM5B	Cr 83.69 (34.89) I Cr 33.55 (19.27) I	
4PM5B	Cr 89.36 (40.29) I Cr 53.94 (0.38) I	
5PM5B	Cr ₁ 73.46 (2.38) Cr ₂ 90.41 (24.93) N 202.58 (1.41) I Cr 31.49 (17.21) N 194.73 (1.37) I	
6PM5B	Cr ₁ 53.41 (2.80) Cr ₂ 93.47 (23.87) N 203.28 (1.57) I Cr 53.74 (21.24) N 196.98 (1.62) I	
7PM5B	Cr ₁ 48.76 (7.75) Cr ₂ 68.23 (20.15) N 185.11 (1.39) I Cr 48.11 (20.67) N 182.23 (1.13) I	
8PM5B	Cr ₁ 47.44 (1.13) Cr ₂ 75.84 (35.56) N 191.88 (1.63) I Cr 38.16 (24.45) N 189.96 (1.32) I	
9PM5B	Cr ₁ 49.57 (0.91) Cr ₂ 78.80 (33.56) N 179.54 (0.85) I Cr 48.38 (28.02) N 177.43 (1.50) I	
10PM5B	Cr ₁ 55.67 (4.24) Cr ₂ 79.48 (33.92) N 178.63 (1.43) I Cr 26.36 (18.88) N 175.80 (1.67) I	
12PM5B	Cr ₁ 72.84 (29.53) Cr 81.14 (48.72) N 179.08 (1.12) I Cr 54.43 (30.56) SmC 71.46 (1.49) N 176.99 (0.22) I	
14PM5B	Cr 58.89 (44.67) SmA 114.67 (1.15) N 130.68 (1.35) I Cr 25.81 (24.14) SmA 111.20 (1.50) N 127.19 (1.09) I	
16PM5B	Cr 66.9 (53.59) SmA 77.82(5.45) I Cr 42.44 (40.05) SmA 73.18 (3.92) I	
18PM5B	Cr ₁ 72.75 (9.22) Cr ₂ 82.68 (80.72) I Cr 53.89 (69.28) SmA 81.94(6.67) I	

Observation under POM has revealed that all compounds in series **nPM5B** exhibited liquid crystals properties except short chain derivatives (n =2, 3, 4).

Compounds C₂-C₄ = non-mesomorphic

Compounds C₅-C₁₀ = Nematic phase (Figure 5.50)

Compounds C₁₂ = SmC (monotropic) and nematic phase (Figure 5.51)

Compounds C₁₄-C₁₈ = Sm A and nematic phase (Figure 5.52)

For **12PM5B**, on further cooling the nematic phase, it has been transformed into SmC phase with transition bars and formed SmC phase with *Schlieren* texture. Upon further cooling of **14PM5B**, nematic mesophase was transformed to SmA phase with fan-shape (elliptical) texture.

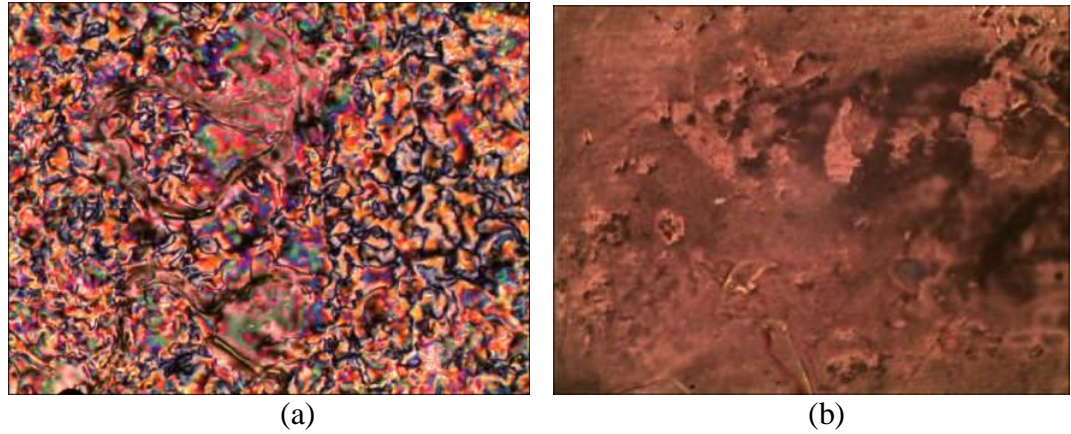


Figure 5.50: (a) Optical photomicrographs of typical *Schlieren* texture of nematic phase exhibited by 8PM5B. (b) Optical photomicrographs of typical *marble-like* texture of nematic phase exhibited by 10PM5B.

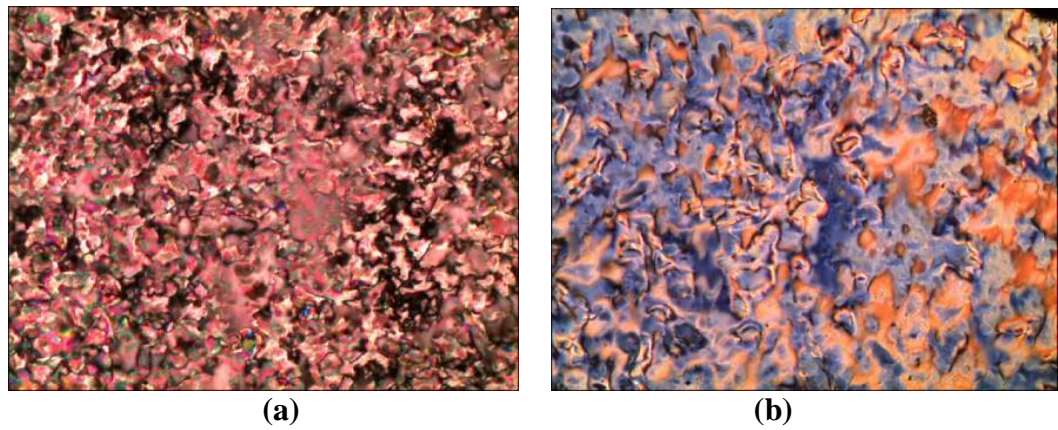
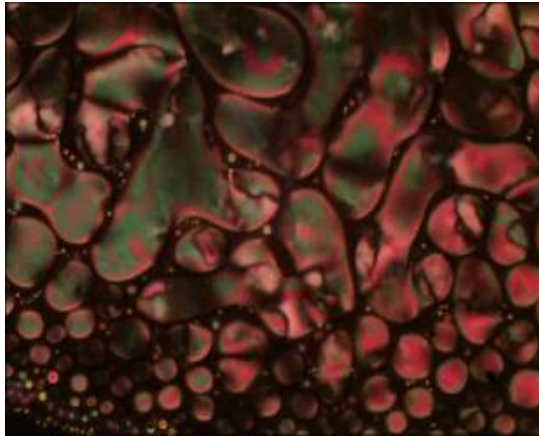
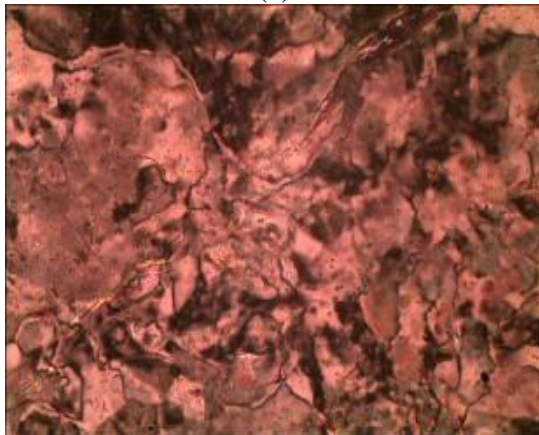


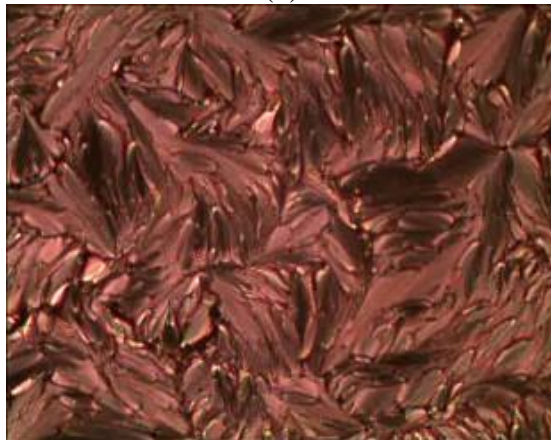
Figure 5.51: (a) Optical photomicrographs of 12PM5B exhibiting nematic phase with *Schlieren* texture and (b) SmC phase with *Schlieren* texture.



(a)



(b)



(c)

Figure 5.52: (a) Optical photomicrographs of 14PM5B exhibiting droplets of nematic phase and then coalesced with *marble-like* nematic texture (b) and SmA phase with fan-shape (elliptical) texture was observed upon further cooling.

Figure 5.53 illustrates the mesomorphic properties, transition temperatures and the influences of number of carbons in the alkoxy chains for series **nPM5B**. From the plot, no mesophase was noticed for high rigidity derivatives ($n = 2$ to 4). On the whole, an inflexible molecular structure is unfavoured in producing mesophase (Ha *et al.*, 2009b). The odd-even effect on transition temperature was not clearly observed. Based on the plot, both melting (Cr-Sm/N) and clearing (Sm/N-I) points showed a decreasing trends as the carbon chain length grow in number.

According to the plot, nematic mesophase range (Δ_N) seemingly reduced as the terminal chain length increased. C_{12} members exhibited monotropic SmC phase during cooling scan. When the carbon chain length elongated from C_{12} member to C_{14} member, the compound showed an enantiotropic SmA mesophase. Instead of exhibiting SmC phase in cooling scan, the SmA mesophase was now being noticed in both cooling and heating scans. When increased the carbon chain length to C_{16} member, it was found to increased the SmA phase range to 30.98 °C from 16.01 °C, although the melting and clearing temperatures were decreasing. A decrement of phase range will be noted as the elongation of carbon chain length. It was proved by the monotropic SmA phase which was observed in C_{18} member.

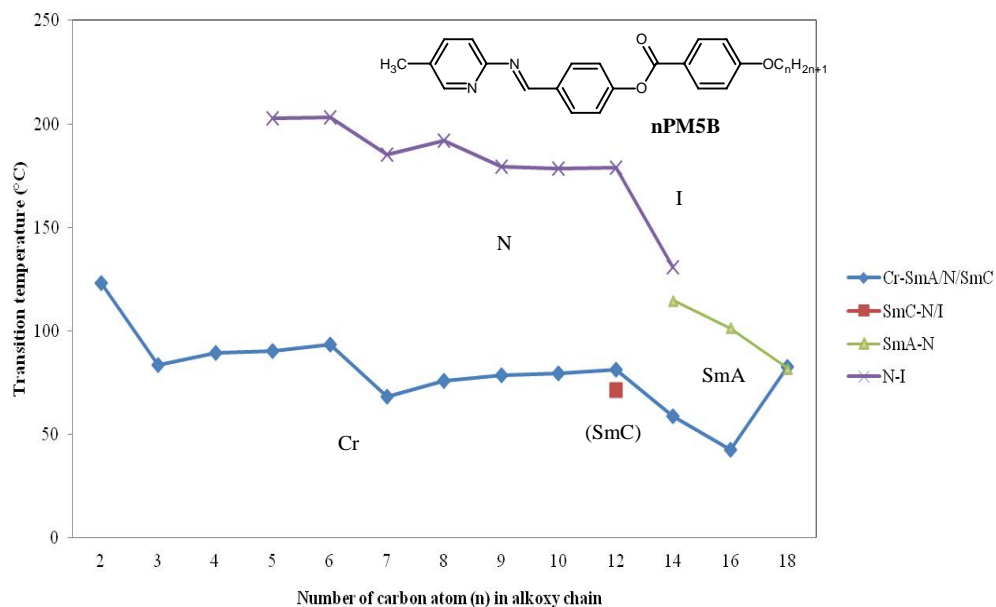


Figure 5.53: Plot of clearing temperature (°C) versus the carbon atoms (n) in alkoxy chain of homologous series nPM5B.

5.5.2 XRD study of nPM5B

XRD diffractogram of **12PM5B** as the representative compound are shown in Figure 5.54 and the XRD data is summarized in Table 5.20.

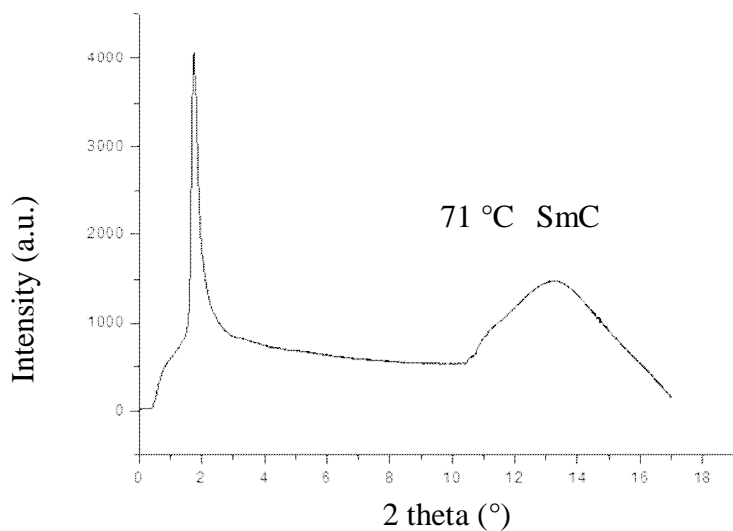


Figure 5.54: XRD diffractogram of compound 12PM5B.

In Figure 5.54, the sharp and intense peak at lower region angle (1.76 °) as proved that the lamellar layer is occurred. A broadly diffuse signal at wide region showed the liquid-like state of the mesophase (Yamaguchi *et al.*, 2004). The X-ray diffraction pattern obtained for compound **12PM5B** exhibits a sharp reflection with d (spacing) = 33.3 Å in the low-angle region and a diffuse one in the wide-angle region. The calculated molecular length, L (32.55 Å) is much smaller compared to the d -spacing value. By combining the data from POM and DSC, SmC phase was identified to be present in compound **12PM5B**.

Table 5.20: Powder XRD data of 12PM5B

2 theta (°)	1.76
d -spacing	33.3 Å
L	32.62 Å
d/L	1.02
Phase	SmC

5.6 Series 6: Mesomorphic properties of 2-[4-(4-Alkyloxybenzoyloxy)benzylidenanilines]thiophenes (nTAP)

5.6.1 Optical and Thermal studies

In thermal study, transition temperatures and associated enthalpy changes of **nTAP** are summarized in Table 5.21.

DSC studies revealed that traces of short members in **nTAP** ($n = 3, 4, 5$ and 7) exhibited monotropic liquid crystal phase. The DSC thermogram of **6TAP** is illustrated in Figure 5.55. **6TAP** exhibited enantiotropic properties in which liquid crystal phase can be examined in both scans, there is two transition peaks can be observed which are due to the transition of Cr-N and N-I.

Table 5.21: Phase transition temperature and associated enthalpy changes of series nTAP

Compound	Transition Temperature, °C (ΔH , kJmol ⁻¹)	Heating Cooling
2TAP	Cr 138.4(29.93) N 151.5 (0.79) I <i>Cr 93.41(24.51) N 150.32 (0.90)I</i>	
3TAP	Cr ₁ 111.92 (13.59) Cr ₂ 116.01 (7.12)I <i>Cr 76.70 (15.77) N 115.25 (0.52)I</i>	
4TAP	Cr ₁ 43.51 (2.33) Cr ₂ 58.54 (11.28) Cr ₃ 131.5(30.67)I <i>Cr₁ 40.96 (1.98) Cr₂ 56.85 (9.55) Cr₃ 84.39 (23.21) N 120.30(1.13) I</i>	
5TAP	Cr 118.06 (34.37)I <i>Cr 76.93(25.61) N 117.49 (0.59) I</i>	
6TAP	Cr 121.32 (38.21) N 128.63 (0.75) I <i>Cr 66.40 (26.27) N 127.00(0.94) I</i>	
7TAP	*Cr 118.01 N 120.33 (32.46)I <i>Cr₁ 36.75 (2.50) Cr 53.19 (22.01)N 118.81 (0.74) I</i>	
8TAP	Cr 110.99 (40.36) N 125.34 (1.01) I <i>Cr 69.75 (33.23) N 123.67 (1.11) I</i>	
9TAP	Cr 100.80 (35.82) N 118.51 (0.96) I <i>Cr 66.80 (31.14) N 116.37 (0.97)I</i>	
10TAP	Cr 103.74 (38.82) N 121.41 (1.23) I <i>Cr 72.16 (36.00) N 119.50(1.15) I</i>	
12TAP	Cr 103.78 (41.99) N 120.28 (1.17) I <i>Cr 67.78 (37.20) N 118.36(1.46) I</i>	
14TAP	Cr ₁ 86.98 (8.39) Cr ₂ 103.19 (47.25) N 117.25 (1.73) I <i>Cr 71.52 (46.89) N 115.37(1.88) I</i>	
16TAP	Cr ₁ 95.03 (42.20) Cr ₂ 102.52 (53.05) N 114.23 (1.69) I <i>Cr 76.85 (59.55) N 112.36 (2.15) I</i>	
18TAP	Cr 118.05 (49.59) I <i>Cr 108.06 (53.06)I</i>	

*POM data

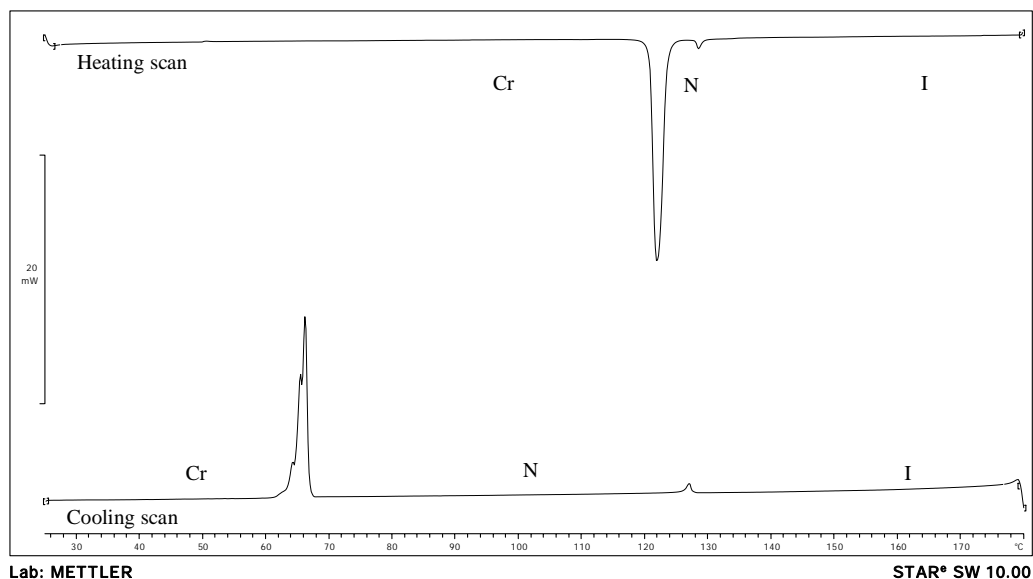


Figure 5.55: DSC thermogram of compound 6TAP during heating and cooling scans.

Observation under the polarizing microscope revealed that compounds in series **nTAP** exhibited nematic phase.

Compounds C₂-C₁₈ = Nematic phase (Figure 5.56)

During cooling scan of **6TAP** and **10TAP**, the nematic mesophase appeared as droplets and then coalesced to form a nematic mesophase with *thread-like* texture.

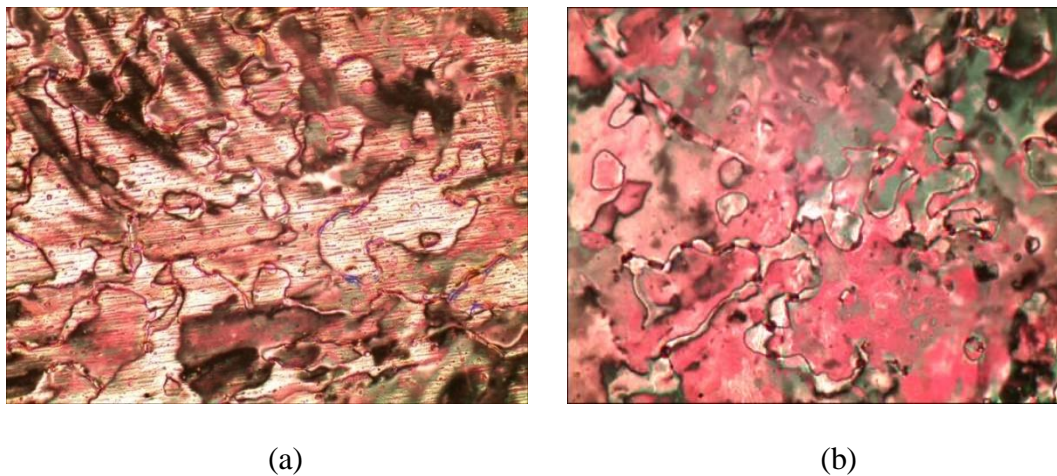


Figure 5.56: (a) Photomicrograph of 6TAP during cooling scan showing nematic phase with *thread-like* textures. (b) Photomicrograph of 10TAP during cooling scan showing nematic phase with *thread-like* textures.

Figure 5.57 illustrates the chart of phase transition temperature versus the number of carbon chain of **nTAP**. From the graph, the odd-even effect on the liquid crystalline properties were distinct in this series. All compounds exhibited mesomorphic properties except C_{18} derivative. The melting temperatures show a decreasing trend from the C_2 to C_{16} derivatives. Liquid crystal phase for short chain derivatives C_3 , C_4 and C_5 exhibited as monotropic (metastable) nematic mesophase. When the chain length increased from C_6 member, the compounds exhibit an enantiotropic (stable) nematic phase and it persisted till C_{16} derivative. Hence, it was believed that certain flexible chain length is prerequisite to promote enantiotropic (stable) liquid crystal phase. It was proven when the clearing temperature alighted with the raise in the carbon chain length due to the dilution of the mesogenic core leading from the flexibility offered by the alkoxy chain. The

nematic mesophase range (Δ_N) seemingly reduced as the terminal chain length increased from C_9 ($\Delta_N = 17.7$ °C) to C_{16} ($\Delta_N = 11.7$ °C) derivatives. This is due to the long carbon chain being attracted and intertwined which in turn facilitates the lamellar packing causing a slight reduce in the nematic phase range (Yeap *et al.*, 2006a).

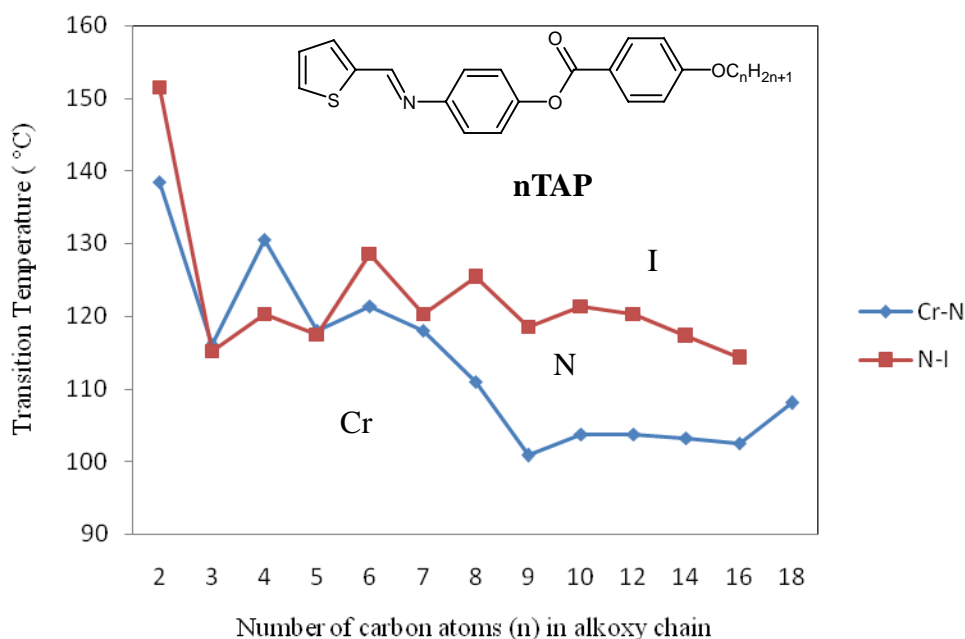


Figure 5.57: Plot of clearing temperature (°C) versus the carbon atoms (n) in alkoxy chain of homologous series nTAP.

5.7 Comparison to Others Structurally Related Compounds

By comparing the present series of compounds with other structurally related compounds aided to understand some of the structure-properties relationship. Several reported compounds were selected to be compared in order to

evolve the effects of terminal alkoxy group, heterocyclic core (benzothiazole, pyridine and thiophene), extended core ring system, lateral substitution, terminal polar group and alkoxy spacer on the mesomorphic properties.

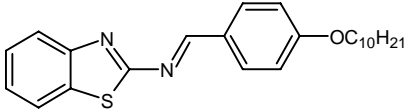
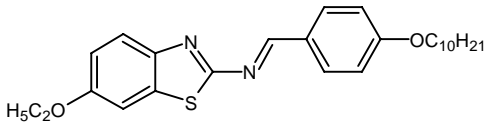
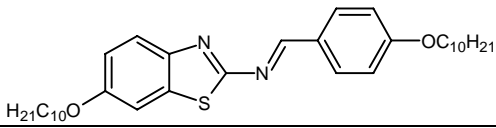
5.7.1 Effect of Sixth-Substituted Alkoxy Group

Table 5.22 extracts the molecular structures, average mesophase range and transition temperatures of **10HBZT**, **10OEtBTH** and **compound A**. Comparison among these compounds helps to understand the effect of 6-alkoxy group on benzothiazole core.

First, **10HBZT** exhibited enantiotropic SmA phase, **10OEtBTH** exhibited enantiotropic nematic and SmA phase. However, **compound A** exhibited nematic and SmC phases. The difference between these molecular structures is the additional sixth-substituted alkoxy group in **10OEtBTH** and **compound A**. By comparing the exhibited mesophase, it was believed that six-substituted alkoxy group on benzothiazole tends to induce smectic phase. The ethoxyl group in **10OEtBTH** not only affected the types of mesophase but also reflected on the phase stability and mesophase range. By comparing **10OEtBTH** (SmA= 6.9 °C and nematic = 35.6 °C) and **10HBZT** (SmA= 2.1 °C), it can be noted that a stable mesophase with broader mesophase range were obtained once ethoxyl group has been introduced. However, the presence of the nematic phase in **10OEtBTH** was probably due to the azomethine (-C=N-) linkage which conferred a step structure that preventing it from the lamellar packing in smectic phase (Collings and Hird,

1997b). Thus, a longer alkoxy chain tend to become favour the intermolecular interactions giving rise to a tilted arrangement of the molecules in the smectic layers (Ha *et al.*, 2009b).

Table 5.22: Molecular structures, phase transition temperatures and average mesophase range of 10HBZT, 10OEtBTH and compound A

Compound	Transition Temperature (°C)	Mesophase range	
		Sm	N
			
10HBZT			
			
10OEtBTH			
			
Compound A (Belmar <i>et al.</i> , 1999)			
10HBZT	Cr 82.5 SmA 84.6 I	2.1	-
10OEtBTH	Cr 88.7 SmA 95.6 N 131.2 I	6.9	35.6
Compound A	Cr 116.0 SmC 124.5 N 127.5 I	8.5	3.0

Longer chain of 6-decyloxy group may induce the tilted SmC phase in **compound A**. In addition, it also altered the mesophase range of smectic and nematic phase. It can be clearly noted that the smectic phase range of **compound A** is much higher than that in **10OEtBTH** while nematic phase range of **compound A** is comparatively lower than that in **10OEtBTH**. Such an observed phenomenon was attributed to the 6-decyloxy group which increased the length of the chain domain in favouring the lamellar packing due to its enhancing *Van der Waals* forces. Thus, the increased smectogenic tendency subsequently decreased the nematogenic properties as the sixth-substituted alkoxy group increasing.

5.7.2 Effect of Extended Core Ring System

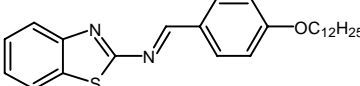
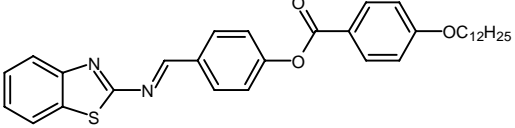
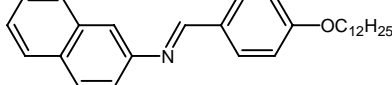
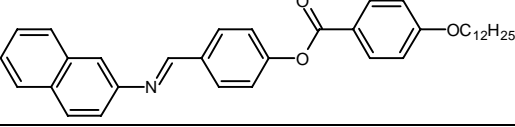
Table 5.23 summarizes the molecular structure, transition temperatures and average mesophase range of **12HBZT**, **12HB3R**, compounds **B** and **C**. Several comparisons are made to evolve the effects of extended core ring system to the compounds.

Compound **12HB3R** exhibited both SmA and nematic mesophases, whereas compound **12HBZT** exhibited only SmA mesophase. It can be clearly noticed that the tendency to stabilize the smectic mesophase and its thermal range in **12HB3R** (Sm = 68.8 °C) is greater than that of **12HBZT** (Sm = 8.2 °C). The molecular structure of **12HB3R** differs from **12HBZT** only in the number of benzene nuclei and ester central linkage. Gray has explained that give rise in the molecule length, enhanced the anisotropy of polarizability, increase the intermolecular cohesive forces which responsible for induction of the nematic mesophase and further more resulted in higher smectic phase transition temperatures for compound **12HB3R** (Gray, 1962). Compound **12HB3R** also exhibited nematic mesophase with phase range of 15 °C. This is due to the heightened polarizability and grows in intermolecular cohesive forces (Prajapati and Bonde, 2009). Similar phenomenon can be seen between **compound B** with **compound C**.

The addition phenyl ring increases the length of the molecule which supported by the central linking group (-COO-), which preserves the linear shape

of the molecule. This central linking group also increases the molecular polarity of compound and these factors are responsible for the higher thermal stability and mesophase length of two rings structures in comparison of three rings structures (Prajapati and Bonde, 2006a).

Table 5.23: Molecular structures, phase transition temperatures and average mesophase range of 12HBZT, 12HB3R, compound B and C

	12HBZT		
	12HB3R		
	Compound B (Vora and Prajapati, 1998)		
	Compound C (Vora and Prajapati, 1998)		
Compound	Transition Temperature (°C)	Mesophase range (°C)	
		Sm	N
12HBZT	Cr 81.9 SmA 90.1 I	8.2	-
12HB3R	Cr 95.8 SmA 164.6 N 179.6 I	68.8	15.0
Compound B	Cr (76.0) SmA (79.0) N 92.0 I	3.0	13.0
Compound C	Cr 106.0 SmC 157.0 N 198.0 I	51.0	41.0

() Monotropic value

5.7.3 Effect of Lateral Substituent

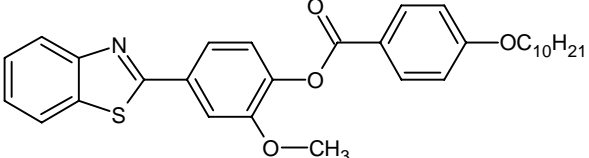
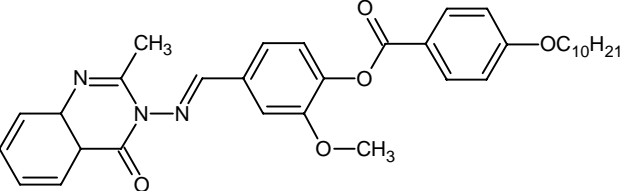
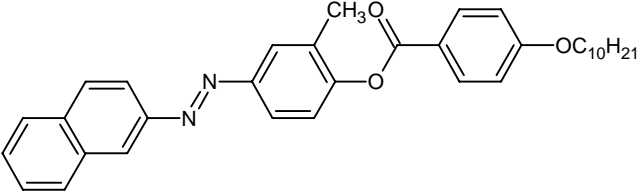
It is well known that thermotropic liquid crystals are highly sensitive to their molecular constitution. Table 5.24 summarizes the molecular structures, average mesophase range and transition temperatures of **10MOBZT**, **compound E** and **F**. **10MOBZT** and **compound F** exhibited nematic phase, while **compound E** exhibited only monotropic nematic mesophase.

The lateral methoxyl group increases the breadth of the molecule of **10MOBZT** and **compound E** and also the non-polar arrangement of the system due to steric interactions (Prajapati and Modi, 2010). All these factors would be responsible for the elimination of the smectogenic tendencies for all the compounds. This factor was also responsible for the monotropic nature of the mesophase observed in **compound E**. Gray has illustrated that the enhance in the width of the molecules lower both nematic and smectic thermal stabilities (Gray, 1962).

Similarly for **compound F**, the lateral methyl group not only increases the breadth of the molecules, but also increases the acoplanarity in the system due to steric interaction. The nematic mesophase range of **10MOBZT** (4.6 °C) is lower than **compound F** (40.0 °C) and the thermal stability of **compound F** (146.0 °C) is higher than **10MOBZT** (88.3 °C). It is due to the existence of benzothiazole heterocyclic ring in compound **10MOBZT** increase entire polarizability of the molecule, as well as lateral polar methoxy substituent which actually lead to a

reduction in the polarizability anisotropy and also increases the overall molecular breadth as compared with unsubstituted naphthyl derivatives. The thickening effect caused by the naphthalene moiety increased the breadth of molecules and making them more linear. Thus, nematic thermal stability of **compound F** is probably higher compared to **10MOBZT** (Prajapati *et al*, 2003).

Table 5.24: Molecular structures, phase transition temperatures and average mesophase range of 10MOBZT, compound E and F

	10MOBZT		
	Compound E (Prajapati and Modi, 2010)		
	Compound F (Prajapati, 2000)		
Compound	Transition Temperature (°C)	Mesophase range (°C)	
		Sm	N
10MOBZT	Cr 83.7 N 88.3 I	-	4.6
Compound E	Cr 132.0 (N 92.0) I	-	-
Compound F	Cr 106.0 N 146.0 I	-	40.0

() Monotropic value

5.7.4 Effect of Benzothiazole Core

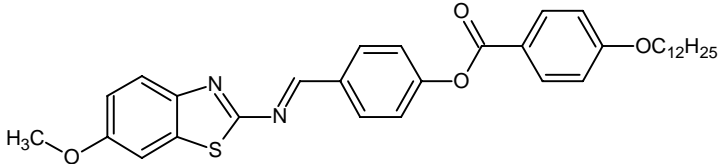
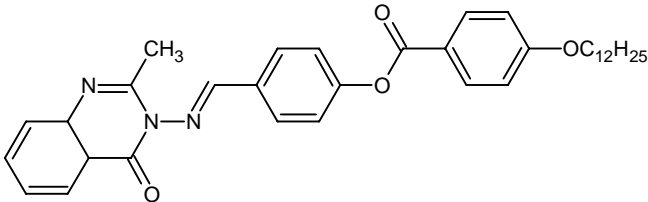
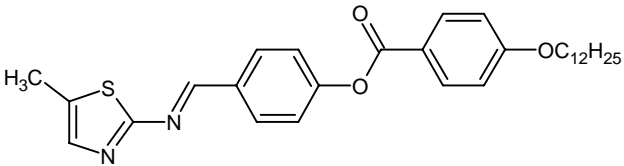
Table 5.25 illustrates the comparison of transition temperature, thermal stabilities and range of mesophase of related compounds **12OMe3R**, **compounds G** and **H** are reported in literature.

Compound **12OMe3R** exhibited enantiotropic SmC and nematic mesophases whereas **compound G** displayed enantiotropic SmA and nematic mesophases. Compound **12OMe3R** has 6-methoxybenzothiazole ring instead of the 2-methylquinazolone rings of **compound G**. Transition temperature of **12OMe3R** is relatively higher than **compound G** by 67.7 °C and the nematic and smectic phase range of **12OMe3R** are higher than **compound G** by 50.9 °C and 31.1 °C, respectively. The presence of the terminal benzothiazole ring amplifies the overall polarizability of the molecule while reducing the symmetry of the molecule as compared to quinazolone derivatives and provides higher transition temperature. The lateral methyl substituent in quinazolone ring actually leads to a reduction in polarizability anisotropy and also increases the overall molecular breadth as compared with benzothiazole ring (Prajapati and Modi, 2010 and Gray, 1962).

Similarly, **compound H** and **12OMe3R** differ only in their aromatic moiety at one end. **Compound H** has a 5-methylthiazole heterocyclic moiety, whereas **12OMe3R** has a 6-methoxybenzothiazole moiety at the same position. The polar nature of methoxy group exists in **12OMe3R** also richness the

polarizability of the molecule, at the same time, also helps to increase the thermal stability of the compound (Prajapati and Bonde, 2009). **Compound H** is purely nematogenic whereas **12OMe3R** exhibited smectic and nematic mesophases. **Compound H** did not exhibit smectic mesophase may be due to the five-membered thiazole core with methyl substituent, which diminishes the smectic mesophase.

Table 5.25: Molecular structures, phase transition temperatures and average mesophase range of 12OMe3R, compound G and H

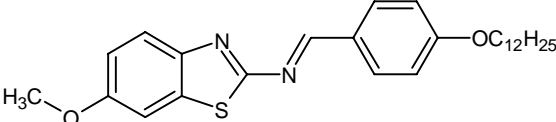
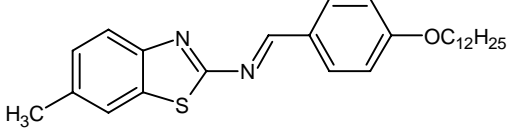
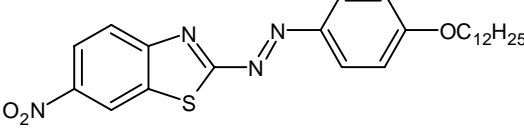
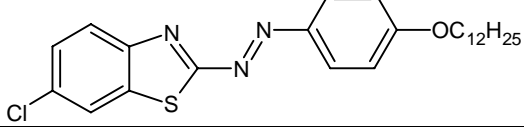
	12OMe3R		
	Compound G (Prajapati and Modi, 2010)		
	Compound H (Thaker <i>et al.</i> , 2007)		
Compound	Transition Temperature (°C)	Mesophase range (°C)	
		Sm	N
12OMe3R	Cr 75.69 SmC 126.8 N 205.7 I	51.1	78.9
G	Cr 90.0 SmA 110.0 N 138.0 I	20.0	28.0
H	Cr 63.0 N 87.0 I	-	24.0

5.7.5 Effect of Terminal Polar Substituent

Table 5.26 illustrates the comparison of transition temperatures, molecular structures and mesophase range of the representative compounds **12OMeBTH** and **12MeBTH** with other similarity structural related compounds (compounds **I** and **J**) reported in the literatures. All four different compounds exhibited enantiotropic SmA phase except **12OMeBTH** exhibited an enantiotropic SmA phase along with nematic mesophase. Reference to molecular structure shows that all compounds have distinct substituent at the sixth position of the benzothiazole moiety. Compound **12MeBTH** has the $-\text{CH}_3$ group, whereas **compound I** has the $-\text{NO}_2$ group. The higher smectic thermal stability of the **compound I** may due to the nitro group has richer polarizability contrasted to the methyl group which is responsible for the higher transition temperatures and greater mesophase thermal range (Prajapati *et al.*, 2005).

Compound **12OMeBTH** shows an enantiotropic nematic phase with smectic A phase. However, **compound J** shows only enantiotropic SmA mesophase. The thermal stability and smectic mesophase length of **compound J** is higher by 71.9 °C and 50.1 °C compare to compound **12OMeBTH**. These may due to the polar chloro group at the sixth position in **compound J** compared to the less polar methoxy group in compound **12OMeBTH** (Prajapati and Bonde, 2006).

Table 5.26: Molecular structures, phase transition temperatures and average mesophase range of 12OMeBTH, 12MeBTH, Compound I and Compound J

	12OMeBTH		
	12MeBTH		
	Compound I (Prajapati and Bonde, 2009)		
	Compound J (Prajapati and Bonde, 2006)		
Compound	Transition Temperature (°C)	Mesophase range (°C)	
		Sm	N
12OMeBTH	Cr 84.1 SmA 101.8 N 121.9 I	20.1	20.1
12MeBTH	Cr 81.6 SmA 116.1 I	34.5	-
I	Cr 156.0 SmA 194.0 I	38.0	-
J	Cr 80.0 SmA 172.0 I	92.0	-

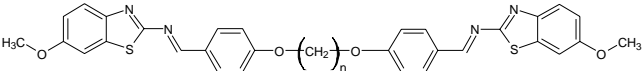
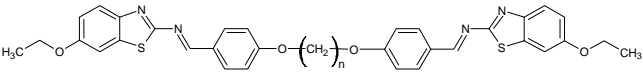
Same phenomenon can be seen in previous comparison between **compound I** and **12OMeBTH**. The nematic thermal stability of the methoxy group is higher than that of other terminal groups. This could be due to the methoxy group which the lone pair of electrons of oxygen is shielded by an insulator-like methyl group. The repulsive forces involving the oxygen lone pairs are thereby substantially reduced and allow a close approach of the neighboring molecules, increasing bonding forces. This leads to an increase in the nematic phase transition temperature (Thaker *et al*, 2010).

5.7.6 Effect of Alkoxy Spacers

Series **nOMeD** and **nOEtD** are four rings dimer mesogens which possess with benzothiazole core ring system (Table 5.27). Both series exhibited only nematic phase. This is probably due to the spacer carbon chain existed between the benzothiazole core systems. The terminal methoxyl and ethoxyl groups tend to induce the tilted structure in smectic phase but due to the short terminal carbon chains, both series showed only nematic phase. Both series are absence of smectic phase; it may be due to the alkoxy substituents, which compress the smectic mesophase (Prajapati and Bonde, 2006b).

The higher mesophase thermal stability of both series may cause by the heterocyclic benzothiazole system. The terminal benzothiazole ring enriches the overall polarizability of the molecules while reducing the symmetry of the molecule as compared to phenyl/naphthyl derivatives and given higher transition temperature (Prajapati and Bonde, 2006b). Table 6.6 shows that the average nematic mesophase length and nematic thermal stability of series **nOEtD** are higher by 12.0 °C and 52.4 °C, respectively, than for series **nOMeD**. The additional phenyl ring increases the the length of the molecule, and is well supported by the central linking group which preserves the linear shape of the molecule. All these factors are responsible for the higher thermal stability and the greater mesophase length for both series of compounds (Prajapati and Bonde, 2006a).

Table 5.27: Molecular structures, phase transition temperatures and average mesophase range of compounds nOMeD and nOEtD

Compound	Average mesophase range (°C)	Average thermal stability (°C)			Commencement of nematic phase
		T _M	T _N	T _C	
nOMeD 	31.5	141.4	172.9	186.6	C ₆
nOEtD 	43.5	181.7	225.3	223.8	C ₆

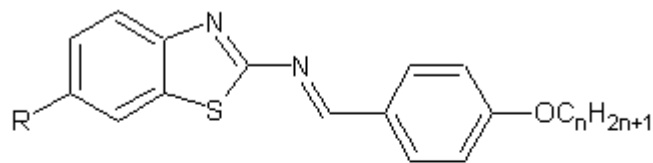
CHAPTER 6.0

CONCLUSIONS

A total of six series of heterocyclic-based calamitic liquid crystals possessing either two to four mesogenic cores were successfully synthesized and characterized. In addition, structural elucidations of the synthesized compounds were established via HPLC & TLC technique and spectroscopic techniques such as FT-IR, 1D & 2D NMR and EI-MS. The mesomorphic properties of the compounds were studied by using polarizing optical microscopy (POM), differential scanning calorimetry (DSC) and XRD analysis. The results of each series are concluded in the following sections, section 6.1 to 6.6. The summary of phase transition data of all synthesized compounds were stated in Appendix 1A.

6.1 Series 1: 6-Methyl-2-(4-alkoxybenzylidenamino)benzothiazoles (nMeBTH), 6-methoxy-2-(4-alkoxybenzylidenamino)benzothiazoles (nOMeBTH), 6-ethoxy-2-(4-alkoxybenzylidenamino)benzothiazoles (nOEtBTH) and 2-(4-alkoxybenzylidenamino)benzothiazoles (nHBZT)

Four sub-series of methyl-substituted benzothiazole-based liquid crystals possessing two mesogenic core units connected by Schiff base linkage were successfully synthesized and characterized.



nMeBTH	R= CH ₃
nOMeBTH	R= OCH ₃
nOEtBTH	R= OC ₂ H ₃
nHBZT	R= H

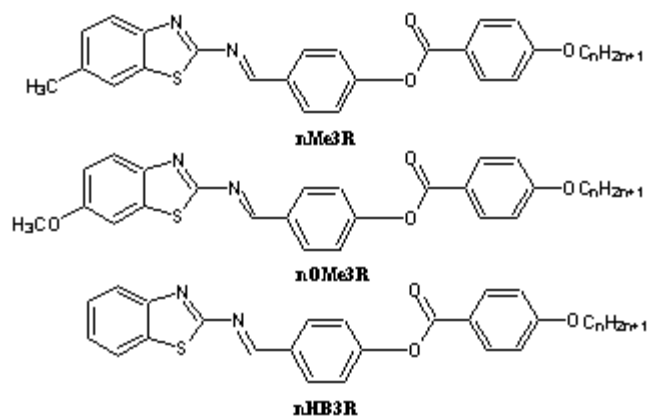
Where n = C2-C10, C12, C14, C16, C18

For sub-series **nMeBTH**, all compounds exhibited liquid crystalline properties. Short carbon chain members (n = 2 to 6) showed enantiotropic nematic mesophase. The presence of nematic and SmA was observed for medium chain members (n = 7 to 10). The long chain members (n = 12 to 16) exhibited only SmA phase. The smectic phase in **nMeBTH** was further studied using XRD analysis in which tilted SmA phase was observed. All compounds in sub-series **nOMeBTH** exhibited liquid crystal properties. Short to medium carbon chain members (n = 2 to 9) showed enantiotropic nematic mesophase while enantiotropic smectic phase was emerged from *n*-decyloxy derivatives onwards. Odd-even effect was showed at short to medium chain members. Short chain members have higher tendency to exhibit nematic phase while longer chain members have great potential to exhibit tilted smectic phase. For series **nOEtBTH**, all members are mesogenic compounds. Short chain members exhibited only nematic phase and smectic phase emerged from C₉ member onwards. The nematic mesophase range was suppressed while the emerging of the smectic phase. The enhancing *van der Waals* forces resulted from the lengthening of the alkoxy chain stabilizing the SmA and SmC phases by favouring the lamellar packing. For series

nHBZT, shorter carbon chain members ($n= 2$ to 6) are unflavourbale to form mesophase, however, the monotropic SmA phase start to emerges from C_7 derivatives. Compounds with long chain carbon ($n =10$ to 18) exhibited enantiotropic SmA phase. High rigidity is the short carbon chain members becomes an obstacle in promoting liquid crystalline properties. XRD analysis revealed that there is a partial bilayer arranged SmA phase while start from C_{14} to C_{16} derivatives, smectic A phase emerged and persisted till the end.

6.2 Series 2: 6-Methyl-2-[4-(4-alkoxybenzoyloxy)benzylidenamino]benzothiazoles (nMe3R), 6-methoxy-2-[4-(4-alkoxybenzoyloxy)benzylidenamino]benzothiazoles (nOMe3R) and 2-[4-(4-alkoxybenzoyloxy)benzylidenamino]benzothiazoles (nHB3R)

Three sub-series of methoxy-substituted benzothiazole-based liquid crystals comprising three mesogenic core units connected by Schiff base linkage were successfully synthesized and characterized.

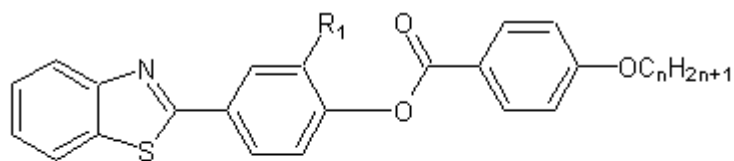


Where $n = C_2-C_{10}, C_{12}, C_{14}, C_{16}, C_{18}$

For series **nMe3R**, the short chain members ($n = 2, 3, 4$) are non-mesogen compounds. When the terminal chain ascended from C_5 to C_{10} derivatives, the alkyl chain has the ability to promote mesophase (nematic phase). Similarly, once the alkyl carbon elongated further from C_{12} to C_{16} members, the enantiotropic liquid crystal (smectic phase) was induced. For series **OMe3R**, nematic mesophase was exhibited at the compounds which having short to medium chain lengths. It is because the terminal chain lengths are sufficiently promote mesophase. When the alkyl chain reached a certain length ($n \geq 12$), SmC and nematic mesophase in higher temperature was induced. The phenomenon continues until C_{14} members. However, for C_{16} member, only SmA mesophase was observed. All the synthesized compounds in sub-series **nHB3R** exhibited mesomorphic properties. An obvious odd-even effect was noted in shorter homologous in **nHB3R**. The clearing temperatures indicated decreasing trend as the chain length increasing due to dilution effect from the flexible terminal chain.

6.3 Series 3: 2-[3-Methoxy-(4-alkoxybenzoyloxy)phenyl]-benzothiazoles (nMOBZT) and 2-[3-ethoxy-(4-alkoxybenzoyloxy)-phenyl]benzothiazoles (nEOBZT)

Two sub-series of lateral-methoxy and ethoxy-substituted benzothiazole-based liquid crystals possessing two mesogenic core units connected by Schiff base linkage were successfully synthesized and characterized.



nMOBZT $R_1 = \text{OCH}_3$

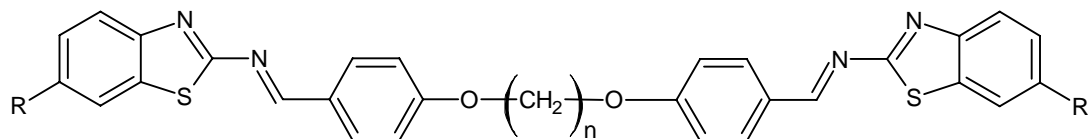
nEOBZT $R_1 = \text{OC}_2\text{H}_5$

Where $n = \text{C2-C10, C12, C14, C16, C18}$

For sub-series **nMOBZT**, short and higher chain members ($n = 2$ to $9, 16$ and 18) exhibited monotropic nematic phase while enantiotropic nematic phase was emerged from C_{10} to C_{14} derivatives. No smectic phase was observed in this series owing to the broader molecules resulted from the lateral methoxy group. All the synthesized compounds in sub-series **nEOBZT** exhibited mesomorphic properties. Monotropic nematic phase were observed in all the compounds. The clearing temperatures showed descending trend as the chain length increasing due to dilution effect from the flexible terminal chain.

6.4 Series 4: α,ω -Bis[6-methoxy-2-(4-alkoxybenzylidenamino)]-benzothiazoles(nOMeD) and α,ω -Bis[6-ethoxy-2-(4-alkoxybenzylidenamino)]-benzothiazoles (nOEtD).

Two sub-series of dimeric benzothiazole liquid crystals comprising 6-methoxy and 6-ethoxy substituted core units connected by Schiff base linkage were successfully prepared and characterized.



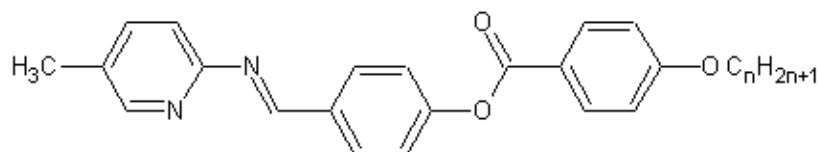
OMeD R= OCH₃ where n = C4, C6, C8, C10, C12

nOEtD R=OC₂H₅ where n = C4, C6, C8, C10, C12

For series **OMeD** and **OEtD**, all members are mesogenic compounds and exhibited only nematic phase.

6.5 Series 5: 5-Methyl-2-[4-(4-alkoxybenzoyloxy)benzylidenamino]-pyridines (**nPM5B**)

A series of thirteen pyridine-based liquid crystals possessing three mesogenic core units connected by Schiff base linkage were successfully prepared and characterized.

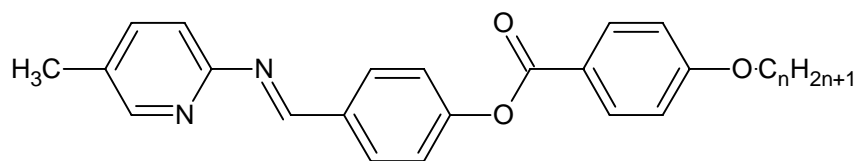


where n = C2- C10, C12, C14, C16, C18

For series **nPM5B**, it is clearly noticed that no liquid crystal phase was noticeable for those short carbon chain members (n = 2, 3, 4). In general, a rigid molecular structure is unfavoured in promoting mesophase. C5 to C10 members exhibited enantiotopic nematic phase. C₁₂ member exhibited monotropic SmC phase during cooling scan. However, C14 to C18 members exhibited SmA phase.

6.6 Series 6: 2-[4-(4-Alkoxybenzoyloxy)benzylidenanilines]-thiophenes (nTAP)

A series of thirteen thiophene-based liquid crystals comprising three mesogenic core units connected by Schiff base linkage were successfully synthesized and characterized.



where n = C2- C10, C12, C14, C16, C18

For series **nTAP**, all members are mesogenic compounds and exhibited only nematic phase.

6.7 Recommendation for Future Research

The calamitic liquid crystals reported in this thesis can be further analyzed in many ways and one example is the measurement of their dielectric properties. Heterocyclic derivatives have been considered as potential light-emitting materials due to their photophysical and fluorescent properties. The luminescent properties observed by such compounds were often affected by substituents and/or conjugation length. The study of UV-vis absorption and photoluminescence spectroscopy will definitely help us to understand the electron excitation and photoluminescent properties of the compounds.

Liquid crystals are fascinating materials with intermediate properties between those of solid and liquids. It is well known that molecular shape has a dominant influence on the existence of the liquid crystalline state. The design of novel thermotropic liquid crystals as advanced functional materials involves the suitable selection of a core fragment, linking group and terminal functionality. Therefore, the synthesis of liquid crystals is important. Materials must be prepared before their physical properties can be evaluated. Hence, they can be assessed for their suitability for use in devices such as liquid crystal display. The information obtained from this project hopefully leads to a better understanding of the chemistry of liquid crystals.

LIST OF REFERENCES

Journals:

- Aldred, M. P. *et al.*, 2005a. Synthesis and Mesomorphic Behaviour of Novel Light-emitting Liquid Crystals. *Liquid Crystals*, 32 (10), pp. 1251-1264.
- Aldred, M. P. *et al.*, 2005b. Heterocyclic Reactive Mesogens: Synthesis, Characterisation and Mesomorphic Behaviour. *Liquid Crystals*, 32 (8), pp. 951-965.
- Belmar, J. *et al.*, 1998. New Liquid Crystals Containing The Benzothiazol Unit: Amides and Azo Compounds. *Liquid Crystals*, 26 (3), pp. 389-396.
- Brown, J. *et al.*, 1989. Some Three-Ring Esters Containing a Five-Membered Heteroaromatic Ring. A Comparison of Liquid Crystal Properties. *Molecular Crystals and Liquid Crystals*, 173, pp. 121-140.
- Castles, F. *et al.*, 2010. Thermodynamically Stable Blue Phases, *Physical Review Letters*, 104, pp. 157801.
- Champa, R.A., 1973. Low Melting Liquid Crystalline Heterocycle Anils. *Molecular Crystals and Liquid Crystals*, 19 (3), pp. 233-247.
- Daneila, R.d.S. *et al.*, 2008. Synthesis of Liquid Crystals Materials Derived from Oxadiazole, Isoxazole and Tetrazole Heterocycles. *General Papers (Arkivoc)*, xvii, pp. 157-166.
- Dutta, G. K., Guha, S. and Patil, S., 2010. Synthesis of Liquid Crystalline Benzothiazole based Derivatives: A Study of Their Optical and Electrical Properties. *Organic Electronic*, 11, pp. 1-9.
- Gray, G. W., Harrison, K. J. and Nash, J. A., 1973. New Family of Nematic Liquid Crystals for Displays. *Electronic Letters*, 9, pp. 130-131.

- Godwon, J., Sienkowska, M.J., and Galewski, Z., 2006. Smectic Polymorphism of 4-decyloxybenzylidene-4'-alkyloxyanilines and Their Mixtures with Polar Standards of Mesophase. *Phase Transition*, 80 (3), pp. 217-229.
- Gallardo, H. *et al.*, 2009. Optical and Thermal Properties of Unsymmetrical Liquid Crystalline Compounds Based on Isoxazole. *Liquid Crystals*, 36 (8), pp. 839-845.
- Ha, S.T. *et al.*, 2009a. Heterocyclic Benzothiazole-based Liquid Crystals: Synthesis and Mesomorphic Properties. *Liquid Crystals*, 36 (9), pp. 917-925.
- Ha, S.T. *et al.*, 2009b. New Mesogenic Schiff Base Esters Comprising Benzothiazole Moiety: Synthesis and Mesomorphic Properties. *Chinese Chemical Letters*, 20, pp. 1081-1084.
- Ha, S.T. *et al.*, 2009c. Synthesis and Mesomorphic Behavior of Benzothiazole-based Liquid Crystals Having Terminal Methoxyl Group. *Chinese Chemical Letters*, 20, pp. 1449-1452.
- Ha, S.T. *et al.*, 2010a. Synthesis and Mesomorphic Properties of 6-Methoxy- and 6-Ethoxy-2-(2-hydroxy-4-alkanoxybenzylidenamino)benzothiazole. *Molecular Crystals Liquid Crystals*, 528, pp. 10-22.
- Ha, S.T. *et al.*, 2010b. Synthesis of New Schiff Base Ester Liquid Crystals with a Benzothiazole Core. *Liquid Crystals*, 37 (5), pp. 547-554.
- Ha, S.T. *et al.*, 2010c. Mesogenic Schiff Base Esters with benzothiazole Core: Synthesis and Phase Transition Studies. *Phase Transitions*, 83 (3), pp. 195-204.
- Ha, S.T. *et al.*, 2012, Mesomorphic Behaviour of New Benzothiazole Liquid Crystals Having Schiff Base Linker and Terminal Methyl group. *Chinese Chemical Letters*, 23, pp. 761-764.
- Henderson, P. A., Seddon, J. M., Imrie, C. T., 2005. Methylene- and Ether-linked Liquid Crystal Dimers II. Effect of Mesogenic Linking Unit and Terminal Chain Length. *Liquid Crystals*, 32 (11-12), pp. 1499-1513.

- Hird, M., 2007. Fluorinated Liquid Crystals-Properties and Applications, *Chemical Society Reviews*, 36, pp. 2070-2095.
- Hsieh, C. C., Liu, K.T. and Lai, C.K., 2006. Banana-shaped Mesogens: Odd-even Effect in Dimeric Twins. *Journal of the Chemical Society*, 53 (6), pp. 1397-1404.
- Huang, Y. *et al.*, 2009. Synthesis and Mesomorphic Behaviour of New 5-substituted-4-(thien-2-yl)phenyl Benzoates. *Liquid Crystals*, 36 (1), pp. 61-66.
- Huang, Y. and Ma, Q.L., 2010. Synthesis and Mesomorphic Properties of Three-Benzene-Ring-Containing Banana-Shaped Liquid Crystals. *Liquid Crystals*, 3637 (19), pp. 1119-1126.
- Iino, H. and Hanna, J., 2005. Ambipolar Charge Carrier Transport In Liquid Crystals. *Opto-Electronics Review*, 13 (4), pp. 295-302.
- Kadkin, O.N., Han, H. and Galyametdinov, Y. G., 2007. Synthesis, Computational Modeling and Liquid Crystalline Properties of Some [3] Ferrocenophane-Containing Schiff Bases and β -Aminovinylketone: Molecular Geometry –Phase Behaviour Relationship. *Journal of Organometallic Chemistry*, 692, pp. 5571-5582.
- Kardas, D. *et al.*, 2001. Synthesis and Properties of New Series of Mesogenic Compounds with Pyridine, Oxidopyridinium, Thienyl, and Furyl Moieties. *Journal of Materials Chemistry*, 11, pp. 741-748.
- Lai, C.K. *et al.*, 2005. Heterocyclic Benzoxazole-based Liquid Crystals. *Liquid Crystals*, 32 (1), pp. 85-94.
- Lai, L. L. *et al.*, 1996. Synthesis and Characterization of Liquid Crystalline Molecules Containing the Quinoline Unit. *Molecular Crystals Liquid Crystals*, 287, pp. 177-181.
- Liao, C.C. *et al.*, Wang, C.S., Sheu, H.S. and Lai, C.K., 2008. Symmetrical Dimer Liquid Crystals Derived from Benzoxazole. *Tetrahedron*, 64, pp. 7977-7985.

- Lu, Z. R and Yang L., 1991. A DSC Study of A New Series of Liquid Crystal-2(4-Alkoxybenzene)-6-Substituted Benthiazoles. *Thermochimica Acta*, 178, pp. 305-309.
- Luciano d. S. *et al.*, 2008. Synthesis of Liquid Crystals Materials Derived From Oxadiazole, Isoxazole and Tetrazole Heterocycles. *Arkivoc*, xvii, pp. 157-166.
- Majumdar K. C. *et al.*, 2009. Synthesis and Mesomorphic Behaviour of New Mesogenic Compounds Possessing a Cholesteryl Ester Moiety Connected to a Pyrimidine Core. *Tetrahedron Letters*, 50, pp. 1992-1995.
- Marin, L. *et al.*, 2009. Synthesis and Characterization of New Azomethine Derivatives Exhibiting Liquid Crystalline Properties. *Liquid Crystals*, 36 (1), pp. 21-32.
- Naganime, T. *et al.*, 2008. The Effect of the Linking Group on Mesogenic Properties of Three-ring Derivatives of P-caborane and Biphenyl. *Liquid Crystals*, 35, pp. 865-884.
- Nash, J. A. and Gray, G. W., 1974. Studies of Some Heterocyclic Mesogens. *Molecular Crystals Liquid Crystals*. 25, pp. 299-321.
- Prajapati, A. K., 1999. Effect of a Lateral Methyl Group on Azo-mesogens Containing The Naphthalene Moiety. *Liquid Crystals*, 27, pp. 1017-1020.
- Prajapati, A. K., Thakker, V. and Bonde, N., 2003. New Mesogenic Homologous Series of Schiff Base Cinnamates Comprising Naphthalene Moiety. *Molecular Crystals Liquid Crystals*, 393, pp. 41-48.
- Prajapati, A.K., Pandya, H. M. and Bonde, N. L., 2004. Naphthyl Azomesogens with Lateral Chloro Groups. *Journal of Chemical Sciences*, 116 (4), pp. 1-7.
- Prajapati, A.K., Bonde, N. L. and Patel, H. N., 2005. Mesogenic Schiff's Base Ester with Chloroethyl Tail. *Phase Transition*, 78, (6), pp. 507-513.

- Prajapati, A. K. and Bonde, N. L., 2006a. Synthesis of Two Naphthyl-containing Homologous Series of Mesogenic Ligands and the Related Metallomesogens Containing Cu(II). *Liquid Crystals*, 33, pp. 1189-1197
- Prajapati, A.K. and Bonde, N.L., 2006b. Mesogenic Benzothiazole Derivatives with Methoxy Substituents. *Journal of Chemical Sciences*, 118, pp. 203-210.
- Prajapati, A. K. and Varia, M. C., 2008. Azomesogens with Polar Chloro, Nitro and Phenolic –OH Substituents. *Liquid Crystals*, 35 (11), pp. 1271-1277.
- Prajapati, A. K. and Bonde, N. L., 2009. Mesogenic Benzothiazole Derivatives with a Polar Nitro Substituents. *Molecular Crystals Liquid Crystals*, 501, pp. 72-85.
- Prajapati, A.K. and Modi, V., 2010. Mesogenic Quinazolone Derivatives: Synthesis and Chracterisation. *Liquid Crystals*, 37 (10), pp. 1281-1288.
- Parra M. L. *et al.*, 2005. New Supramolecular Liquid Crystals Induced By Hydrogen Bonding Between Pyridyl-1,2,4,-Oxdiazole Derivatives and 2,5-Thiophene Dicarboxylic Acid.. *Liquid Crystals*, 32 (4), pp. 449-455.
- Reddy, R.A. and Sadashiva, B.K., 2004. Direct Transition From a Nematic Phase to a Polar Biaxial Smectic A Phase in a Homologous Series of Unsymmetrically Substituted Bent-Core Compounds, *Journal of Materials Chemistry*, 14, pp. 310-319.
- Rao, N.V.S. *et al.*, 2009. Mononuclear and Binuclear Complexes of Salicylidene Schiff Bases: Synthesis and Mesogenic Properties. *Liquid Crystals*, 36 (4), pp. 409-423.
- Seed, A. J. *et al.*, 2003. Novel, Highly Polarizable Thiophene Derivatives for Use in Nonlinear Optical Applications. *Liquid Crystals*, 30 (9), pp. 1089-1107.
- Seed, A., 2007. Synthesis of Self-organizing Mesogenic Materials Containing a Sulfur-based Five-membered Heterocyclic Core, *Chemistry Society Reviews*, 36, pp. 2046-2069.

- Shama, S., Lacey, D. and Wilson, P. 2003a. The Synthesis and Thermal Properties of Novel Heterocyclic Liquid Crystalline Materials. *Molecular Crystals Liquid Crystals*, 401, pp. 111[225]-121[235].
- Shama, S., Lacey, D. and Wilson, P. 2003b. Synthesis and Characterization of a Range of Heterocyclic Liquid Crystalline Material Incorporating the Novel Thiophene-Pyrimidine Moiety. *Liquid Crystals*, 30, No. 4, pp. 451-461.
- Sung, H. H. and Lin, H. C., 2004. Effect of Polar Substituents on the Properties of 1,3,4-Oxadiazole-based Liquid Crystalline Materials Containing Asymmetric Cores. *Liquid Crystals*, 31, pp. 831-396.
- Six, K. *et al.*, 2001. Investigation of Thermal Properties of Glassy Itraconazole: Identification of a Monotropic Mesophase. *Thermochimica Acta*, 376, pp. 175-181.
- Thaker, B. T., Kanojiya, J. B. and Tandel, R. S., 2010. Effects of Different Terminal Substituents on The Mesomorphic Behavior of Some Azo-Schiff Base and Azo-ester-Based Liquid Crystals. *Molecular Crystals Liquid Crystals*, 528, pp. 120-137.
- Thaker, B. T. *et al.*, 2007. Synthesis, Characterization, and Mesomorphic Properties of New Liquid-Crystalline Compounds involving Ester-Azomethine Central Linkages, Lateral Substitution, and a Thiazole Ring. *Molecular Crystals Liquid Crystals*, 466, pp. 13-22.
- Toba, M. *et al.*, 2005. Synthesis and Optical Properties of Poly(thiophene) Derivatives with Benzothiazole Moiety. *Journal of Synthetic Metals*, 152, pp. 197-200.
- Tokunaga, K., Iin H. and Hanna, J., 2007. Reinvestigation of Carrier Transport Properties in Liquid Crystalline 2-Phenylbenzothiazole Derivatives. *The Journal of Physical Chemistry B*, 111 (42), pp. 12041-12044.
- Venema, F. *et al.*, 1994. Synthesis and Conformation Behaviour of Novel Cyclodextrin Hetero-Dimers. *Tetrahedron Letters*, 35 (46), pp. 8661-8664.
- Wang, H. S. *et al.*, 2008. Novel Metallomesogens Derived from Heterocyclic

- Benzoxazoles. *Tetrahedron*, 64, pp. 4939-4948.
- Yang, P.J. and Lin, H.C., 2006. Synthesis and Characterization of Achiral Banana-Shaped Liquid Crystalline Molecules Containing Bisnaphthyl Moieties. *Liquid Crystals*, 33 (5), pp. 587-603.
- Yeap, G. Y. *et al.*, 2002. Synthesis and Mesomorphic Properties of Schiff Base Ester *p*-n-octadecanoyloxybenzylidene-*p*-cyano, *p*-hydroxy, *p*-nitro, and *p*-carboxyanilines. *Molecular Crystals Liquid Crystals*, 381, pp. 169-178.
- Yeap, G. Y. *et al.*, 2004. Synthesis and Mesomorphic Properties of Schiff Base Esters *Ortho*-hydroxy-*para*-alkyloxybenzylidene-*para*-substituted Anilines. *Molecular Crystals Liquid Crystals*, 423, pp. 73-84.
- Yeap, G. Y. *et al.*, 2006a. Synthesis, Physical and Mesomorphic Properties of Schiff's Base Esters Containing *ortho*-, *meta*, and *para*-Substituents in Benzylidene-4'-alkanoyloxyanilines. *Liquid Crystals*, 33, pp. 205-211.
- Yeap, G. Y. *et al.*, 2006b. Nematic and Smectic A Phases in *Ortho*-Hydroxy-*Para*-Hexadecanoyloxybenzylidene-*Para*-Substituted Anilines. *Molecular Crystals Liquid Crystals*, 452, pp. 63-72.
- Yeap, G. Y. *et al.*, 2009. Non-Symmertric Liquid Crystal Dimers: High Thermal Stability in Nematic Phase Enhanced by Thiophene-2-Carboxylate Moiety. *Molecular Crystals Liquid Crystals*, 506, pp. 134-149.
- Yelamaggad, C.V. *et al.*, 2006. Blue Phase, Smectic Fluids and Unprecedented Sequences in Liquid Crystal Dimers. *Chemistry Material*, 18, pp. 6100-6102.
- Yamaguchi, A. *et al.*, 2004. Unusual Smectic Phases Organized by Novel λ -shaped Mesogenic Molecules. *Journal of Material Chemistry*, 15, pp. 280-288.
- Zhang, D. *et al.*, 1997. Synthesis of Novel Liquid Crystal Compounds with Aromatic Amide Mesogenic Cores. *Liquid Crystals*, 23 (3), pp. 357-363.

Book Chapter:

- Collings , P. J. and Hird, M., 1997a. Introduction to a Special Phase of Matter. In: *Introduction to Liquid Crystal Chemistry and Physic.* (pp 1-16). London: Taylor and Francis Ltd.
- Collings , P. J. and Hird, M., 1997b. Calamitic Liquid Crystals - Nematic and Smectic Mesophases. In: *Introduction to Liquid Crystal Chemistry and Physic.* (pp 43-77). London: Taylor and Francis Ltd.
- Collings , P. J. and Hird, M., 1997c. Identification of Liquid Crystal Phases - Mesophase Characterisation. In: *Introduction to Liquid Crystal Chemistry and Physic.* (pp 177-194). London: Taylor and Francis Ltd.
- Demus, D and Richter, L., 1978. Plates, In: *Texture of Liquid Crystals.* (pp 105-211). New York: Verlag Chemie.
- Dierking, I., 2003. Color Plates. In: *Texture of Liquid Crystals.* (pp 167-212). Weinheim: Wiley-Vch GmbH & Co. KGaA.
- Fisch, M.R. and Kumar, S., 2001. *Introduction of Liquid Crystals.* In: *Liquid Crystals: Experimental Study and Physical Properties and Phase Transition.* (pp 1-26). United Kingdom: Cambridge University Press.
- Field, L.D., Sternhell, S. and Kalman, J.R., 1995. Mass Spectrometry. In: *Organic Structures from Spectra.* 2nd Edition.(pp 18-28). New York: John Wiley.
- Gray, G. W., 1962. The Regular Trends of Mesomorphic Transition Temperatures for Homologous Series. In: *Molecular Structure and the Properties of Liquid Crystals.* (pp 197-238). London: Academic Press.
- Kelker, H. and Hatz, R., 1980. Chemical Constitution. In: *Handbook of Liquid Crystal.* (pp 35-67). Florida: Verlag Chemie.
- Neubert, M. E., 2001. Chemical Structure-Properties Relationship. In: *Liquid Crystal: Experimental Study of Physical Properties and Phase Transitions.*

(pp 393-465). United Kingdom: Cambridge University Press.

Pavia, D. L., Lampman, G. M. and Kriz, G. S., 2001. Mass Spectrometry. In: *Introduction to Spectroscopy*. 3rd Edition. (pp 394-430). Australia: Thomson Learning, Inc.

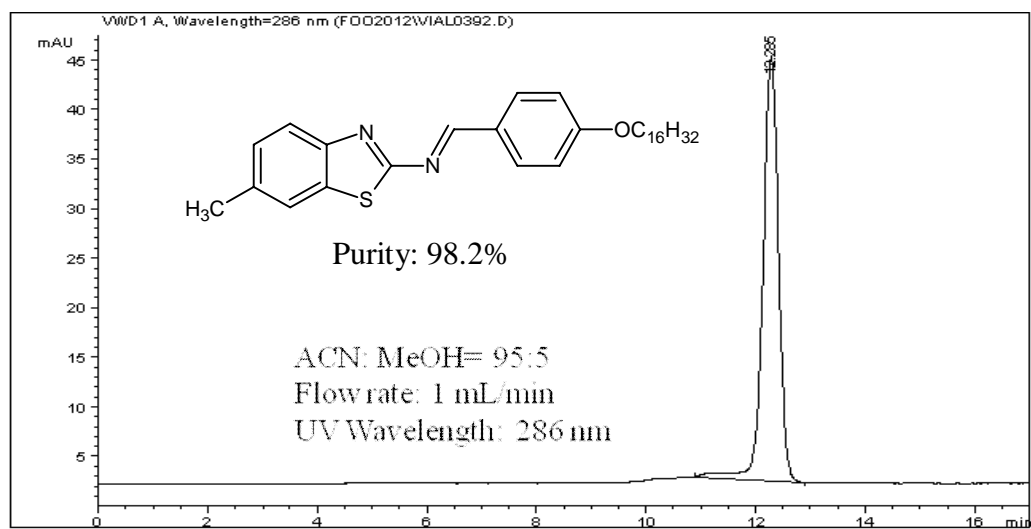
Silverstein, R. M. and Webster, F. X., 1997. Mass Spectrometry. In: *Spectrometric Identification of Organic Compounds*. 6th Edition. (pp 2-36). New York: John Wiley & Sons.

Singh, S., 2002. Lyotropic Liquid Crystals. In: *Liquid Crystals Fundamentals*. (pp 453-457). Singapore: World Scientific Publishing Co. Pte. Ltd.

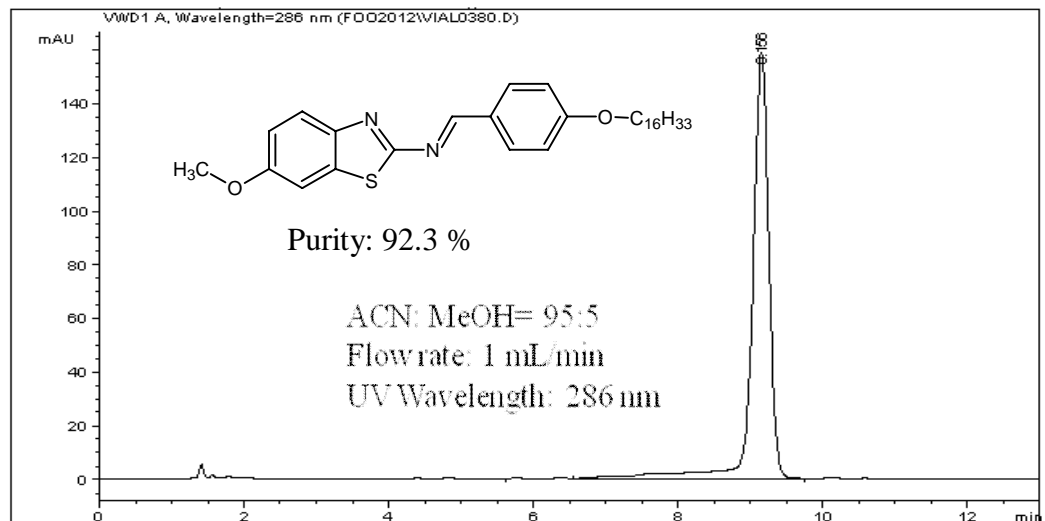
LIST OF PUBLICATIONS

Ha, S.T., Foo, K.L., Lin, H.C., Ito, M.M., Abe, K., Kunbo, K. and Sastry, S.S. 2012, Mesomorphic Behaviour of New Benzothiazole Liquid Crystals Having Schiff Base Linker and Terminal Methyl group. *Chinese Chemical Letters*, 23, pp. 761-764. (Appendix 8)

Appendix 1A

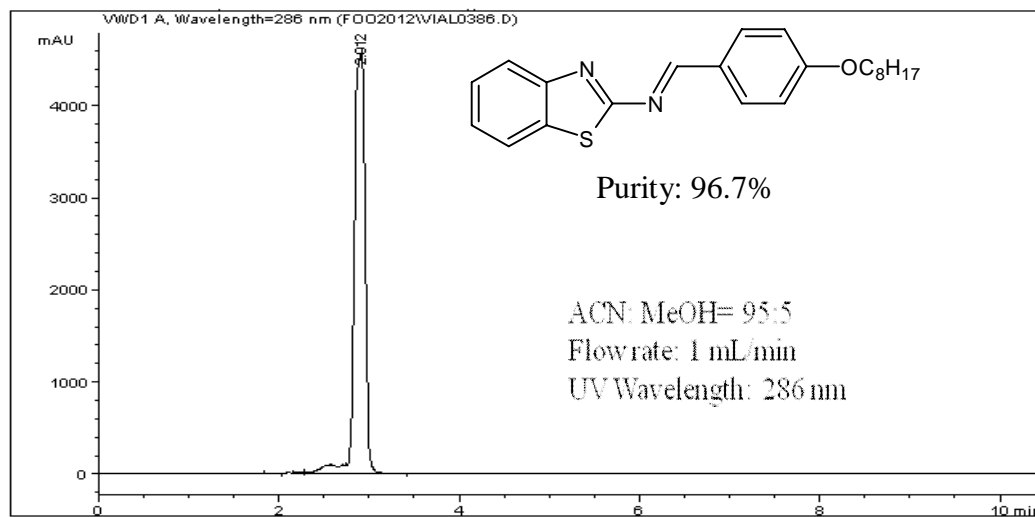


HPLC chromatogram of the representative compound 16MeBTH.

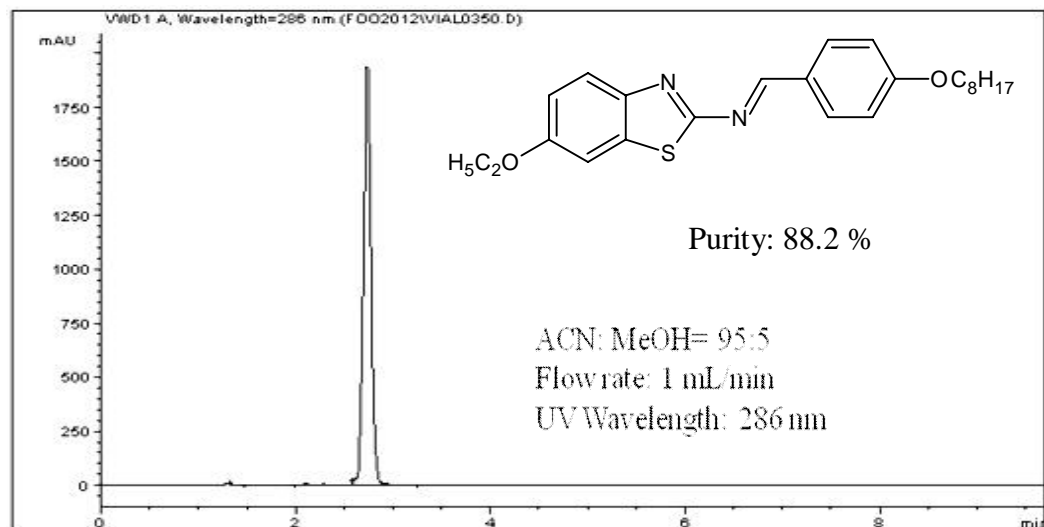


HPLC chromatogram of the representative compound 16OMeBTH.

Appendix 1B



HPLC chromatogram of the representative compound 8HBZT.



HPLC chromatogram of the representative compound 8OEtBTH.

Appendix 1C

Retardation factor of compounds nMeBTH.

Compound	R _f value	
	Chloroform	Chloroform: Ethyl Acetate (1:1)
2MeBTH	0.76	0.70
3MeBTH	0.75	0.71
4MeBTH	0.77	0.68
5MeBTH	0.73	0.69
6MeBTH	0.75	0.70
7MeBTH	0.78	0.74
8MeBTH	0.76	0.74
9MeBTH	0.75	0.73
10MeBTH	0.77	0.71
12MeBTH	0.75	0.70
14MeBTH	0.75	0.72
16MeBTH	0.79	0.71
18MeBTH	0.78	0.72

Retardation factor of compounds nOMeBTH.

Compound	R _f value	
	Chloroform	Chloroform: Ethyl Acetate (1:1)
2OMeBTH	0.83	0.67
3OMeBTH	0.82	0.68
4OMeBTH	0.83	0.68
5OMeBTH	0.84	0.69
6OMeBTH	0.86	0.70
7OMeBTH	0.83	0.70
8OMeBTH	0.84	0.71
9OMeBTH	0.82	0.68
10OMeBTH	0.81	0.69
12OMeBTH	0.84	0.67
14OMeBTH	0.82	0.71
16OMeBTH	0.82	0.70
18OMeBTH	0.83	0.71

Appendix 1D

Retardation factor of compounds nHBZT.

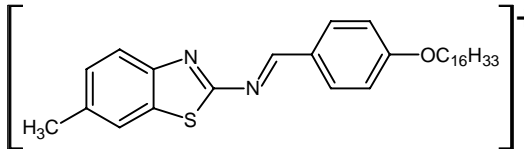
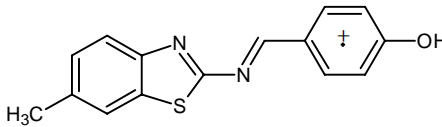
Compound	R _f value	
	Chloroform	Chloroform: Ethyl Acetate (1:1)
2HBZT	0.77	0.85
3HBZT	0.76	0.86
4HBZT	0.78	0.85
5HBZT	0.76	0.86
6HBZT	0.78	0.84
7HBZT	0.78	0.85
8HBZT	0.77	0.85
9HBZT	0.77	0.85
10HBZT	0.77	0.84
12HBZT	0.78	0.83
14HBZT	0.76	0.86
16HBZT	0.77	0.84
18HBZT	0.77	0.85

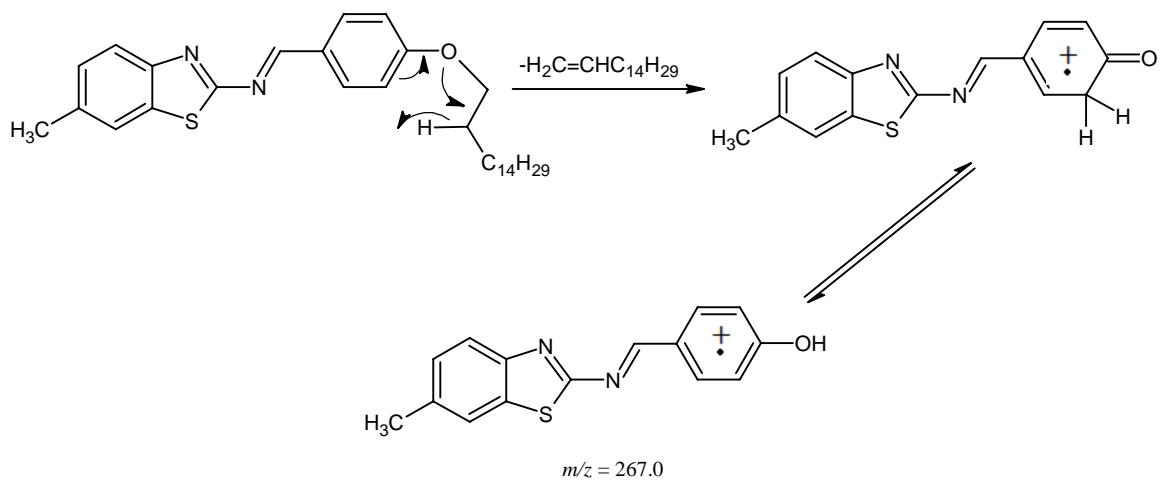
Retardation factor of compounds nOEtBTH.

Compound	R _f value	
	Chloroform	Chloroform: Ethyl Acetate (1:1)
2OEtBTH	0.64	0.76
3OEtBTH	0.65	0.76
4OEtBTH	0.64	0.78
5OEtBTH	0.66	0.78
6OEtBTH	0.67	0.77
7OEtBTH	0.68	0.78
8OEtBTH	0.68	0.80
9OEtBTH	0.66	0.79
10OEtBTH	0.67	0.78
12OEtBTH	0.68	0.76
14OEtBTH	0.66	0.77
16OEtBTH	0.67	0.78
18OEtBTH	0.68	0.78

Appendix 1E

Mass spectrometry data of 16MeBTH

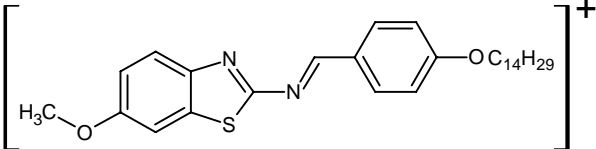
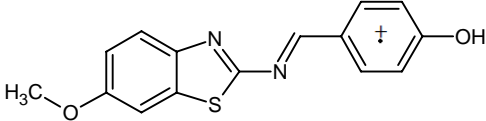
m/z	Relative abundance	Corresponding fragment
494.4	10.64	M+2, with isotope of ^{34}S
493.4	31.31	M+1, with isotope such as ^{13}C , ^2H , ^{15}N or ^{17}O
492.4	91.57	
267.0	100.0	

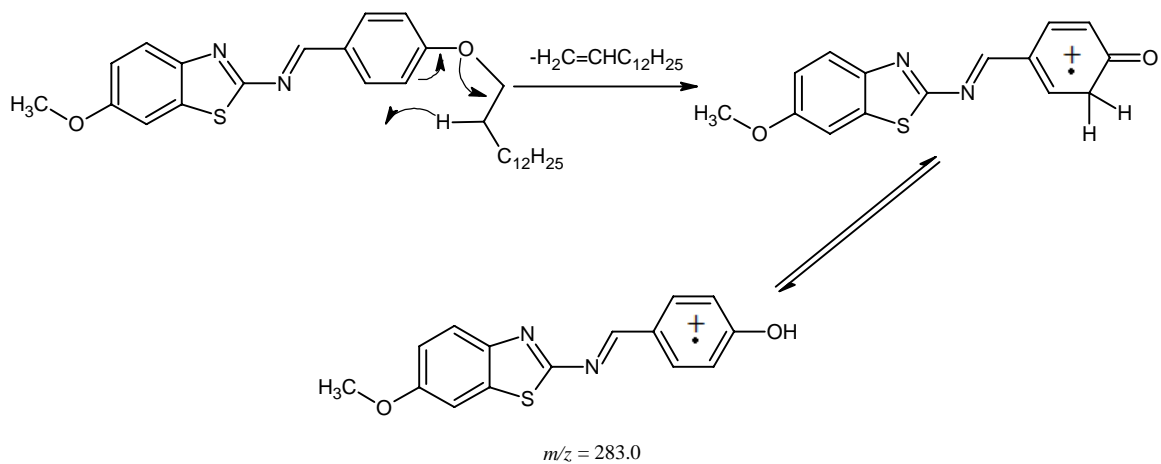


Mass fragmentation of β cleavage of 16MeBTH

Appendix 1F

Mass spectrometry data of 14OMeBTH

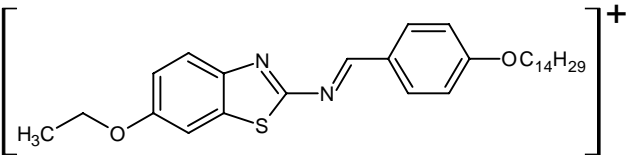
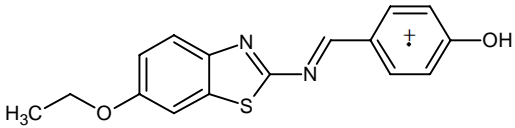
m/z	Relative abundance	Corresponding fragment
482.4	10.61	M+2, with isotope of ^{34}S
481.4	32.21	M+1, with isotope such as ^{13}C , ^2H , ^{15}N or ^{17}O
480.4	100.0	
283.0	49.45	

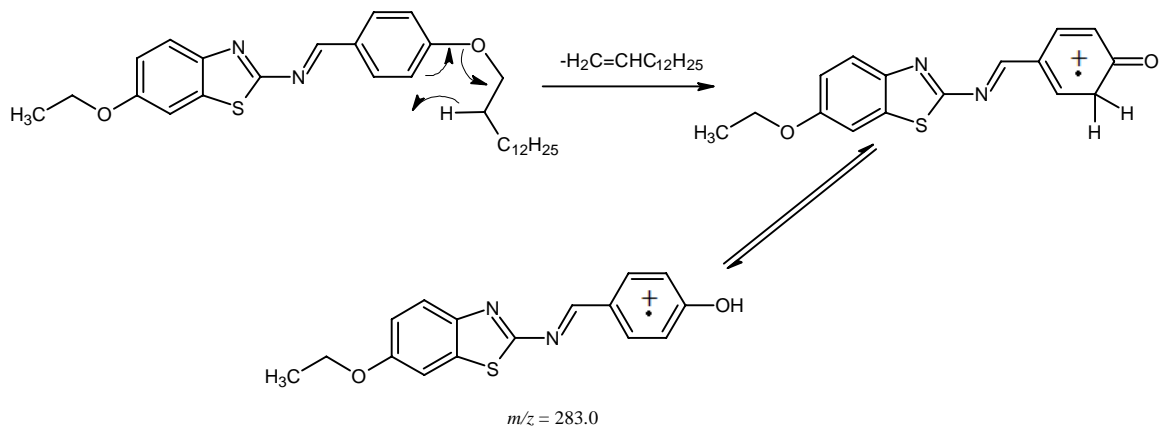


Mass fragmentation of β -cleavage of 14OMeBTH

Appendix 1G

Mass spectrometry data of 14OEtBTH

m/z	Relative abundance	Corresponding fragment
496.4	11.65	M+2, with isotope of ^{34}S
495.4	33.59	M+1, with isotope such as ^{13}C , ^2H , ^{15}N or ^{17}O
494.4	100.0	
297.1	22.56	

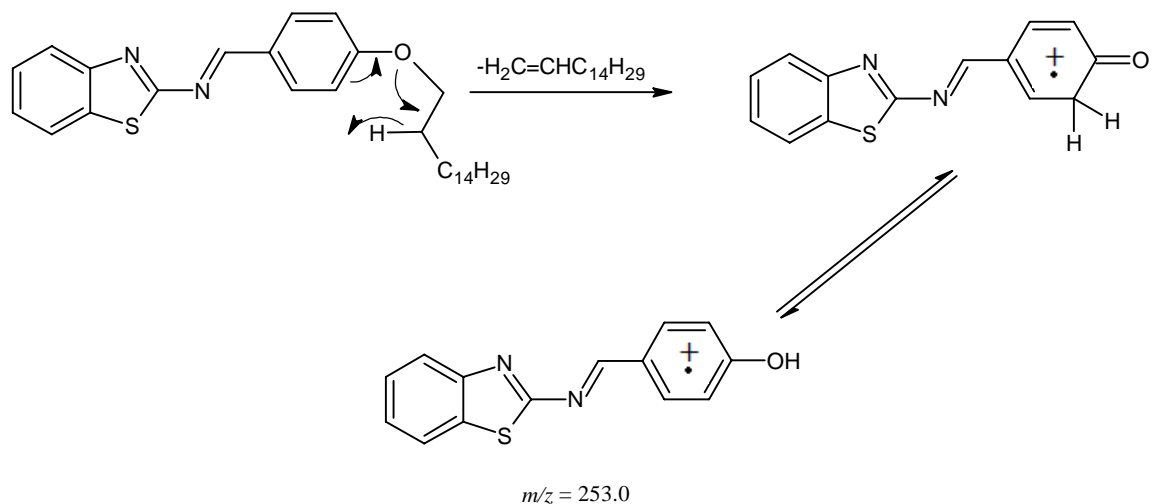


Mass fragmentation of β -cleavage of 14OEtBTH

Appendix 1H

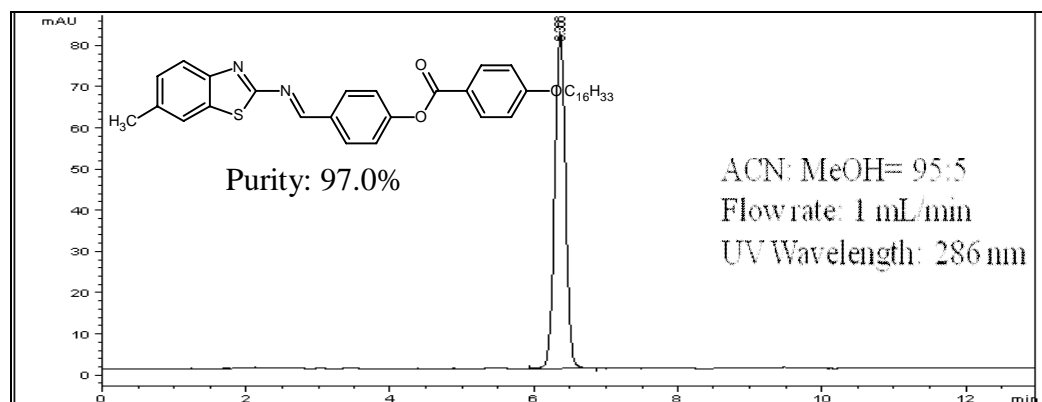
Mass spectrometry data of 16HBZT

m/z	Relative abundance	Corresponding fragment
480.4	6.99	M+2, with isotope of ^{34}S
479.4	21.92	M+1, with isotope such as ^{13}C , ^2H , ^{15}N or ^{17}O
478.4	63.35	
253.0	100.0	

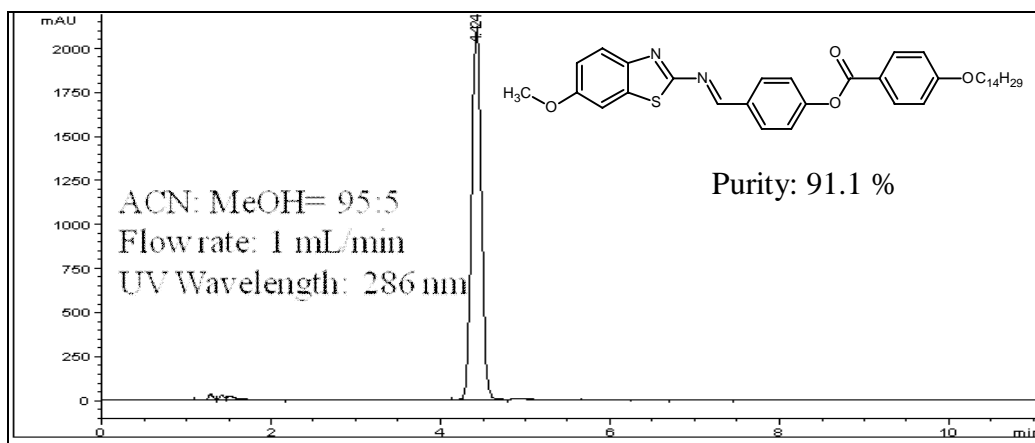


Mass fragmentation of β cleavage of 16HBZT.

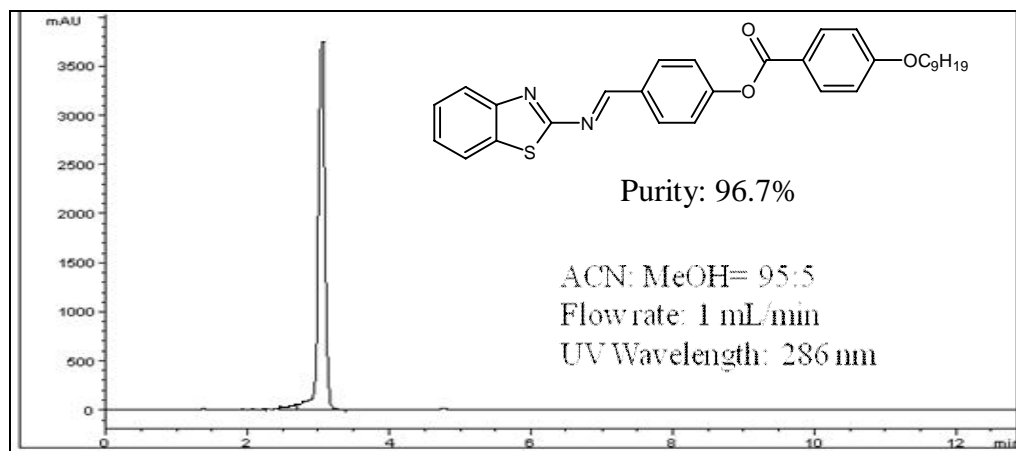
Appendix 2A



HPLC chromatogram of the representative compound 16Me3R.



HPLC chromatogram of the representative compound 14OMe3R.



HPLC chromatogram of the representative compound 9HB3R.

Appendix 2B

Retardation factor of compounds nMe3R.

Compound	R _f value	
	Chloroform	Chloroform: Ethyl Acetate (1:1)
2Me3R	0.66	0.81
3Me3R	0.68	0.83
4Me3R	0.67	0.84
5Me3R	0.67	0.82
6Me3R	0.66	0.81
7Me3R	0.67	0.80
8Me3R	0.68	0.83
9Me3R	0.67	0.84
10Me3R	0.68	0.85
12Me3R	0.69	0.81
14Me3R	0.69	0.82
16Me3R	0.71	0.87
18Me3R	0.70	0.88

Retardation factor of compounds nOMe3R.

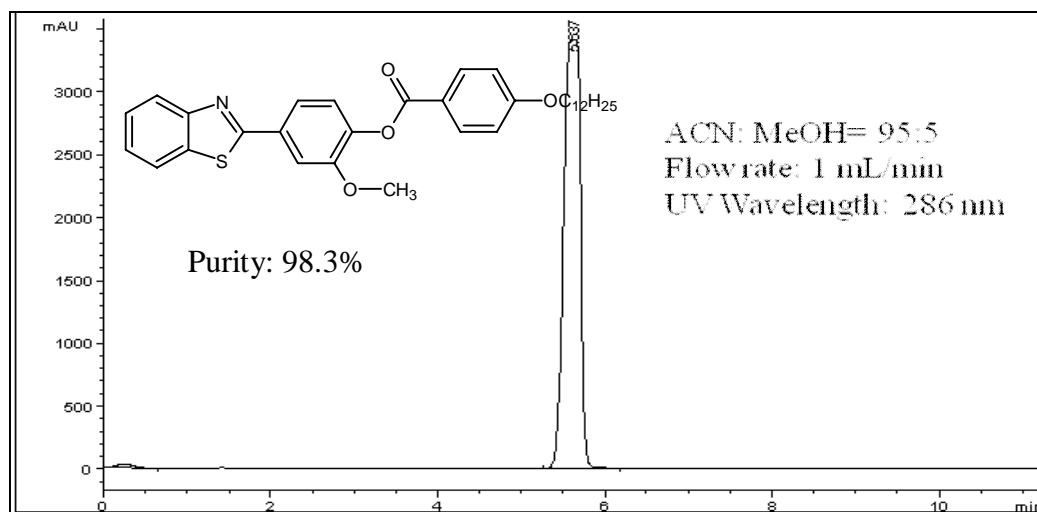
Compound	R _f value	
	Chloroform	Chloroform: Ethyl Acetate (1:1)
2OMe3R	0.70	0.80
3OMe3R	0.71	0.82
4OMe3R	0.71	0.82
5OMe3R	0.72	0.83
6OMe3R	0.71	0.84
7OMe3R	0.72	0.85
8OMe3R	0.71	0.84
9OMe3R	0.71	0.84
10OMe3R	0.72	0.83
12OMe3R	0.73	0.85
14OMe3R	0.74	0.86
16OMe3R	0.73	0.84
18OMe3R	0.74	0.85

Appendix 2C

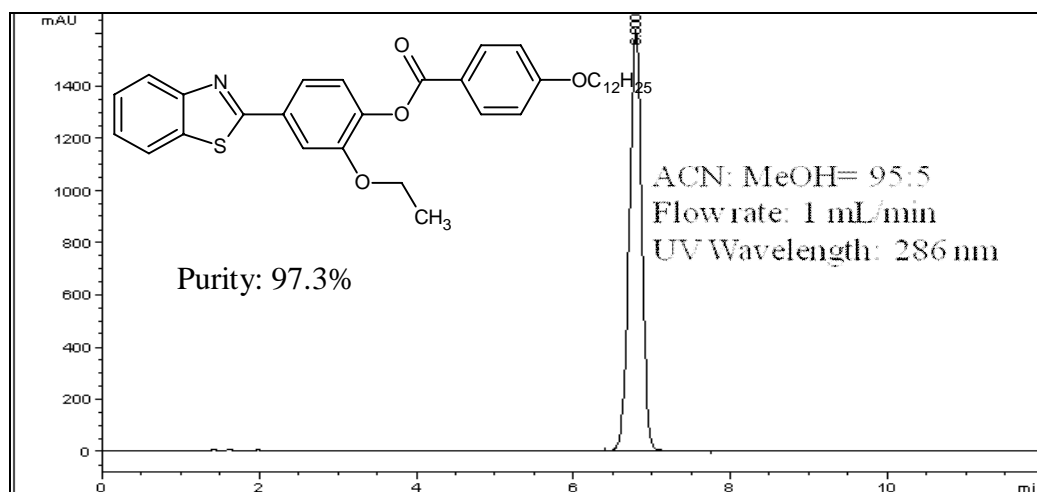
Retardation factor of compounds nHB3R.

Compound	R _f value	
	Chloroform	Chloroform: Ethyl Acetate (1:1)
2HB3R	0.61	0.80
3HB3R	0.62	0.81
4HB3R	0.61	0.85
5HB3R	0.61	0.82
6HB3R	0.63	0.84
7HB3R	0.62	0.84
8HB3R	0.61	0.83
9HB3R	0.62	0.84
10HB3R	0.63	0.82
12HB3R	0.63	0.84
14HB3R	0.64	0.85
16HB3R	0.63	0.84
18HB3R	0.64	0.86

Appendix 3A



HPLC chromatogram of the representative compound 12MOBZT.



HPLC chromatogram of the representative compound 12EOBZT.

Appendix 3B

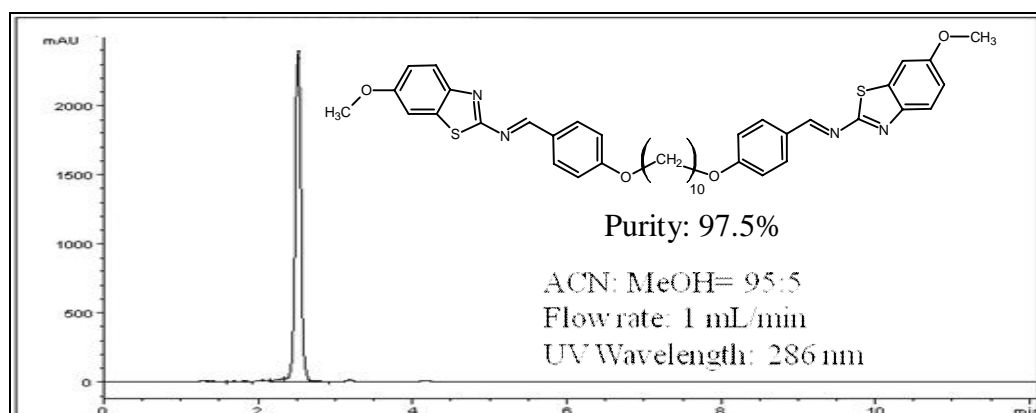
Retardation factor of compounds nMOBZT.

Compound	R _f value	
	Chloroform	Chloroform: Ethyl Acetate (1:1)
2MOBZT	0.74	0.80
3MOBZT	0.73	0.82
4MOBZT	0.71	0.81
5MOBZT	0.73	0.82
6MOBZT	0.72	0.80
7MOBZT	0.71	0.83
8MOBZT	0.75	0.80
9MOBZT	0.72	0.82
10MOBZT	0.75	0.81
12MOBZT	0.72	0.80
14MOBZT	0.73	0.82
16MOBZT	0.71	0.80
18MOBZT	0.75	0.83

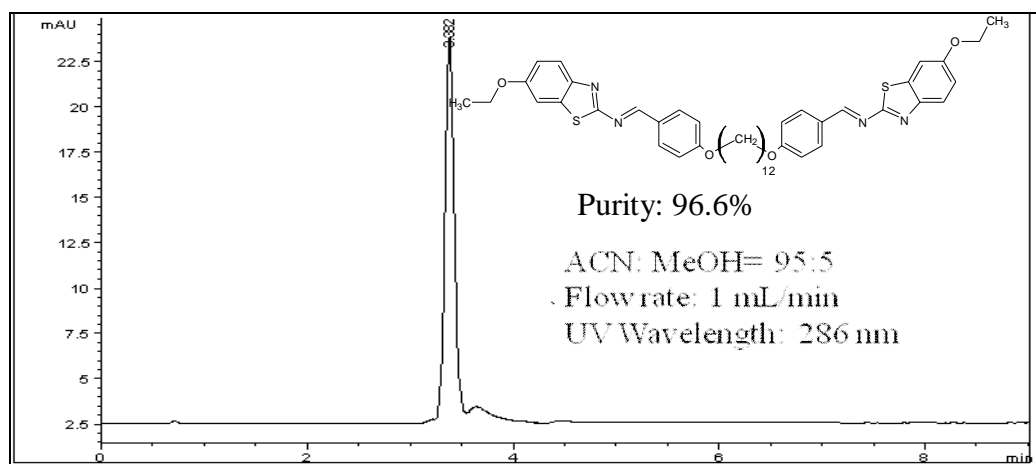
Retardation factor of compounds nEOBZT.

Compound	R _f value	
	Chloroform	Chloroform: Ethyl Acetate (1:1)
2EOBZT	0.71	0.80
3EOBZT	0.72	0.82
4EOBZT	0.71	0.81
5EOBZT	0.68	0.82
6EOBZT	0.69	0.82
7EOBZT	0.71	0.81
8EOBZT	0.71	0.80
9EOBZT	0.69	0.80
10EOBZT	0.70	0.81
12EOBZT	0.69	0.82
14EOBZT	0.68	0.82
16EOBZT	0.70	0.83
18EOBZT	0.71	0.84

Appendix 4A



HPLC chromatogram of the representative compound 10OMeD.



HPLC chromatogram of the representative compound 12OEtD.

Appendix 4B

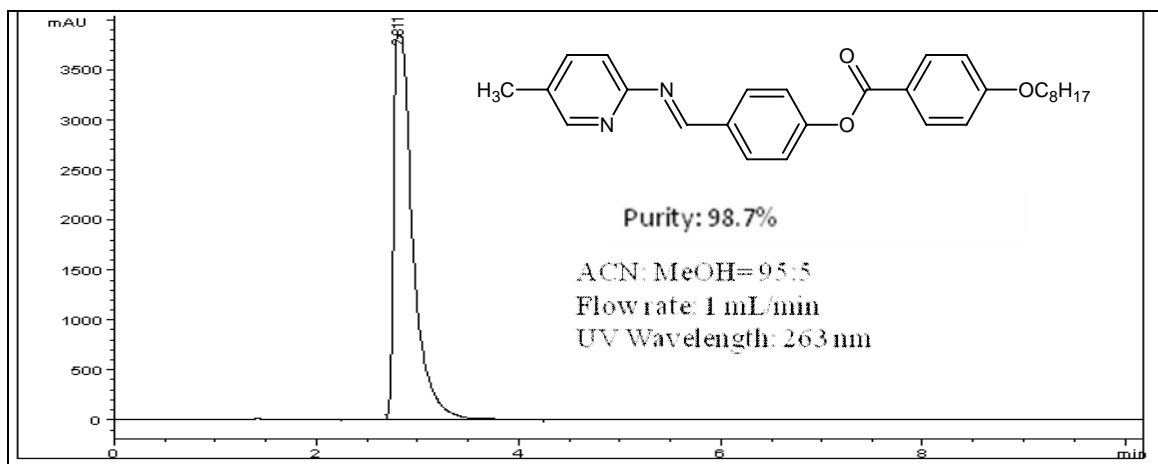
Retardation factor of compounds nOMeD.

Compound	R _f value	
	Chloroform	Chloroform: Ethyl Acetate (1:1)
4OMeD	0.83	0.68
6OMeD	0.86	0.70
8OMeD	0.84	0.71
10OMeD	0.81	0.69
12OMeD	0.84	0.67

Retardation factor of compounds nOEtD.

Compound	R _f value	
	Chloroform	Chloroform: Ethyl Acetate (1:1)
4OEtD	0.83	0.68
6OEtD	0.86	0.70
8OEtD	0.84	0.71
10OEtD	0.81	0.69
12OEtD	0.84	0.67

Appendix 5A

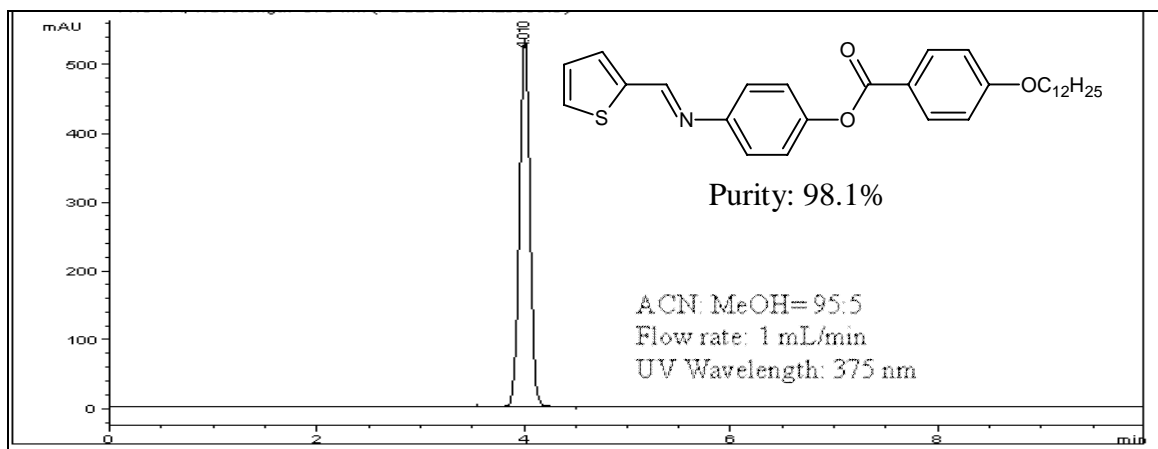


The HPLC chromatogram of the representative compound 8PM5B.

Retardation factor of compounds nPM5B.

Compound	R _f value	
	Chloroform	Chloroform: Ethyl Acetate (1:1)
2PM5B	0.68	0.76
3PM5B	0.69	0.78
4PM5B	0.70	0.77
5PM5B	0.70	0.76
6PM5B	0.69	0.78
7PM5B	0.70	0.77
8PM5B	0.69	0.78
9PM5B	0.71	0.77
10PM5B	0.70	0.78
12PM5B	0.71	0.77
14PM5B	0.66	0.76
16PM5B	0.65	0.78
18PM5B	0.65	0.79

Appendix 6A



The HPLC chromatogram of the representative compound 12TAP.

Retardation factor of compounds nTAP.

Compound	R _f value	
	Chloroform	Chloroform: Ethyl Acetate (1:1)
2TAP	0.68	0.81
3TAP	0.69	0.82
4TAP	0.70	0.83
5TAP	0.70	0.82
6TAP	0.69	0.84
7TAP	0.70	0.82
8TAP	0.69	0.83
9TAP	0.71	0.80
10TAP	0.70	0.81
12TAP	0.71	0.80
14TAP	0.66	0.79
16TAP	0.65	0.79
18TAP	0.65	0.76

Appendix 7A

¹H NMR spectral data of compound 12OMeBTH in CDCl₃

Proton Number	Chemical Shift, δ (ppm)	Integrals	Multiplicity*	Coupling Constant, J (Hz)
H11	8.92	1H	s	-
H13,H13'	7.96	2H	d	8.7
H9	7.87	1H	d	9.0
H6	7.31	1H	s	-
H8	7.06	1H	d	8.7
H14,H14'	6.92	2H	d	8.7
H19	4.06	2H	t	6.6
H17	3.90	2H	s	-
H20	1.81	2H	p	7.8
H21-H29	1.29-1.47	18H	m	-
H30	0.90	3H	t	6.6

Note:

TMS was used as an internal standard.

*s=singlet,

d=doublet

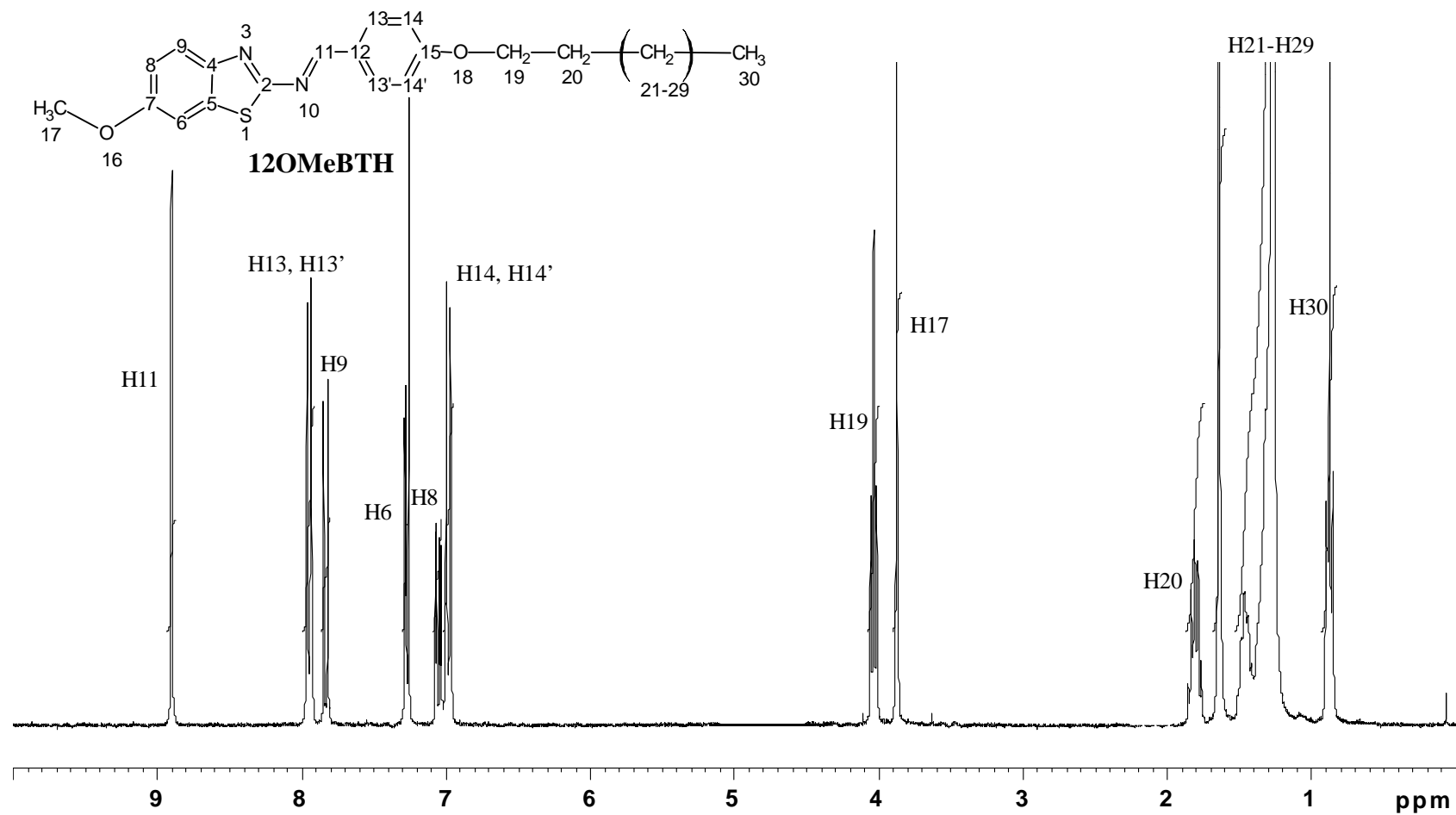
t=triplet

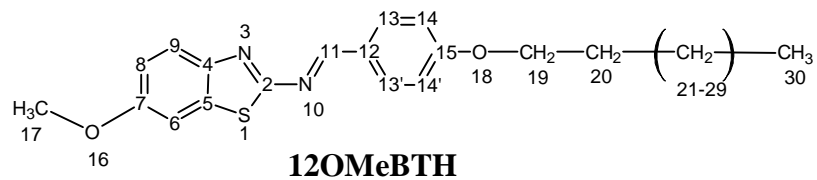
p=quintet

m=multiplet

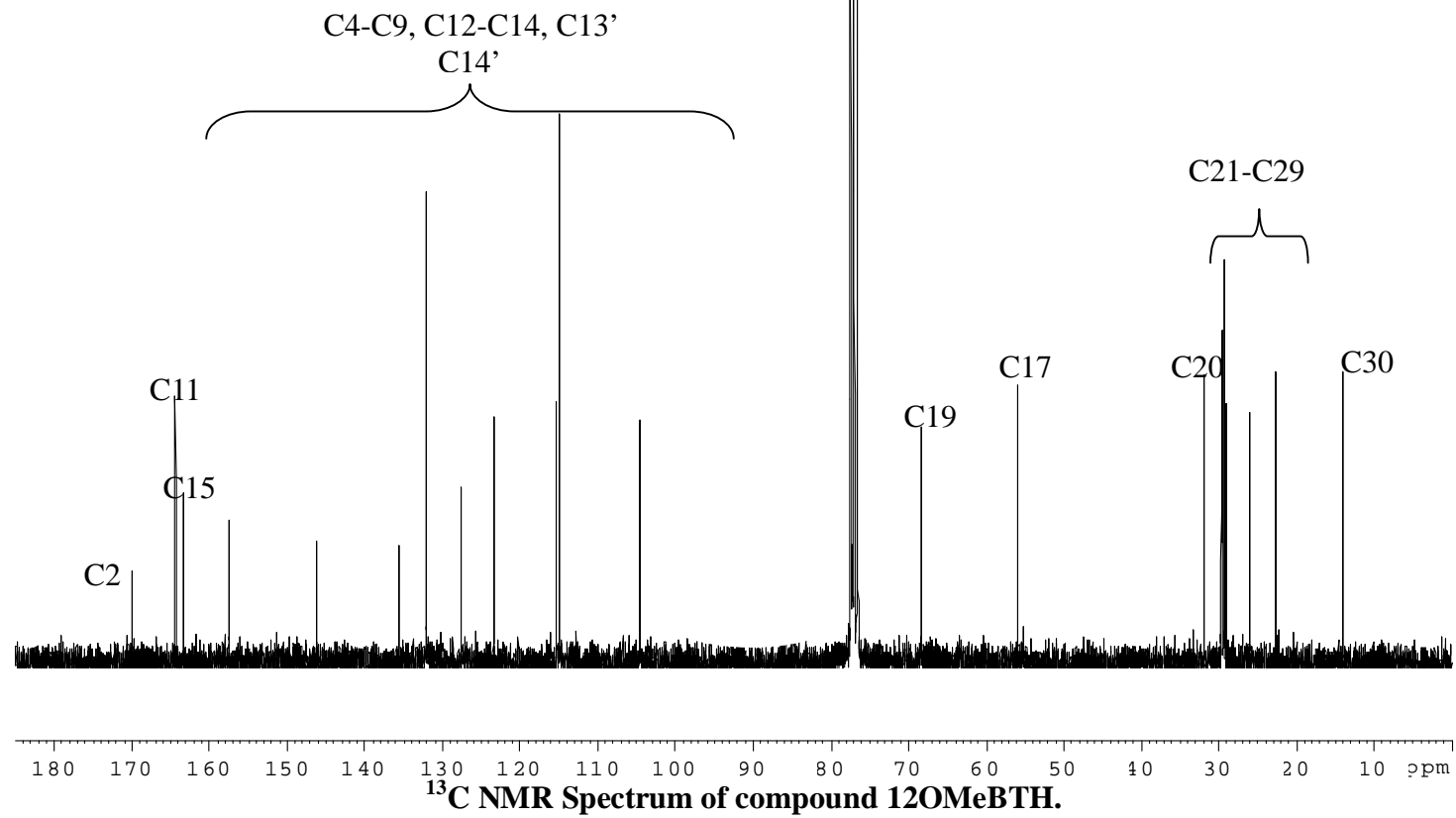
¹³C NMR spectral data of compound 12OMeBTH in CDCl₃

Carbon Number	Chemical Shift , δ (ppm)
C2	169.94
C11	164.45
C15	163.44
C4-C9, C12-C14, C13' and C14'	157.54
	146.18
	135.58
	132.15
	127.59
	123.47
	115.38
	114.99
	104.56
C19	68.39
C17	55.81
C20	31.90
C19-C30	29.64
	29.62
	29.57
	29.54
	29.33
	29.10
	25.97
C29	22.67
C30	14.08





CDCl₃



Appendix 7B

¹H NMR spectral data of compound 12OEtBTH in CDCl₃

Proton Number	Chemical Shift, δ (ppm)	Integrals	Multiplicity*	Coupling Constant, J (Hz)
H11	8.92	1H	s	-
H13,H13'	7.95	2H	d	9.0
H9	7.83	1H	d	9.0
H6	7.29	1H	s	-
H8	7.05	1H	d	9.0
H14,H14'	6.99	2H	d	8.7
H17	4.08	2H	q	7.2
H20	4.03	2H	t	6.6
H21	1.79	2H	p	7.8
H18	1.45	3H	t	6.9
H22-H30	1.29-1.45	18H	m	-
H31	0.88	3H	t	6.3

Note:

TMS was used as an internal standard.

*s=singlet,

d=doublet

t=triplet

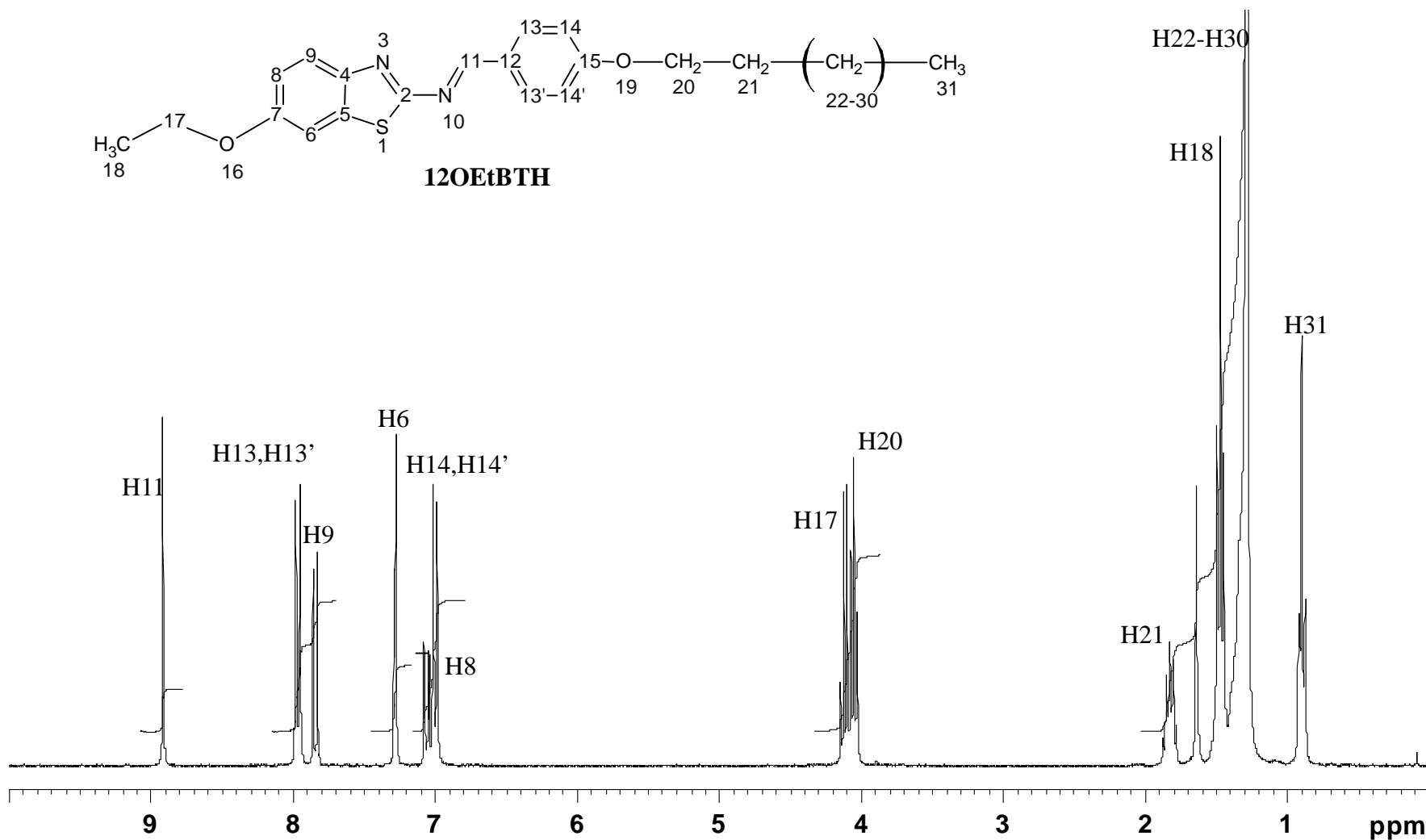
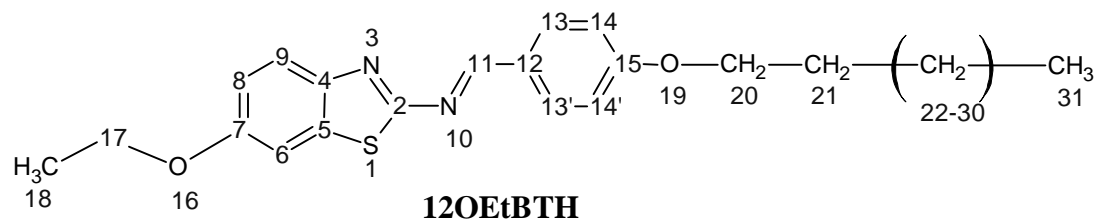
q=quartet

p=pentet

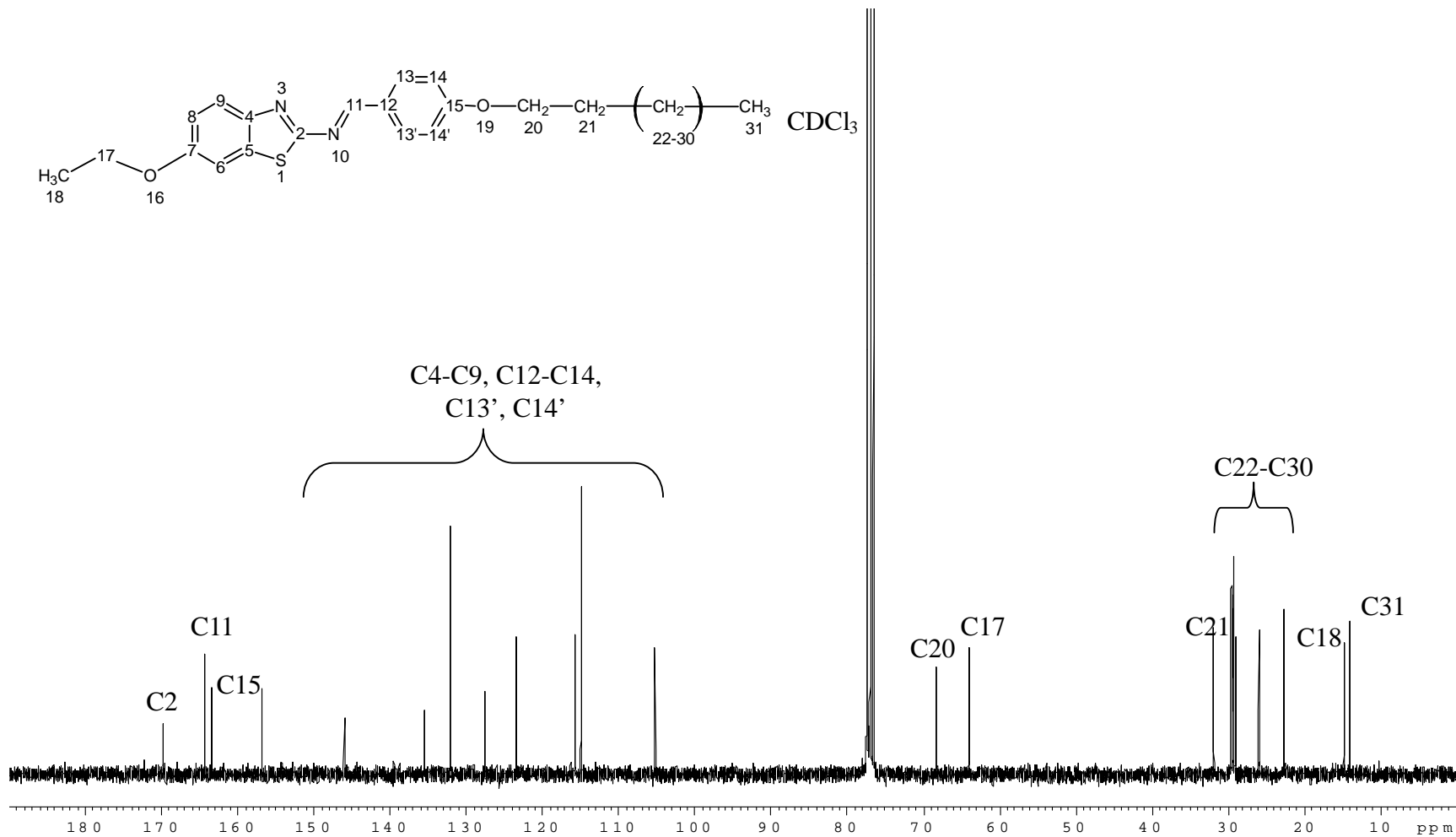
m=multiplet

¹³C NMR spectral data of compound 12OEtBTH in CDCl₃

Carbon Number	Chemical Shift , δ (ppm)
C2	169.84
C11	164.34
C15	163.41
C4-C9, C12-C14, C13' and C14'	156.88
	146.11
	135.57
	132.12
	127.63
	123.46
	115.85
	114.98
	105.25
C20	68.38
C17	64.12
C21	31.91
C19-C30	29.64
	29.62
	29.58
	29.55
	29.34
	29.11
	25.98
C31	22.67
C18	14.84
C33	14.09



¹H NMR spectrum of compound 12OEtBTH.



^{13}C NMR spectrum of compound 12OEtBTH.

Appendix 7C

¹H NMR spectral data of compound 12HBZT in CDCl₃

Proton Number	Chemical Shift, δ (ppm)	Integrals	Multiplicity*	Coupling Constant, J (Hz)
H11	8.99	1H	s	-
H13,H13'	7.98	2H	d	8.7
H9	7.96	1H	d	7.5
H6	7.82	1H	t	7.8
H8	7.48	1H	t	7.8
H7	7.36	1H	d	7.8
H14,H14'	7.00	2H	d	8.7
H17	4.04	2H	t	6.6
H18	1.79	2H	p	6.9
H19-H27	1.29-1.47	18H	m	-
H28	0.88	3H	t	6.3

Note:

TMS was used as an internal standard.

*s=singlet,

d=doublet

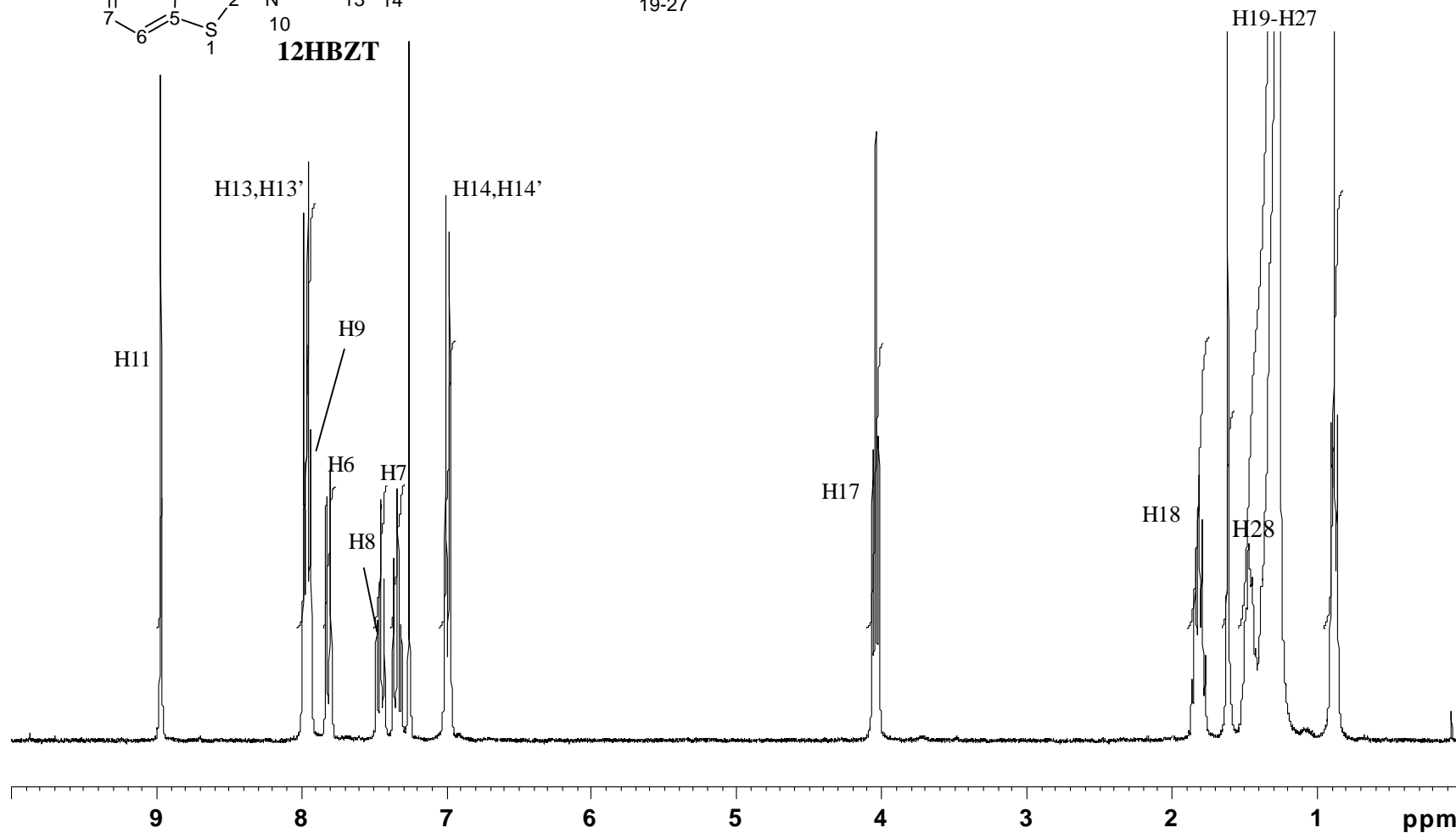
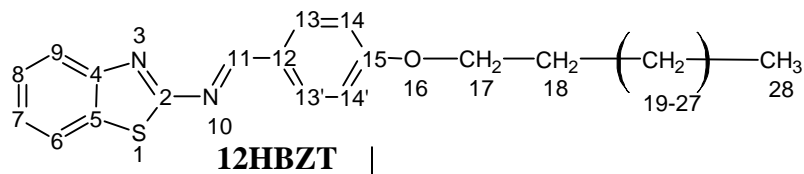
t=triplet

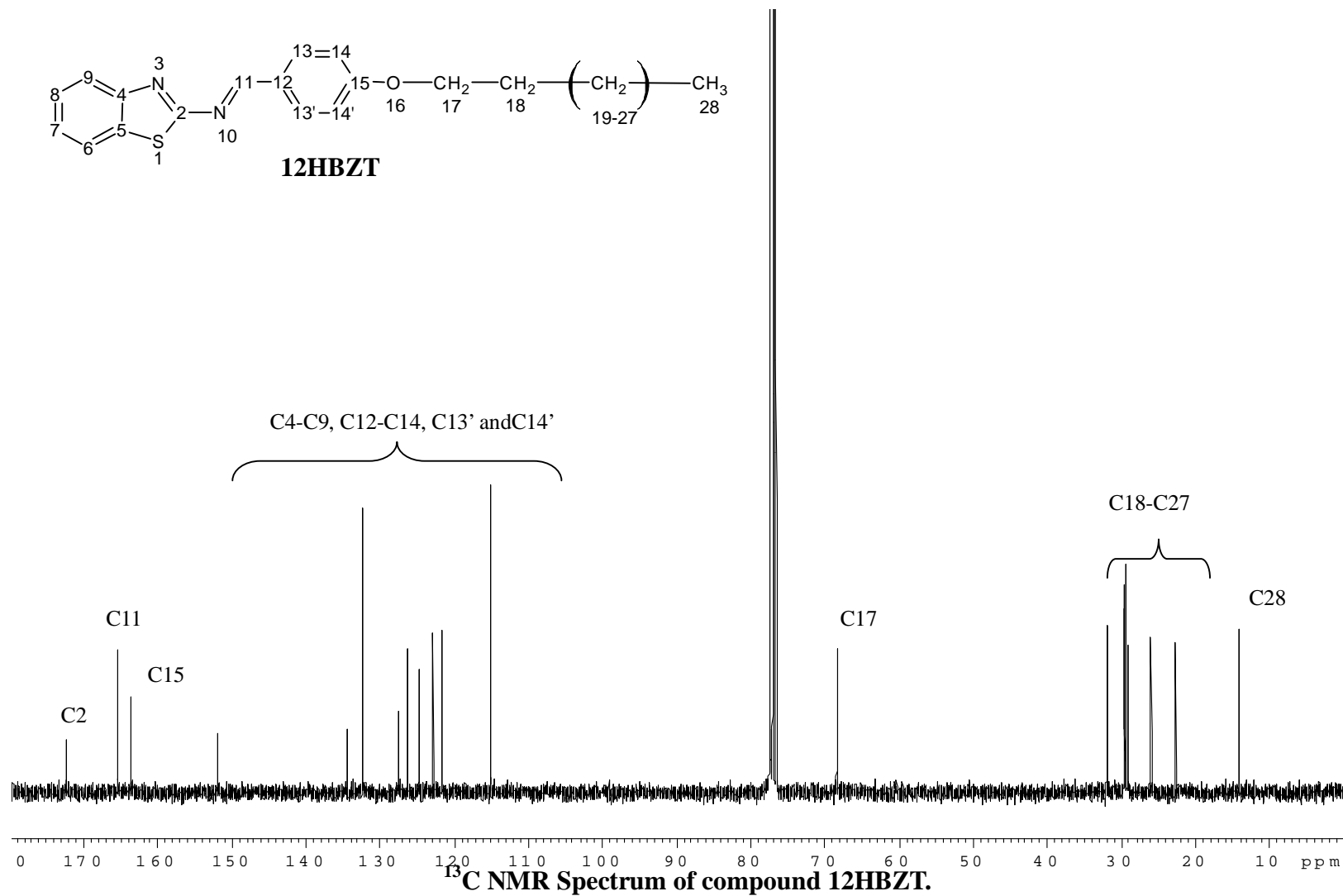
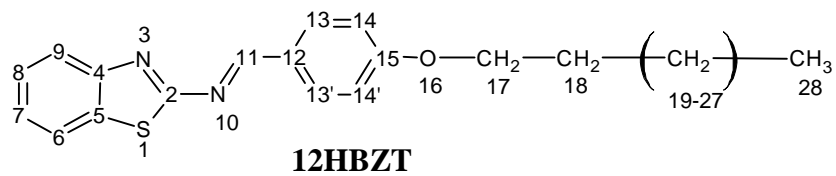
p=pentet

m=multiplet

¹³C NMR spectral data of compound 12HBZT in CDCl₃

Carbon number	Chemical Shift, δ (ppm)
C2	172.34
C11	165.37
C15	163.63
C4-C9, C12-C14, C13' and C14'	151.85
	134.47
	132.36
	127.50
	126.30
	124.77
	122.83
	121.60
	115.20
C17	68.41
C18	31.91
C19-C25	29.64
	29.62
	29.57
	29.54
	29.33
	29.10
C26	25.98
C27	22.67
C28	14.09





Appendix 8A

¹H NMR spectral data of compound 8OMe3R in CDCl₃

Proton Number	Chemical Shift, δ (ppm)	Integrals	Multiplicity*	Coupling Constant, J (Hz)
H11	9.03	1H	s	-
H20,H20'	8.13	2H	d	8.7
H13,H13'	8.07	2H	d	8.7
H9	7.86	1H	d	8.7
H14,H14'	7.37	2H	d	8.4
H6	7.30	1H	s	-
H8	7.06	2H	d	9.0
H21,H21'	6.97	2H	d	9.0
H24	4.05	3H	t	6.6
H26	3.89	2H	s	
H27	1.78	2H	p	7.8
H28-H32	1.30-1.50	26H	m	-
H33	0.87	3H	t	6.9

Note:

TMS was used as an Internal standard.

*s=singlet,

d=doublet

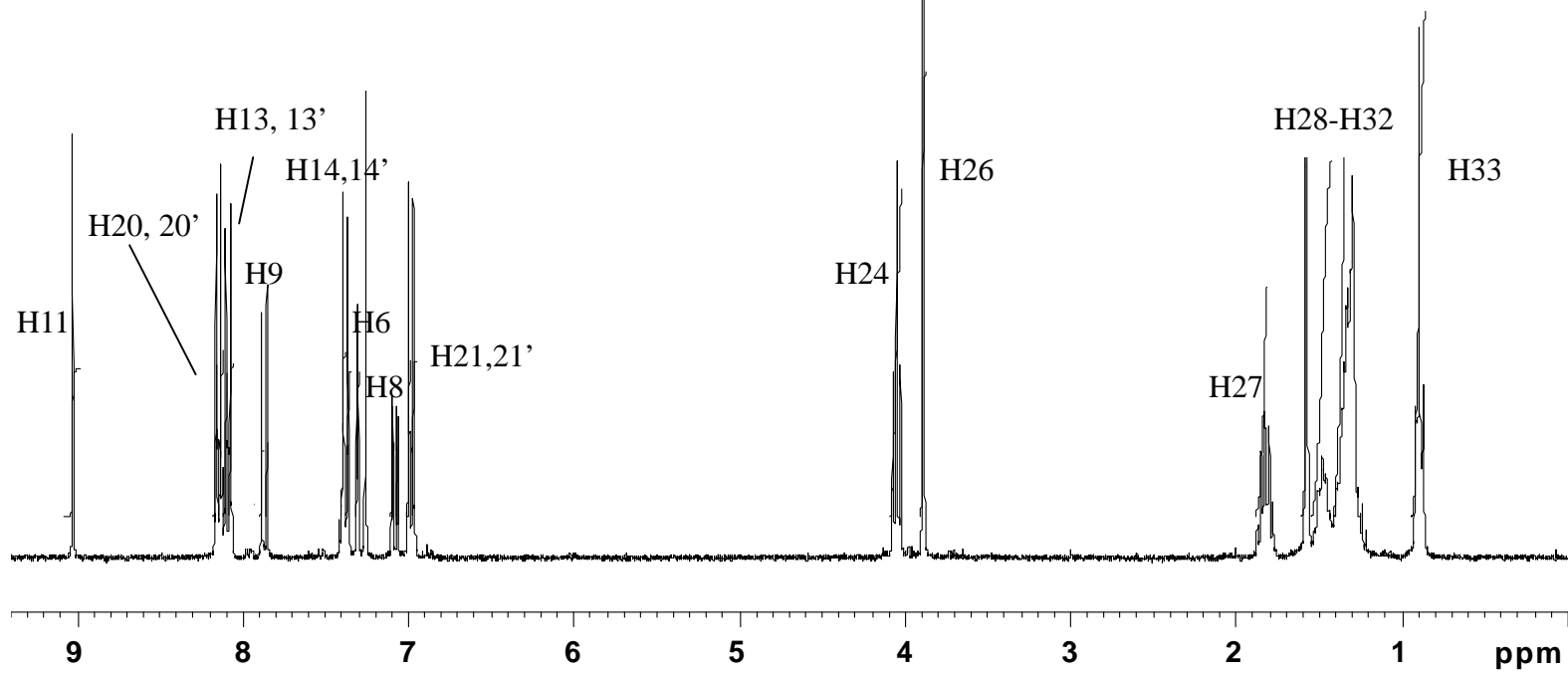
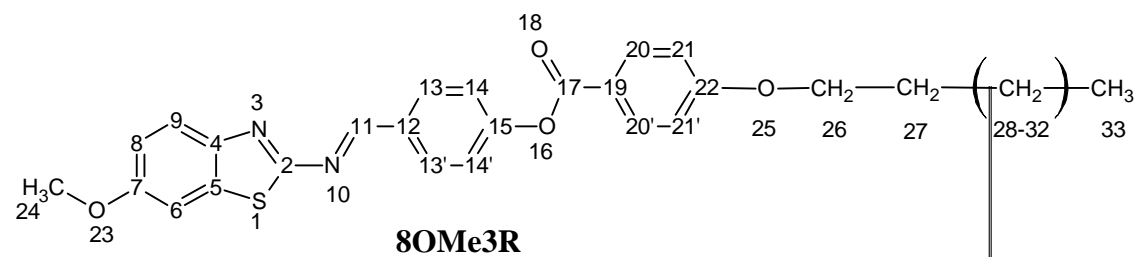
t=triplet

p=quintet

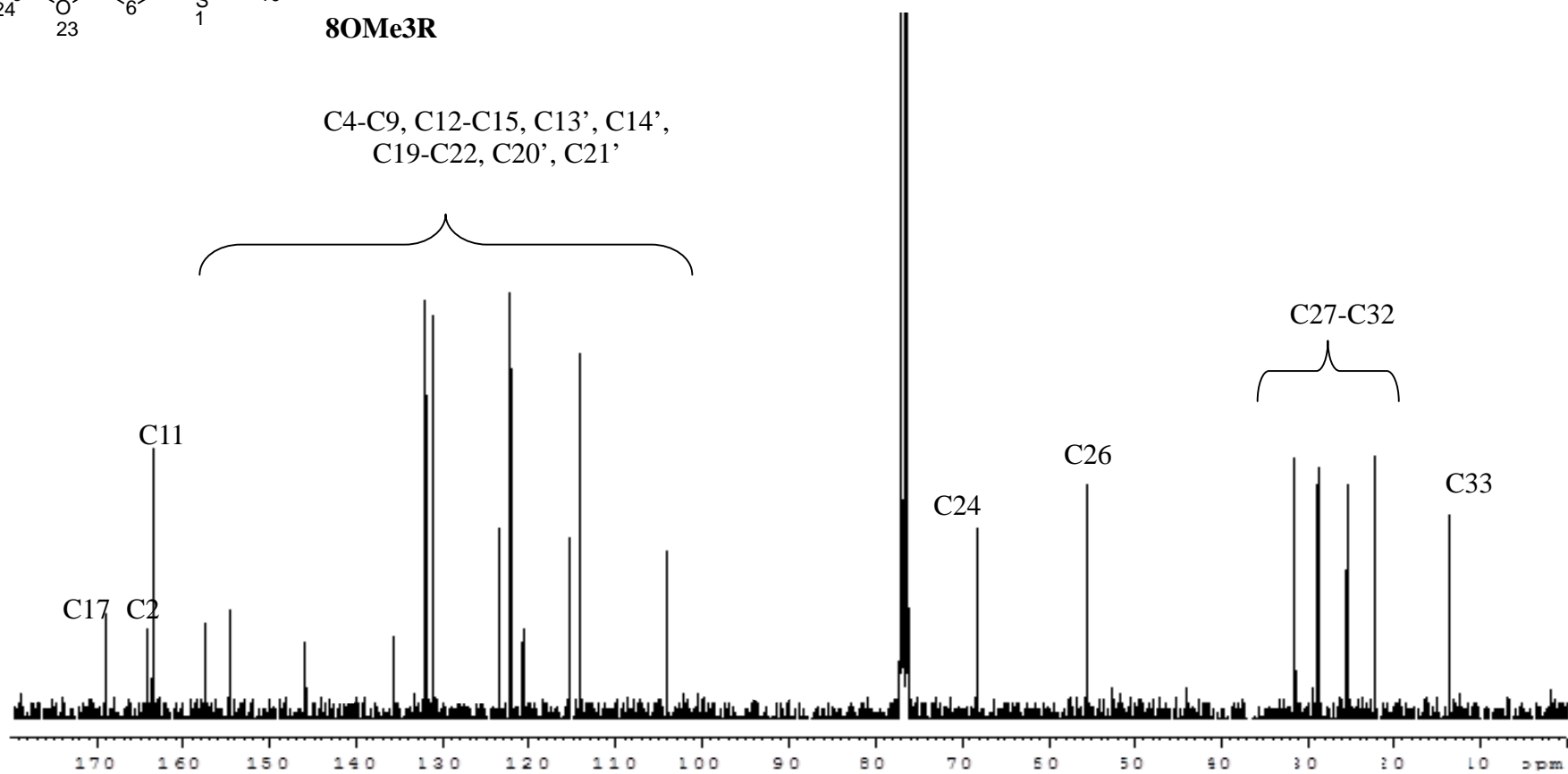
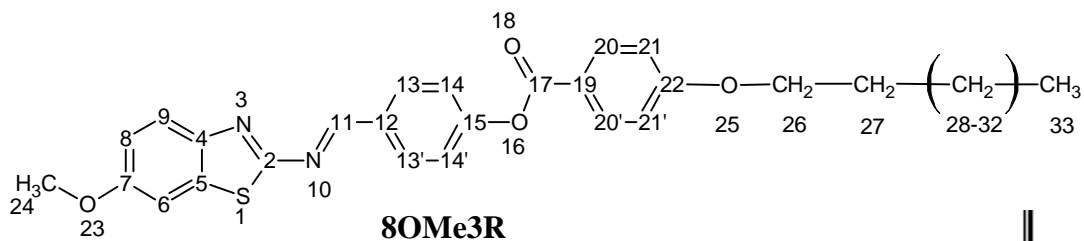
m=multiplet

¹³C NMR spectral data of compound 8OMe3R in CDCl₃

Carbon Number	Chemical Shift , δ (ppm)
C17	169.24
C2	164.36
C11	163.82
C4-C9, C12-C15, C13', C14', C19-C22, C20', C21'	157.75
	154.88
	146.13
	135.92
	132.76
	132.39
	131.35
	123.77
	122.52
	127.57
	121.03
	115.68
	114.42
	104.47
C24	68.40
C26	55.81
C27-C32	31.78
	29.30
	29.19
	29.08
	25.97
	22.63
C33	14.06



¹H NMR spectrum of compound 8OMe3R.



^{13}C NMR spectrum of compound 8OMe3R.

Appendix 8B

¹H NMR spectral data of compound 16HB3R in CDCl₃

Proton Number	Chemical Shift, δ (ppm)	Integrals	Multiplicity*	Coupling Constant, J (Hz)
H11	9.10	1H	s	-
H20,H20'	8.14	2H	d	9.0
H13,H13'	8.10	2H	d	8.7
H9	7.98	1H	d	8.1
H6	7.95	1H	d	8.1
H8	7.46	1H	t	8.4
H7	7.40	1H	t	8.4
H14,H14'	7.38	2H	d	8.7
H21,H21'	6.97	2H	d	9.0
H24	4.03	2H	t	6.6
H25	1.78	2H	p	7.8
H26-H38	1.27-1.48	26H	m	-
H39	0.86	3H	t	6.9

Note:

TMS was used as an internal standard.

*s=singlet,

d=doublet

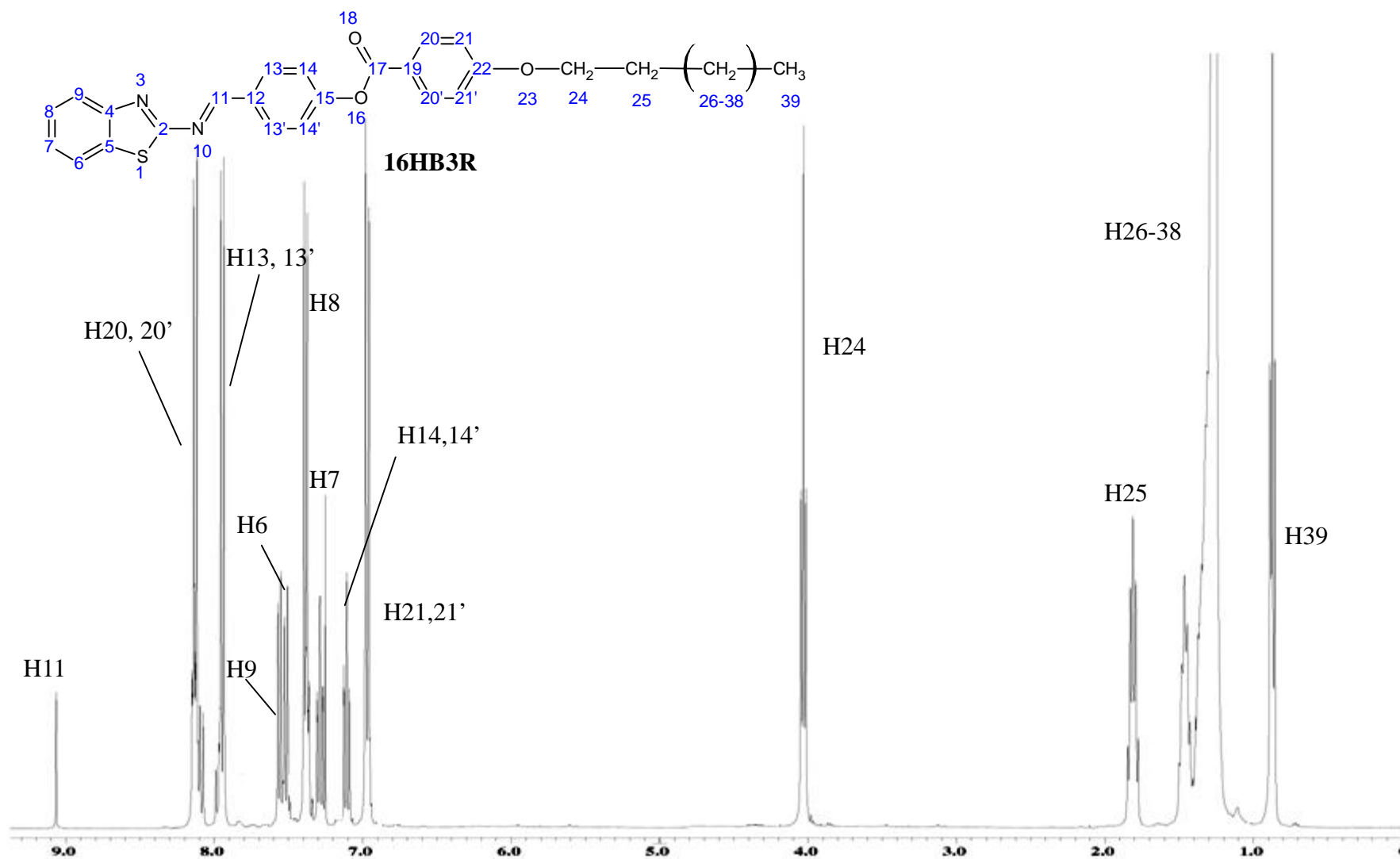
t=triplet

p=quintet

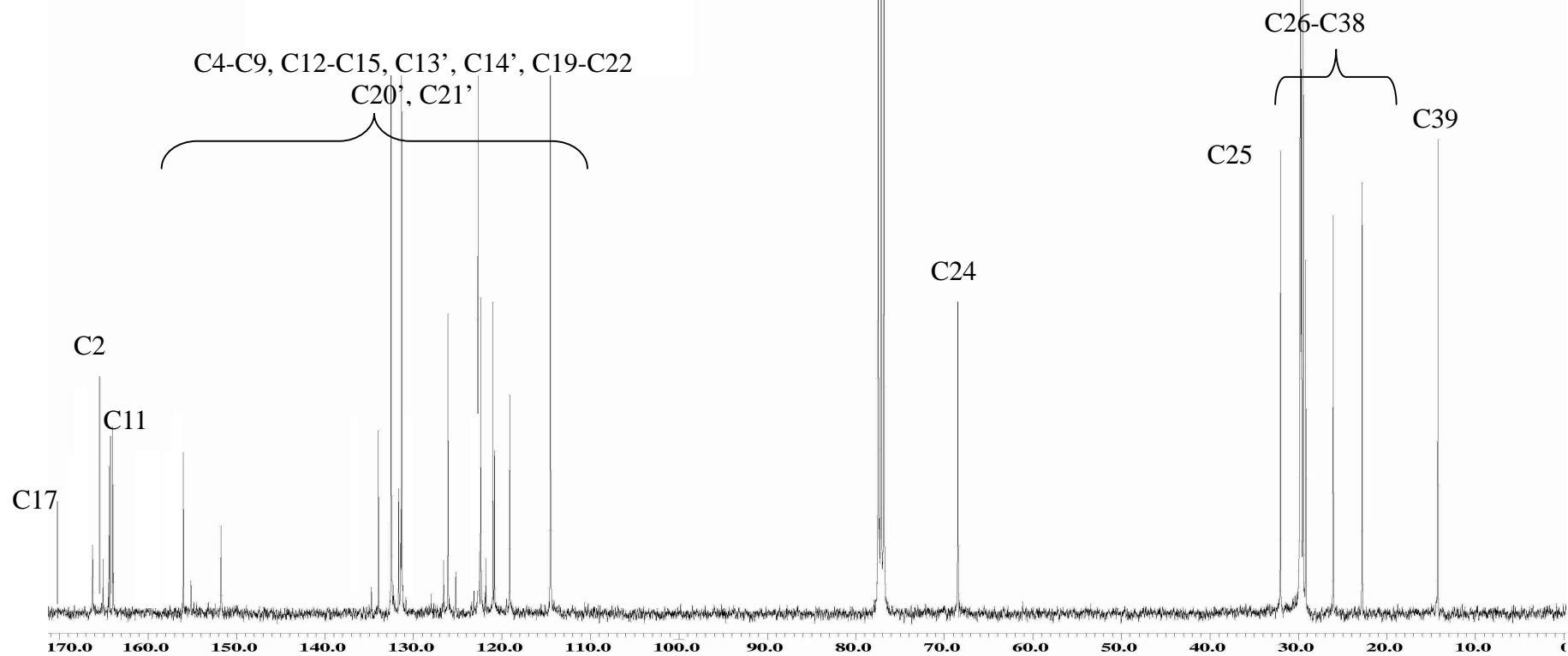
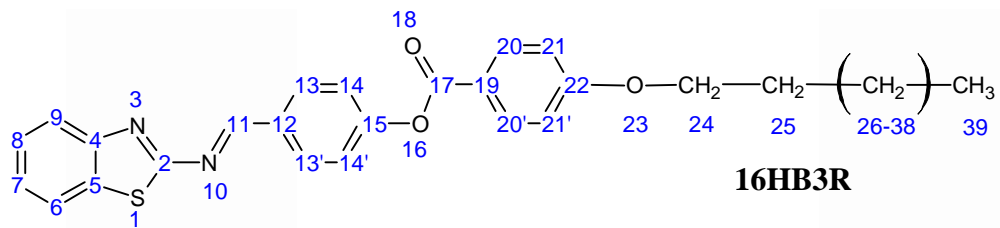
m=multiplet

¹³C NMR spectral data of compound 16HB3R in CDCl₃

Carbon Number	Chemical Shift , δ (ppm)
C17	169.35
C2	164.89
C11	163.85
C4-C9, C12-C15, C13', C14', C19-C22, C20', C21'	152.84
	132.41
	131.56
	131.21
	126.48
	125.08
	124.56
	123.41
	123.11
	122.58
	121.69
	120.43
	117.75
	114.45
C24	68.42
C25	31.92
C26-C36	29.68
	29.65
	29.58
	29.55
	29.35
	29.09
C37	25.97
C38	22.68
C39	14.09



¹H NMR spectrum of compound 16HB3R.



¹³C NMR spectrum of compound 16HB3R

Appendix 9A

¹H NMR spectral data of compound 16EOBZT in CDCl₃

Proton Number	Chemical Shift, δ ppm	Integrals	Multiplicity*	Coupling Constant, J (Hz)
H21,H21'	8.15	1H	d	9.0
H14	8.06	1H	d	7.8
H15	7.89	1H	d	8.1
H11	7.82	1H	s	-
H5	7.63	1H	d	8.4
H8	7.47	1H	d	8.4
H6	7.36	1H	t	8.1
H7	7.29	1H	t	8.4
H22,H22'	6.97	2H	d	8.7
H25	4.18	2H	q	6.4
H17	4.03	2H	t	-
H26	1.78	3H	p	6.8
H41	1.33	3H	t	7.2
H27-H39	1.27-1.45	26H	m	-
H40	0.86	3H	t	6.8

Note:

TMS was used as an internal standard.

*s=singlet,

d=doublet

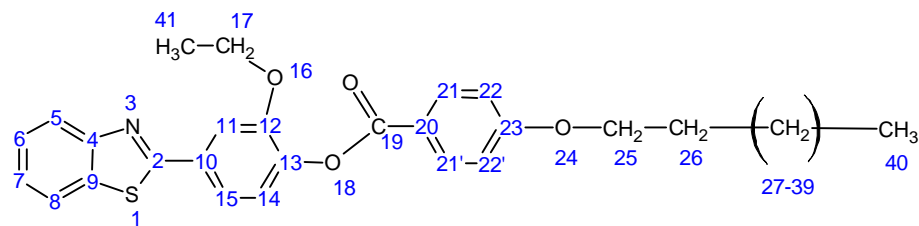
t=triplet

p=quintet

m=multiplet

¹³C NMR spectral data of compound 16EOBZT in CDCl₃.

Carbon Number	Chemical Shift , δ (ppm)
C19	167.40
C2	164.29
C4-C9,C11-C15,C20-C23, C21', C22'	163.59
	151.35
	142.97
	135.21
	132.40
	132.24
	126.33
	125.20
	123.56
	123.22
	121.60
	121.34
	120.51
	114.32
	112.41
C25	68.36
C17	64.91
C26	31.92
C27-C38	29.68
	29.65
	29.59
	29.35
	29.13
	26.00
C39	22.68
C41	14.69
C40	14.09



16EOBZT

H27-H39

H21,H21'

H22,H22'

H17

H40

H11

H7

H25

H14

H6

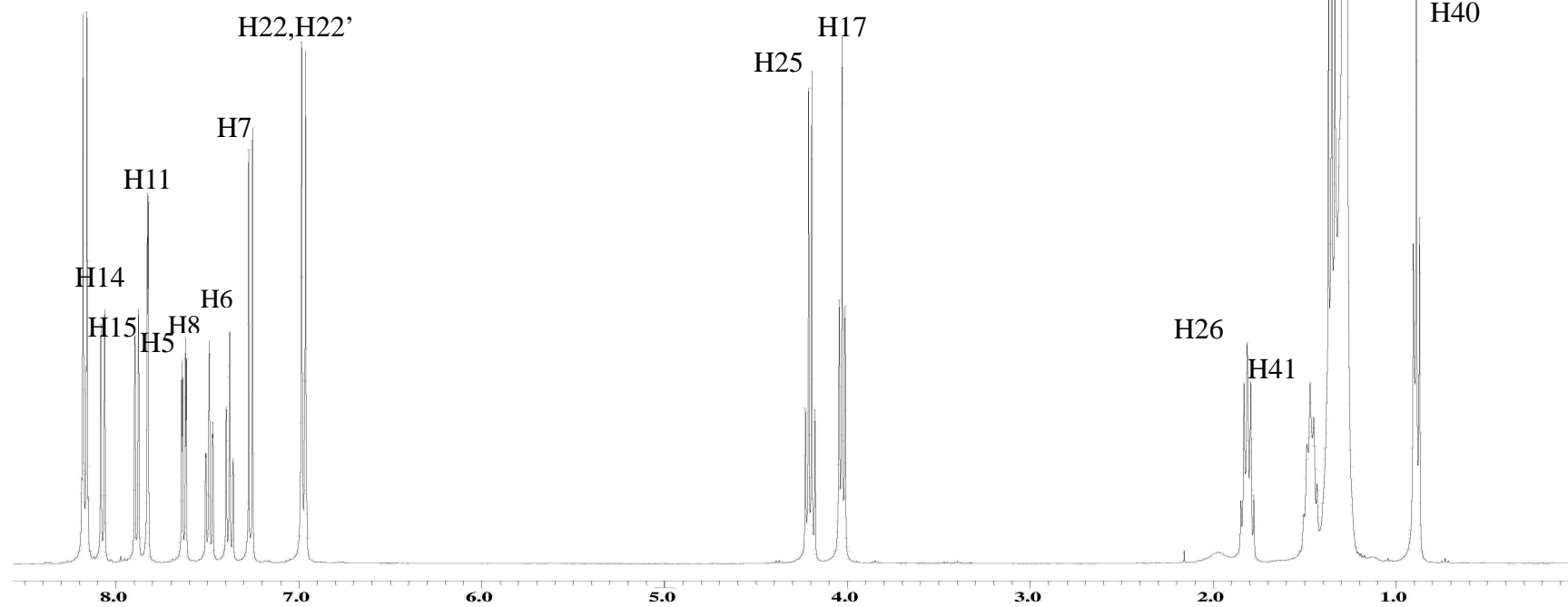
H26

H15

H5

H8

H41



¹H NMR spectrum of compound 16EOBZT.

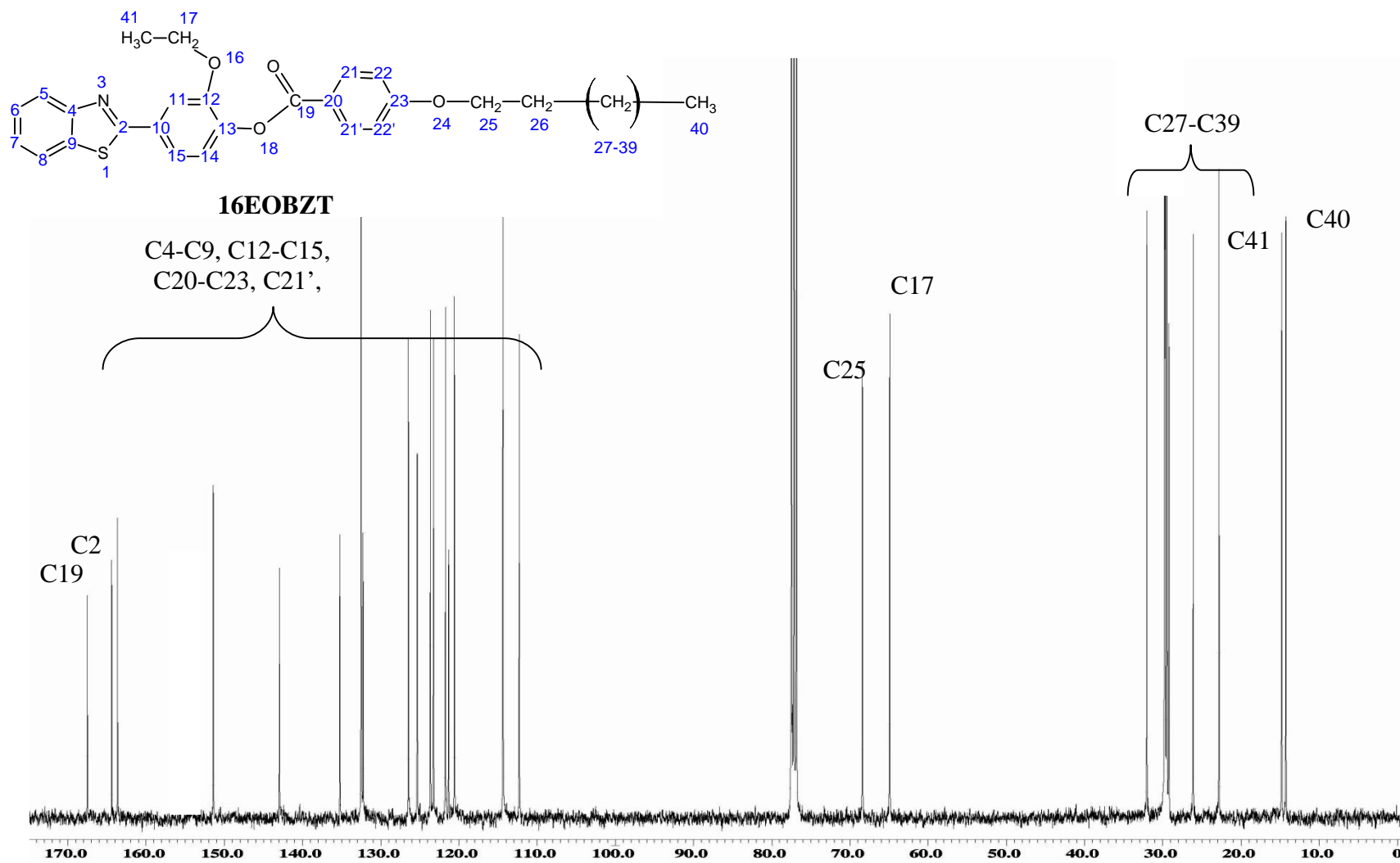


Figure 4.42: ¹³C NMR spectrum of compound 16EOBZT.

Appendix 10A

¹H NMR spectral data of compound 8OEtD in CDCl₃

Proton Number		Chemical Shift, δ ppm	Integrals	Multiplicity*	Coupling Constant
H11	H11	8.90	2H	s	-
H13,H13'	H13,H13'	7.94	4H	d	9.0
H9	H9	7.81	2H	d	9.0
H6	H6	7.27	2H	s	-
H8	H8	7.03	2H	d	9.0
H14,H14'	H14,H14'	6.97	4H	d	8.7
H20	H20	4.07	4H	q	7.2
H17	H17	4.03	4H	t	6.6
H21	H21	1.78	4H	p	7.8
H18	H18	1.59	6H	t	6.3
H22-23	H22-23	1.43-1.48	8H	m	-

Note:

TMS was used as an internal standard.

^aBased on the atomic numbering scheme in Figure .

*s=singlet,

d=doublet

t=triplet

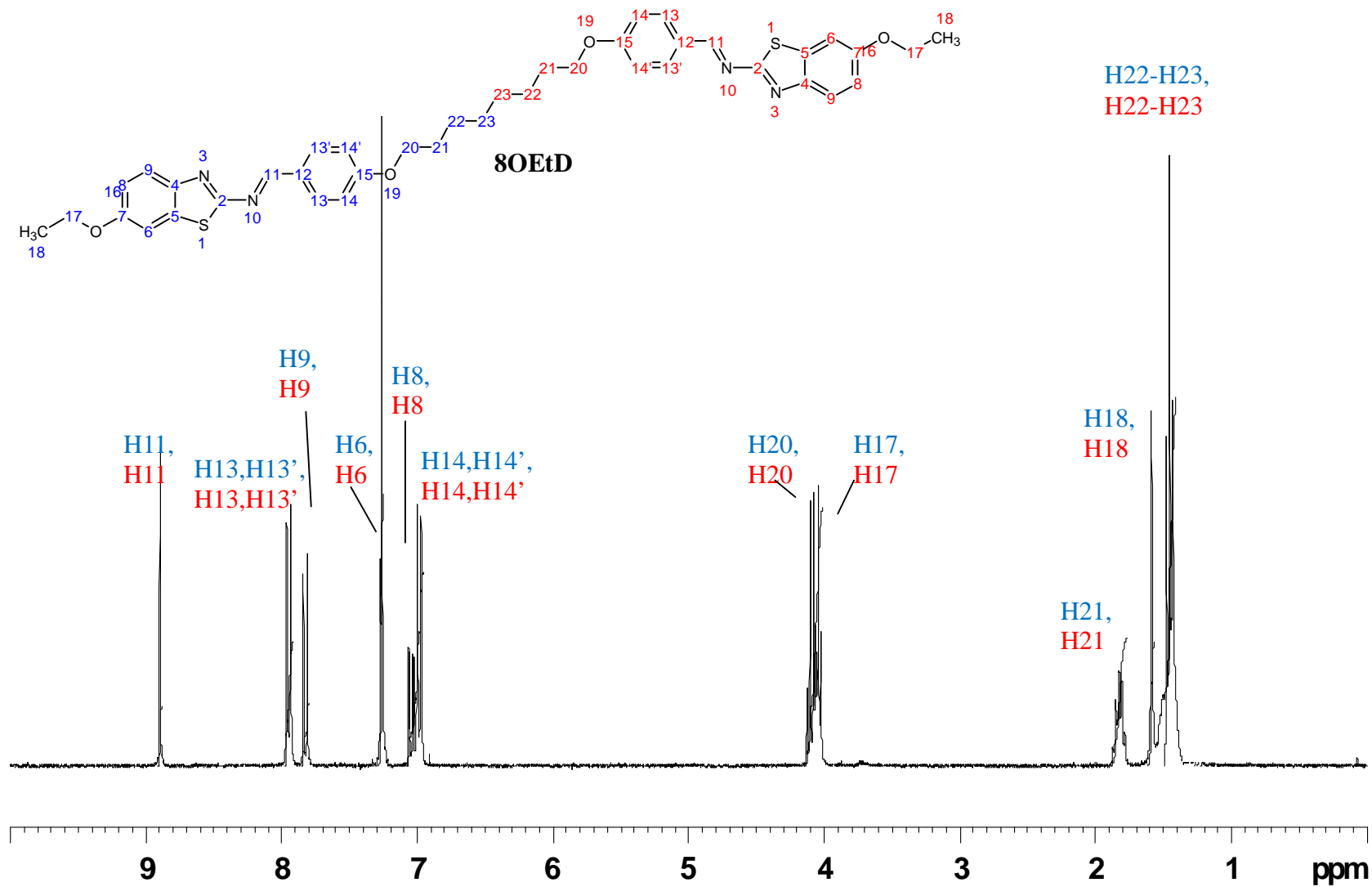
q= quartet

p=pentet

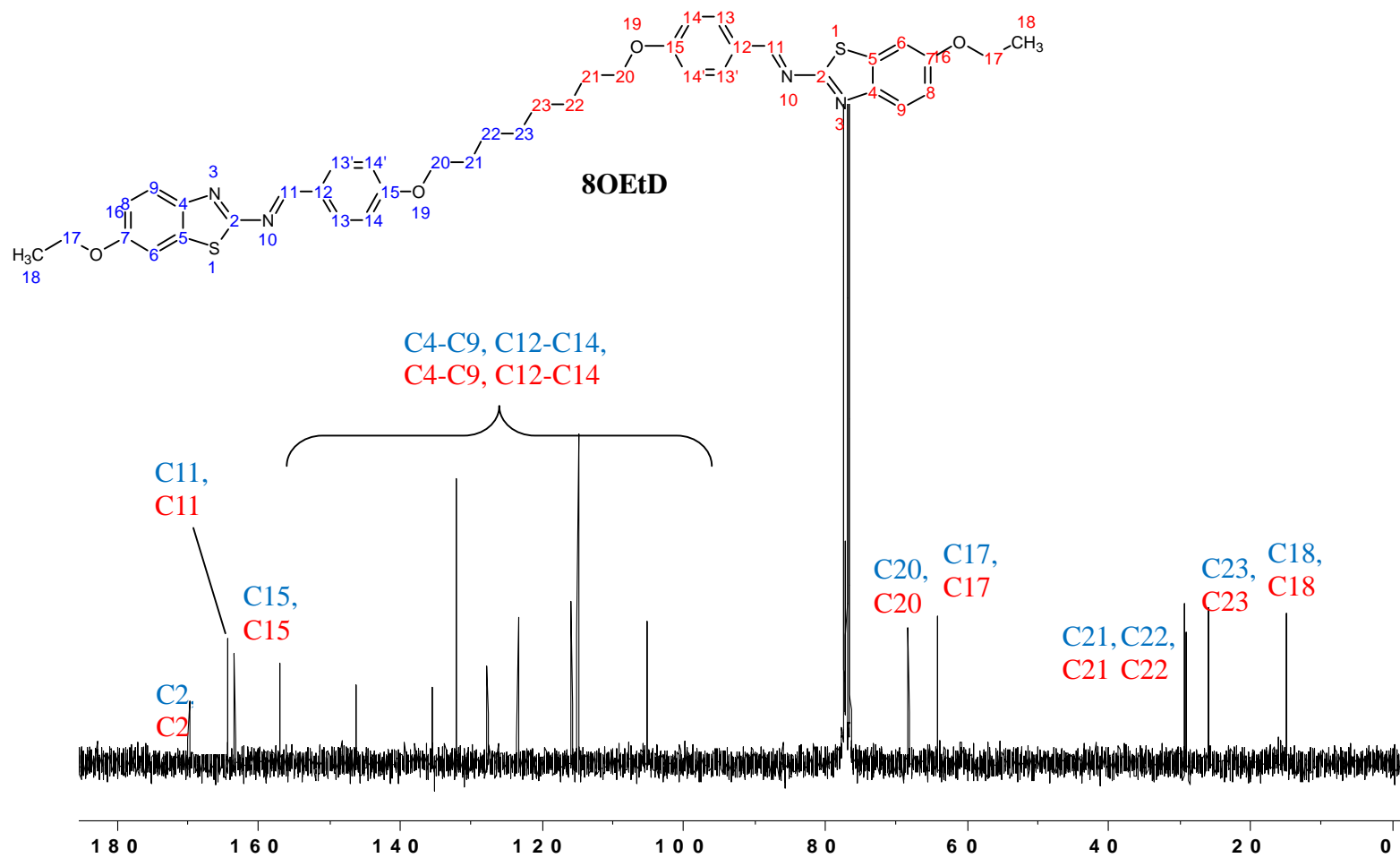
m=multiplet

¹³C NMR spectral data of compound 8OEtD in CDCl₃

Carbon Number		Chemical Shift , δ (ppm)
C2	C2	169.82
C11	C11	164.31
C15	C15	163.35
C4-C9, C12-C14	C4-C9, C12-C14	156.89
		146.12
		135.58
		132.13
		127.69
		123.47
		115.86
		114.97
		105.27
C20	C20	68.29
C17	C17	64.13
C21	C21	29.21
C22	C22	29.08
C23	C23	25.90
C18	C18	14.83



¹H NMR spectrum of compound 8OEtD.



¹³C NMR spectrum of compound 8OEtD.

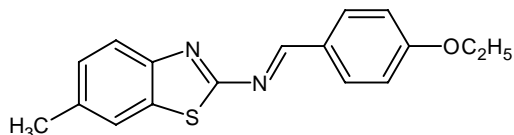
Appendix 11A

Summary of Phase Transition Data of Synthesized Compounds

Series 1: (I) nMeBTH

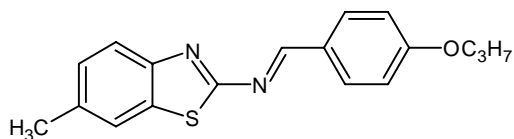
Compound Molecular Structural and Phase Transition Temperature (°C)

2MeBTH



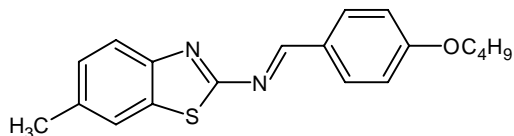
Cr 117.0 N 140 I

3MeBTH



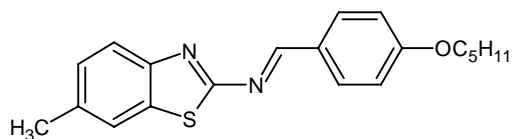
Cr 117.0 N 140 I

4MeBTH



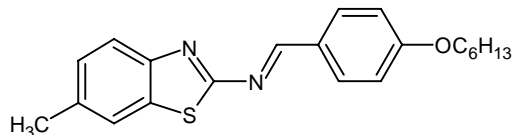
Cr 99.6 N 125.3 I

5MeBTH



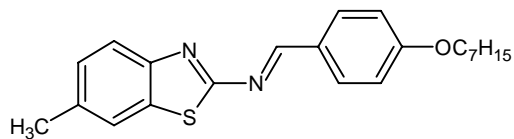
Cr 93.6 N 114.7 I

6MeBTH



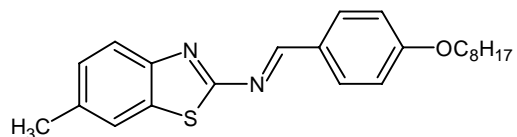
Cr 105.5 N 119.5 I

7MeBTH



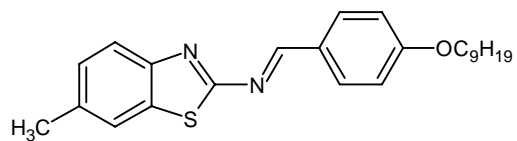
Cr 102.5 N 116.5 I

8MeBTH



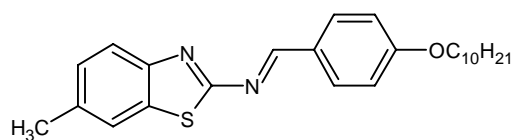
Cr 108.2 N 118.3 I

9MeBTH



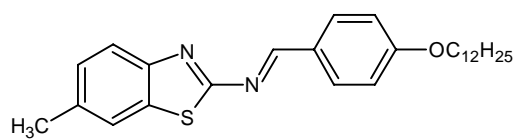
Cr 92.9 SmA 104.5 N 117.1 I

10MeBTH



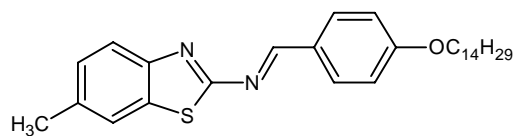
Cr 99.1 SmA 110.8 N 118.5I

12MeBTH



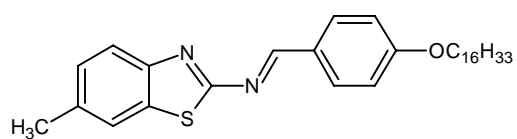
Cr 81.5 SmA 116.2 I

14MeBTH



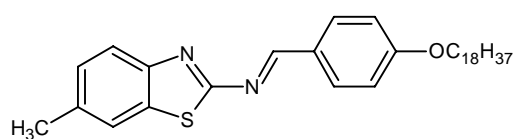
Cr 83.1 SmA 113.5 I

16MeBTH



Cr 88.4 SmA 115.8 I

18MeBTH

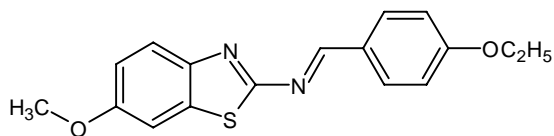


Cr₁ 55.6 Cr₂ 91.2 SmA 109.6 I

Series 1: (II) nOMeBTH

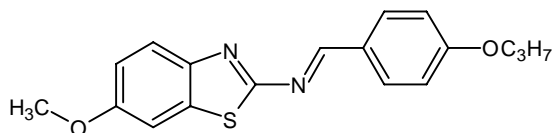
Compound Molecular Structural and Phase Transition Temperature (°C)

2OMeBTH



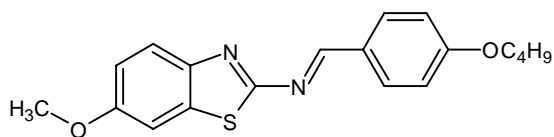
Cr 85.2 N 130.1 I

3OMeBTH



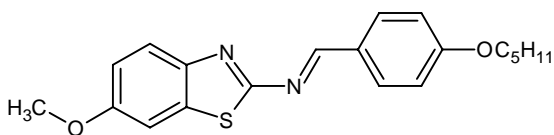
Cr 102.2 N 130.4 I

4OMeBTH



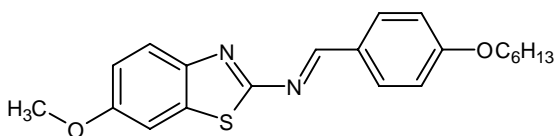
Cr 132.1 N 139.9 I

5OMeBTH



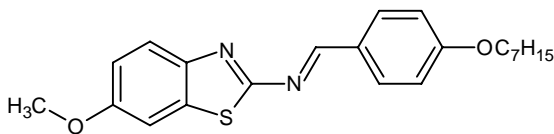
Cr 102.2 N 123.7 I

6OMeBTH



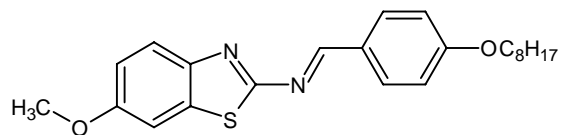
Cr 84.7 N 128.8 I

7OMeBTH



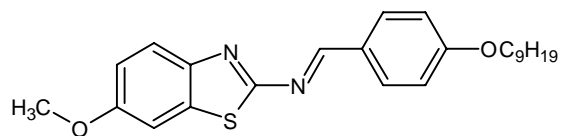
Cr 91.4 N 123.1 I

80MeBTH



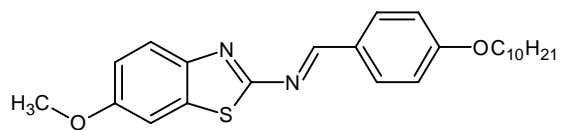
Cr 95.7 N126.3 I

90MeBTH



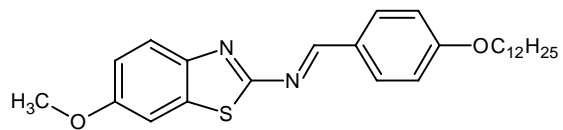
Cr 86.5 (SmA 78.6) N 123.7 I

100MeBTH



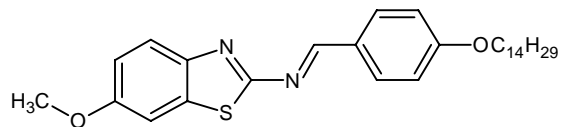
Cr 91.2 (SmA 90.4) N 124.5 I

120MeBTH



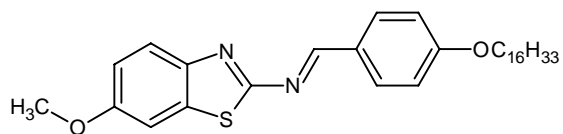
Cr 84.1 SmA 101.8 N 121.9 I

140MeBTH



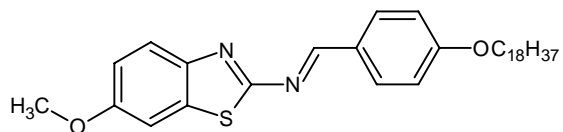
Cr 77.9 SmA 107.8 N 118.8 I

160MeBTH



Cr 84.5 SmA 110.6 N 116.1 I

180MeBTH

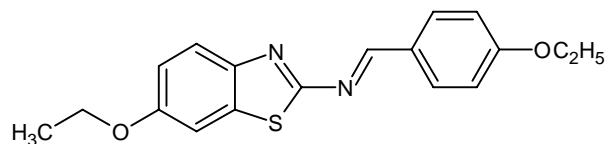


Cr 86.9 (53.68) SmA 108.4 (6.98) I

Series 1: (III) nOEtBTH

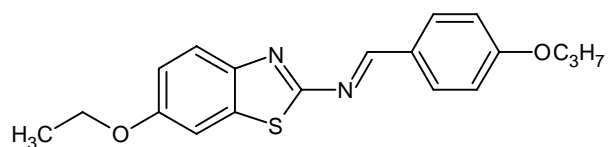
Compound Molecular Structural and Phase Transition Temperature (°C)

2OEtBTH



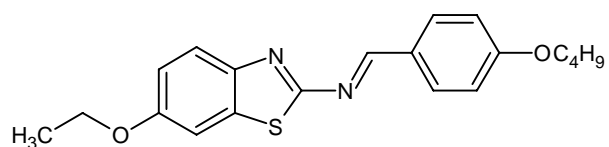
Cr 136.2 N 168.1 I

3OEtBTH



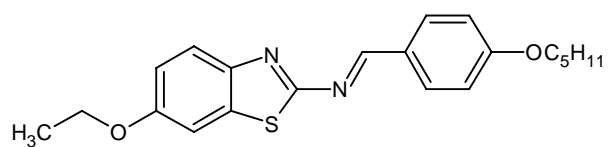
Cr 106.8 N 145.6 I

4OEtBTH



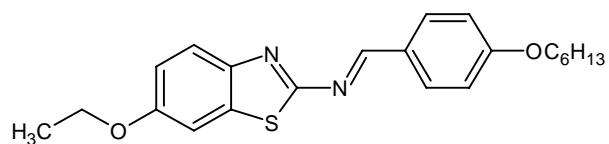
Cr 105.0 N 151.9 I

5OEtBTH



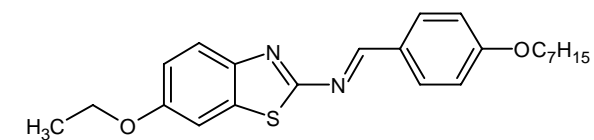
Cr 75.4 N 139.3 I

6OEtBTH

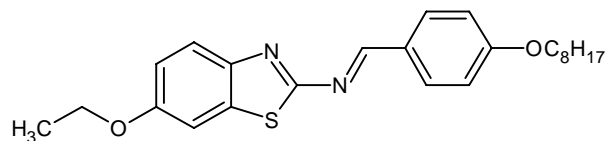


Cr 94.57 N 116.33 I

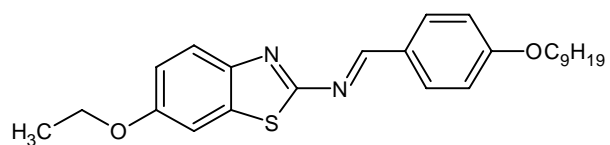
7OEtBTH



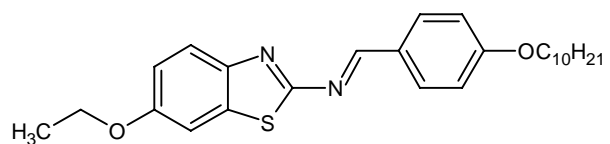
Cr 76.8 N 133.0 I

8OEtBTH

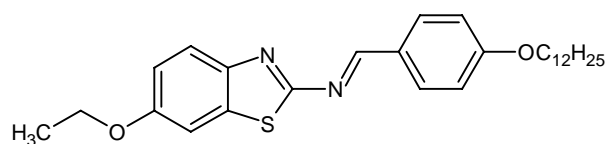
Cr 85.4 (34.75) N 134.1 (1.24) I

9OEtBTH

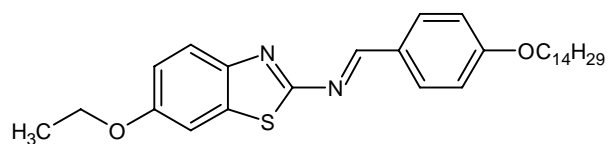
Cr 82.0 (SmC 81.3) N 130.2 I

10OEtBTH

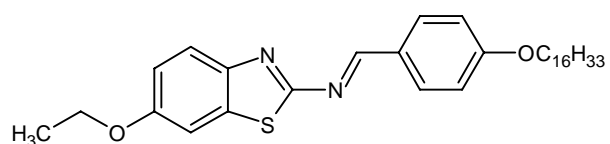
Cr 88.7 SmC 95.6 N 131.2 I

12OEtBTH

Cr 97.7 SmC 97.67 SmA 109.1 N 126.9 I

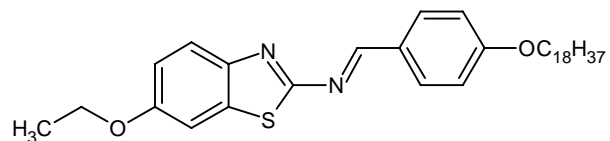
14OEtBTH

Cr 91.3 SmA 113.2 N 121.8 I

16OEtBTH

Cr 96.5 SmA 116.1 N 120.1 I

18OEtBTH

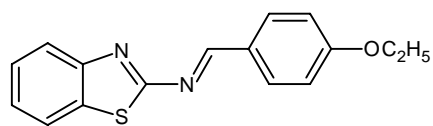


Cr 98.8 (83.73) SmA 116.0 (7.55) I

Series 1: (IV) nHBZT

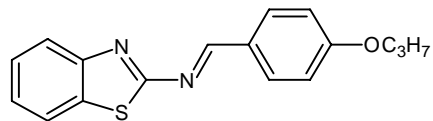
Compound Molecular Structural and Phase Transition Temperature (°C)

2HBZT



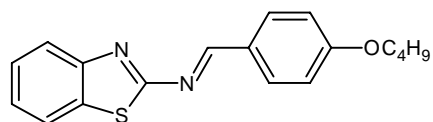
Cr 85.0 I

3HBZT



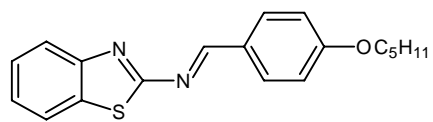
Cr 83.97 I

4HBZT



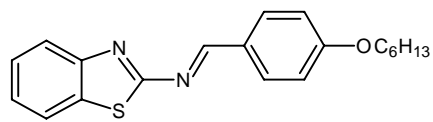
Cr 86.46 I

5HBZT



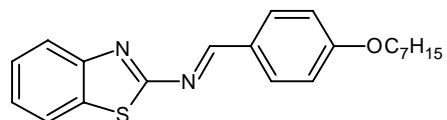
Cr 82.76 I

6HBZT



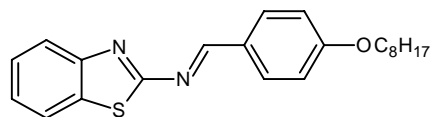
Cr₁ 74.18 Cr₂ 90.69 I

7HBZT



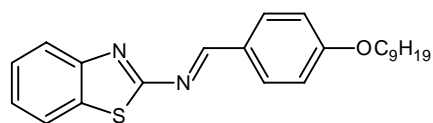
Cr 76.73 (SmA 64.46) I

8HBZT



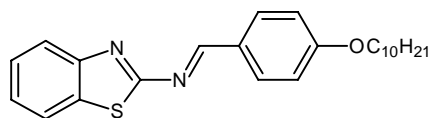
Cr 79.57 (SmA 76.34) I

9HBZT



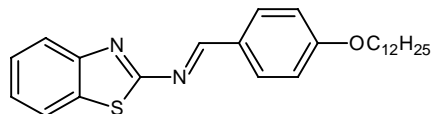
Cr 79.14 (SmA 75.86) I

10HBZT



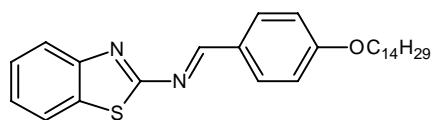
Cr 82.52 SmA 84.62 I

12HBZT



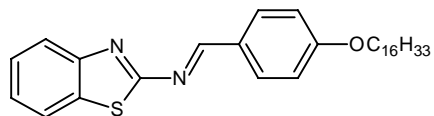
Cr 81.88 SmA 90.1 I

14HBZT



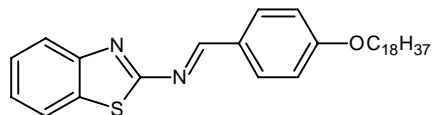
Cr 77.65 SmA 91.93 I

16HBZT



Cr 84.69 SmA 90.75 I

18HBZT

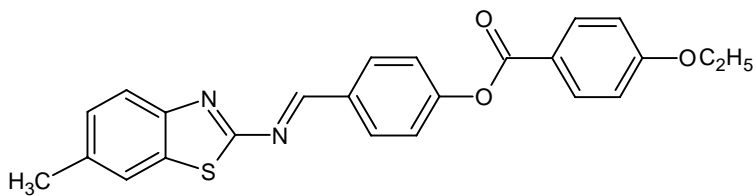


Cr 83.78 SmA 90.36 I

Series 2: (I) nMe3R

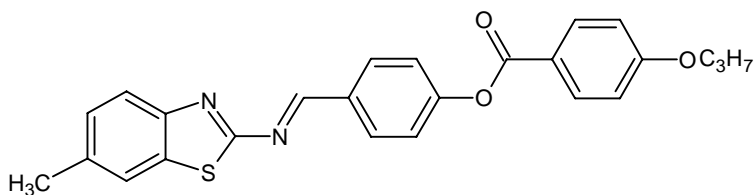
Compound Molecular Structural and Phase Transition Temperature (°C)

2Me3R



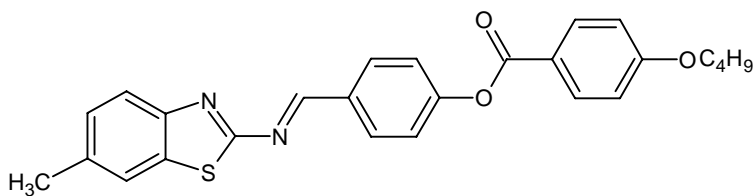
Cr₁38.80 Cr₂ 168.04 I

3Me3R



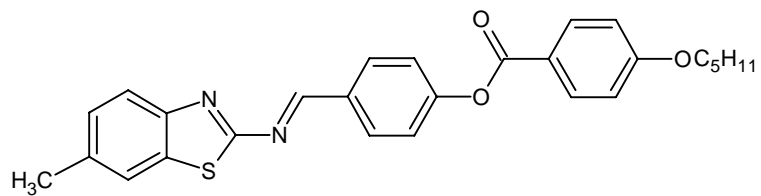
Cr₁ 121.99 Cr₂154.44 I

4Me3R



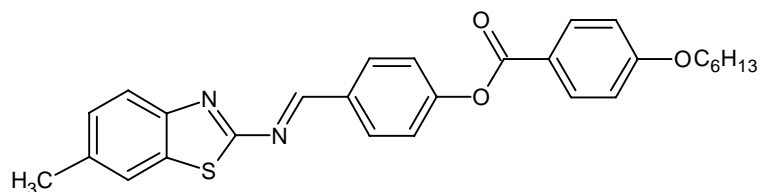
Cr 136.91 I

5Me3R



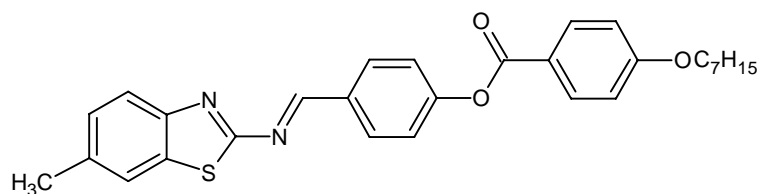
Cr₁ 122.91 Cr₂ 142.54 N 243.41 I

6Me3R



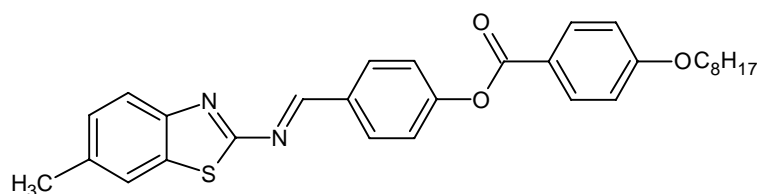
Cr₁ 121.73 Cr₂ 140.84 N 255.14 I

7Me3R



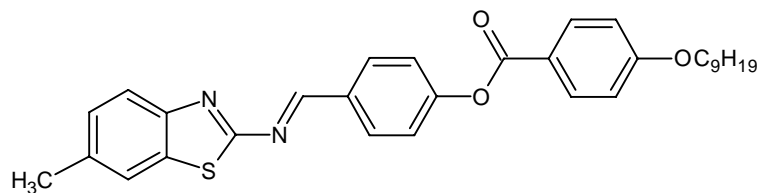
Cr₁ 116.99 Cr₂ 146.41 N 241.53 I

8Me3R



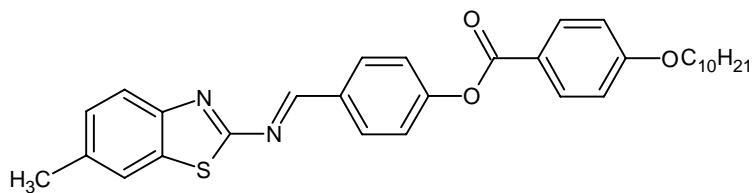
Cr₁ 98.45 Cr₂ 129.69 N 226.23 I

9Me3R



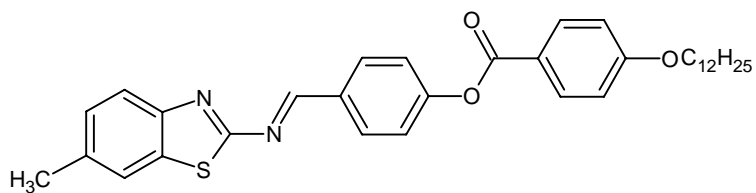
Cr₁ 97.25 Cr₂ 131.60 N 219.29 I

10Me3R



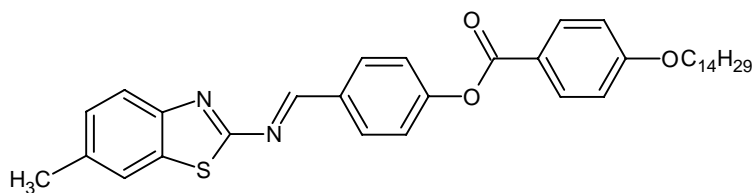
Cr₁ 94.09 Cr₂ 123.78 N 221.68 I

12Me3R



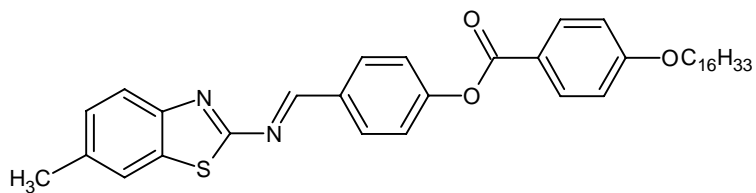
Cr₁ 81.53 Cr₂ 111.08 SmC 162.98 N 218.08 I

14Me3R



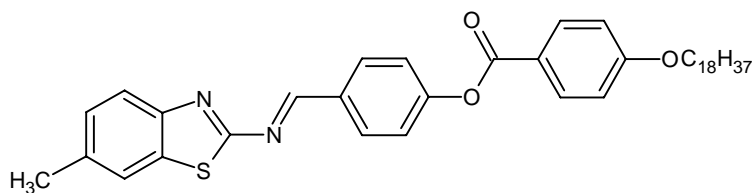
Cr₁ 96.66 Cr₂ 109.79 SmC 179.48 N 216.53 I

16Me3R



Cr₁ 86.43 Cr₂ 104.24 SmA 179.2 N 198.71 I

18Me3R

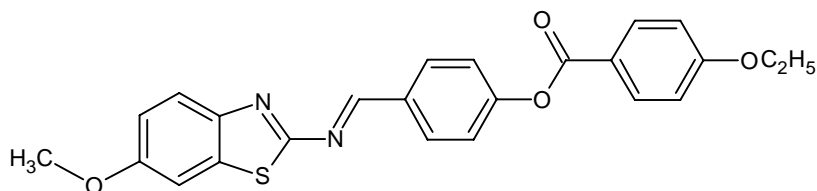


Cr₁ 77.74 Cr₂ 108.01 I

Series 2: (II) nOMe3R

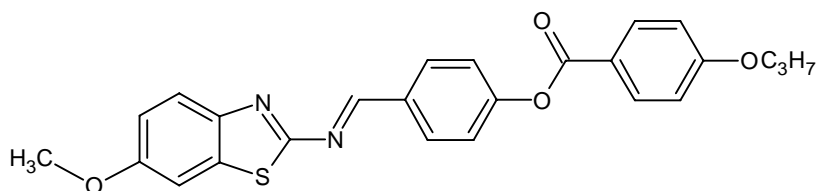
Compound Molecular Structural and Phase Transition Temperature (°C)

2OMe3R



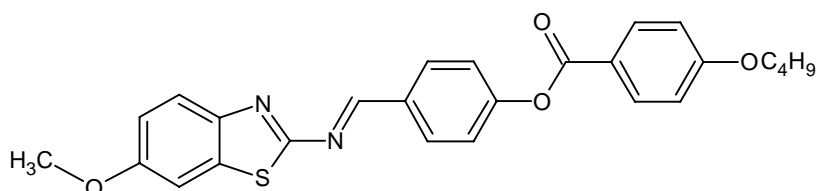
Cr 116.5 I

3OMe3R



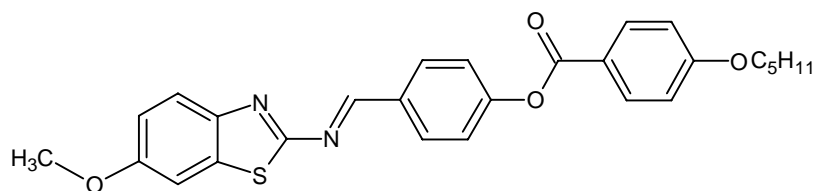
Cr 179.2 I

4OMe3R



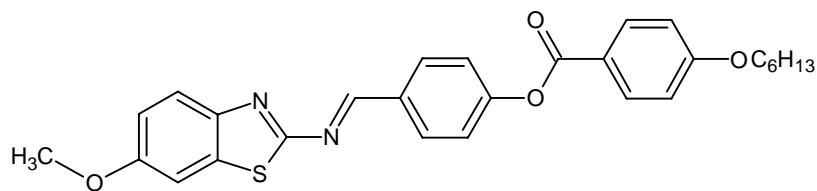
Cr₁ 82.62 Cr₂ 136.9 N 257.99 I

5OMe3R



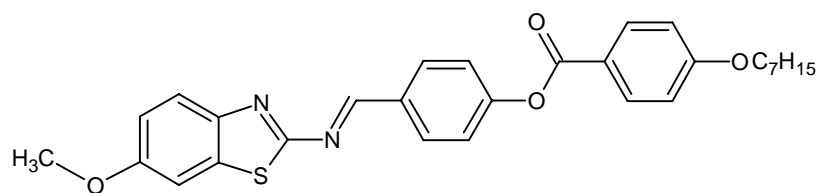
Cr 129.06 N 246.20 I

6OMe3R



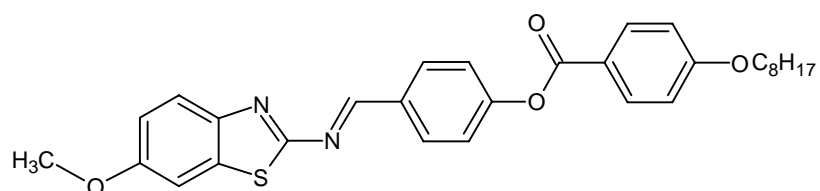
Cr 118.75 N 243.44 I

7OMe3R



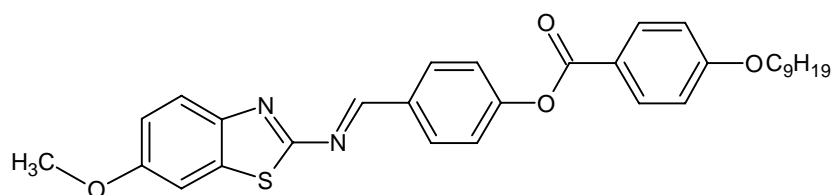
Cr₁ 60.04 Cr₂ 124.51 N 238.16 I

8OMe3R



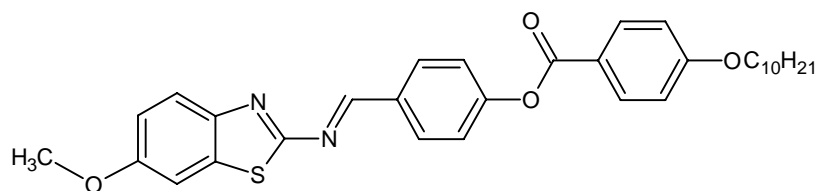
Cr₁ 87.47 Cr₂ 126.97 N 233.77 I

9OMe3R



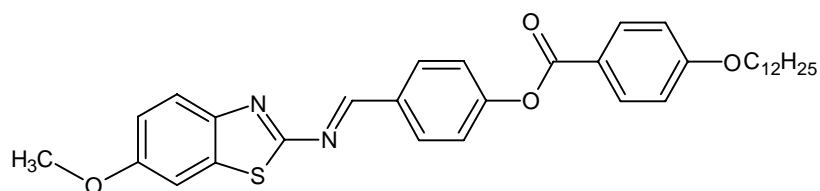
Cr 116.82 N 237.95 I

10OMe3R



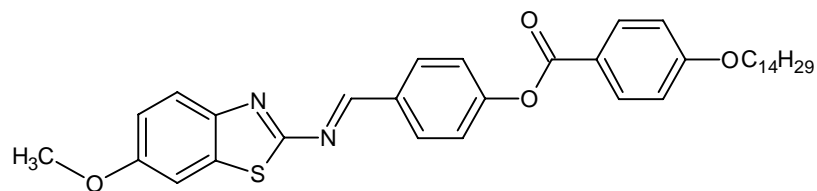
Cr 97.34 N 225.88 I

12OMe3R



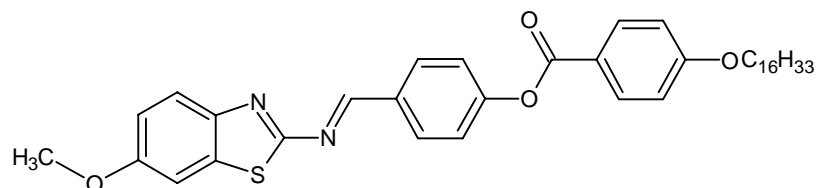
Cr 75.69 SmC 126.75 N 205.65 I

14OMe3R



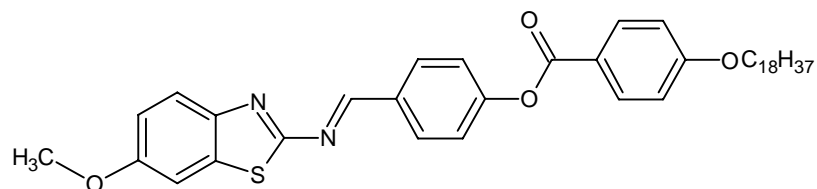
Cr₁ 42.75 Cr₂ 80.76 SmC 139.72 N 183.22 I

16OMe3R



Cr 67.98 SmA 101.33 I

18OMe3R



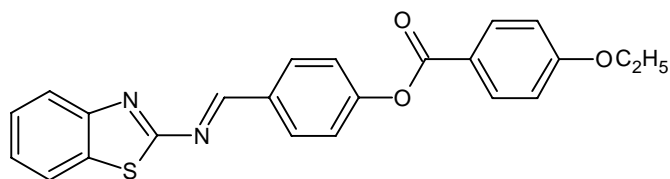
Cr 66.61 SmA 92.32 I

Series 2: (III) nHB3R

Compound

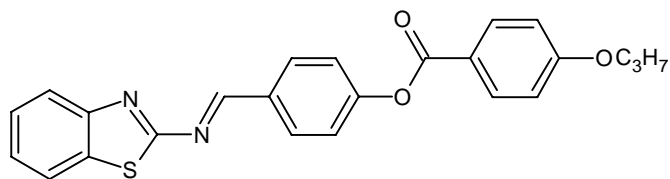
Molecular Structural and Phase Transition Temperature (°C)

2HB3R



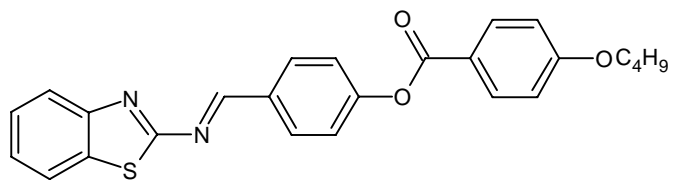
Cr₁ 56.51 Cr₂ 167.01 N 216.85 I

3HB3R



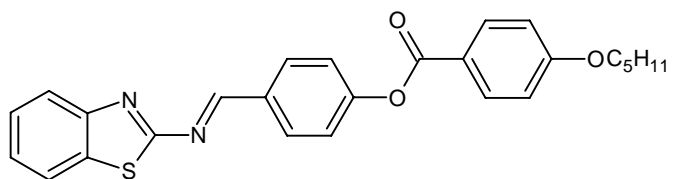
Cr 134.79 N 234.14 I

4HB3R



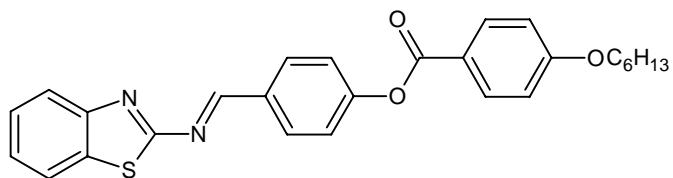
Cr 143.38 N 231.10 I

5HB3R



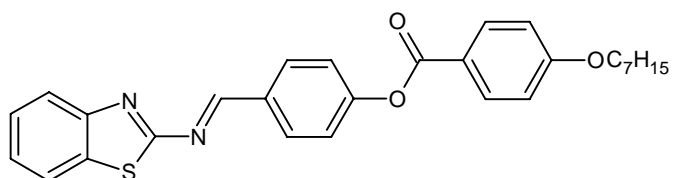
Cr 113.47 (SmA 86.75) N 222.01 I

6HB3R



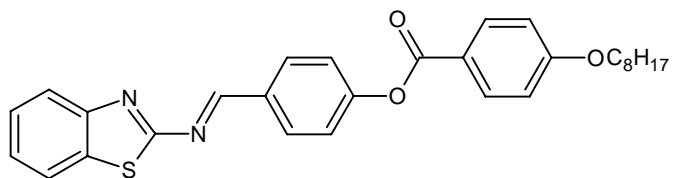
Cr 110.04 SmA 123.86 N 209.25 I

7HB3R



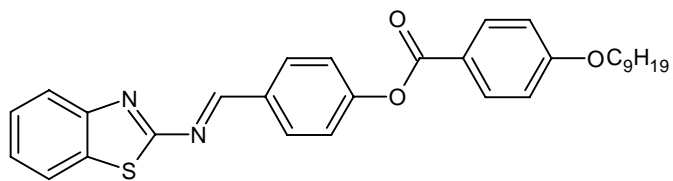
Cr 107.16 SmA 139.88 N 212.28 I

8HB3R



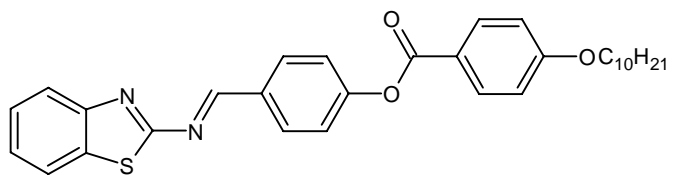
Cr₁ 50.23 Cr₂ 95.36 SmA 128.43 N 171.78 I

9HB3R



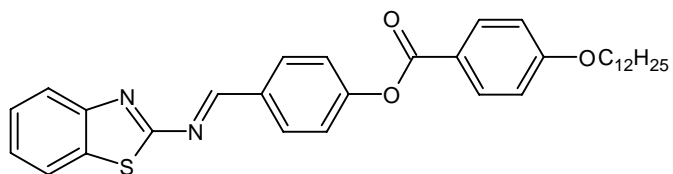
Cr 97.25 SmA 145.75 N 176.92 I

10HB3R



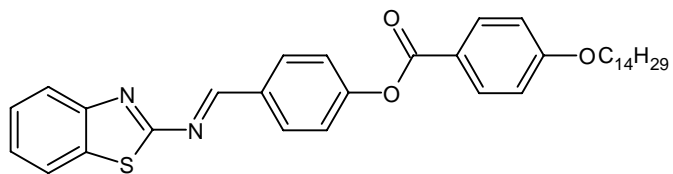
Cr₁ 56.70 Cr₂ 96.99 SmA 157.83 N 182.01 I

12HB3R



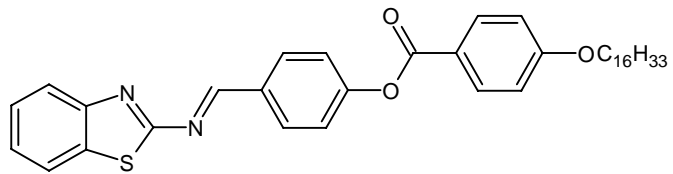
Cr 95.75 SmA 164.63 N 179.64 I

14HB3R



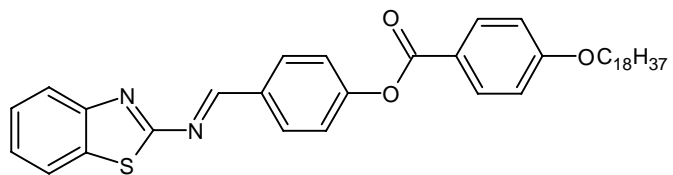
Cr 94.23 SmA 173.89 N 179.70 I

16HB3R



Cr₁ 63.12 Cr 94.77 SmA 163.37 I

18HB3R

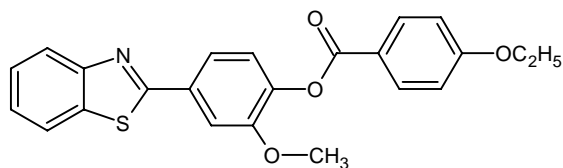


Cr 70.80 SmA 112.15 I

Series 3: (I) nMOBZT

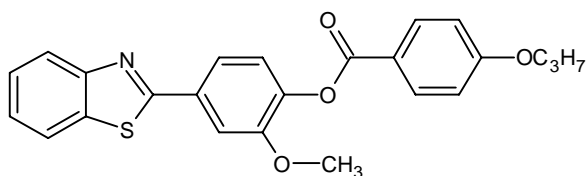
Compound Molecular Structural and Phase Transition Temperature (°C)

2MOBZT



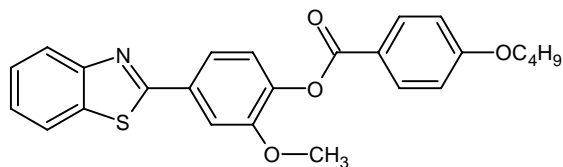
Cr 141.16 I

3MOBZT



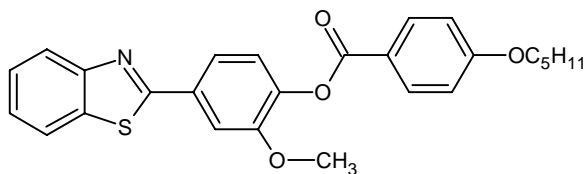
Cr 129.08 (N 93.31) I

4MOBZT



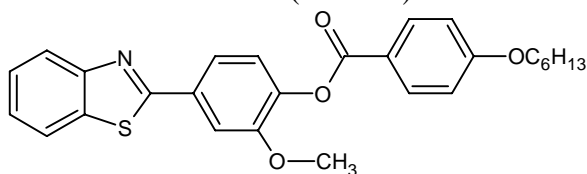
Cr 124.69 (N 109.66) I

5MOBZT



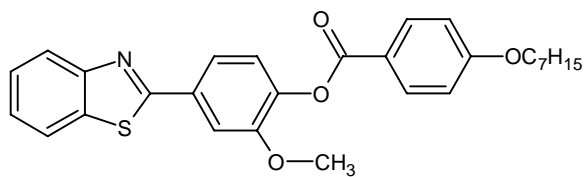
Cr 103.23 (N 85.71) I

6MOBZT



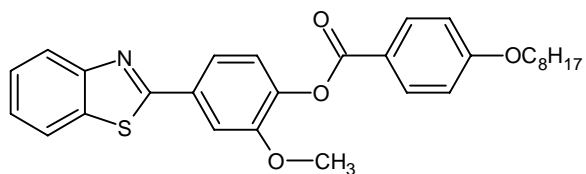
Cr 91.36 N 96.34 I

7MOBZT



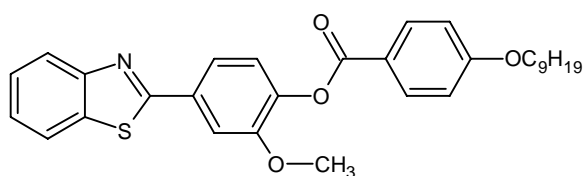
Cr 89.59 (N 87.31) I

8MOBZT



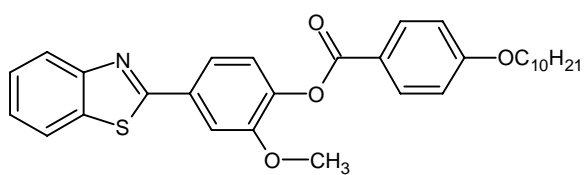
Cr 87.02 N 95.83 I

9MOBZT



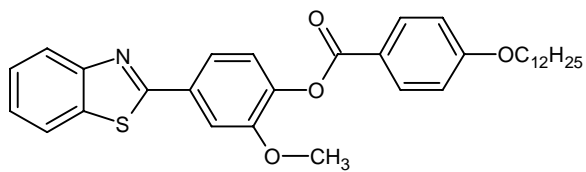
Cr 85.58 (N 86.17) I

10MOBZT



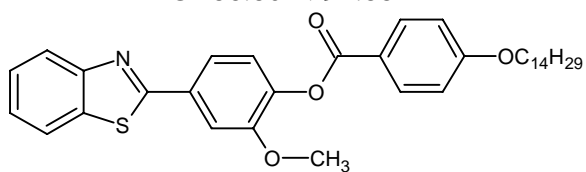
Cr 83.73 N 88.34 I

12MOBZT



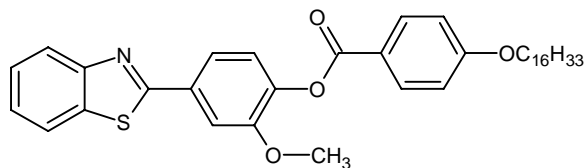
Cr 86.80 N 92.88 I

14MOBZT



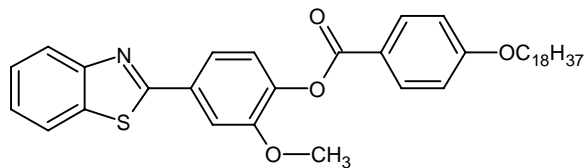
Cr 86.80 N 91.99 I

16MOBZT



Cr 94.81 (N 89.2) I

18MOBZT



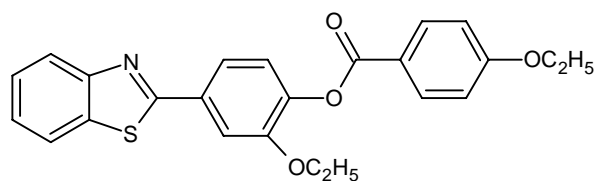
Cr 98.14 (N 85.64) I

Series 3: (II) nEOBZT

Compound

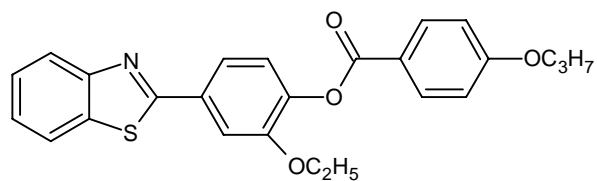
Molecular Structural and Phase Transition Temperature (°C)

2EOBZT



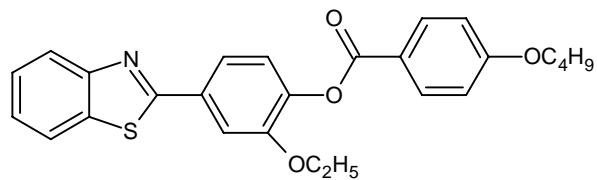
Cr 142.35 I

3EOBZT



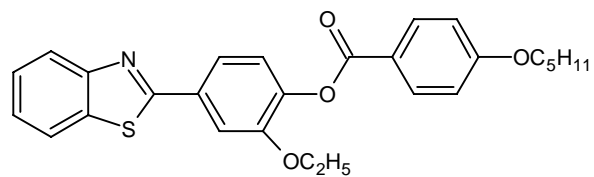
Cr 140.93 (N 51.06) I

4EOBZT



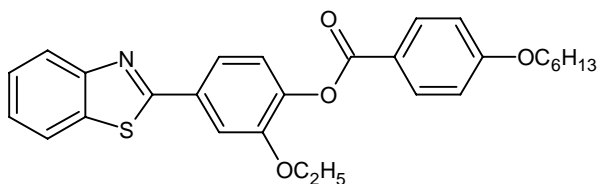
Cr 132.12 (N 68.34) I

5EOBZT



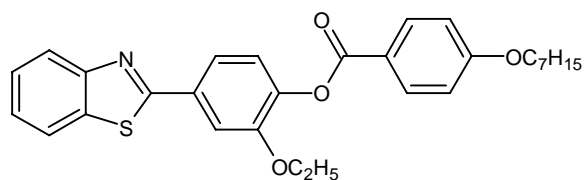
Cr 123.76 (N 49.69) I

6EOBZT



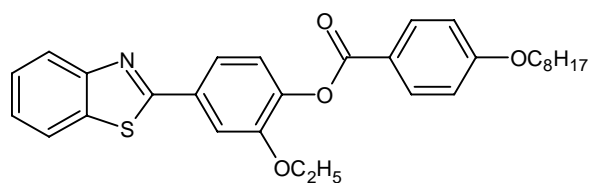
Cr 122.86 (N 64.69) I

7EOBZT



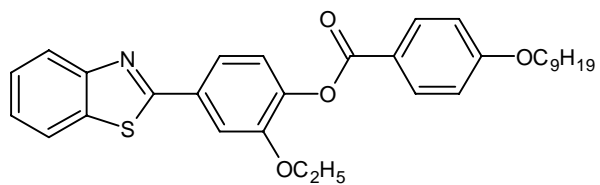
Cr 110.44 (N 60.83) I

8EOBZT



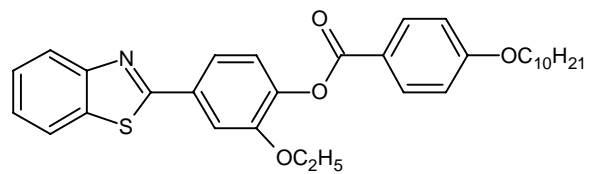
Cr 101.97 (N 56.27) I

9EOBZT



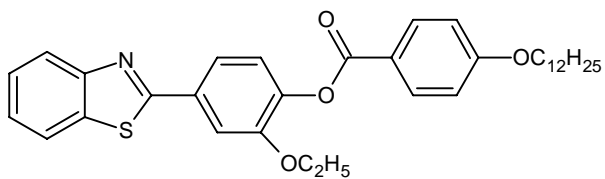
Cr 103.15 (N 59.80) I

10EOBZT



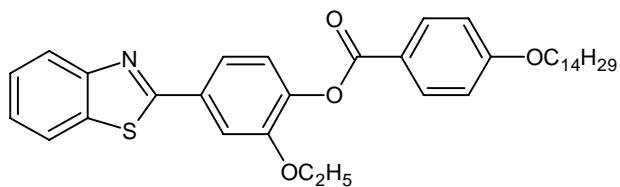
Cr 86.24 (N 65.24) I

12EOBZT



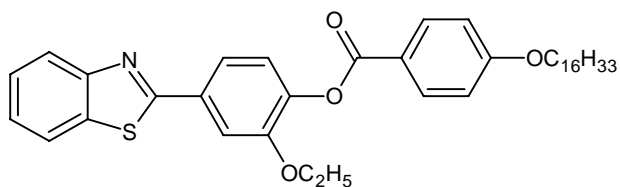
Cr 99.02 (N 68.67) I

14EOBZT



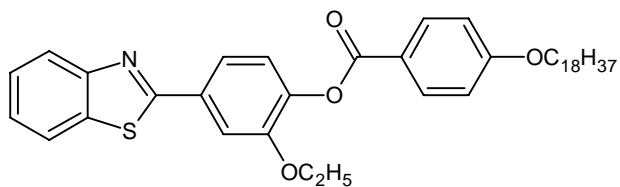
Cr 96.63 (N 66.91) I

16EOBZT



Cr 93.58 (N 66.57) I

18EOBZT



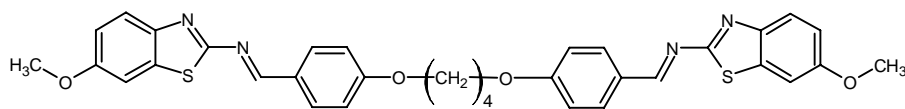
Cr 96.71 (N 62.48) I

Series 4: (I) nOMeD

Compound

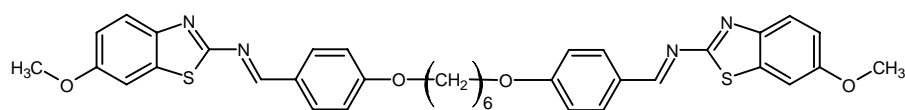
Molecular Structural and Phase Transition Temperature (°C)

4OMeD



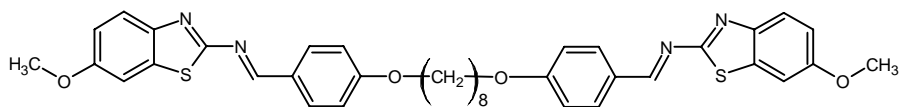
Cr 191.4 I

6OMeD



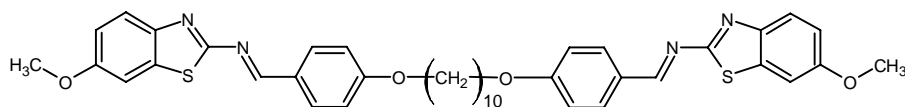
Cr 201.1 I

8OMeD



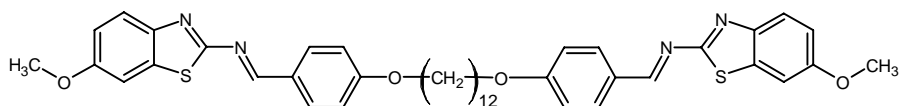
Cr 163.75 N 201.8 I

100MeD



Cr 194.4 I

120MeD



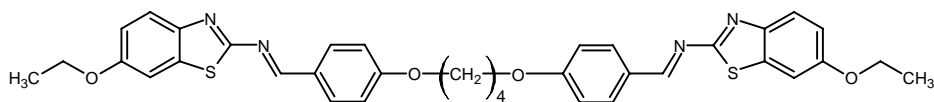
Cr 119.1 N 144.1 I

Series 4: (II) nOEtD

Compound

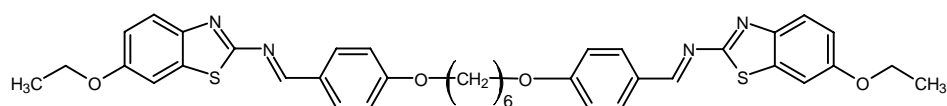
Molecular Structural and Phase Transition Temperature (°C)

4OEtD



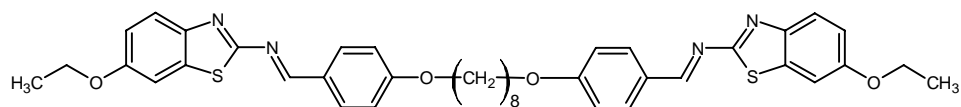
Cr 217.6 I

6OEtD



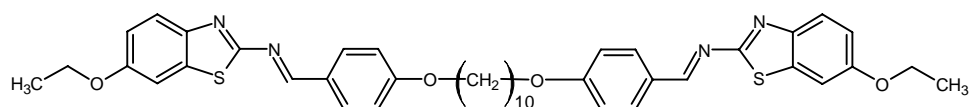
Cr 199.5 N 264.8 I

8OEtD



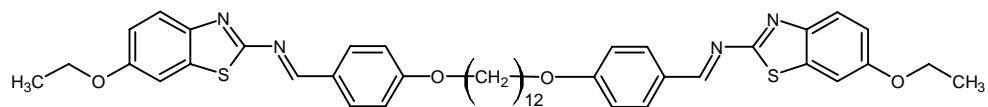
Cr 191.6 N 242.8 I

100EtD



Cr 170.2 N 190.1 I

12OEtD

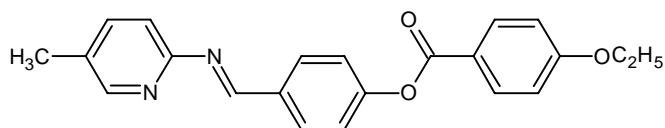


Cr 165.3 N 203.6 I

Series 5: nPM5B

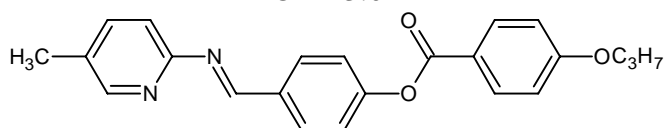
Compound Molecular Structural and Phase Transition Temperature (°C)

2PM5B



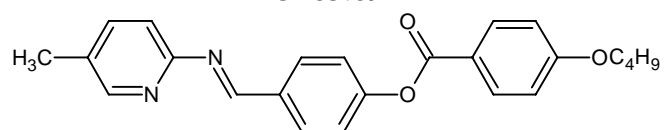
Cr 123.0 I

3PM5B



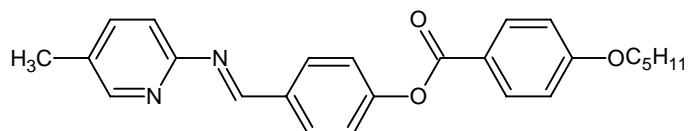
Cr 83.69 I

4PM5B



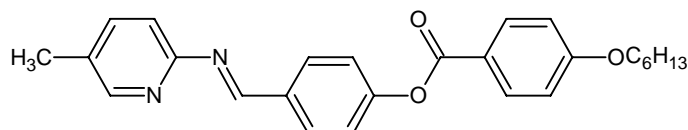
Cr 89.36 I

5PM5B



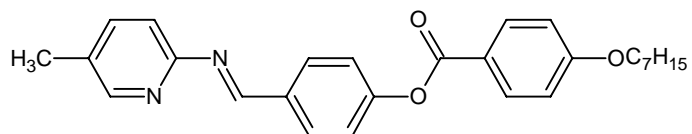
Cr₁ 73.46 Cr₂ 90.41 N 202.58 I

6PM5B



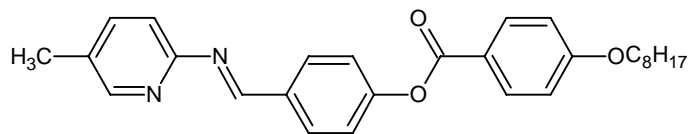
Cr₁ 53.41 Cr₂ 93.47 N 203.28 I

7PM5B



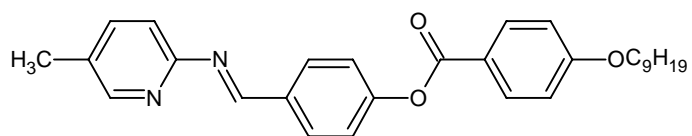
Cr₁ 48.76 Cr₂ 68.23 N 185.11 I

8PM5B



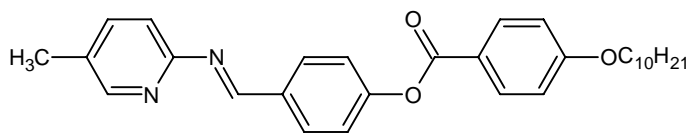
Cr₁ 47.44 Cr₂ 75.84 N 191.88 I

9PM5B



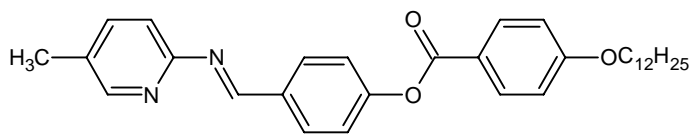
Cr₁ 49.57 Cr₂ 78.80 N 179.54 I

10PM5B



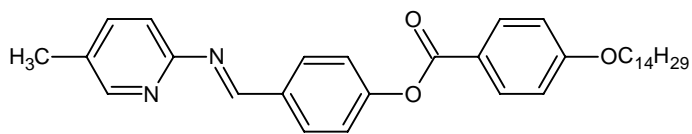
Cr₁ 55.67 Cr₂ 79.48 N 178.63 I

12PM5B



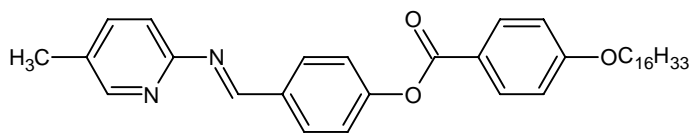
Cr₁ 72.84 Cr 81.14 N 179.08 I

14PM5B



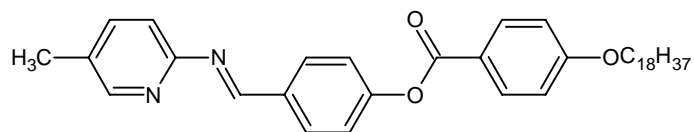
Cr 58.89 SmA 114.67 N 130.68 I

16PM5B



Cr 66.9 SmA 77.82 I

18PM5B

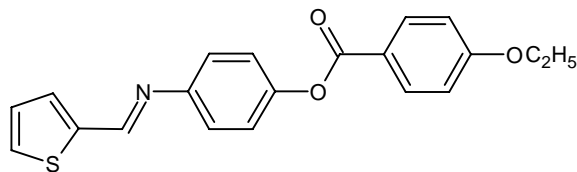


Cr₁ 72.75 Cr₂ 82.68 I

Series 6: nTAP

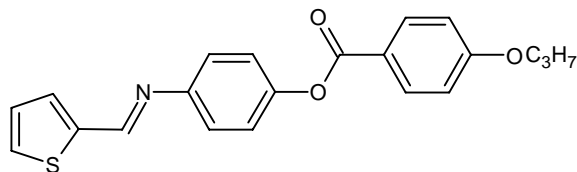
Compound Molecular Structural and Phase Transition Temperature (°C)

2TAP



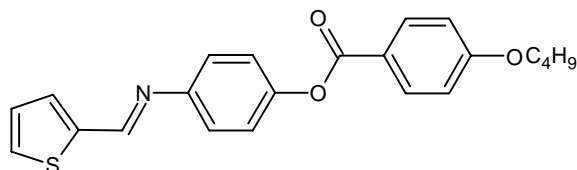
Cr 138.4 N 151.5 I

3TAP



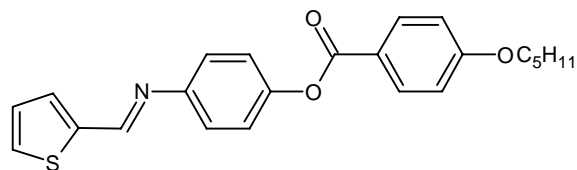
Cr₁ 111.92 Cr₂ 116.01 I

4TAP



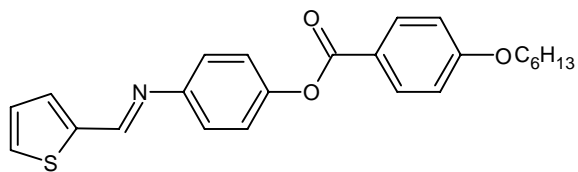
Cr₁ 43.51 Cr₂ 58.54 Cr₃ 131.5 I

5TAP



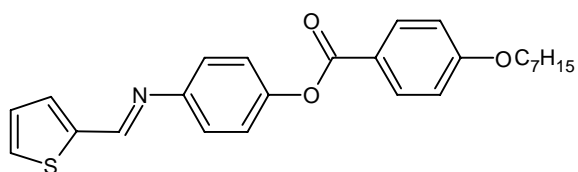
6TAP

Cr 118.06 I



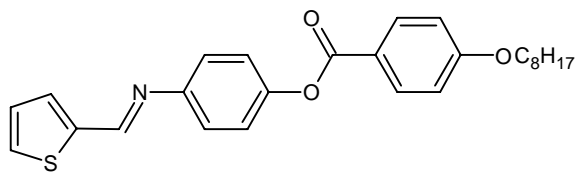
7TAP

Cr 121.32 N 128.63 I



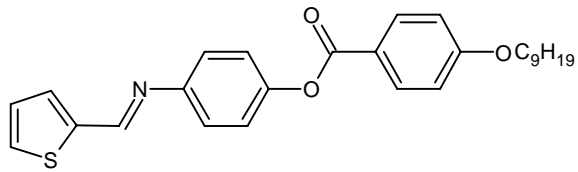
8TAP

Cr 118 N 120.33 I



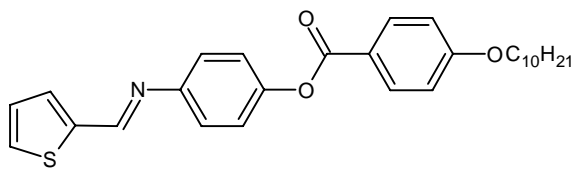
9TAP

Cr 110.99 N 125.34 I



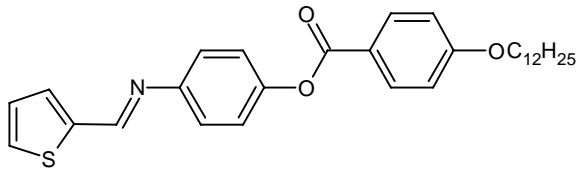
10TAP

Cr 100.80 N 118.51 I



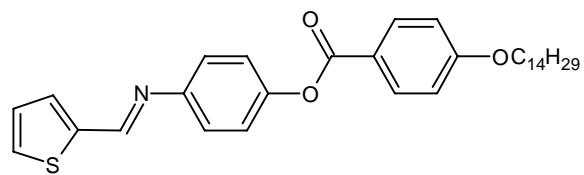
12TAP

Cr 103.74 N 121.41 I



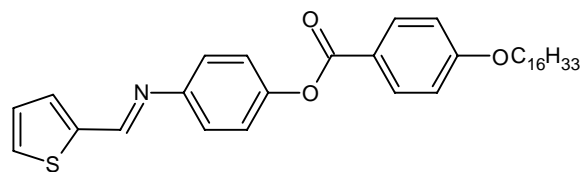
Cr 103.78 N 120.28 I

14TAP



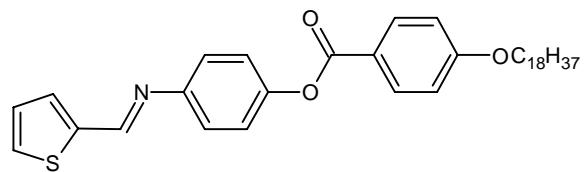
Cr₁ 86.98 Cr₂ 103.19 N 117.25 I

16TAP



Cr₁ 95.03 Cr₂ 102.52 N 114.23 I

18TAP



Cr 118.05 I

Appendix 12

Ha, S.T., Foo, K.L. *et al.*, Chin. Chem. Lett, 2012, 23, pp. 761-764.



SciVerse ScienceDirect

Chinese Chemical Letters 23 (2012) 761–764

CHINESE
CHEMICAL
LETTERS

www.elsevier.com/locate/ccllet

Mesomorphic behavior of new benzothiazole liquid crystals having Schiff base linker and terminal methyl group

Sie Tiong Ha^{a,*}, Kok Leei Foo^a, Hong Cheu Lin^b, Masato M. Ito^c, Kazuma Abe^c, Kenji Kunbo^c, S. Sreehari Sastry^d

^a Department of Chemical Science, Faculty of Science, Centre for Biodiversity Research, Universiti Tunku Abdul Rahman, Jln Universiti, Bandar Barat, 31900 Kampar, Perak, Malaysia

^b Department of Material Science & Engineering, National Chiao Tung University, Hsinchu 300, Taiwan, China

^c Faculty of Engineering, Soka University, 1-236 Tangi-cho, Hachioji, Tokyo 192-8577, Japan

^d Department of Physics, Acharya Nagarjuna University, Nagarjuna Nagar 522 510, India

Received 15 February 2012

Available online 9 June 2012

Abstract

A homologous series of heterocycles, 6-methyl-2-(4-alkoxybenzylidenamino)benzothiazoles, were synthesized and characterized using FT-IR, ¹H and ¹³C NMR and mass spectrometric analysis. Enantiotropic nematic phase was observed for shorter members. Smectic A phase only emerged from octyloxy derivative onwards. The terminal methyl group at the benzothiazole fragment and the Schiff base linkage influenced the mesomorphic behavior of the present series.

© 2012 Sie Tiong Ha. Published by Elsevier B.V. on behalf of Chinese Chemical Society. All rights reserved.

Keywords: Schiff bases; Benzothiazole; Liquid crystal; Smectic A; Nematic

Over the past thirty years, liquid crystals have become the quintessential molecular electronic materials of our present day era. Their applications encompass research activities in the field of surfactant and detergents, membrane for air separation, high strength polymers, heat resistant materials, photonic, thin films, semiconductors *etc.* [1]. Heterocycles are of great importance as core units in thermotropic liquid crystals due to their ability to impart lateral and/or longitudinal dipoles combined with changes in the molecular shape [2]. A great deal of mesomorphic compounds containing heterocyclic units have been synthesized, and interest in such structures is constantly growing [2,3]. However, only scant information on the inclusion of benzothiazole core into liquid crystal system is available [4–6]. Funahashi and Hanna have reported the fast hole transport property of the photoconductive calamitic liquid crystal, 2-(4-heptyloxyphenyl)-6-dodecylthiobenzothiazole [7]. A benzothiazole ring containing the electron-rich sulphur atom can contribute to a low ionization potential and also induce a smectic phase. The flat molecular shape with little interannular twisting in fused heterocyclic rings may also facilitate a high degree of overlapping molecular wave function for an efficient hopping mechanism of charge transport [8]. Benzothiazole unit was also found in fluorescent compounds, which is useful in applications as a result of high fluorescence quantum yields in the presence

* Corresponding author.

Email addresses: hast_utar@yahoo.com, hast@utar.edu.my (S.T. Ha).